An exploratory study for the $\omega - \pi$ transition form factor with WASA-at-COSY

Dissertation zur Erlangung des Grades
Doktor der Naturwissenschaften
am Fachbereich für Mathematik und Naturwissenschaften
der Bergischen Universität Wuppertal

vorgelegt von
Farha Anjum Khan

unter Führung von
Prof. Frank Goldenbaum

November, 2022

To my family, friends, teachers and especially to my late grandmother.

Contents

Abstract

The electromagnetic transition form factor allows probing the internal structure of mesons by studying them in the rare Dalitz mode. The internal structure here reveals the information on the quark composition, constituent quark mass, quark-gluon structure and their interactions, quark confinement mechanism, and the fact that how confinement affects meson internal structure. These form factors are provided as an input to the hadronic contribution of the anomalous magnetic momentum of muon $a_\mu = (g_\mu - 2)/2$, which is an interesting quantity and could be a potential hint for physics beyond the Standard Model [1, 2, 3, 4, 5, 6, 7, 8, 9]. It is well known that the gyromagnetic ratio g of a lone muon, which is its rate of precession in an external magnetic field, should be 2 according to the Paul Dirac formula. However, the value of the ratio g deviates from 2 due to muons interactions with a quantum foam of subatomic particles popping in and out of existence. Although, the Standard Model is able to predict this anomaly called anomalous magnetic moment $a_\mu = (g_\mu - 2)/2$ extremely precisely, the difference between the accepted theoretical predictions reviewed by Aoyama et al. (2020) [7] ($116591810(43)\times10^{-11}$) and the experimental global average published by Albahri et al. (2021) [8, 9] ($116592061(41)\times10^{-11}$) is at a significance of 4.2 sigma. The theoretical efforts by Aoyama et al. (2020) [7] account for both the non-perturbative methods of computation, the dispersion relations and the lattice approach to QCD. This is compelling evidence of new physics and hints at the existence of unknown interactions involving additional particles or forces that are not accounted for by the Standard Model. Subsequently, Borsanyi et al. (2021) [10] computed the value of $(g_\mu - 2)/2$, which is $7075(55)\times10^{-11}$, using lattice approach to QCD. This result favours the experimentally measured value of $(g_\mu - 2)/2$ over the results based on the dispersion relation.

The electromagnetic transition form factors of mesons have been studied experimentally as well as theoretically. Among various mesons, the ω is one of the mesons which shows disagreement with the standard vector meson dominance prediction, as determined from the decay $\omega \to l^+ l^- \pi^0$ [11, 12, 13, 14, 15]. However, its form factor seems to agree with the data except at larger four-momentum transfer (q^2) when theoretical efforts attempt to go beyond the vector meson dominance [16, 17, 18, 19, 20, 21, 22, 23, 24, 25, 26]. Earlier experiments provided results on the electromagnetic transition form factor for the ω-π vertex in the $\omega \to \mu^+\mu^-\pi^0$ mode, as reviewed by L. G. Landsberg in Ref. [11]. Thereafter, the NA60 collaboration has confirmed the results in AA as well as pA collisions [13, 14, 15]. Furthermore, in the immediate past, the transition form factor has been recomputed using spin-improved holographic light-front wave-functions for the mesons, which shows an agreement with the NA60 data in all invariant mass ranges [27]. Moreover, the recent measurement from the photon-induced reactions with A2 tagged-photon facility at MAMI shows a better agreement with most of the theoretical calculations as compared to the previous experiments [28]. However, no final conclusion could be drawn from the MAMI data due to the lack of precision and NA60 measurements are limited by its inability to reconstruct the π^0 meson and the analysis approach, which is entirely based on the MC models. Consequently, more measurements with a different experimental approach, other than heavy-ion collision

or photon-induced reactions, and with alternative analysis methods that solely not rely on the MC models, and with much better statistics are invigorated.

WASA-at-COSY detector, which consists of a forward and a central part that nearly covers 4π steradian, is capable of reconstructing the recoil particle in the forward direction and the decay products, e^+, e^-, γ, in the central part. Thus, inclusive, as well as exclusive reconstruction of the decaying meson, is possible. This reduces the obscurities in background subtraction as compared to NA60 measurements. Moreover, detecting e^+e^- pairs gives access to the full range of q^2 due to kinematics. Furthermore, WASA-at-COSY uses a completely different experimental approach of elementary reactions (hadron-hadron collisions) and produces the mesons close to the meson production threshold. Considering these advantages, WASA-at-COSY could be proved to be a potential tool to improve our understanding of the form factor of ω meson. This allowed WASA-at-COSY to investigate the issues noticed by other experiments.

The data available for such studies are recorded with WASA-at-COSY using *pd* and *pp* collisions with the focus on doing a feasibility study for the $\omega - \pi$ transition form factor in the $\omega \to e^+e^-\pi^0$ decay mode. The main goal of this thesis is the feasibility study to reconstruct the $\omega \to e^+e^-\pi^0$ decay with the WASA-at-COSY *pd* collision data recorded at 1.45 GeV and 1.50 GeV beam kinetic energies. This feasibility study has been conducted by firstly studying the two major background contributions $\omega \to \pi^0\gamma$ and $\omega \to \pi^0\pi^+\pi^-$, followed by the $\omega \to e^+e^-\pi^0$ decay.

As a first step, the analysis of the prominent real photon case $\omega \to \pi^0\gamma$ is established as a reference decay for the $\omega \to e^+e^-\pi^0$ mode and its branching ratio is determined. A branching ratio study of the $\omega \to \pi^0\gamma$ mode as a reference decay will ensure the control and quality of the analysis procedure and the data. Furthermore, the most prominent background contribution $\omega \to \pi^0\pi^+\pi^-$, which is having the same topology as that of the signal $\omega \to e^+e^-\pi^0$, has been investigated as a background study and the data quality cross-check. Finally, the analysis of the $\omega \to e^+e^-\pi^0$ exclusive final state is established.

1. Theory and Motivation

1.1. The ω meson

The particle ω is a meson, consisting of quark $(u,d,s,..)$ and anti-quark $(\bar{u},\bar{d},\bar{s},..)$ pairs combined as $((u\bar{u}-d\bar{d})/\sqrt{2})$. The quark model classifies ω as a vector meson under SU(3) group. The ω meson is a member of one of the three generated octets where the parallel aligned quark and anti-quark pair sets the spin angular momentum to be 1. The spin angular momentum in combination with 0 orbital angular momentum gives the total angular momentum as 1 (J = l+s = 1). As a consequence of the 0 orbital angular momentum, the ω meson has odd parity. Moreover, the wave-function of the ω meson is asymmetric under the charge conjugation or C-parity transformation. The same is true for the C-parity and isospin I_z (z-component of the isospin I) derived G-parity transformation ($G=-1$). The zero strangeness, zero isospin and zero hypercharge of the ω meson makes it a truly neutral particle. The final quantum number of the ω meson is written as $I^G(J^{PC}) = 0^-(1^{--})$ (see Table 1.1 for reference).

s	l	J	P	C	G	S	I_z	Q
1	0	1	-1	-1	-1	0	0	0

Table 1.1.: Quantum numbers of the ω meson.

Since 1955, many theorists predicted ω as a neutral vector meson [29, 30, 31, 32, 33, 34, 35, 36] for different reactions, and since then many experimental searches have been performed. The ω meson was experimentally discovered first by B. Maglich in the 1961 at the Lawrence Berkeley National Laboratory Bevatron [37, 38] in the $\bar{p}p \to \pi^+\pi^-\pi^+\pi^-\pi^0$ reaction. Its quantum number and lifetime were first determined at Berkeley [37, 38]. Ever since, many investigations have been made to understand its properties. Experimentally, the mass of the ω meson was found to be (782.65±0.12) GeV/c^2 [39].

Due to the very short lifetime of the omega meson (0.8×10^{-22}) s the classical method of particle scattering can not be used to reveal any structural information. However, the information about its quark content and quark wave function is accessible via studying the decay processes of the ω meson.

The constituent quark mass value can be found from the decay width, by considering the meson radiative decays ($\omega \to \pi^0\gamma$) within the framework of $U_0(1)\times U(1)\times SU(2)$ gauge symmetry, based on the linear sigma-model extended by the gauge and quark-meson interactions [40]. The quark-gluon structural information can be obtained by studying the ω decay in the rare Dalitz mode where a pseudoscalar meson and a virtual photon (γ^*) is produced. The virtual particles violate the relativistic energy-momentum relation $E^2 = p^2 + m^2$, and therefore, the virtual photon involved in the exchange mechanism becomes off-shell. Hence the squared four-momentum transferred by the virtual photon can be measured as the invariant mass of the dilepton. The dileptons invariant mass distributions, obtained from the empirical result, are compared with the theoretical predictions

for the point-like particle. Any deviation from the expectation reveals the inner structure of the meson, which is characterized by the transition form factor. The various form factors describing the photon-hadron interaction are needed as an input for calculations of the hadronic light-by-light (LBL) contribution to the anomalous magnetic momentum of muon $a_\mu = (g_\mu - 2)/2$ [1, 2, 3, 4, 5, 6, 7, 8, 9]. The most important contribution is from the lightest state, the pion. The form factor that describes the interaction of off-shell pions ($E^2 - p^2 \neq M^2$) with off-shell (or on-shell ($E^2 - p^2 = M^2$)) photons $\pi^{0*} \to \gamma^*\gamma^*$ enters in the pion-exchange contribution to LbL in the $(g_\mu - 2)$. The recent experimental world-average result announced by the Muon g-2 collaboration at Fermilab is significantly away from the Standard Model (SM) based theoretical prediction [7, 8, 9, 10]. The form factor of the vector meson (ω) is just a special case of the pseudoscalar meson π^0, where one of the virtual photons couples to an ω and the other to a dilepton. The focus of this work is to perform the feasibility studies for the $\omega - \pi$ transition form factor measurement using $\omega \to \pi^0 e^+ e^-$ decay mode.

1.2. The Form Factor

The study of the structure of hadron is important in elaborating the present knowledge on the nature of matter. The structure of an atom is represented by the electrons' spatial distribution, which is described by the ground state wave function. The electron probability density function of a hydrogen like atom at a point x is defined in term of the electron wave function $\psi(x)$ as $\rho(x) = \psi^*(x)\psi(x)$, if spin is neglected. The charge density and the probability density function of an atom are proportional to each other and hence, the charge density of the atom is defined as $e\rho(x)$. The wave functions of all possible atomic states must be known to determine an atom's complete structure. The idea of the charge distribution is still acceptable in nuclei, but the charge distribution and spatial distribution are not directly proportional any more. A new complication comes into existence while going deep inside an atom for the nucleons. As an impact of the high momentum, needed for the structural exploration, nucleons recoil with the velocities near light ($\Delta p \cdot \Delta x \geq \hbar/2$). Consequently, it becomes difficult to evaluate the nucleon charge distribution from the cross-section. Therefore, this problem was addressed by introducing a term called form factor describing the nucleon structure. No structure is found for leptons up to the smallest distances studied ($\leq 10^{-18}$), apparently, they are found to be point-like Dirac particles.

The history of form factor begins with the Rutherford scattering. In Rutherford scattering, both the projectile and target were considered as point particles with no spin. The process is modified by introducing the spin $\frac{1}{2}$ to the projectile, called Mott scattering. The cross section, considering the extended structure of the target, is then further modified by introducing the form factor. The differential cross section ($d\sigma/dq^2$) for the scattering of a point particle such as an electron from a particle with a specific space structure is given as

$$\frac{d\sigma}{dq^2} = \frac{d\sigma}{dq^2}\Big|_{point-like} \mid F(\mathbf{q}^2) \mid^2 . \tag{1.1}$$

The multiplicative factor $F(\mathbf{q}^2)$ is called the *form factor*, where $\mathbf{q^2} = (\mathbf{p} - \mathbf{p'})^\mathbf{2}$ is the square of the momentum transfer. The form factor at zero momentum transfer is 1 for both negative and positive particles. The form factor can be found by comparing the experimental data with the differential cross-section of the scattering of an electron off a point like particle ($d\sigma/dq^2{}_{point-like}$).

1.3. The Electromagnetic Form Factor

The form factor described in the previous section is the simplest case of the spin-$\frac{1}{2}$ electron scattering off the spin-less nucleus. The target spin is introduced further to achieve a more realistic picture. The magnetic moment due to spin has its own spatial distribution, and consequently the magnetic form factor comes into play. The description of the electromagnetic structure in such cases is given by two different form factors, namely, electric and magnetic. Therefore, termed as electromagnetic form factor. The form factor here carries

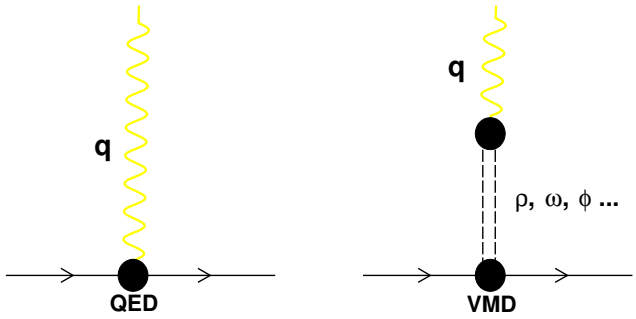

Figure 1.1.: A simple picture representation of the coupling of the photon (with four-momentum q) to a nucleon in the quantum electro-dynamics (QED) and vector meson dominance (VMD).

complete information of the electromagnetic structure of particles and is a directly measurable characteristic of the particle's structure, both in the relativistic and the non-relativistic processes. However, in the relativistic case, no simple correlation between the form factor and the spatial distribution of the hadron can be obtained. The Quantum Field Theory (QFT) suggests that the interaction between the particles in these processes occurs via exchange of virtual photons. The simplest of such mechanisms, as given by the Quantum Electro-Dynamics (QED), is the exchange of one virtual photon, as illustrated in Fig. 1.1. The virtual photon can provide the information about the probability amplitude of a particle traveling through space and time. The momentum transfer (**q**) in these processes is a four-dimensional quantity defined as $q^2 = (\Delta E)^2 - \Delta p^2$. The virtual photon can be *space-like* or *time-like*, depending upon whether the $|q^2|$ is negative or positive, respectively.

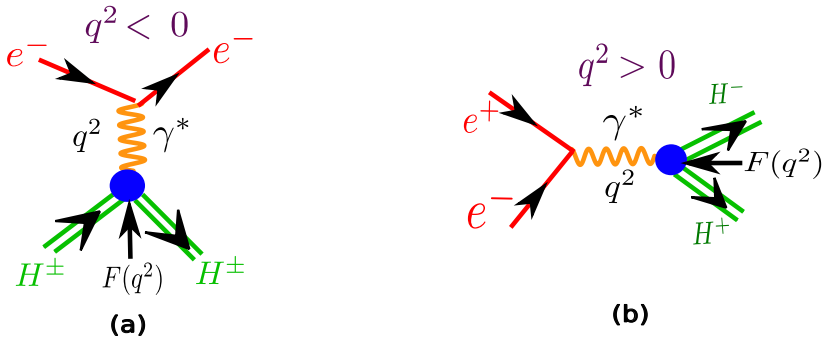

Figure 1.2.: **(a):** The left panel represents the Feynman diagram for electron-hadron elastic scattering via photon (γ^*) exchange in the space-like momentum transfer region ($q^2 < 0$). **(b):** The Feynman diagram of the electron-positron annihilation is shown on the right panel. Where a pair of hadron and anti-hadron is created via a virtual photon exchange in the time-like momentum transfer region ($q^2 > 0$).

The simplest example of space-like form factors is the elastic electron-hadron (eH) scattering, such as ep, en, $e\pi^{\pm}$ and $eK^{\pm}$ scattering. The Feynman diagram of the eH scattering is illustrated in the (a) panel of Fig. 1.2. Here, the direction of electron's momentum in the center-of-mass (CM) frame is altered, i.e., $\Delta\mathbf{p}^2 = (2p \cdot sin\frac{\theta}{2})^2 \neq 0$, where θ is the scattering angle. While the energy transfer remains constant in the CM frame, i.e., $(\Delta E)^2 = 0$. Therefore, $q^2 = -\Delta\mathbf{p}^2 = -4p^2 \cdot sin^2\frac{\theta}{2} < 0$, where $0 \leq \frac{\theta}{2} \leq \frac{\pi}{2}$. The smaller $\frac{\theta}{2}$ corresponds to the smaller values of $sin^2\frac{\theta}{2}$ and thus larger q^2 values. In other words the larger the momentum transfer is, the smaller will be the space where the electron gets scattered by hadron, which is a corollary of the uncertainty principle. Here the magnitude of the momentum transferred by the virtual photon can be altered by tuning the momentum of the incident electron.

Alternatively, the electron-positron annihilation to create hadron(s), such as, $e^+e^- \rightarrow \pi^+\pi^-$ and $e^+e^- \rightarrow K^+K^-$, is one of the example of the time-like momentum transfer. The (b) panel of Fig. 1.2 shows the Feynman diagram of the same. In these processes, equal energetic electron and positron with equal and opposite momentum annihilate to create an intermediate virtual photon. The virtual photon transfers no momentum $\Delta\mathbf{p}^2 = 0$ but transfers an energy twice that of the energy of each electron, i.e., $\Delta E^2 = (2E)^2$. The four-momentum transferred by the virtual photon is $q^2 = 4E^2 > 0$. In such processes, the four-momentum transfer can be varied by changing the projectile energy.

In a nutshell, the form factor of a hadron can be studied experimentally in the full kinematically allowed q^2 range by performing the elastic scattering and annihilation experiments, which are complementary to each other. The four-momentum transfer of the virtual photon is plotted in the full (q^2) range in the left panel of Fig. 1.3. The range of the space-like and time-like virtual photons are also shown in the figure. As mentioned earlier, in the case of elastic scattering or in the space-like region, the charge particle's form-factor decreases as $|q^2|$ increases. Herewith, for higher momentum transfer, the virtual photon is sensitive only to the inner part of the hadron charge density. The same is true for the time-like region. However, in the time-like region, other phenomena like vector-meson dominance (VMD) dominates and are well evident.

In photon-hadron interaction, a dominant phenomenon comes into play. Where a photon can interact with hadrons not only directly, but also via a virtual vector meson state with the same quantum number as that of the photon. These intermediate propagator mesons are ρ, ω, ϕ, η'. Such type of photon-hadron interaction is predominant and hence is called the vector meson dominance [11]. Here the hadronic electromagnetic current J_μ is proportional to the vector meson fields V_μ [41, 42], i.e., $J_\mu(x) = \sum_V [eM_V^2/2g_{V\gamma}]V_\mu(x)$. Where M_V^2 is the vector meson mass, e is the charge of an electron, $g_{V\gamma}$ is the vector meson and photon coupling constant and μ represents the space-time coordinate. The strength of the vector meson transitions into photons is determined by the coefficient $eM_V^2/2g_{V\gamma}$. A simple pictorial representation of VMD is illustrated in Fig. 1.1, where the intermediate virtual meson state can be seen as propagators in photon-nucleon interaction. The Feynman diagrams of the previously discussed processes, electron scattering and pair annihilation, under the VMD model are shown in the left panel of Fig. 1.3 for illustration.

The qualitative feature of the form factor under VMD model up to the ρ meson is illustrated in the left panel of Fig. 1.3. Here, as q^2 increases and approaches to the vector meson mass ($q^2 = M_V$), the virtual meson will immediately decay via its prominent channel like a real particle after reaching the on-mass shell. At this value of q^2, a strong resonance enhancement can be seen in the distribution of form factor. After passing the resonance ($q^2 > M_\rho$), the form factor will start to diminish until the mass of the next vector meson is reached. This mechanism is seen well pronounced in the time-like virtual photons ranges. The resonance

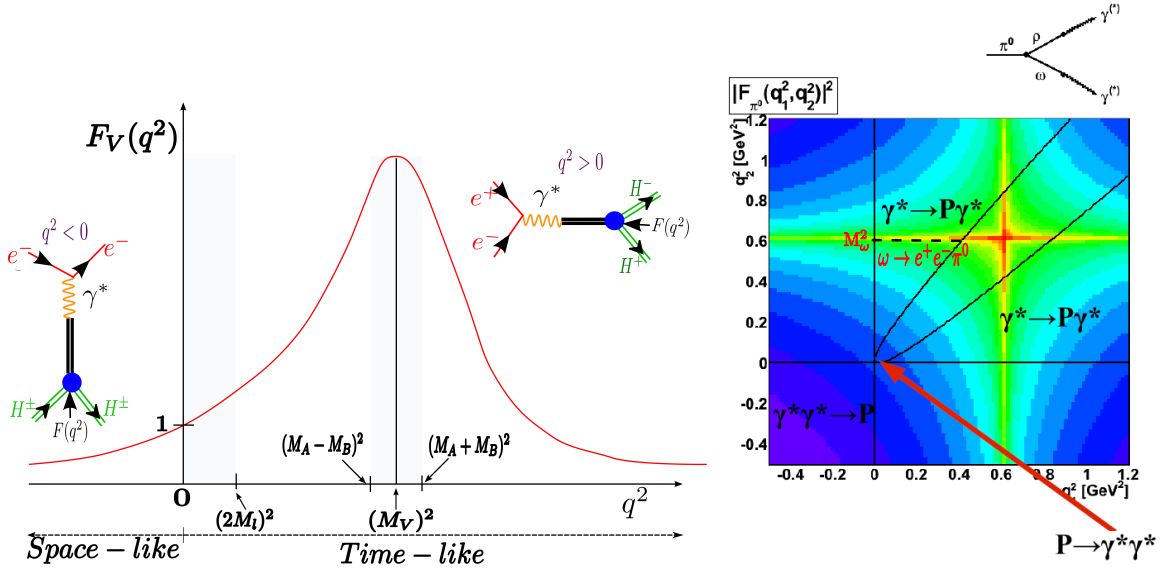

Figure 1.3.: Left panel: The qualitative behavior of the electromagnetic form factor in the whole physically accessible range of q^2. The shaded portions represent the kinematically prohibited region $q^2 > 0$ to $q^2 < (2M_l)^2$ and $q^2 > (M_A - M_B)^2$ to $q^2 > (M_A + M_B)^2$ [11]. The Feynman diagrams for the elastic scattering and annihilation processes in the VMD are shown. **Right panel:** The π^0 meson form factor squared in naive VMD, taken from Ref. [1].

enhancement at the vector meson mass is parameterized by the pole approximation using the BreitWigner formula [1, 39, 41, 43], where the form factor distribution is fitted with the pole formula shown in Equation 1.5. The kinematic limits for the form factor are determined by the masses of the particles involved in the process. The greater the mass of the decaying meson, the larger is the range of the momenta transferred q^2 by the virtual photon. Thus, the quantitative behavior of the form factor for different mesons will be different.

The single-photon exchange processes discussed above (electron scattering and pair annihilation) were for the charged particles. There are particles, truly neutral in nature like γ, such as the π^0, η, η′, ρ^0, ω, and ϕ, which do not possess any kind of charge, i.e., identical to their antiparticles. They can be either symmetric (C=1 for pseudoscalar mesons π^0, η, η′) or asymmetric (C=-1 for photons and vector mesons ρ^0, ω and ϕ) under charge conjugation parity (C), which is conserved in electromagnetic and strong interactions. The form factor information of these truly neutral particles (A) can be accessed from some of their allowed electromagnetic decays into at least one virtual photon ($\gamma^* \to e^+e^-$) and another truly neutral particle (B, γ).

Let's understand and compare the simplest of these processes diagrammatically for two types of mesons. The electromagnetic decay of a pseudoscalar meson (A) into two photons ($A \to \gamma\gamma$) is allowed under the C, and hence their conversion Dalitz decay ($A \to \gamma\gamma^* \to A \to \gamma e^+e^-$). The Feynman diagrams for these types of decays are illustrated in Fig. 1.4. In these types of single photon exchange processes, the electromagnetic form factor can be extracted from the transition amplitude, as both are proportional. Here, the form factor defines the electromagnetic properties of the meson 'A' only, as a single meson is involved. On the other hand, these single photon exchange processes and thus, their corresponding conversion decays are not allowed for the vector mesons due to C parity conservation (see Fig. 1.4). Which lead the decay amplitude, and hence the electromagnetic form factor of the single photon exchange process to zero. Resultantly, for the vector mesons, the electromagnetic form fac-

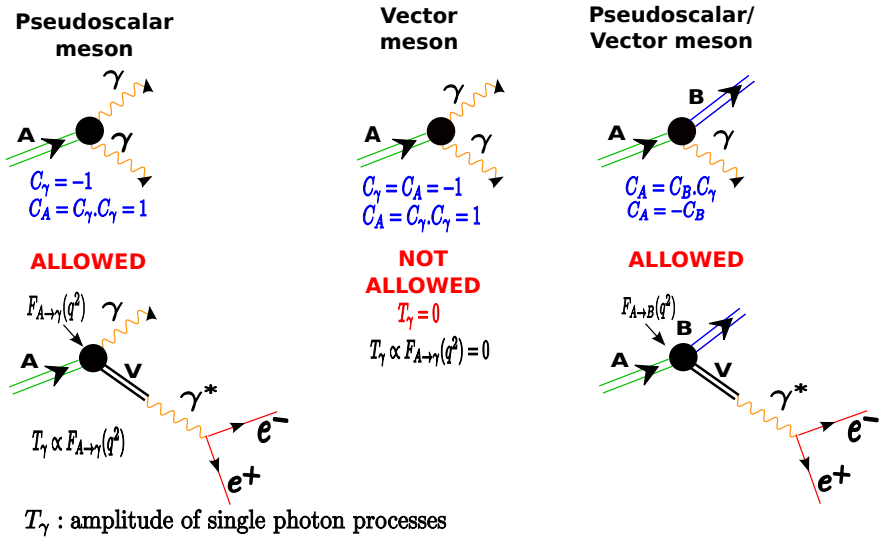

Figure 1.4.: The Feynman diagram for the electromagnetic decays of the truly neutral particles. The first column shows the allowed two photon decay of the pseudoscalar mesons involving single photon exchange process and the corresponding conversion decay. The second column illustrates the forbidden, under C parity conservation, two photon decay of the vector mesons. The third column represents the allowed decay of a meson (A) into another meson (B) and a real or virtual photon.

tor cannot be calculated explicitly, but can be calculated as a transition vertex of one particle (A) transforming into another (B), as illustrated in the third column of Fig. 1.4. The virtual photons in such decay modes transfer the 4-momentum to the lepton pair. The transition form factors in meson conversion decays $A \to B\gamma^*$ are described in the VDM according to Equation 1.5.

Furthermore, these single photon exchange processes in photon-meson interactions discussed so far are the special cases of the double photon exchange processes in π^0 meson $\pi^{0*} \to \gamma^*\gamma^*$ [1], which is a generic representation. Wherein, because the off-shell pion π^{0*} is not a physical quantity, a model-dependent approach is used to describe the interactions of on-shell pions (π^0) with off-shell (γ^*) or on-shell (γ) photons. Similar to the electron-hadron interactions, the inherited virtuality could be both the space-like or the time-like. As mentioned in the beginning, these models are therefore helping to define the constraints for the models used to evaluate hadronic LbL scattering. A brief overview of the generalized case of the pion transition form factor under VMD based models, and further the specificity related to the vector meson transition form factor is presented next.

1.4. The Electromagnetic Meson Transition Form Factor

A naive VMD model picture for the double photon exchange process in π^0 meson is presented in the right panel of Fig. 1.3. The boundaries of the experimentally accessible regions are defined by the parabola and the axes of the plots. Three regions are accessible via the experimental probes Region 1, Region 2, and Region 3. Region 1, $q^2_{1,2} \geq 0$ and $\sqrt{q_1^2} + \sqrt{q_2^2} \leq m_P$, can be probed by the $P \to \gamma^{(*)}\gamma^{(*)}$ decays. Region 2, $\sqrt{q_1^2} > m_P$, $0 \leq \sqrt{q_2^2} \leq \sqrt{q_1^2} - m_P$, is accessible via the processes $e^+e^- \to P\gamma^{(*)}$. Region 3, $q_1^2, q_2^2 \leq 0$,

is approachable via the $\gamma^{(*)}\gamma^{(*)} \to P$ processes (e^+e collisions). The region inside the second and fourth quarters of the diagrams and inside the parabola are not accessible experimentally. The list of reactions that are relevant in the context of transition form factors can be found in Ref. [1].

A large class of models for form factors are based on the VMD model. The VMD based isobar model can describe the resonances in the form factor of the double- and single-photon exchange process. Wherein the relation between the vector-meson-conversion and the pseudoscalar (π^0) transition form factors can be understood with the pion transition form factor, which is characterized as [1]

$$F_{\pi^0}(q_1^2, q_2^2) = F_{vs}(q_1^2, q_2^2) + F_{sv}(q_1^2, q_2^2), \tag{1.2}$$

where one of the virtual photons couples to an isovector v and other to an isoscalar s state due to the isospin and G-parity. The first and second subscripts in the right-hand term refer to the photons with momentum q1 and q2, respectively. The $F_{sv}(q_1^2, q_2^2)$ can be neglected, provided $\sqrt{q_2^2}$ is close to a resonance mass M_ω or M_ϕ and $\sqrt{q_1^2}$ is not. The resonance mass M_ω is highlighted as the black dashed line in the right panel of Fig. 1.3.

Furthermore, in the isobar model, the quantity $F_{vs}(q_1^2, q_2^2)$ can be approximated by using the BreitWigner formula [1, 39, 41, 43]. Thus, $F_{\pi^0}(q_1^2, q_2^2)$ becomes

$$F_{\pi^0}(q_1^2, q_2^2) \approx f_{V\to\pi}(q_1^2) \frac{1}{q_2^2 - M_V^2 + iM_V\Gamma_{\text{tot}}} g V_\gamma, \qquad \text{for } q_2^2 \approx M_V^2, \tag{1.3}$$

where Γ_{tot} and $f_{V\to\pi}(q_1^2)$ is the total width of the isoscalar vector meson V and an appropriately normalized form factor of the transition $V \to \pi^0\gamma^*$, respectively. This gives

$$\frac{F_{\pi^0}(q_1^2, M_V^2)}{F_{\pi^0}(0, M_V^2)} \approx \frac{f_{V\to\pi}(q_1^2)}{f_{V\to\pi}(0)} = F_{V\to\pi}(q_1^2), \tag{1.4}$$

where at the photon point the vector-to-pion transition form factor $F_{V\to\pi}$ is normalized to 1. Clearly, the form factor of the transition of the ω meson to a π^0 meson can be expressed as $|F_{\pi^0}(q_1^2, M_\omega^2)/F_{\pi^0}(0, M_\omega^2)|^2$, which is the two-dimensional π^0 form factor. The form factor of the single-photon exchange process reduces to the Equation 1.5, which at low energies ($q^2 \ll \Lambda^2$) can be approximated successively as [1]

$$F(q^2, 0) \;=\; \frac{M_V^2}{M_V^2 - q^2 - iM_V\Gamma_{\text{tot}}} \approx \left[1 - \frac{q^2}{M_V^2}\right]^{-1} \approx 1 + \frac{q^2}{\Lambda^2}, \tag{1.5}$$

where parameter Λ is related to the mass of the intermediate vector meson. The above relation is known as the single-pole formula, which is often fitted to the q^2 dependence to obtain the mass corresponding to the resonance enhancement. This mass value Λ is called the characteristic pole mass. Furthermore, the Fourier transform of the form factor in Equation 1.5 to the coordinate space gives the charge distribution of the transition region [11].

For the specific case of the ω meson, the example processes where the $\omega - \pi$ transition form factor can be studied are, the Dalitz decay $\omega \to \pi^0 e^+(\mu^+)e^-(\mu^-)$ (measured), μ, $e^+e^- \to \pi^0\omega$ (measured), $\eta' \to \omega\gamma$ (measured) and $\eta' \to \omega e^+e^-$ (not measured) [1]. As a continuation, the Dalitz decay of the ω meson to probe the $\omega - \pi$ transition form factor is discussed next.

1.5. The $\omega - \pi$ Transition Form Factor via Dalitz Decay

For the Dalitz decay of the vector mesons $\omega \to e^+e^-\pi^0$, the effective mass $m_{l^+l^-}$ is proportional to the probability of emitting a virtual time-like photon, which is given as

$$s = q^2 = m^2_{l^+l^-} = (E_{l^+} + E_{l^-})^2 - (p_{l^+} + p_{l^-})^2. \tag{1.6}$$

The kinematic limits for the electromagnetic transition form factor in the $A \to B\gamma^* \to Bl^+l^-$ decay is determined as

$$(2M_l)^2 \leq s = q^2 = m^2_{l^+l^-} \leq (M_A - M_B)^2. \tag{1.7}$$

The VMD diagram for the specific case of the ω Dalitz decay $\omega \to \pi^0\ l^+l^-$ is illustrated

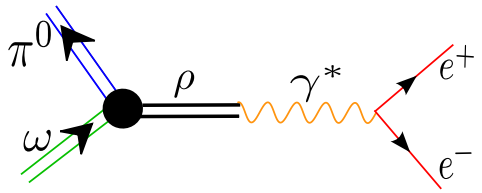

Figure 1.5.: The VMD diagram of the ω Dalitz decay.

in Fig. 1.5. The electromagnetic structure of the region of transition of ω into π^0 can be obtained by studying the probability of the decay as a function of the squared effective mass of the lepton pair ($m_{l^+l^-}$). The leptonic pair mass spectrum of the decay rate of the ω meson is defined as

$$\begin{aligned}\frac{d\Gamma_{\omega\to\pi^0\ l^+l^-}}{dq^2\Gamma_{\omega\to\pi^0\gamma}} &= \frac{\alpha}{3\pi}\left[1-\frac{4m_l^2}{q^2}\right]^{\frac{1}{2}}\left[1+2\frac{m_l^2}{q^2}\right]\frac{1}{q^2}\left[\left(1+\frac{q^2}{m_\omega^2-m_{\pi^0}^2}\right)^2-\frac{4m_\omega^2 q^2}{m_\omega^2-m_{\pi^0}^2}\right]^{\frac{3}{2}} \\ &\qquad \times \mid F_{\omega-\pi}(q^2)\mid^2 \\ &= [QED]_{point-like} \times \mid F_{\omega-\pi}(q^2)\mid^2 .\end{aligned} \tag{1.8}$$

The dilepton mass spectrum for the Dalitz decay of a point-like ω meson is theoretically described in the framework of QED by the Kroll-Wada formula [44]. Equation 1.8 shows that the measured spectrum of lepton pairs is compared with QED calculations for the point-like particles to determine the transition form factor $\mid F_{\omega\to\pi^0\ l^+l^-}(q^2)\mid^2$ in the time-like region. The q^2 distribution of the $\omega - \pi$ transition form factor is fitted using a single-pole formula, as stated in Equation 1.5. The slope parameter b at small q^2 can be obtained by taking the derivative,

$$b_{\omega-\pi} = \frac{dF_{\omega-\pi}(q^2)}{dq^2}\mid_{q^2=0} \ = \frac{1}{\Lambda^2}. \tag{1.9}$$

The slope parameter for the ω Dalitz decay $b_{\omega-\pi}$ is estimated to be 1.70 GeV^{-2} under the simple VMD framework [11]. Correspondingly, the characteristic mass for ρ meson is $\Lambda \approx m_\rho \approx 0.770$ GeV.

The slope parameter is used to determine the characteristic size $< r^2 >^{1/2}$, which is the Root Mean Squared (RMS) "radius " of the $\omega - \pi$ vertex structure. In the range of small

momentum transfers, form factor can be given as

$$F_{\omega-\pi}(q^2) = 1 + q^2 \frac{dF_{\omega-\pi}(q^2)}{dq^2} \mid_{q^2=0} = 1 + q^2 b_{\omega-\pi} = 1 + \frac{1}{6} q^2 < r^2 > \\ \text{where,} \quad < r^2 >^{1/2} = [6 \frac{dF_{\omega-\pi}(q^2)}{dq^2} \mid_{q^2=0}]^{1/2} = [6 b_{\omega-\pi}]^{1/2} . \tag{1.10}$$

The RMS "radius " $< r^2 >^{1/2}$ connected with the region of the $\omega - \pi$ transition is calculated to be 0.63×10^{-13} cm, according to VMD [11].

An overview of the experimental inputs and theoretical predictions under different models in the direction of describing $\omega - \pi$ transition form factor will be presented in Section 1.6 and Section 1.7, respectively.

1.6. Existing Experimental Data and VMD Comparison

The first experimental result was published in 1981 by the Lepton-G collaboration [12], where the characteristic mass Λ_ω is found to be $\Lambda_{\omega-\pi}^{Lepton-G} \approx m_\rho \approx (0.65 \pm 0.03)$ GeV, established in the decay $\omega \to \pi^0 \mu^+ \mu^-$. The corresponding slope parameter of the form factor is found to be $[\Lambda_{\omega-\pi}^{-2}]^{Lepton-G} = (2.4 \pm 0.2)$ GeV^{-2}. Clearly, the value obtained from the experiment has four σ deviation from the VMD calculation. In the range of large $q^2 = m^2_{\mu^+\mu^-}$ the form factor distribution obtained by the experiment rises faster than what is predicted by the VDM. Fig. 1.6 shows the steep rise towards the end of the decay region (higher q^2 ranges). This discrepancy from VMD, statistically significant, remains unexplained up to today. In year 2009, high quality data were taken by the NA60 collaboration using heavy ion collision (peripheral In$-$In measurement [13]). The statistical errors are improved by a factor of nearly 4 in this case. This data set shows a significant improvement in terms of accuracy in the measured transition form factor compared to Lepton-G experiment. The characteristic pole mass of this NA60 data set is found to be $\Lambda_{\omega-\pi}^{NA60_{In-In}} \approx m_\rho \approx (0.668 \pm 0.009_{(stat.)} \pm 0.003_{(syst.)})$ GeV and the slope parameter is $[\Lambda_{\omega-\pi}^{-2}]^{NA60_{In-In}} = (2.24 \pm 0.06_{(stat.)} \pm 0.02_{(syst.)})$ GeV^{-2}. Despite improved statistics, the $[\Lambda_{\omega-\pi}^{-2}]^{NA60_{In-In}}$ obtained from NA60 measurement differed from the VMD expectation by 10σ. Another measurement to study $\omega \to \pi^0 \mu^+ \mu^-$ form factor was performed by NA60 collaboration in 2011 using p$-$A collision [14]. The measured characteristic pole mass of this data set is found to be $\Lambda_{\omega-\pi}^{NA60^{2011}_{p-A}} \approx m_\rho \approx 0.667$ GeV, while the corresponding slope parameter is $[\Lambda_{\omega-\pi}^{-2}]^{NA60^{2011}_{p-A}} = (2.248 \pm 0.030_{(stat.)} \pm 0.009_{(syst.)})$ GeV^{-2}. In this data set, a relative increase is seen close to the kinematic cutoff by a factor of ≈ 10 and the measured form factor strongly deviates from the VMD. Furthermore, in 2016, a new high-precision measurement of the electromagnetic transition form factors of the ω was performed where the data sample is 10 times larger than the previously collected In-In data [15]. The measured slope parameter in new data $[\Lambda_{\omega-\pi}^{-2}]^{NA60^{2016}_{p-A}} = (2.223 \pm 0.026_{(stat.)} \pm 0.037_{(syst.)})$ GeV^{-2} characterized the pole mass as $\Lambda_{\omega-\pi}^{NA60^{2016}_{p-A}} \approx m_\rho \approx 0.671$ GeV. Within the errors, a perfect agreement between the four data sets is observed. The data for the NA60 collaboration for both In$-$In and p$-$A collisions are shown in Fig. 1.6. The results from the new measurement confirms on more strong basis the discrepancy between the VMD predictions for ω meson form factor and the experimental measurements. In spite of having gigantic statis-

tics, NA60 analysis relies heavily on Monte Carlo simulations to extract the ωπ transition form factor because it is unable to reconstruct all final state particles. Which is an advantage for the WASA-at-COSY data over the NA60 and a motivation to contribute to this field of study. Recently, the A2 tagged-photon facility at the Mainz Microtron, MAMI, have measured the Dalitz decays $\omega \to \pi^0 e^+ e^-$ in the $\gamma p \to \omega p$ reaction [28]. The slope parameter, $[\Lambda^{-2}_{\omega-\pi}]^{MAMI} = (1.988 \pm 0.210_{(tot.)} \pm 0.009_{(syst.)})$ GeV^{-2}, is slightly lower than previous NA60 measurements based on $\omega \to \pi^0 \mu^+ \mu^-$ channel. The derived characteristic pole mass is $\Lambda_{\omega-\pi}^{NA60^{p-A}_{2016}} \approx m_\rho \approx 0.707$ GeV. Though the result from the MAMI measurement is in better agreement with the VMD calculations as compared to the previous experiments, no final conclusion could be drawn about the discrepancy at the higher masses. This is due to the significantly large statistical uncertainty in this region. Therefore, more high statistical measurements of the $\omega \to \pi^0 e^+ e^-$ decay is strongly encouraged. Correspondingly, most recent preliminary results from the CLAS g12 experiment, as presented in Ref. [45], indicates an agreement with the observations of the previous MAMI experiment. However, the analysis is in the preliminary state and not precise enough to resolve the deviations from VMD at larger masses. All in all, the discrepancy between VMD predictions and experimental data remained unsolved till now.

1.7. Beyond the VMD Model

As mentioned previously, the measured transition form factor of the $\omega - \pi$ transition vertex shows a significant discrepancy from the standard VMD prediction. There are theoretical efforts that attempt to go beyond the vector meson dominance in a systematic way. Some of the major approaches beyond VMD are effective field theory calculations, dispersion analysis based approaches, and Light-front holographic approach, as discussed briefly in the following subsections.

1.7.1. Effective Field Theories

The models based on vector meson dominance could not explain the steep rise of the ω form factor. A systematic improvement of these phenomenologically successful models is not clear in the energy range of hadronic resonances, unlike the effective field theory. The effective field theories are extended towards higher energies using a new counting scheme, based on the hadrogenesis conjecture, for the Goldstone bosons (π, K, η) and the light vector mesons (π, ω, K^*, ϕ), as described in Ref. [46] and further explored in Ref. [47]. Unlike the standard counting scheme in Chiral Perturbation Theory (ChPT), the new scheme treats both the Goldstone bosons (P) and the light vector mesons (V) on equal footing and their masses as soft, i.e., of the order of a typical momentum q ($m_P \sim q$ and $m_V \sim q$). Consequently, within the framework of this counting scheme, masses up to the ϕ meson mass ($m_\phi \approx 1.02\ GeV$) are soft [16]. Additionally, in order to describe the decays of the light vector or pseudoscalar mesons, all involved momenta are necessarily smaller than the mass of the decaying particle and thus, also of the order of q ($\partial_\mu \sim q$). The restriction to these mesons can be justified by the hadrogenesis conjecture [48], wherein it is considered that all other low-lying mesons are dynamically generated by the interactions between the Goldstone bosons and vector mesons.

The range for q is limited (on tree level) in ChPT by the not-considered mesons (in practice by m_V) and (for loops) by the scale $4\pi f$, where f is the pion decay constant [17]. This

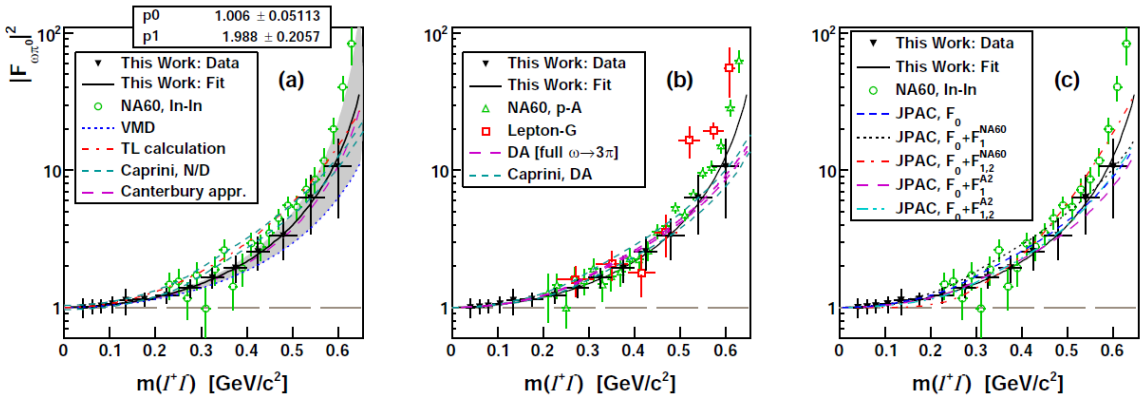

Figure 1.6.: The black filled triangles in figures, taken from Ref. [28], are the data from MAMI experiment [28]. These data points are referred to as *"This Work: Data"* in Ref. [28], as seen in the legends. The pole approximation fit is shown as the black solid line, indicated as *"This Work: Fit"* in Ref. [28]. p0 and p1 are the normalization and the slope parameter Λ^{-2}, respectively. The measurements from the Lepton−G [12] are shown as open red squares in panel (b). The NA60 results obtained in In−In measurement [13] are shown by open green circles in (a) and (c). The measurements from p−A collisions [15] are indicated by open green triangles in (b). The blue dashed line in (a) represents the VMD prediction. The results of a chiral Lagrangian treatment with explicit vector mesons are shown with a red dash-dotted line in (a) [18, 19]. The dispersive solution calculated by the Bonn group for the full 3π re-scattering is shown by the error-band borders as magenta dashed lines in (b) [20]. The cyan dashed lines in (a) represent the upper and lower bounds by Caprini [22] for the discontinuity calculated with the partial-wave amplitude $f_1(s)$ based on the improved N/D model [49], and in (b) are the simplified VMD-inspired partial wave solutions of the discontinuity equation from Ref. [20]. The model-independent calculations using Canterbury approximants taken from a private communication of P. Masjuan [28] is shown by a magenta dashed line covering a gray error band. The blue dashed line in (c) represents the basic calculation from JPAC [21]. The effect from including higher-order terms of the inelastic contributions in the $\omega-\pi$ transition form factor, by fitting them to the NA60 In−In data, is shown as the black dotted and red dash-dotted lines in (c). Wherein the solutions with adding one and the two terms are shown by the black dotted and red dash-dotted lines, respectively. Similarly, the effects of fitting the higher-order terms to the MAMI results for the solutions with one (magenta long-dashed line) and two (cyan dash-double-dotted line) terms are shown in (c).

limitation is overcome in the scheme presented in Ref. [46], by including the vector mesons and resumming the two-particle reducible diagrams (rescattering processes). The theory which calculated the leading-order chiral Lagrangian for the decay $\omega \to \pi^0\gamma^*$ using the new counting scheme is presented in [16, 46]. In principle, the vector meson (ω) can either directly decay into a pseudoscalar meson (π^0) and a photon (real (γ) or virtual (γ^*)) or indirectly via an intermediate vector meson (ρ^0), as drawn in Fig. 1.7. For the decay of an ω meson into a neutral pion (π^0) and a real (γ) or virtual photon (γ^*), the Lagrangian becomes [16]

$$\mathcal{L}_{\omega\pi} = \mathcal{L}^{dir}_{\omega\pi} + \mathcal{L}^{indir}_{\omega\pi}. \tag{1.11}$$

To check the Lagrangian in terms of the diagram, please refer to Fig. 1.7. The leading-order Lagrangian of Ref. [46] allows only for the indirect decay. The relevant part of the

leading-order Lagrangian $\mathcal{L}_{\omega\pi}^{indir}$ is given as [16, 17, 18, 19]

$$\mathcal{L}_{\omega\pi}^{indir} = \mathcal{L}_{\omega\pi}^{indir}(\omega \to \pi^0) + \mathcal{L}_{\omega\pi}^{indir}(\omega \to \rho^0) + \mathcal{L}_{\omega\pi}^{indir}(\rho^0 \to \gamma/\gamma^*). \tag{1.12}$$

The constitute Lagrangians are expressed as [16, 17, 18, 19]

$$\begin{aligned}
\mathcal{L}_{\omega\pi}^{indir}(\omega \to \pi^0) &= -\frac{h_A}{16f}\varepsilon^{\mu\nu\alpha\beta}\mathrm{tr}\left\{\left[V_{\mu\nu}, \partial^\tau V_{\tau\alpha}\right]_+ \partial_\beta \Phi\right\}, \\
\mathcal{L}_{\omega\pi}^{indir}(\omega \to \rho^0) &= -\frac{b_A}{16f}\varepsilon^{\mu\nu\alpha\beta}\mathrm{tr}\left\{\left[V_{\mu\nu}, V_{\alpha,\beta}\right]_+ \left[\Phi, \chi_0\right]_+\right\}, \\
\mathcal{L}_{\omega\pi}^{indir}(\rho^0 \to \gamma/\gamma^*) &= -\frac{e_V m^V}{4}\mathrm{tr}\left\{V^{\mu\nu} Q\right\} \partial_\mu A_\nu,
\end{aligned} \tag{1.13}$$

where h_A and b_A are the constant parameters, $\chi_0 = diag(m_\pi^2, m_\pi^2, 2m_K^2 - m_\pi^2)$ is the mass matrix, $Q = diag(2/3, -1/3, -1/3)$ is the quark charge matrix and A_ν denotes the photon field. The vector mesons are represented by the antisymmetric tensor fields described by the matrix $V_{\mu\nu}$ and the Goldstone bosons are described by the matrix Φ,

$$V_{\mu\nu} = \begin{pmatrix} \rho^0_{\mu\nu} + \omega_{\mu\nu} & \sqrt{2}\rho^+_{\mu\nu} & \sqrt{2}K^+_{\mu\nu} \\ \sqrt{2}\rho^-_{\mu\nu} & -\rho^0_{\mu\nu} + \omega_{\mu\nu} & \sqrt{2}K^0_{\mu\nu} \\ \sqrt{2}K^-_{\mu\nu} & \sqrt{2}K^0_{\mu\nu} & \sqrt{2}\phi_{\mu\nu} \end{pmatrix}, \qquad \Phi = \begin{pmatrix} \pi^0 + \frac{1}{\sqrt{3}}\eta & \sqrt{2}\pi^+ & \sqrt{2}K^+ \\ \sqrt{2}\pi^- & -\pi^0 + \frac{1}{\sqrt{3}}\eta & \sqrt{2}K^0 \\ \sqrt{2}K^- & \sqrt{2}K^0 & -\frac{2}{\sqrt{3}}\eta \end{pmatrix}. \tag{1.14}$$

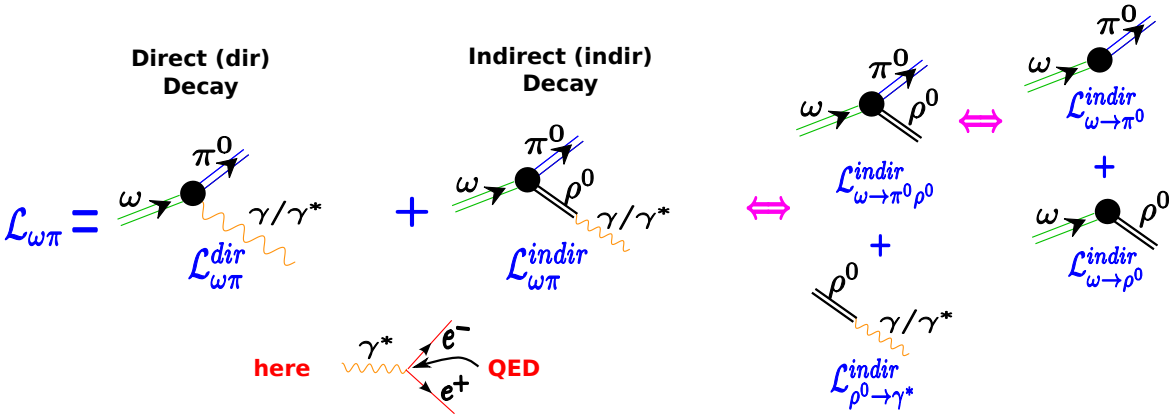

Figure 1.7.: The above figure shows diagrams for the direct and indirect decays of the ω meson into a neutral pion (π^0) and a real (γ) or virtual (γ^*) photon. The full Lagrangian $\mathcal{L}_{\omega\pi}$ and the constituent direct ($\mathcal{L}_{\omega\pi}^{dir}$: next-to-leading order correction) and indirect ($\mathcal{L}_{\omega\pi}^{indir}$: leading-order term) Lagrangians are shown with each diagram. The $\mathcal{L}_{\omega\pi}^{indir}$ constitutes three terms, one for each transition $\omega \to \pi^0$, $\omega \to \rho^0$ and $\rho^0 \to \gamma^*$, i.e., $\mathcal{L}_{\omega\pi}^{indir} = \left\{\mathcal{L}_{\omega\to\pi^0\rho^0}^{indir} + \mathcal{L}_{\rho^0\to\gamma^*}^{indir}\right\} = \left\{\left[\mathcal{L}_{\omega\to\pi^0}^{indir} + \mathcal{L}_{\omega\to\rho^0}^{indir}\right] + \mathcal{L}_{\rho^0\to\gamma^*}^{indir}\right\}$. The diagrams for each transition and the corresponding Lagrangian are shown. The decay of the photon into a dilepton ($\gamma^* \to e^+e^-$) is described by QED.

In order to determine the uncertainties in the calculations, a very rough estimation of one particular next-to-leading-order term of the Lagrangian ($\mathcal{L}_{\omega\pi}^{dir}$) is performed in Refs. [16, 17, 18, 19]. This term describes the direct decay of a vector meson (ω) into a Goldstone boson

(π^0) and a photon (γ/γ^*),

$$\mathcal{L}^{dir}_{\omega\pi} = -\frac{e_A}{4fm_V}\varepsilon^{\mu\nu\alpha\beta}\mathrm{tr}\left\{[Q,\partial^\tau V_{\tau\alpha}]_+\,\partial_\beta\Phi\right\}\partial_\mu A_\nu, \tag{1.15}$$

where e_A is a constant parameter. The diagram for the direct process is shown in Fig. 1.7.

The constants h_A, b_A and e_A in Equation 1.11 are the open parameters, which can be fixed by fitting the partial decay widths for the two-body decays $\omega \to \pi^0\gamma$ to the available experimental data. Two parameter sets are fixed in [16, 17, 18, 19]: P1 with $e_A = 0$, $h_A = 2.32$ and $h_A = 0.27$ (describes the leading-order calculation) and P2 with $e_A = 0.015$, $h_A = 2.10$ and $h_A = 0.19$ (includes the particular next-to-leading-order term).

The form factors calculated with the Lagrangian in Equation 1.11, using the parameter sets P1 and P2, contain both, a term of VMD type (Equation 1.5) and a constant term [16, 17, 18, 19],

$$\begin{aligned} F_{\omega-\pi}(q^2) &= g_{\omega\pi}\frac{m_\rho^2}{m_\rho^2 - q^2} + (1 - g_{\omega\pi}) \\ \text{where } g_{\omega\pi} &= \frac{h_A(m_\rho^2 + m_\omega^2) - 8b_A m_\pi^2}{(h_A + 4\frac{e_A}{e_V})m_\omega^2 - 8b_A m_\pi^2} = 2.01 \pm 0.24. \end{aligned} \tag{1.16}$$

For $g_{\omega\pi} = 2$, one can obtain a particularly simple form

$$F_{\omega-\pi}(q^2) = \frac{m_\rho^2 + q^2}{m_\rho^2 - q^2}, \tag{1.17}$$

which is very different from the VMD in Equation 1.5.

This approach is regarded as an important step forward and the corresponding results [16, 17, 18, 19] are plotted in Fig. 1.6. The $\omega - \pi$ transition form factor obtained by this calculation gives a much better description of the NA60 data than the standard VMD model, except for high dilepton masses close to the kinematic boundary. Though the results of the MAMI group [28] are in better agreement with the theoretical approaches as compared to NA60, no conclusive remark could be made about the large invariant masses due to the significant measurement error.

The calculation in Refs. [16, 17, 18, 19] yields a significantly larger theoretical value of pole parameter, which is around twice the pole parameter from VMD, $[\Lambda^{-2}_{\omega-\pi}]^{ChPT} \approx 3.32\ \mathrm{GeV}^{-2} \approx 2M_\rho^{-2}$. The adopted ρ meson mass in the reference is $M_\rho = 776\ MeV$. The new calculated pole parameter is closer to the pole parameter obtained from the experiments Refs.[12, 13, 14, 15, 28], as compared to the VMD. However, the problem with the steep rise at the higher mass range is not resolved conclusively. The alternative theoretical calculation developed for the form factor description using the dispersion analysis approach is discussed next.

1.7.2. Dispersion Relation Calculations

Another theoretical attempt to describe the $\omega - \pi$ transition form factor is made by conducting the calculations with the effective method of dispersion relations [20, 49]. In Ref. [49], the input parameter dependence of the $\gamma\pi\omega$ vertex functions had been studied on the basis of partial-wave dispersion relations and unitarity. Wherein the right-hand cut is approximated by the 2π contribution and the left-hand cut by the nearest s- and u-channel

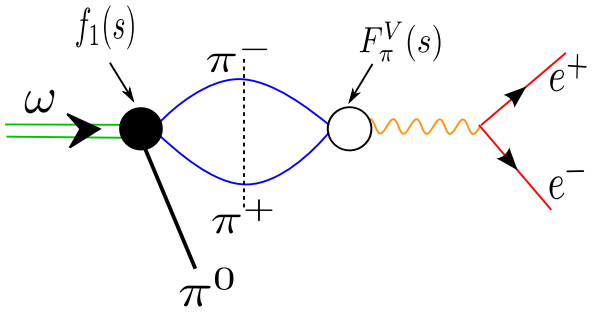

Figure 1.8.: Diagrammatic representation of the discontinuity of the $\omega \to \pi^0 e^+ e^-$ transition form factor. The black circle denotes the $\omega \to 3\pi$ amplitude ($f_1(s)$). The white circle represents the pion vector form factor ($F_\pi^V(s)$) [20].

poles. Further, the electromagnetic $\omega\pi$ transition form factor is calculated as a function of s in the time-like and space-like region. The $\omega \to \pi^0\gamma^*$ electromagnetic transition form factors in Ref. [20] have been calculated using dispersion theory, which relies on a previous dispersive analysis of the $\omega \to \pi^+\pi^-\pi^0$ decay in Ref. [50] and the pion vector form factor. The corresponding P-wave projection of the $\omega \to \pi^+\pi^-\pi^0$ decay $f_1(s)$ and the pion vector form factor $F_\pi^V(s)$ is used as an input. The decay $\omega \to \pi^+\pi^-\pi^0$ in Ref. [20] is treated in the isospin limit with the assumption that $M_{\pi^0} = M_{\pi^+} = M_{\pi^-} = M_\pi$. For the analysis in Ref. [20] only $l = 1$ partial-wave projection has been used and the higher partial wave contributions are neglected. This is because in Ref. [50] a simplified model for additional F-wave contributions was studied and it was found out that they correspond to the negligible corrections. The dispersion relation for the transition form factor have been set by calculating the two-pion discontinuity $\mathrm{disc} f_{V\pi^0}(s)$ of the diagram shown in Fig. 1.8 as [20]

$$\mathrm{disc} f_{V\pi^0}(s) = \frac{iq^3_{\pi\pi}(s)}{6\pi\sqrt{s}} F_\pi^{V*}(s) f_1(s) \theta(s - 4M_\pi^2), \tag{1.18}$$

where $s = (p_\omega - p_{\pi^0})^2$, p is the particle momenta, θ denotes the center-of-mass scattering angle between the initial- and final-state momenta, and $q^3_{\pi\pi}(s) = (s^2 - 4sM_\pi^2)^{3/2}$. The discontinuity relation for the two ingredients to the dispersion integral, the $F_\pi^V(s)$ and $f_1(s)$, have been solved under elastic $\pi\pi$ final state approximation [20]. In order to suppress inelastic contributions, the analysis in Ref. [20] is confined to two-pion intermediate states and neglects any higher contributions, and further a once-subtracted solution is employed.

The resulting form factor obtained from the dispersive approach is plotted in Fig. 1.6. The error-band borders are shown as the magenta dashed lines in the b panel of Fig. 1.6, which represent the simplified VMD-inspired $\omega \to 3\pi$ partial wave $f_1(s) = a\Omega(s)$ inside the dispersion integral in Ref. [20]. Where 'a' is the subtraction constant in the solution of the $f_1(s)$'s unitarity relation or discontinuity equation. This serves as an overall normalization and is adjusted to reproduce the $\omega \to 3\pi$ partial width. $\Omega(s)$ is the Omnés function, which is a solution to the $F_\pi^V(s)$'s unitarity relation, $\Omega(s) = exp\left\{\frac{s}{\pi}\int_{4M_\pi^2}^{\infty} ds' \frac{\delta(s')}{s'(s'-s)}\right\}$. An enhancement over the pure VMD result is observed even with the simplified version of the partial wave in Ref. [20], that is similar to the pink curve shown in the left panel of Fig. 1.9. The area covered between the cyan dashed lines in the b panel of Fig. 1.6 is the correct full $\omega \to 3\pi$ P wave [20], which leads to a further enhancement for invariant masses of the lepton pair near and slightly above the two-pion threshold. This suggests that the three-pion effects, in particular, lead to an enhancement in the two-pion-threshold region [20]. The approach leads

to a significant enhancement of the transition form factor over the pure VMD result. The results are an improved description of the data.

The dispersive analysis returns the pole parameter

$$[\Lambda_{\omega-\pi}^{-2}]^{dispersive} \approx (2.34....2.41)\ GeV^{-2} \approx (1.41...1.45) M_{\rho}^{-2}\ [20]. \tag{1.19}$$

The ρ meson mass used for this comparison is $M_{\rho} = 775.5\ MeV$ [20]. This value shows that there is a significant enhancement with respect to the VMD value, but not as large as the theoretical value obtained from the effective field theory calculations. The new pole parameter values are still significantly smaller than the experimental measurements obtained in Refs. [12, 13, 14, 15]. Instead, the results and the pole-approximations from the MAMI group [28] indicates no contradiction with these solutions. However, as mentioned earlier, the MAMI measurements lack precision and are indecisive hitherto. In essence, the dispersive calculation cannot explain the steep rise towards the end of the decaying region in Lepton-G and NA60 data [12, 13, 14, 15], which is comparably better described by the effective field theory calculations of Refs. [16, 17, 18, 19]. Further, various other theoretical formalisms based on the dispersive framework are discussed.

1.7.3. Dispersive Framework Based Subenergy Unitarity Approach

The two-pion approximation discussed previously is precise in the lower energy ranges, up to the ωπ threshold. Due to the availability of the insufficient information on the discontinuity, the dispersion integral in Refs. [20, 49] had been evaluated by applying the two-pion approximation above this threshold. However, some of the constraints are missing on the high energy behavior in this approach, specifically for the inelastic channels' contribution. Some of these deficiencies are taken care of by the Joint Physics Analysis Center (JPAC) group [21] by adopting the alternative method for incorporating these three-body effects. In Ref. [21], the electromagnetic form factor of the ω meson has been analyzed within the framework of dispersive formalism, which is based on the isobar decomposition and sub-energy unitarity. The inelastic contributions from the isobar decomposition have been parametrized through a conformal expansion with a coefficient, that can either be fitted to the data or determined by comparing with other theoretical studies such as Lattice QCD of EFT expansion. As an extension of this approach, Ananthanarayan. et. al. [23, 24] have investigated the ωπ transition form factor by exploiting a model-independent integral condition on the modulus. The upper and lower bounds on the modulus of the ωπ form factor in the region below the ωπ threshold (elastic region) have been derived with this formalism.

The basic calculations from JPAC, shown as a blue dashed line Fig. 1.6c, is obtained by using the first term in the expansion of the inelastic contribution in terms of conformal variables. The weight parameter of the conformal variables is determined from the experimental value for $\Lambda(\omega \to \pi^0\gamma)$. In addition, other solutions obtained by including the higher-order inelastic-contribution terms in the transition form factor and fitting their parameters to the experimental data are shown in Fig. 1.6c. Clearly, the basic calculation from JPAC lies below the NA60 In−In measurements at large invariant masses. However, it is closer to the MAMI data points. Moreover, the estimations by including another conformal variable term in the form factor fit produce the same results as the base calculations. Although, a better agreement with NA60 is obtained by appending the two more conformal variables terms [23, 24]. However, the steep rise at the larger invariant masses (inelastic form factor) is still not justified. The new solution for MAMI measurement is close to the basic calculation, which shows an agreement with the expectations for higher-order terms of the inelastic contributions. As said earlier, the conclusions with the present MAMI measurements are

ambiguous.

1.7.4. Dispersive Framework Based Unitarity and Analyticity Approach

The discrepancies between the recent calculations [18, 20, 21, 23] of the $\omega\pi$ transition form factor and the recent measurements at higher invariant masses have intrigued I. Caprini [22] to strive in this direction. Unlike the dispersive analysis approaches so far, the new approach in Ref. [22] included the available experimental data above $\omega\pi$ threshold in the dispersive analysis framework. Herein the form factor is analyzed using the discontinuity from Equation 1.18 as an input below the $\omega\pi$ threshold $(m_\omega + m_\pi)^2$. The N/D formalism for the P partial wave of the scattering process $\omega \to \pi\pi$ from Ref [49] is used to estimate the dependence on the input parameters in the unitarity relation. Which is further improved by a simple prescription that simulates the rescattering in the crossed channels. The upper and lower bounds on the modulus of the $\omega\pi$ form factor are evaluated using a N/D formalism based partial-wave amplitude $f_1(s)$. However, above the threshold $(m_\omega + m_\pi)^2$, the experimental information on the modulus is used as input. The estimated bounds have been shown as cyan dashed lines in Fig. 1.6b. This approach provides a ground to test the consistency of the experimental data on the $\omega - \pi$ electromagnetic form factor, which exploits analyticity and unitarity in a parameterization free way [22]. Clearly, the effect is quite modest in the frame of the N/D model. However, the narrow band calculated with this approach is significantly lower than the experimental data in the inelastic region except for the MAMI measurement, which is anyway inconclusive due to the lack of precision.

1.7.5. Model-Independent Calculations using Canterbury Approximants

Furthermore, a model-independent formalism estimated the $\omega\pi$ transition form factor using Canterbury approximants [25]. These approximants are an extension of the Padé theory for bivariate functions [25]. The simple monopole obtained by fitting Equation 1.5 to the predictions from this method is $\Lambda^{-2}_{\omega-\pi} = (1.93 \pm 0.26) GeV^{-2}$ and the parameter $\Lambda_{\omega-\pi}$ is (0.72±0.05) GeV. Which is taken from Masjuan's private communication, as mentioned in Ref. [28]. In this approach, the Λ parameter for the $\omega - \pi$ transition is accomplished by considering isospin breaking and assuming that the slope of the $\omega - \pi$ transition form factor is the same as for the π^0 transition form factor. An overview of the π^0 transition form factor can be found in Ref. [1]. The double virtuality of the π^0 transition form factor is accounted for by fixing one virtual photon to the ω-meson mass and other to the dilepton invariant mass. The output of the methodology has been shown in Fig. 1.6a as a gray error band. Clearly, the prediction has the large uncertainty at higher invariant masses, which is estimated from the uncertainty originate due to the extrapolation of the π^0 transition form factor in the larger q^2 ranges. Despite the predictions is able to describe both NA60 and MAMI data sets within the errors, the predictions are not convincing due to the large uncertainties.

1.7.6. Dispersive Analysis Within the Framework of the Khuri-Treiman Equations

In pursuit of resolving the puzzle of the persisted discrepancy between experimental measurements and theoretical predictions, the dispersive analysis of the $\omega - \pi$ transition form factor has been revisited recently by JPAC collaboration [26]. The modified framework is based on the Khuri-Treiman (KT) equations [51]. In this approach, simultaneous analysis

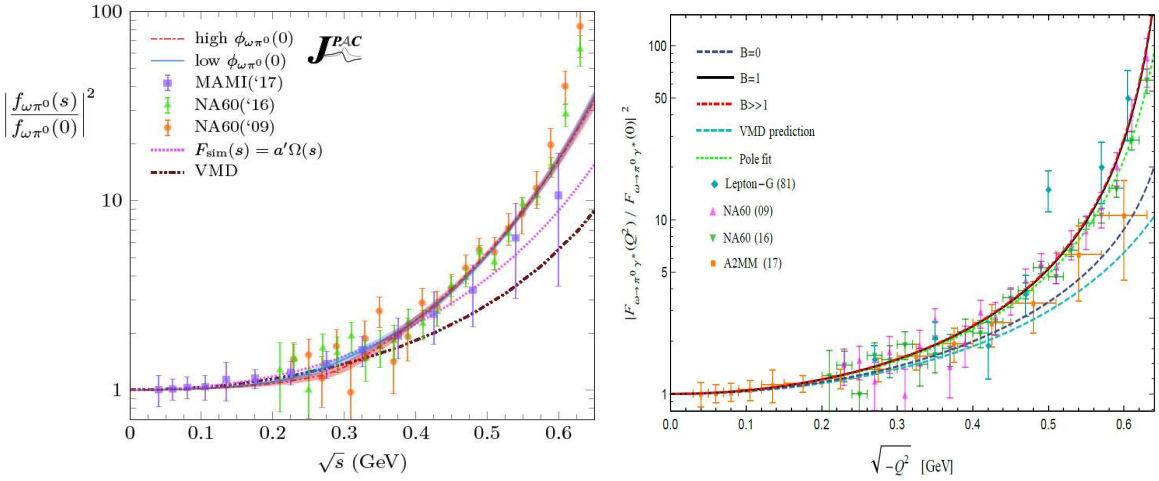

Figure 1.9.: Left Panel: A representation of the normalized $\omega-\pi$ transition form factor estimated in Ref. [26]. Figure is picked from Ref. [26]. The data shown are the results from Refs. [13, 15, 28]. The two different solutions from Ref. [26] are presented as lines and their associated error bands. The solutions overlap almost completely in the $\omega-\pi$ invariant mass range are shown. The Vector Meson Dominance prediction is shown as dot-dot-dashed brown lines for comparison. The simpler model without Khuri-Treiman equations, $F_{sim}(s) = \acute{a}\Omega(s)$, is shown as a dotted pink curve. **Right Panel:** The plot, which is taken from Ref. [27], compares the theoretical calculations for the time-like $\omega-\pi$ transition form factor from Ref. [27] to data from Refs. [12, 13, 15, 28]. The solid blue, solid-black and dot-dashed red curves are the predictions with B = 0, B = 1, and B$\gg$1, respectively. The VMD prediction and the empirical pole fit are shown as dashed-cyan and dotted-green curves, respectively. The Λ in pole fit Equation 1.5 is averaged over the fitted values reported by Lepton-G, MAMI, and NA60 experiments.

of the $\omega\to 3\pi$ decay and the $\omega-\pi$ transition form factor has been explored. A dispersive representation with subtractions, which emerged from the solution of the KT equation, has been followed for the $\omega\to 3\pi$ amplitude. The amplitude is obtained entirely by the $\pi\pi$ P-wave scattering phase shift, except for the values of the subtraction constants. Only one subtraction is performed here. The subtraction introduced a free parameter b in addition to the existed global normalization parameter a. Please refer to Ref. [26] for the parameter descriptions. The normalization parameter a is fixed from the partial decay widths. The modulus $|b|$ and phase ϕ_b of the new parameter b is fixed from fits to experimental data. As a first step, the free parameters ($|a|$, $|b|$, ϕ_b, $|f_{\omega\pi^0}(0)|$) are fixed to the two different sets of Dalitz-plot parameters given by BESIII and the corresponding partial decay widths. The calculations have been performed for two set of parameters, two ("2par.") and three ("3par."), depending upon if the Dalitz plot distribution is assumed to be described by two (α and β) or three (α, β and γ) parameters, respectively [26]. In any case, the Dalitz plot parameters α, β and γ, obtained by previous theoretical [21, 50, 52] and experimental [53, 54] result.

The $\omega\pi$ transition form factor is fully determined by the discontinuity across the right-hand cut, up to the possible subtractions. To be coherent with the elastic approximation in the $\omega\to 3\pi$ analysis, the only two-pion contribution is incorporated in the discontinuity Equation 1.18. The full s-channel P-waves $\omega\to 3\pi$ amplitude $f_1(s)$ and the pion vector form factor $F_\pi^V(s)$ was provided as input. Its solution is approximated by the Omnès function $\Omega(s)$. Like $\omega\to 3\pi$ amplitude, the sensitivity to the high energy region is reduced by using a once-subtracted dispersion relation. Resultantly, a new parameter $\phi_{\omega\pi^0}(0)$, defining the phase

at s=0, is introduced to the $\omega - \pi$ transition form factor calculations [26]. Consequently, the functions $F_\pi^V(s)$ and $f_1(s)$ have different phases, and the discontinuity of the transition form factor is complex for all phases. Here the modulus of subtraction constant is fixed to the PDG average [39] of the $\omega \to \pi^0\gamma$ partial decay width $\Gamma(\omega \to \pi^0\gamma)$ at s=0. The dependence of the $\omega - \pi$ transition form factor on the new free parameter $\phi_{\omega\pi^0}(0)$ is studied in relation to the MAMI and NA60 data as the second step. Two well separated minima, one at $\phi_{\omega\pi^0}(0) \simeq 0.2$ and another at $\phi_{\omega\pi^0}(0) \simeq 2.5$, are observed in this variable, as discussed in Ref. [26]. These two solutions are referred to as "low $\phi_{\omega\pi^0}(0)$" and "high $\phi_{\omega\pi^0}(0)$" in Ref. [26] and adopted in this document.

The calculations using both solutions, as shown in the left panel of Fig. 1.9, are almost indistinguishable. The new predictions are consistent with the NA60 and MAMI data [13, 15, 28], except for the highest two points of the NA60 data. However, the large uncertainty in MAMI data left the inference about MAMI measurement inconclusive. Noticeably, the theoretical description of the data from this approach represents an improvement over previous theoretical analyses [19, 20, 21].

A comparison of the simplest description of this approach is made with the simpler frameworks of other approaches. Where a KT formalism with no subtractions and no crossed channel effects is used. Similar to Ref. [20], a simpler model which ignores the crossed-channel effects by inserting the $f_1(s) = \acute{a}\Omega(s)$ into the partial wave equation have been examined. The results from this simple model are shown as a pink dotted line in the left panel of Fig. 1.9. The simplified calculation lies below the experimental points and is very similar to that of Ref. [20] mentioned previously. However, this simplified estimation is able to describe the Dalitz-plot, as reported in Ref. [26]. Therefore, the solution of the KT equation for the $\omega \to 3\pi$ amplitude with an additional subtraction is the minimum requirement to describe both sets of data, the Dalitz-plot and the transition form factor, simultaneously. All in all, the KT formalism offers a simple framework which allows to provide the partial waves in the direct channel with left hand cuts in terms of the isobars of the crossed channels, while allowing to incorporate crossing symmetry, unitarity and analyticity (to some extent) [26].

1.7.7. Light-front holographic radiative transition form factors

In addition to the dispersive analysis framework, there are alternative efforts that attempt to predict the $\omega\pi$ transition form factor. One of the completely different frameworks is using the overlap integrals of the meson light-front wavefunctions [55, 56, 57]. As an extension, recently, M. Ahmady et. al [27] have computed the transition form factors and the decay widths for the light vector mesons (ρ, ω, K^* ϕ) and pseudoscalar mesons (π, K, η, η') using spin-improved holographic light-front wavefunctions for the mesons. These spin-improved wavefunctions were proposed for the vector mesons V = (ρ, K^*, ϕ) in Refs. [58, 59, 60]. The vector meson wavefunctions were used to predict their decay constants, the cross-sections for diffractive (ρ/ϕ)-electroproduction, and several observables for the semileptonic decays $B_{(s)} \to (\rho, K^*, \phi) + l\bar{l}$ [27]. The spin-improved holographic wavefunctions have been used in processes involving only one light (pseudoscalar or vector) meson. The $\mathcal{V} \to \mathcal{P}\gamma^*$ transition form factors and the corresponding $\mathcal{V} \to \mathcal{P}\gamma$ decay widths have been predicted simultaneously [27]. The difference between pseudoscalar and vector mesons lies in the quark-antiquark helicity wavefunction that modifies their universal holographic wavefunction. Indeed, in light-front holography, there is no distinction between the dynamical wavefunctions of light pseudoscalar and vector mesons. The mixing of the neutral mesons (η, η') and (ϕ, ω) have been accounted by using the SU(3) octet-singlet mixing scheme. In the formalism, the

importance of dynamical spin effects has been quantified as dimensionless constants A and B. The system will only carry the non-dynamical $\gamma^{+}\gamma^{5}$ spin structure under the setting A = B = 0. The value of A required by data is 0 [27]. However, B$\geq$1 will be favored by the pion data and B = 0 will be preferred by the (charged) kaon data. Consequently, B is treated as a free parameter in this framework.

The numerical predictions for the $\omega \to \pi^{0}\gamma^{*}$ time-like transition form factor from Ref. [61] is presented in the right panel of Fig. 1.9. The pole approximation from Equation 1.5 is fitted to the average data of the Lepton-G, MAMI, and NA60 and shown as a dotted-green curve. The obtained average Λ value of data is 0.676 GeV [27]. The predictions for the B=1 and B$\gg$1 are in perfect agreement with the Lepton-G [13] and NA60 measurements [15]. However, the MAMI [28] data lies below both the predictions. For B=0, predictions lie below the predictions for the B=1 and B$\gg$1 as well as the data from Lepton-G and NA60. On the other hand, predictions for B=0 aligns with the MAMI measurement in all invariant mass ranges. Yet, the large uncertainty in MAMI data restrains to draw any conclusive remark. Nonetheless, the predictions for the (ρ, ω, ϕ) $\to \pi\gamma$ radiative decay widths show that B$\geq$1 is favored by the data, i.e., B$\geq$1 is favored for the pion. Overall an excellent agreement with the available data for the decay widths as well as the time-like transition form factors in the low-momentum region has been observed. This approach supports the idea that light pseudoscalar and vector mesons share a universal holographic light-front wavefunction which is modified differently by dynamical spin effects [27].

1.7.8. Miscellaneous

In addition to the approaches discussed so far, Faessler et al. [62, 63] strives to describe the $\omega - \pi$ transition form factor. The predictions from their calculations show good agreement with the data up to $\approx$0.55 GeV/c^{2}. The corresponding prediction is not shown here, however, figure. 3 of Ref. [15] can be referred for the illustration. In a nutshell, their theoretical computation is unable to describe the data from Refs. [12, 13, 14, 15] close to the upper kinematical boundary, M$\approx m_{\omega} - m_{\pi^{0}}$. Moreover, the results from the MAMI group [28] agree with the predictions within error, but their measurements are limited by the precision. Another theoretical approach in Ref. [64] has re-studied the transition form factors of the vector mesons ρ, ω, ϕ with $\rho - \omega - \phi$ in the tri-meson-mixing pattern. This is described by the tri-mixing matrices in the light-cone constituent quark model. The limitation of this approach is that the calculations are restricted to masses below $\approx$0.4 GeV/c^{2}. Please refer to figure 5 of Ref. [64] for visualization.

1.8. Data with WASA-at-COSY

Hitherto, it has been seen that the data collected for the $\omega - \pi$ transition form factor during the measurements by Lepton-G and NA60 are not described by the VMD. Despite, the data from the MAMI experiment aligned with the VMD predictions within error, the inference is inconclusive due to significantly large measurement error. Theoretical efforts are being made to explain the dataset, using effective field theory calculations, dispersive analysis based frameworks under different assumptions, model-independent calculations with Canterbury approximants, and using spin-improved holographic light-front wavefunctions for mesons. All calculations show better results than VMD. Amongst them, the latest approach using spin-improved holographic light-front wavefunctions for the mesons is in excellent

agreement with the available NA60. Furthermore, the results from other theoretical frameworks are in a reasonable agreement with the MAMI points within errors. These approaches cannot completely account for the steep rise close to the end of the decay region in the NA60 and Lepton-G measurements. However, as mentioned earlier, the interpretations from the MAMI measurement are indecisive due to significantly larger total uncertainties. NA60, despite having a sufficiently precise data, is unable to exclusively reconstruct the elementary decay products. Moreover, its entire analysis approach is based upon the Monte Carlo simulations. These features are enabled in the WASA-at-COSY facility and it's analysis approach. Which are the advantages for the WASA over NA60. In order to verify the position of points on the higher invariant mass range, theoretical approaches strongly encourage more experimental investigation of the ω Dalitz decay. More data from a different experimental approach and analysis methods is helpful to verify the accurate position of data points in different mass ranges and to have data points with smaller errors (better precision). The data with WASA-at-COSY is using a completely different experimental approach of elementary reactions, instead of heavy-ion collisions [12, 13, 14]. The WASA-at-COSY detector is capable of reconstructing the electrons. Therefore, e^+e^- pairs can be detected, giving access to the full range of virtual photon mass (larger as well as smaller). It is also possible to reconstruct two photons from the π^0 and hence the exclusive reconstruction of the decaying meson ($\omega \to \pi^0 e^+ e^-$) is possible.

Two test beam-times were proposed for near threshold ω meson production, using two reaction mechanisms: proton beam on deuteron target $pd \to {}^3\mathrm{He}\,\omega$ (at 1.45 GeV and 1.50 GeV kinetic energies) [65] and proton beam on proton target $pp \to pp\,\omega$ (at 2.063 GeV kinetic energy) [66]. Both methods are complementary and have different advantages and disadvantages. The focus of this work is based on the analysis of the data recorded using the proton beam bombarded on deuteron target $pd \to {}^3\mathrm{He}\omega$ (at 1.45 GeV and 1.50 GeV kinetic energies). Before approaching toward the search of the $\omega \to \pi^0 e^+ e^-$ event candidates, the decay $\omega \to \pi^0\gamma$ will be analyzed as one of the reference channel and the branching ratio will be established. This will also help to judge the quality of the data set and the analysis procedure.

2. Experimental Setup

The Wide Angle Shower Apparatus (WASA) was built by an international collaboration and was first used at the CELSIUS (Cooling with Electrons and Storing of Ions from the Uppsala Synchrotron) facility of the TSL (The Svedberg Laboratory, Uppsala) in 1990 [67]. The WASA was installed at the COoler SYnchroton (COSY) facility at Forschungszentrum Jülich, Germany [68] in 2006 and data has been taken since April 2007.

WASA has been designed to study the light mesons such as η and π^0 near the production threshold using pp and pd reactions. Its unique feature to detect charged as well as neutral particles allows for the reconstruction of the full final state of the decaying meson. An inclusive tagging of mesons is also possible using the missing mass technique.

2.1. The COoler SYnchroton (COSY) Facility

COSY is a COoler SYnchrotron and storage ring operated at Forschungszentrum Jülich, Germany. The schematic view of the COSY accelerator complex is shown in Fig 2.1. The two major components of the COSY are: the injector isochronous cyclotron and (unpolarized and polarized) H^- ion sources for the purpose of particle injection. The cooler synchrotron has a circumference of 184 m and three extraction beam lines serving external experimental areas [69, 70]. The COSY facility delivers polarized and unpolarized beams of protons and deuterons in the momentum range of 270 MeV/c to 3.7 GeV/c.

Up to 10^{11} particles can be stored in the ring, yielding typical luminosities up to 10^{31} cm^{-2} s^{-1} for internal experiments with unpolarized beams and targets at COSY [71]. In combination with the pellet target system of the WASA facility, luminosities of up to 10^{32} cm^{-2} s^{-1} are feasible [72].

At COSY, two cooling methods can be used during injection and the accumulation of the beam to reduce the phase space volume: the electron cooling and the stochastic cooling. The electron cooling can be used at the injection energies up to 38 MeV and the stochastic cooling can be used over an energy range of 0.8−2.5 GeV [73, 74]. The beam cooling at COSY results in a high momentum resolution up to $\delta_{rms} = (\Delta p/p)_{rms} \approx 1 \times 10^{-4}$ [74].

The thick target of the WASA makes the above two cooling methods inadequate to compensate for the energy loss, which is experienced by the particles with each revolution. Therefore, the data for this beam time was taken in the barrier-bucket (BB) mode. Where a radio-frequency cavity is used to overcome the mean energy loss of the particles traversing the target by grouping the beam particles in the ring into a single bunch [74]. The proton bunch in the barrier bucket mode occupies nearly the entire circumference of the ring. This leads to a constant beam energy and constant rate of interactions compared to the traditional bunched beam, where protons are grouped into smaller bunches and some of the ring circumference is left empty.

The data for this beam time is taken at two beam kinetic energies 1.45 GeV and 1.50 GeV. The two energies are chosen for the systematic studies of the background subtraction, which will be explained in Chapter 5.

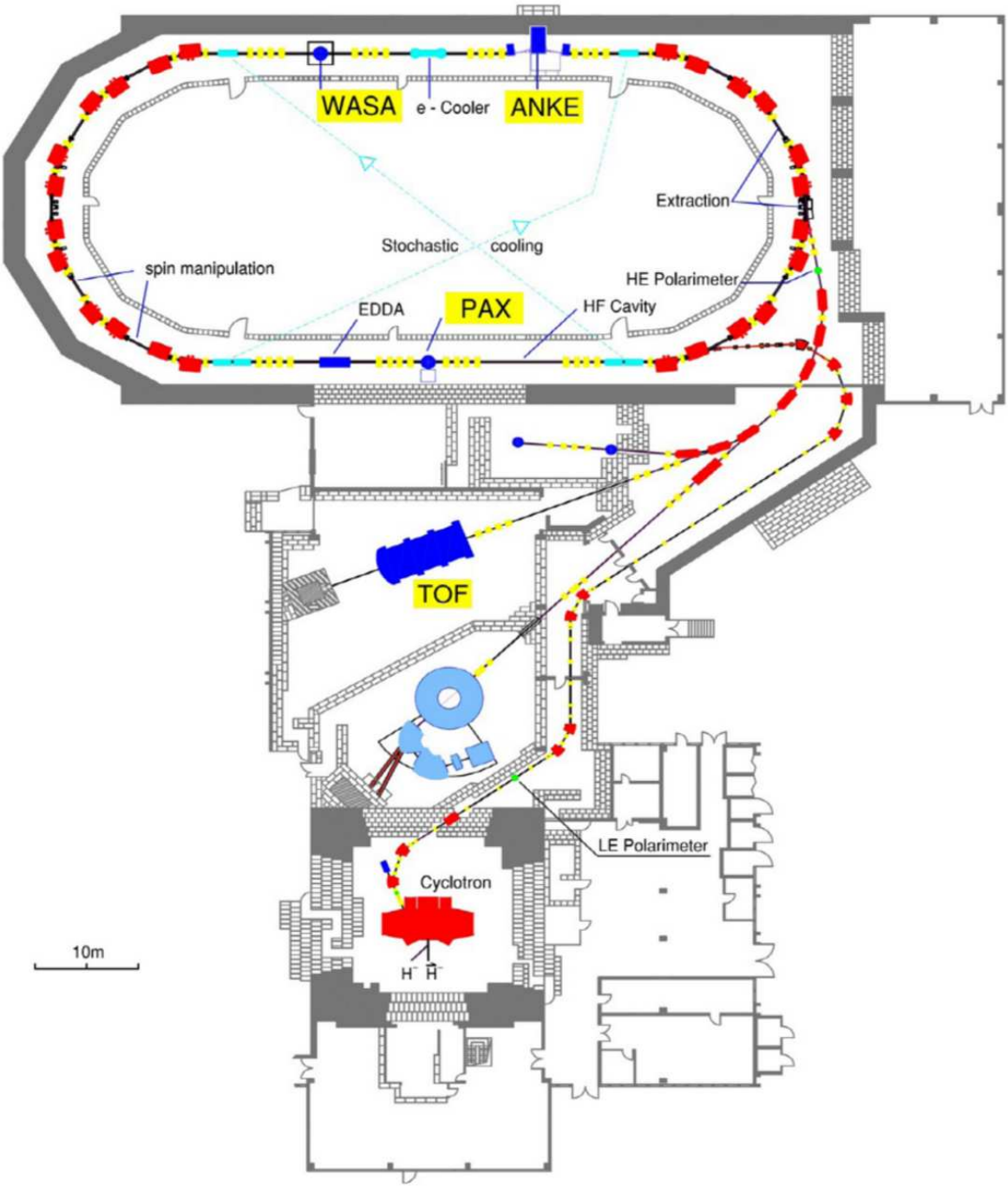

Figure 2.1.: Floor plan of the COSY ring in the Research Center at Jülich (as of 2014). The internal and external experimental set-up are highlighted. The WASA detector is mounted upstream of the electron cooler.

2.2. Wide Angle Shower Apparatus (WASA)

The WASA is a nearly 4π detector, installed in one of the straight sections of the COSY storage ring [68]. A cross sectional view of the detector can be seen in Fig. 2.2. For both, the cartesian (x,y,z) and the spherical (r,θ,ϕ) coordinate system, the origin is located in the interaction point of the COSY beam and the pellet target. Both systems are based on a right-

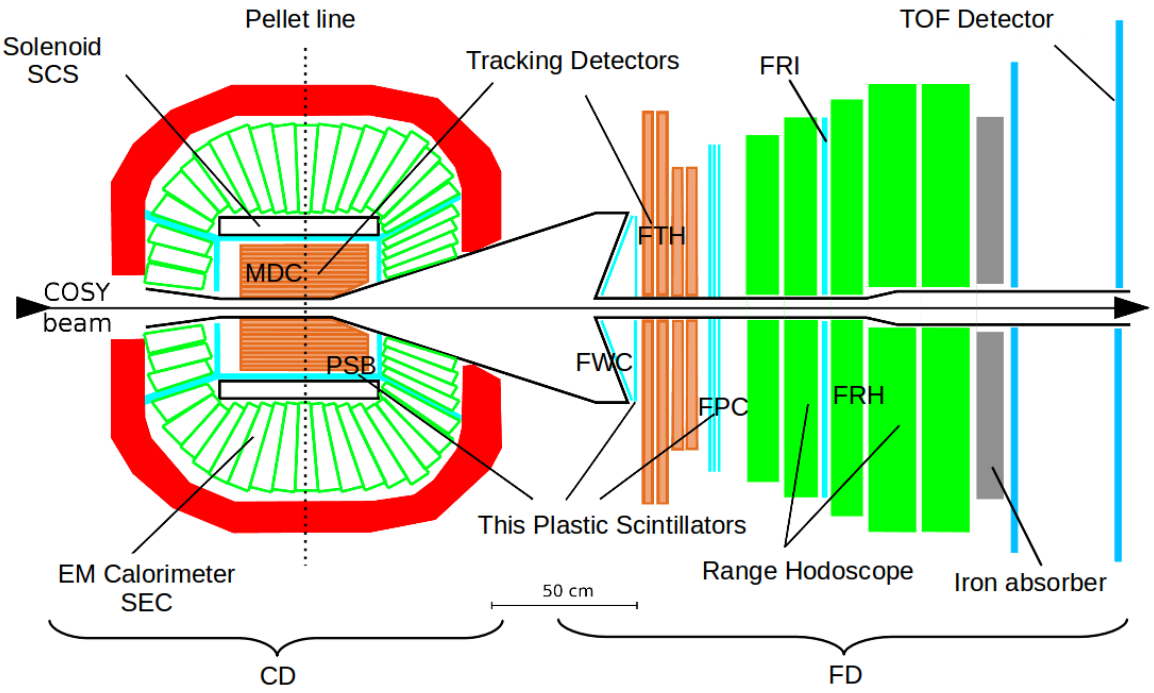

Figure 2.2.: Layout of the WASA detector at COSY with all sub-detectors labeled.

handed coordinate system with Z-axis parallel to the beam axis and the positive direction as the beam direction. The axis opposite to the flow direction of the pellets is defined as the positive y-axis. A normal to the beam line and pellet stream pointing out of the COSY ring is defined as x-axis in the Cartesian system. The polar angle θ is measured from the positive z-axis and has a range of $0 \leq \theta \leq \pi$. The angle of the vector's projection on the x-y plane, with the positive x-axis, is measured as the azimuthal angle ϕ for the spherical coordinate system which has a range of $0 \leq \phi \leq 2\pi$. The x- and y-components of the beam momentum vector are zero and every detector component is symmetric in ϕ. The following sections provide a brief description of the pellet target system, Forward Detector components and Central Detector components.

2.2.1. The Pellet Target System

The internal experiment WASA-at-COSY is specifically designed in such a fashion that a clean detection of the decay products of the meson should be possible. Which comes with a number of demands and strict constraints on the type of target system of the experiment. If a thin target is used, lower luminosities would be achieved. Which in turn, will lead to the collection of statistics insufficient to study rare meson decays. Thus, a low background (from secondary beam target interactions) thick target is required to achieve desired luminosities requisite for the high-statistics experiments. Being an internal experiment, the thick target for the WASA-at-COSY will exhaust the beam very fast. This suggests that the target must have the capability to turn on and off, as and when required. Additionally, a very thick target increases the photon conversions in the target material. In order to satisfy these requirements, the WASA-at-COSY experiment uses a high-density pellet stream of frozen hydrogen or deuterium directed into the path of the beam at the rate maximum up to 10kHz [68, 75, 76]. It is possible to achieve a luminosity of the order of $10^{32}\text{cm}^{-2}\text{s}^{-1}$ with the effective target

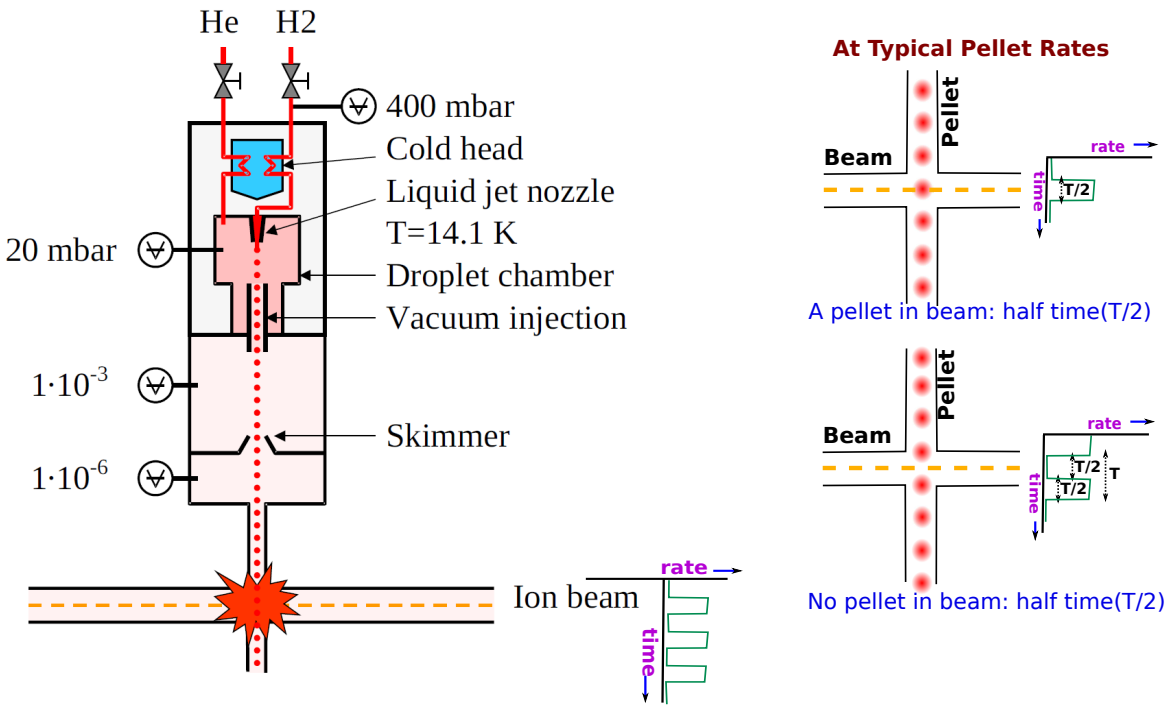

Figure 2.3.: Left: Schematic view of the WASA-at-COSY Pellet Target System. **Right:** Schematic representation of the beam and target interaction at the typical pellet rates. The original idea is to get one pellet in the beam for the total time T (arbitrary), i.e., the rate is a constant function of time. But it could only be achieved that there is a pellet in the beam for the half time T/2 (upper panel) and a hole (no pellet in the beam) for the same time T/2 (lower panel). The discrete spikes of the interactions can be seen as green distribution, drawn arbitrarily.

thickness of $\geq 10^{15}$ atom/cm^2.

The WASA-at-COSY pellet target system is situated directly above the interaction region. The left panel of Fig. 2.3 illustrates the components of the target system. The process of pellet target preparation starts with cooling down the hydrogen or deuterium gas by a cold head until it liquefies. The liquid gas is then pressed out through a liquid jet nozzle with an opening of approximately 12μm in diameter, which is kept close to the triple point temperature of the target gas. The liquid jet nozzle can be seen in the upper part of Fig. 2.3. The liquid stream breaks into equally spaced droplets by a piezo-electrical transducer with a frequency around 70 kHz. The droplets then pass through a vacuum chamber where they get further cooled via evaporation. These droplets are completely frozen after a short distance in a vacuum, providing solid droplets with a diameter between 25 μm and 35 μm called pellets. In the scattering chamber, the pellet beam has a size of 2$-$4 mm. After the interaction with the proton ion beam of COSY, the pellets are deposited in the pellet beam dump. Deuterium, as the target material, needs regular breaks in which the nozzle is heated up to evaporate blockage caused due to frozen materials present in the form of impurities.

The data for the current studies is collected using a deuterium target and the description of data taking is given in Section 2.3. Data taking was consisted of target regenerations after every 48 hours integrated with 9 nozzle changes. The average pellet rate during the beam time was between 2000 - 5000 pellets per second.

The pellet target influences the data analysis in two ways. Firstly, in the form of back-

ground contributions from the evaporated gas and secondly due to several aspects related to the structure of the pellet stream. The background which is produced from the evaporated gas is a direct outcome of the evaporation of the pellets in the beam pipe. The evaporated gas spreads in the beam pipe and has a probability to interact with the beam particles outside the primary interaction point. Accordingly, these interactions will generate events outside the primary vertex. The structure of the pellet stream affects the analysis because, at a typical rate, there is only one pellet in the beam for half the cycle time $T/2$. The scenario is illustrated in the right panel of Fig. 2.3. Resultantly, interactions are seen in the form of discrete spikes appearing at the time when single pellets transit the beam. However, there is no rate for the subsequent half of the cycle time $T/2$. The time gaps when there is no pellet in the beam can be filled by increasing the pellet rate. As an effect, the maximum achievable luminosity directly depends on the pellet rate. Nevertheless, the maximum number of particles in the beam is limited by the instantaneous rate, which may already be at the detector limit. Consequently, it is important that the impact due to systematic effects of high luminosities must be taken care of during the analysis and these effects will be discussed in Chapter 5.

2.2.2. The Forward Detector (FD)

The Forward Detector (FD) is designed for detection and identification of the scattered and charged recoil particles like protons, deuterons and He nuclei in the polar angular range from 3 to 18 degrees. The produced meson can be tagged via the missing mass technique, which will be explained later in Chapter 4.

The Forward Detector consists of twelve planes of plastic scintillator sub-detectors providing energy and time information, and four layers of straw tube tracker used for the measurement of angles up to the precision of 0.2°. The signals of the plastic scintillators are used on the trigger level, exploiting both energy and angular information.

Plastic scintillator counters are widely used for charged particle detection by ionization. The mechanism for detecting ionizing radiation is via the transfer of the energy to the detector material. An inevitable scenario of this detection method is that the charged particle loses an undetectable amount of energy in inelastic collisions with the nucleus of the detector material. These losses in energy are called nuclear losses and are present in prominent amounts to affect the event selection in an unavoidable way. The influence of the nuclear losses on the ^{3}He identification will be seen in Chapter 4.

The individual components are described briefly in the succeeding subsections. More detailed information about the Forward Detector can be found in [68].

2.2.2.1. Forward Window Counter (FWC)

The Forward Window Counter (FWC) is the first sub-system of the Forward Detector along the beam direction. It is mounted on the conical stainless steel vacuum window of the scattering chamber. The window counter has a double layer of the scintillator detector manufactured from 3 mm thick BC408 plastic scintillator material, as shown in Fig. 2.4. Each layer is divided into 24 elements individually read out photomultiplier tubes. The first layer is inclined by 80^0 with respect to the beam axis. The second layer is perpendicular to the beam axis and mounted in front of the supporting steel cross. The elements of the second layer are shifted by half an element with respect to the first layer. Which results in an effective granularity of 48 elements. ^{3}He particles, having a relatively bigger energy loss in FWC as compared to protons and pions, can be characterized effectively on the

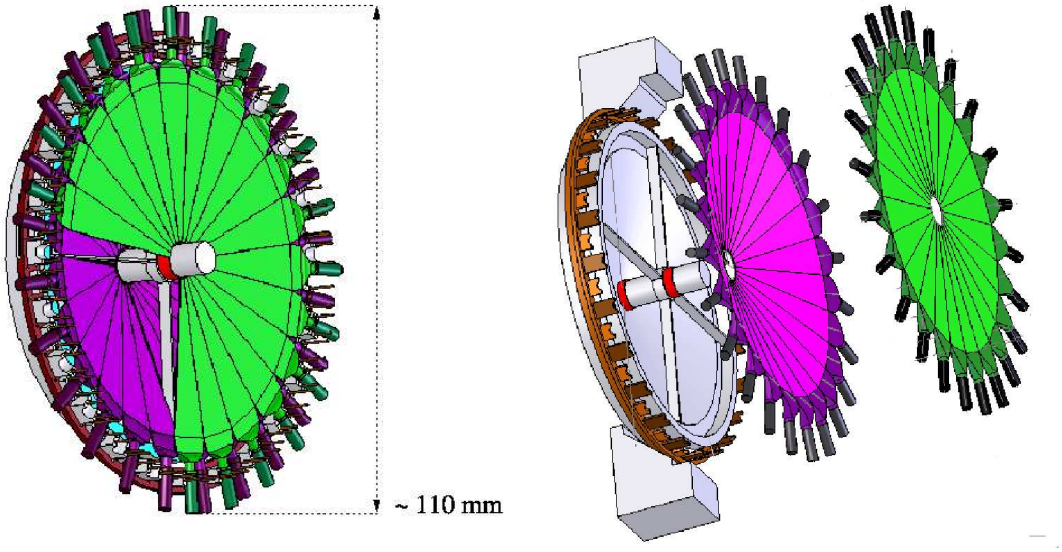

Figure 2.4.: Left picture: 2 layers of the Forward Window Counter. A quarter of the second layer, as indicated by the green color, is removed to show the structure of the first layer. Right picture: The Forward Window Counter, exploded view. Two separate layers of window counter can be seen along with the intervening steel cross.

trigger level. The signal from the FWC, in coincidence with the azimuthal angle in the subsequent detectors, is used in the first level trigger logic, which will be discussed in Section 2.2.5. This trigger is effective to suppress the background from particles not originating from the interaction region.

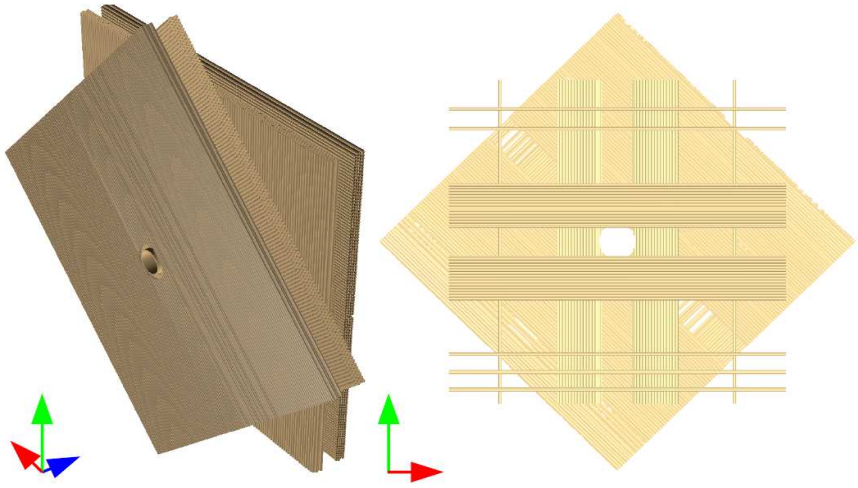

Figure 2.5.: A 3D view of the Forward Proportional Chamber to the left and an upstream view of the Forward Proportional Chamber to the right. Some internal straws are removed to illustrate the structure.

2.2.2.2. Forward Proportional Chamber

The Forward Proportional Chamber (FPC) is a tracking device and is mounted directly over the window counter. The detector consists of four modules and each module is assembled from four layers of 122 proportional drift tubes (straws). Each 8 mm diameter tube is synthesized from 26 μm thick aluminized Mylar foil and 20 μm stainless steel sensing wire. The FPC is used for accurate reconstruction of track coordinates and precise angular information of the particles. The modules are rotated by an azimuthal angle with respect to each other. The first module is oriented by -45^0, the second module is oriented by +45^0 to the beam axis. The third and fourth modules are aligned along the x and y axis. The orientation of the four modules is illustrated in the left panel of Fig. 2.5 and the orientation of the individual straw tubes is shown in the right panel of Fig. 2.5. The FPC, with a geometrical overlap with FTH, improves the azimuthal and polar angles of the reconstructed particle by a factor of two, as compared to using only the FTH pixel [72].

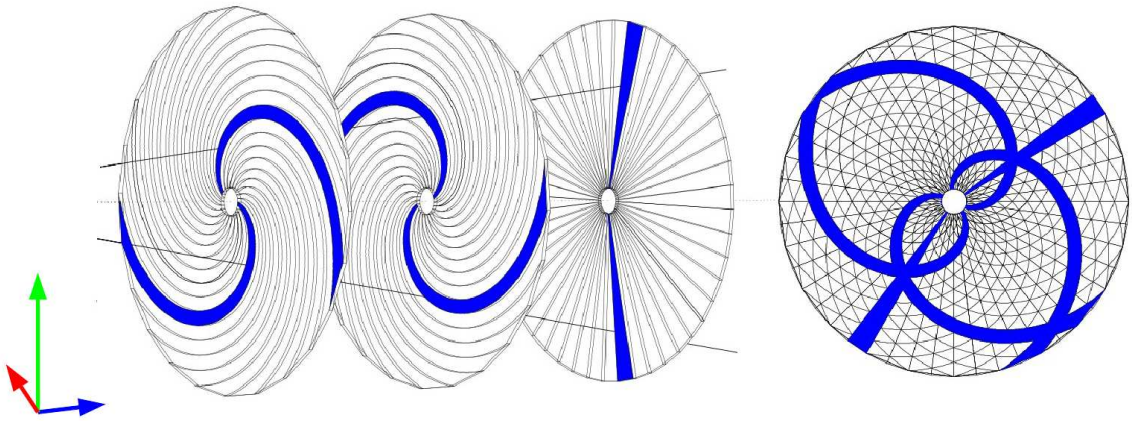

Figure 2.6.: The three layers of the Forward Trigger Hodoscope hit by two particles (left). The intersection of the elements defines pixels as indicated in the projection of the planes (right).

2.2.2.3. Forward Trigger Hodoscope

The Forward Trigger Hodoscope (FTH) is the third sub-detector installed downstream after the proportional chamber. It is used for precise tracking and particle identification. The FTH consists of three layers of BC408 plastic scintillators. Each layer has a thickness of 5 mm. There are 48 radial elements in the first layer. The second and the third layers are divided into 24 elements shaped like an Archimedian spiral oriented in clockwise and counter clockwise directions, respectively, as shown in Fig. 2.6. When a particle passes through the detector, it will deposit energy in the elements of all three layers. Depending on the unique geometric overlap between them, by combining at least two of the three elements, a pixel is formed. The pixel with a constant angular size is used for resolving multi-hit ambiguities. The combination of any two layers forms the special structure called pixel structure, as shown in Fig. 2.6. A hit is the signal from a single detector element. The trigger hodoscope is used in the first level trigger logic in a coincidence with the FWC and the other sub-detectors. Consequently, provides the hit multiplicity as well as polar and azimuthal angles on the trigger level. The FTH is used as the starting point for the offline track reconstruction. Furthermore, it provides accurate timing information of $\sim$ 1 ns for

reconstructed tracks. The FTH is used for identification of the recoil ^{3}He particle(s) in the Forward Detector via the ΔE−E method.

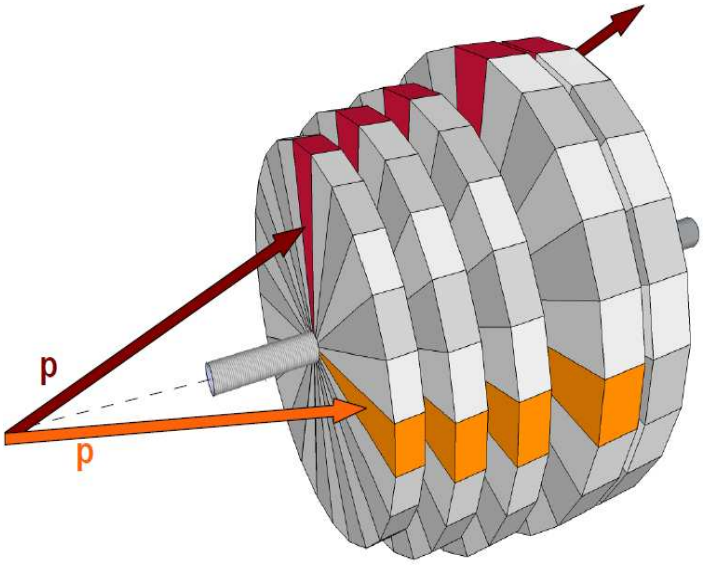

Figure 2.7.: The five layers of the forward range hodoscope consist of 24 elements each. This illustration shows two protons interacting with the FRH with the activated elements colored. Moreover, one proton passes through the FRH while the other stops in layer 4.

2.2.2.4. Forward Range Hodoscope

The Forward Range Hodoscope shown in Fig. 2.7 is the most important sub-detector for the kinetic energy reconstruction and the identification of the particles. It consists of five layers of thick plastic scintillator shaped like a cake piece. Which are installed directly after the FTH contributing the most to the stopping power of the Forward Detector. Each layer is assembled of 24 scintillator bars. The signal from each bar is read out individually by XP2412 photomultiplier tubes. The first three layers have a thickness of 11 cm, whereas the last two have a thickness of 15 cm. Together with the FWC and the FTH, it is used in the trigger to check the track alignment in the azimuthal angle. The stopping power of the Range Hodoscope for different particles is summarized in Table 2.1. It is evident that the ^{3}He has higher energy loss than proton, deuteron and pions, and can be therefore distinguished from other particles during the analysis stage in the ΔE−E plot(s).

Particle	Maximum Energy Deposited
$\pi^{\pm}$	200 MeV
p	360 MeV
d	450 MeV
^{3}He	1000 MeV
^{4}He	1100 MeV

Table 2.1.: Stopping power of particles in forward range hodoscope.

2.2.2.5. Other miscellaneous Components

In addition to the above mentioned sub-detectors, the FD consists of 3 more parts: Forward Range Intermediate (FRI), Forward Veto Hodoscope (FVH), Forward Range Absorber (FRA) and some dead material intervening each sub-detector. The FRI is not used anymore. The purpose of FVH and FRA is to serve as a veto for fast protons, which is not under the scope of this work. A detailed description of FVH and FRI can be found in Ref. [77] and Ref. [78], respectively.

2.2.3. The Central Detector (CD)

The Central Detector surrounds the scattering chamber and the point of interaction. It is designed to detect and identify the decay products, i.e., γ, $\pi^{\pm}$ and $e^{\pm}$, of the light mesons. It covers the polar angular region between 20^0 and 169^0. The CD provides almost 96% of the 4π geometrical acceptance for both charged and neutral particles.

The main components of the Central Detector are described briefly in the subsequent subsections with a more detailed information that can be found in Ref. [68].

2.2.3.1. The Superconducting Solenoid - (SCS)

The Superconducting Solenoid (SCS) is positioned inside the calorimeter. The SCS has a diameter of 554 mm and a length of 465 mm. It surrounds the thin Plastic Scintillator Barrel (PSB) and the Mini Drift Chamber (MDC). This setup provides an axial magnetic field of up to 1.3 T in the interaction region to measure the momentum of the tracks formed in the Mini Drift Chamber. The magnetic field, for the beam time analyzed in this work, is set to 1 T. The return path for the magnetic flux is provided by a yoke made out of soft iron with low carbon content. The yoke shields the readout electronics from the magnetic field while also serving as a support for the calorimeter crystals and directing the field lines. The photomultipliers for the Scintillating Electromagnetic Calorimeter (SEC) are accommodated outside of the iron yoke, connected through the light guides via the holes excavated in the yoke. In this way the PMTs are not influenced by the magnetic field and signals are sufficiently fast to be used for triggering. In order to allow for high accuracy of the energy measurements in the calorimeter, the wall thickness of the aluminum wall in the SCS is minimized to 16 mm. Which is as small as 0.18 radiation lengths. The magnetic field strength is mapped with a Hall probe prior to installation and this map is used for reconstruction and simulations. Detailed information about SCS can be found in Ref. [79].

2.2.3.2. The Mini Drift Chamber - (MDC)

The MDC is a cylindrical drift chamber placed around the beam pipe covering scattering angles from 24^0 (the angle of the front end of the fifth layer) to 159^0. It is used in the determination of the charged particle momenta and the interaction vertex. The Drift Chamber consists of 1738 drift tubes (straws) arranged in 17 cylindrical layers located between 41 and 203 mm of radii.

The straws in nine odd layers are parallel to the beam axis. They are used to reconstruct the axial component of the helical path formed due to the propagation of the charged particle in the drift chamber. The other eight even layers have been skewed by an acute angle (2^0 – 3^0) with respect to the z-axis in order to measure the z-component. These ‘stereo’ layers form a hyperboloidal shape. These arrangements are 60 mm in diameter and assembled around the thin-walled (1.2 mm) beryllium beam pipe, as shown in Fig. 2.8. A helix can be reconstructed using at least three axial and two stereo straws. There are some inefficiencies

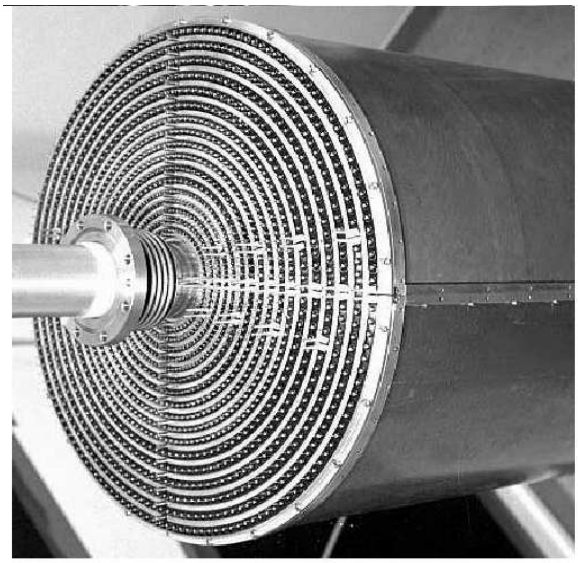

Figure 2.8.: The fully assembled MDC inside Al-Be cylinder.

for particles at lower angles due to a significant number of defective straws.

When ionizing particles cross, free electron pairs are generated in the straw tubes along the trajectory. By measuring the time that electrons need to reach the wire, a precise reconstruction of the trajectory of a transversing particle and hence the closest approach of the particle to the wire can be calculated. The achievable angular resolution of the scattering angle for a charged particle in the Central Detector is $\sim$1.2°. To minimize the amount of structural material and hence to reduce the energy loss of particles and the external conversion of photons, the MDC directly surrounds the beryllium (Z=4) beam pipe. For the same reason, another vertical beryllium tube is used to accommodate the pellet target stream. In order to take care of the particles traveling to the Forward Detector, a flange is carved so that particles fly in a vacuum until they reach the exit window. Details about the MDC can be found in Refs. [80, 81].

2.2.3.3. The Plastic Scintillator Barrel - (PSB)

The PSB is located inside the SCS and surrounds the MDC, as shown in Fig. 2.9. It is consisting of 148 thin plastic scintillator elements. Fig. 2.9a shows the 3-D structure of the central barrel of the PSB colored in blue embedded over the MDC colored in brown. The PSB is, together with MDC and Scintillating Electromagnetic Calorimeter (SEC), used for the identification of charged particles by the $\Delta E - P$ and $\Delta E - E$ methods, as illustrated in Fig. 3.8. Moreover, it serves as a charged particle veto for the $\gamma-$identification. The plastic scintillator barrel provides fast signals for the first level trigger logic. The sensitivity towards charged particles makes it possible to be used in triggers, demanding a certain multiplicity of charged particles in the final state. The PSB provides a time reference to the reconstructed MDC helices for the particle identification. Which substantially reduces the contribution of the artifacts originating from the MDC helix-finding routine. The PSB and SEC coincidences can also be used to identify charged particles, independent of the MDC.

The PSB consists of three parts, one cylindrical part, one forward end cap, and one backward end cap. It is made from 8 mm thin BC-408 the plastic scintillator. The forward and backward parts are assembled from 48 wedge shaped elements. The backward part of the PSB is conical while the forward part is flat shaped and inclined perpendicular to the

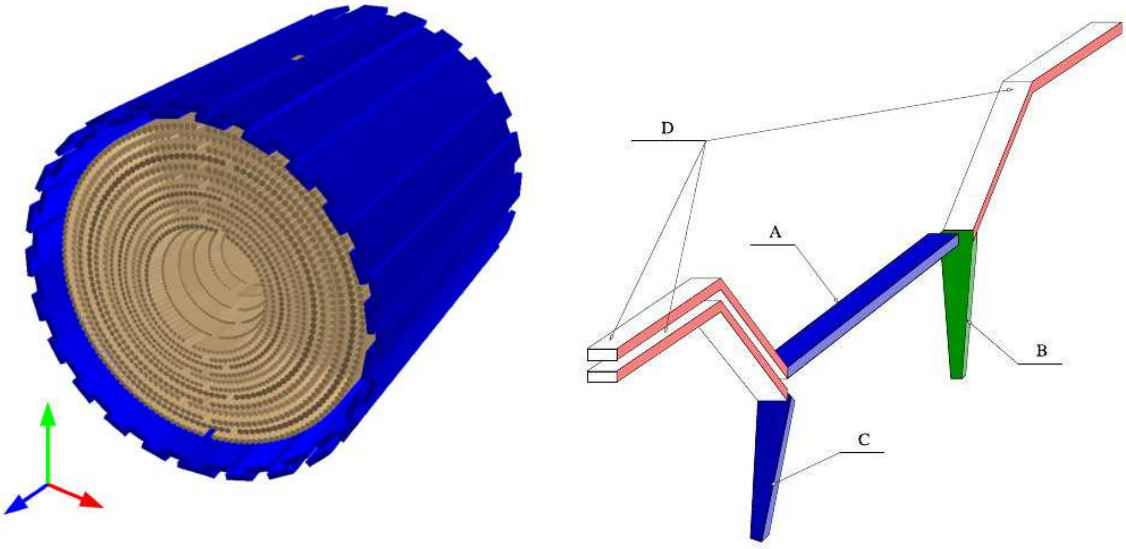

(a) Central Part of PSB over MDC. **(b)** Layout of one section of the PSB detector.

Figure 2.9.: (a) is a 3D view of the central part of the PSB in blue and the Mini Drift Chamber in brown. The end-caps to fit the trapezoidal elements of the backward and forward parts are shown. (b) is one fully equipped element. The central barrel wall is denoted by A. The trapezoidal elements fitted in the forward and backward caps are indicated by B and C, respectively. D represents the light guides (see Refs. [72, 82] for details).

beam axis. Both end caps, with 19 cm diameter at the forward end and 12 cm diameter at the backward end, have a central hole in the beam pipe. The forward end cap is perpendicular to the beam axis while the elements of the backward end cap are inclined by 30^0, forming a conical surface. The cylindrical central part of the detector is 55 cm long and is split into 48 elements. One of the top and one of the bottom element of the central part is split in two to accommodate the target stream at ϕ=90^0 and ϕ=270^0, respectively. The scintillating bars are arranged in a way that there is an overlap with the neighboring element by 6mm. Each bar is attached to a photomultiplier tube (PMT) through an acrylic light guide. Fig. 2.9b shows one section of the complete plastic barrel with both end caps, the barrel element, and the light guides. The PMTs are placed outside of the iron yoke to shield them from the magnetic field. Details of the Plastic Scintillator Barrel can be found in Ref. [80].

2.2.3.4. The Scintillating Electromagnetic Calorimeter - (SEC)

The SEC is the outermost sensitive part of the CD around the solenoid and is used to detect the energy of charged and neutral particles [83]. It consists of 1020 sodium doped cesium iodide (CsI(Na)) crystals shaped like truncated pyramids. The crystals are arranged into 24 layers along the beam axis, as shown in Fig. 2.10a. These layers are divided into three subsections:

- **the central part (SECC):** consists of 17 layers with 48 crystals each and covers scattering angle from 36^0 -150^0,
- **the forward part (SECF):** consists of 4 layers with 36 crystals each and covers scattering angle from $20^0 - 36^0$, and
- **the backward part (SECB):** has 3 layers, two of them have 24 crystals and the innermost layer near the COSY beam pipe has 12 crystals.

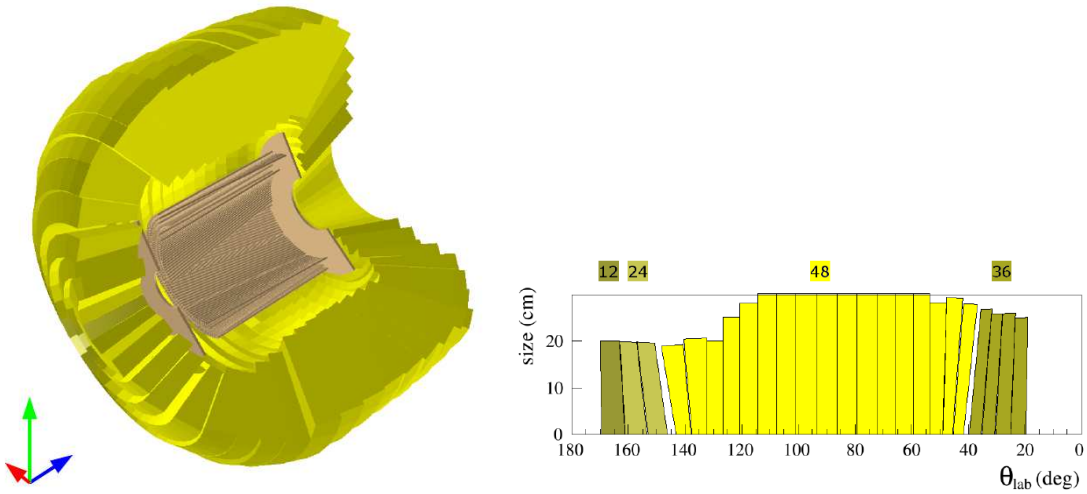

(a) (b)

Figure 2.10.: Cross sectional view of the calorimeter. (a) is a 3-D illustration of calorimeter indicating the positions of the PSB (plane brown area) and the MDC (brown hatched area). The SECB is represented by the lateral side facing the reader with a beam pipe opening. While the central cylindrical part is SECC. The SECF can be seen as the lateral side with an opening for beam pipe where calorimeter ends seen along the blue z-axis. The polar angle coverage, size and shape of the elements in each SEC layer has been illustrated in (b). The shape, size and position of SECF and SECB elements are more explicitly seen here as olive and citron colored strips. Whereas, while yellow strips are the same illustration for the SECC. The number of elements in each layer is given by the numbers at the top of the diagram (details can be found in Refs. [72, 82]).

1020 crystals in 24 layers are arranged in such a way that the central crystal is perpendicular to the beam axis and inclination increases towards the forward and backward parts. The lengths of the crystals are different for all the three parts of the SEC. For instance, the backward part elements are the shortest (20 cm long), the forward part elements are 25 cm long and the central part elements are the longest with 30 cm length. The crystal size is different in the three parts. Fig. 2.10b shows the SEC with the number of layers, crystals, size and the polar angle coverage. There are gaps between the different calorimeter sections for the PSB light guides as well as for the pellet line. It covers a geometric acceptance of $20^\circ < \theta < 170^\circ$ providing nearly 96% of the full solid angle coverage. However, this angular coverage excludes the gaps for the pellet tubes, PSB light guides, forward and backward openings of the scattering chamber, liquid helium supply of the solenoid, and structural supports. Photomultiplier tubes placed outside of the iron yoke are connected to each trapezoidal crystal of SEC (16 radiation length) using long plastic light guides. The use of the light guides enable the PMTs operating outside the magnetic field. A fully equipped single calorimeter module consists of a CsI crystal, a light guide, a PM tube and a high voltage unit, enclosed in a special housing. More details on the construction and the design of the calorimeter can be found in Ref. [83].

The calorimeter is sensitive for detecting the charged particles and photons. $\gamma/e^{\pm}$ in the SEC produces an electromagnetic shower through a chain of pair production and bremsstrahlung. The signal from the shower is detected by PMTs attached to each element. A single shower can laterally expand to several elements, therefore the position of a shower is reconstructed as the weighted average of the contributing crystals. Where

the weight is a function of deposited energy in the corresponding element. A charged hadron ($\pi^{\pm}$), either produces a delayed hadronic shower at these energies via the decay $\pi^{\pm} \rightarrow \mu^{\pm}\nu_{\mu}(\bar{\nu}_{\mu}) \rightarrow [\ e^{\pm} + \nu_e(\bar{\nu}_e) + \nu_{\mu}]\nu_{\mu}(\bar{\nu}_{\mu})$ [84], or deposit energy via ionization. The SEC can also detect the $\pi^{\pm}$ which are stopped in the SEC (see Ref. [84] for details). The energy and angular information from the calorimeter are used for the reconstruction of photons and charged particles. The energy resolution of SEC for photons is given as $\Delta E/E = 5\%/\sqrt{E(GeV)}$ and for stopped charged particles is $3\%/\sqrt{E(GeV)}$ [67, 68]. The typical angular resolution is about 5 and 7.5 degrees in θ and ϕ, respectively. However, the lower limit of angular resolution is defined by the crystal size.

2.2.4. Overview of the Data Acquisition System

The design of the Data Acquisition System (DAQ) is based on the third generation of DAQ systems at COSY [85, 86]. This comprises new readout electronics based on an optimized parallel bus with LVDS technology and FPGA-controlled event and buffer management. A synchronization system and a high speed optical link to the readout computer. Several different digitization modules are used to deal with the differences in the signals from different detector components [87]. The DAQ system is able to cope with the desired high luminosity as well as with the long signal from the inorganic scintillator (SEC) and the shorter signal from the plastic scintillators (Forward Detector and PSB) [86].

The DAQ system is structured into different layers. The signal from the different detector components is received by the front-end electronics preamplifier, splitters and discriminators [86]. The front-end electronics is connected to the 14 crates of the digitizing layer (ADCs and TDCs). Each digitizing crate is connected to the readout computer farm via an optimized protocol over an optical link. Where an event is stored using the event builder. The events from the event builder, at last, are written to the Redundant Array of Independent Disks (RAID) system. The system runs in a mode in which the trigger is coming few μs after the signal has been digitized. The temporarily stored data is split into 20-22 Gigabyte files saved as 'runs' for practical purposes. The saved data files are then transferred from the RAID arrays to the tape archive for long term storage. The DAQ allows count rates of 20k event/s [88]. A description and the performance of the DAQ system can be found in Refs. [85, 86].

2.2.5. Trigger System

The WASA data acquisition system is capable of readout $\sim$20k events per second [88]. The effective event rate can be reduced if only the appropriate events are saved. For high luminosities ($\sim 10^{32}$ cm^{-2} s^{-1}), the event rate exceeds beyond the data acquisition limit, resulting in some dead time of the DAQ. In these cases, a substantial reduction of the event rate becomes necessary. In order to achieve this, a sophisticated set of conditions performing an on-line selection of relevant event is required. Such a set of conditions is called 'trigger'. A trigger selects the significant events before they are written to disk to reduce the data rate [88], using the well discriminated information from each detector.

The trigger conditions are specified using the multiplicities as well as space and time coincidences of different detectors. The information from each scintillating detector has already been discriminated before reaching the trigger system. To restrict the signals emerging from particular particle types, specific triggers can be confined to processing higher or lower energy signals by varying the thresholds on the discriminator levels.

The trigger operates on fast plastic scintillator detectors such as PSB, FTH, FWC and FRH is based on a set of hit multiplicity, geometrical coincidences and time coincidences. This information is combined in the cluster multiplicities within each subdetector. The cluster is considered to be formed by combining the adjacent hits within the time coincidence of 15 ns for thin scintillators (PSB, FTH and FWC) and 20 ns for thick scintillators (FRH) [88]. The conditions on the kinematics of the desired particles can also be used to reduce the huge background left after constraining hit multiplicity. The kinematic conditions will control the angular and energy distribution of the events and hence reduce the crude background in a considerable amount. The background originating due to the particles coming far off the interaction region, cannot be dealt with using only hit multiplicities and it becomes important to use additional conditions on spatial information. In such cases, track matching is done on the trigger level, which cleans up the event rate to a good extent. Track matching involves the angular matching of the clusters in different layers of detectors originating due to the same particles. The trigger will show response if there are hits in FTH, FRH and one of the layers of FWC at the same time and within the same ϕ value. Such a trigger is named as " matching trigger ".

The matching trigger used during data taking for the $pd \rightarrow {}^3\mathrm{He}\ \omega$ reaction employs the unique signature of the ^{3}He ion in the Forward Detector. As mentioned previously, ^{3}He can easily be distinguished from protons and pions on trigger level, due to the relatively higher energy loss of ^{3}He particle in FWC. The background in the form of pion, proton and deuteron is mainly due to the physics of the *pd* reaction. These byproducts lie below the ^{3}He band (see Fig. 3.7) and are rejected in a substantial amount during data taking by setting proper thresholds in FWC, FTH and FRH. This is done by requiring the software based high thresholds over the energy deposited in the different components of the Forward Detector. The trigger for this beam time has already selected the ^{3}He particle and saved the events with at least one ^{3}He particle. For which, the trigger performed a check on the angular information (ϕ), between the modules of the FTH, FRH and FWC. Hits are assigned on the same trajectory if hits in the consecutive detectors are at the same azimuthal angle. Any hit in the first layer of the FTH issued a trigger signal if it is in coincidence with hits in one of the two layers of the FWC and a hit in the first layer of the FRH. At least one element with the signal above the high threshold with the matching condition is required. No additional decay biased trigger is required because a strong rate reduction is observed using ^{3}He based trigger. The efficiency of the ^{3}He trigger for this beam time is found to be close to 99%. The trigger efficiencies of the matching conditions for different cases are discussed in Ref. [89].

The trigger deployed over slower detectors such as SEC uses a quickly calculated deposited energy sum and clusters multiplicity [88]. A cluster in the SEC is defined as a group of hits in adjacent elements, having at least one common edge. The 16-channel discriminators units are used for each digitized signal for the cluster multiplicity trigger system and for TDCs [88]. The output of the discriminator is provided as the analog sum of the signal provided from each channel. This output can again be summed in an external common module to deliver the total-deposited-energy at the trigger level. A piece of more detailed information about the WASA trigger system can be found in Ref. [88].

More than one trigger condition can be used during the experiment. Each condition is a set of basic requirements on several detectors, combined with logical operator AND. There is a possibility that the event rate for one trigger is higher than the data acquisition limit. The particular trigger can be pre-scaled by a factor, so that only a part of the events satisfying the condition will be recorded. For example, if a trigger is pre-scaled to 20, it means every 20th event satisfying the trigger condition will be saved in DAQ. The trigger rates are con-

tinuously monitored and stored as a separate event once every second, which can later be used during analysis.

2.3. Experiment Conditions during ω Production

The data used for this work was collected using the reaction $pd \rightarrow {}^3\mathrm{He}\,\omega$ at two different proton beam energies, T_p = 1.45 and 1.5 GeV during Spring 2011. The beam time is almost equally divided between the two beam energies. The proposed beam time [65] was for 4 weeks in total, but effectively $\approx$ 20 TB of raw data could be acquired on the disk during a time span of $\approx$ 13 days. More than 50% of the beam time was lost because of the pellet target regeneration and nozzle changes due to blockage.

Along with the *pd* data set, few runs for the $pp \rightarrow pp\,\pi^0$ reaction at beam kinetic energy T_p=400 MeV were also recorded. The main purpose of these runs was to gain monitoring and calibration of the Electromagnetic Scintillator Calorimeter, which will be discussed in Section 3.5.1.

A separate dataset was acquired using a proton beam and a proton target ($pp \rightarrow pp\,\omega$) at 2.063 GeV beam kinetic energy [66]. The production cross section of the proton-proton reaction is larger than the proton-deuteron reaction. It was expected that the $pp \rightarrow pp\,\omega$ data should be able to serve for high statistics for the rare ω decays, which are not possible to study with the same amount of the $pd \rightarrow {}^3\mathrm{He}\,\omega$ data. The main purpose of both beam-times is to check the feasibility of the $\omega - \pi$ transition form factor of the Dalitz decay with WASA-at-COSY. The idea was to first develop an analysis procedure for the ω decays using the $pd\omega$ data and then apply it to the $pp\omega$ data.

The production of ω mesons using *pd* reaction is preferred for this study over the *pp* reaction due to various advantages. Although the production cross section for the $pd \rightarrow {}^3\mathrm{He}\,\omega$ reaction at 1.45 GeV beam kinetic energy is (83.6±1.5±2.2) nb [90], while for the $pp \rightarrow pp\,\omega$ reaction at 2.063 GeV is (5.7±0.6±0.8±0.9) μb [91]. The drawback of the small cross sections for the *pd* induced reaction is compensated by the following aspects:

- ^{3}He can easily be identified by their energy loss in the Forward Detector at the trigger level. Trigger conditions are discussed in Section 2.2.5.
- A smaller boost compared to the *pp* induced reaction for the decaying meson increases the acceptance in the Central Detector.

3. Event Reconstruction, Detector Calibration and Run Information

The event reconstruction is the process where digitized information from each sub-detector is stored on the hard disk after the event building, which is further translated to the kinematic information of the particle for physics analysis. The event reconstruction consists of three steps calibration, track reconstruction and energy reconstruction, and particle identification. The comparison with the simulations also goes simultaneously. In this chapter, the tools used for the event reconstruction in addition to the process of event reconstruction are described. Furthermore, the run information about the data set useful for this study is discussed.

3.1. Analysis Tools

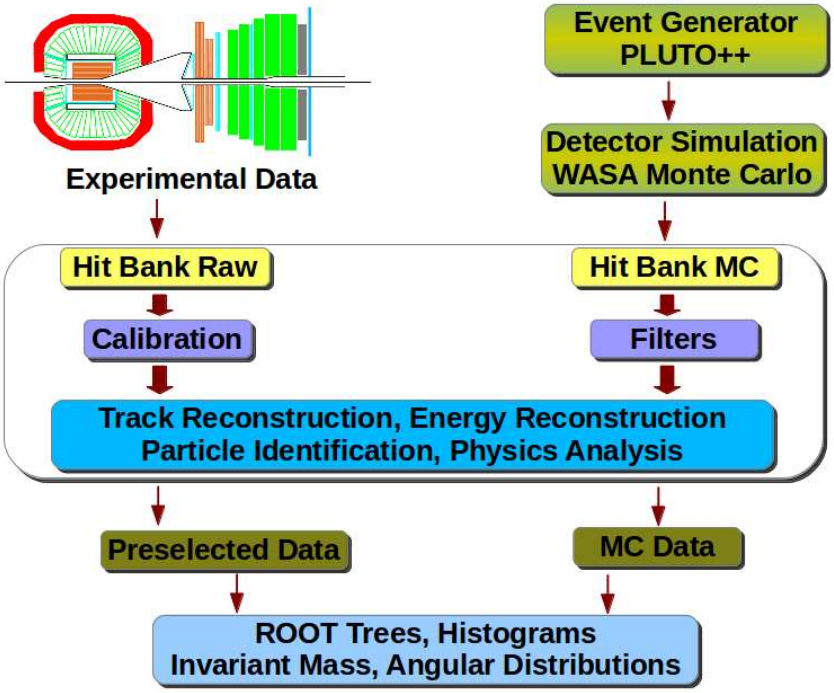

Figure 3.1.: Flow chart of the event reconstruction.

The complete analysis chain is comprised of a number of intermediate steps. The flow chart of the analysis chain used in this work is given in Fig. 3.1. The time and energy information from the individual detector elements are combined into hit objects and stored in the object classes named hit banks. The simulated data is generated using a Monte Carlo simulation tool for hadronic physics named PLUTO [92]. The PLUTO generated events are processed through the GEometry ANd Tracking (GEANT) based WASA Monte Carlo simulation software [93]. The output of the experimental data and the simulated data, then

passes through the WASA RootSorter framework [94]. The ROOT software [95] framework is used as a visualization tool, developed in the European Organization for Nuclear Research (CERN) [96]. The basic description of the PLUTO event generator, WASA Monte Carlo, and WASA Root Sorter are given in the succeeding paragraphs.

3.1.1. The PLUTO Event Generator

PLUTO is a ROOT based Monte Carlo event generator designed for hadronic interactions from pion production threshold to intermediate energies of a few GeV per nucleon and to study the heavy ion reactions [92]. The package has been designed within the HADES collaboration [97]. The input beam and target particles, the final state products and the beam momentum are defined by the user. PLUTO produces the kinematic values of the final state particles by generating the events satisfying the energy and momentum conservation constraint. The events generated by PLUTO are the "true Monte Carlo" events. PLUTO will sample an isotropic phase space distribution using the algorithm as in the GENBOD routine from the CERNLIB software package [98]. If the generated phase space distribution is not adequate to describe the data, PLUTO is capable of incorporating the relevant physics models. These models can be added by the user, which have been implemented for the simulations used for this study.

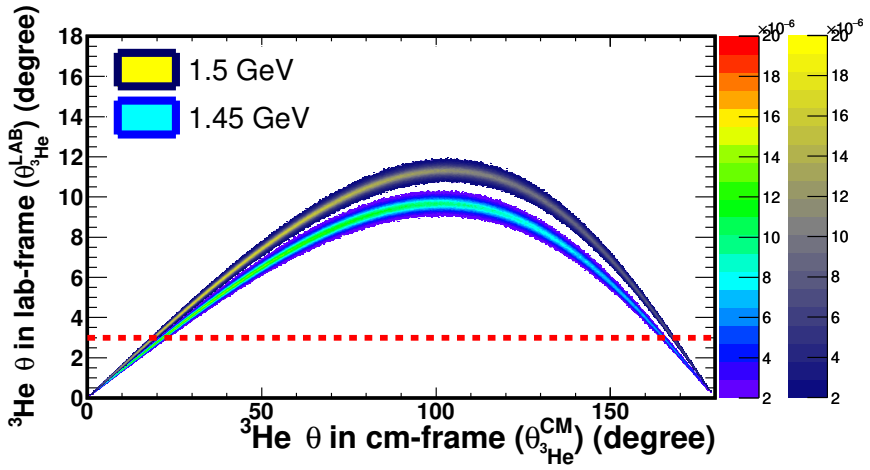

Figure 3.2.: The PLUTO acceptance for the recoil ^{3}He particle using the $pd \rightarrow {}^3$He ω reaction. The distribution of the ^{3}He polar angle θ in lab frame $\theta^{LAB}_{^3He}$ as a function of the ^{3}He polar angle in the center of mass frame $\theta^{CM}_{^3He}$ is shown. The lower limit of the forward detector acceptance is indicated by the red line. The blue-cyan-green palette is the distribution for 1.45 GeV and the violet-yellow palette shows the distribution for 1.50 GeV.

The prominent multi pion background contributions $pd \rightarrow {}^3$He $\pi^+\pi^-\pi^0$, $pd \rightarrow {}^3$He $\pi^+\pi^-$, $pd \rightarrow {}^3$He $\pi^0\pi^0\pi^0$ and $pd \rightarrow {}^3$He $\pi^0\pi^0$ have been generated using PLUTO, where an equal populated phase space distribution is used. To generate the resonance reactions, where unstable particles ω, ρ, η and π^0 mesons are produced, mass dependent Breit Wigner sampling is used. Wherein the total and partial widths of the resonance are calculated recursively in a coupled-channel approach [92]. The production cross sections of the ω meson, η meson, direct $\pi^+\pi^-\pi^0$, direct $\pi^0\pi^0\pi^0$ and direct $\pi^0\pi^0$ are known at current energy [90, 99, 100]. The cross section of the direct $\pi^+\pi^-$ production, π^0 meson production and ρ meson production are not known at current energy, but known on other energies [101, 102, 103, 104]. For the ω meson production, the angular dependence of the production cross-section has been exper-

imentally measured in Ref. [90] and implemented in the simulations. The decays $\omega \to \pi^0\gamma$ and $\omega \to \pi^+\pi^-$ are simulated with the flat phase space. To describe the mass dependence of the decay width, a form factor is implemented in the Dalitz decay $\omega \to \pi^0 e^+ e^-$. The dilepton pair is generated with a mass distribution based on the Quantum Electrodynamics (QED) calculations for a point-like particle, as shown in Equation 1.8. The implemented form factor is as in Equation 1.8, where the characteristic mass $\Lambda_\omega = 0.65$ GeV. In the $\omega \to \pi^+\pi^-\pi^0$ decay, the distribution of the final state particles are based on the matrix elements calculated in Ref. [105]. The matrix elements have been implemented for the decays $\eta \to \pi^+\pi^-\pi^0$ and $\eta \to \gamma\pi^+\pi^-$, based on the parameterization of the Dalitz plot distributions measured in Ref. [106] and Ref. [107], respectively. The $\eta \to \gamma\gamma$, $\pi^0 \to \gamma\gamma$ and the $\rho \to \pi^+\pi^-$ decays are simulated with a flat phase space.

The kinematics of the ^{3}He particles in the ω production reaction (i.e. $pd \to {}^3\text{He}\ \omega$) are studied using the event generator. The scattering angle in the center of mass frame ($\theta^{CM}_{^3\text{He}}$) has been plotted against the scattering angle in the laboratory frame ($\theta^{LAB}_{^3\text{He}}$) in Fig. 3.2. The scattering angle in the laboratory frame has a maximum limit up to $\approx 10^\circ$ for 1.45 GeV and $\approx 12^\circ$ for 1.50 GeV. Both are within the detector acceptance in the forward direction ($3^\circ - 18^\circ$). The lower limit of the detector acceptance is shown as a red dashed line at $\theta^{LAB}_{^3\text{He}}$=3°. Fig. 3.2 shows that 96% of the phase space for 1.50 GeV and 95% for 1.45 GeV is within the detector acceptance in the forward direction. The scattering angle in the laboratory frame for each particle, e^+, e^- and γ, in the central detector is limited to $20 - 169^\circ$. The geometrical acceptance after including the decay products $\omega \to \gamma\gamma\gamma$, is 71% for 1.45 GeV and 72% for 1.50 GeV. However, the total geometrical acceptance for the $\omega \to \pi^0 e^+ e^-$ decay is 68% and 70% for 1.45 GeV and 1.50 GeV, respectively.

3.1.2. WASA MONTE CARLO

The PLUTO simulated kinematic data is tracked for each particle through the defined volumes of detectors from their interaction point. This is done using a GEANT (Ref. [93]) based detector modeling software package called Wasa Monte Carlo (WMC). A virtual model of the WASA detector is set up using the properties of both sensitive detectors and passive support material. To study the response of the detector for single particle tracks, the information can also be generated internally in WMC. The output from the WASA Monte Carlo framework is the "reconstructed Monte Carlo" data. The output data from the WMC are saved in a format similar to the experimental data.

3.1.3. WASA ROOT SORTER

The simulated data is analyzed with the RootSorter analogue to the experimental data. RootSorter is a ROOT data analysis framework based data reconstruction and analysis package developed by members of the COSY-ANKE Collaboration [94]. The RootSorter is a part of the WASA program library and is used to decode and reconstruct both the experimental as well as simulated data. The kinematic variables θ, ϕ and the kinetic energy are obtained by reconstructing the digitized signals from the experimental data and the MC simulated data within the RootSorter framework. In addition, the initial four-momenta of particles delivered by the event generator are also retraced.

3.2. The Track Reconstruction

3.2.1. The Forward Detector

Track Assignment

A track is the trajectory of the particle inside the detector using the corresponding hit information. A signal from a single detector element is called a "hit". Individual hits in time coincidence are combined to form a cluster. The angular information and time of a cluster are estimated as an average of the corresponding information of the contributing hits [72]. The energy of a cluster is calculated by summing up the deposited energies in the individual elements. When more than one adjacent element gets hit, they are treated as part of the cluster.

The clusters are merged to form a track. The merging is done by considering the geometric overlap of the hit elements and the coincidence timing. Clusters in different detectors with a tolerance of ± 1 element within ϕ coincidences are assigned to the tracks. Depending on the azimuthal angle overlap, the time difference, and a minimum amount of deposit energy, the routine searches for overlap between the clusters formed in the FWC, FRH, and FVH. To resolve the ambiguities due to multiple hits, the minimum time difference between the track and the cluster is selected.

Track Reconstruction

The reconstruction procedure provides the four-vector of a particle that involves the θ, ϕ and energy calculation. The track reconstruction routine of charged particles in the FD searches for a geometrical overlap between the clusters in all three layers of the FTH. The overlapping elements form pixels, which define the θ and ϕ of the track, assuming the vertex position is at the interaction point. The angular and time information of FTH is assigned to the track if at least two layers of FTH have hits within time coincidence. The angular information is refined by using information from the FPC. The energy of a track is calculated by summing the energies in the FRH layers, if hits in the FRH are in geometrical and time coincidences with hits in the FTH.

The simulations are used to reconstruct the kinetic energy of the particles in the FRH. The kinetic energy is calculated in the backward direction via the Bethe-Bloch equation [39, 108], by using the information from the stopped particle, until the initial kinetic energy of the particle is achieved. However, as a consequence of the quenching effect and other energy losses in the active and passive material, the original kinetic energy will always be more than the sum of energy deposited in all detectors of FD. The quenching is the group of all radiationless de-excitation modes which do not produce scintillating light, but degrade mainly to heat. These quenching effects, in addition to all types of energy losses, have been taken care of by introducing the correction parameters. These parameters have been implemented in the framework of WASA by calculating individual energy deposit to kinetic energy ($E_{dep} \rightarrow E_{kin}$) tabulated parameters, using the Monte Carlo (MC) simulations for each particle type of known angle and energy. The $E_{dep} \rightarrow E_{kin}$ translation is obtained by plotting the distribution of the relative difference of the reconstructed deposited energy and the initial kinetic energy as a function of deposited energy in specific detector layers. The resulting distributions are fitted with exponential functions and higher order polynomials. One such plot is shown in Fig. 3.3 to illustrate the parameterization used for the reconstruction of protons [78]. The fit parameters are deployed in the $E_{dep} \rightarrow E_{kin}$ translation and thus, the kinetic energy reconstruction for the experimental data.

The kinetic energy of ^{3}He particle is determined from the specific ($E_{dep} \rightarrow E_{kin}$) tables based on the measured angles, energy loss pattern and the layer number where the particle is stopped. The particular tables for kinetic energy reconstruction have been chosen by determining the particle type, which is done using the particle identification methods presented in Section 3.3.1. Most of the ^{3}He particles for the ω meson production reaction at the current beam energies are stopped in the second layer of FRH. The conversion parameter set exists for the ^{3}He particle. However, for the current $pd \rightarrow {}^3$He ω data set, these parameters are able to translate the energy deposited to the kinetic energy up to the third layer of FRH. For the ^{3}He data set, which is a part of this study, a further fine-tuning of these parameters is required to match the simulations and data. A more detailed description of the fine tuning process has been discussed in Refs. [109, 110].

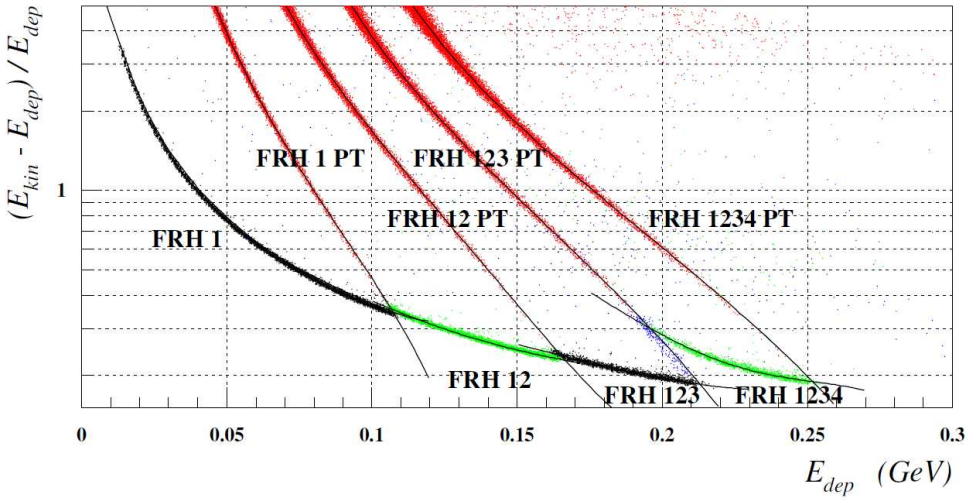

Figure 3.3.: The relative energy difference $(E_{kin} - E_{dep})/E_{dep}$ is plotted as a function of the deposited energy E_{dep} for the Monte Carlo simulations of proton tracks of kinetic energies ranged 0-1 GeV [78]. The lower branches represent the stopped particles while the punch through particles are labeled as "PT". The black graphs represent the parameterization of the respective bands.

The relationship between deposited energy and the initial kinetic energy (True kinetic energy) for the simulated ^{3}He particles is shown in the left panel of Fig 3.4. The ^{3}He particle stopping in different layers of the FRH can be seen as clear structures on the histogram. There is no separate structure seen for the 5th layer of the FRH because the particles stopped in the FRH5 are not distinguished from particles passing through the whole detector. The reconstructed kinetic energy as a function of the true kinetic energy is shown in the right panel of Fig 3.4 for the simulated ^{3}He tracks. The ^{3}He particles stopping in inactive material between the layers can be seen as kinks and the purple background is the nuclear interactions. The energy in the inactive material is lost and these losses cannot be corrected. The energy reconstruction for the particles stopping in the inactive material is done by considering that they are stopping in the previous plane. The resolution of the ^{3}He kinetic energy worsens for ^{3}He at high energies. Since ^{3}He particles in the $pd \rightarrow {}^3$He ω reaction at current beam energies acquire a kinetic energy up to 1.0 GeV, it is not a significant problem here.

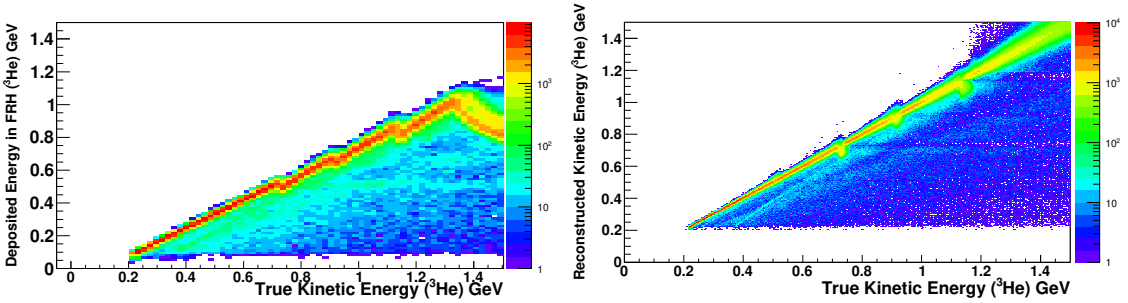

(a) **(b)**

Figure 3.4.: **(a)** The relationship between true kinetic energy and energy deposited in the FRH for simulated single track of ^{3}He, for energy between 200 MeV and 1.50 GeV and θ ranged from 0° to 20°. **(b)** True versus reconstructed kinetic energy for the same simulated tracks.

3.2.2. The Central Detector

The Central Detector consists of three different types of detectors. Each of these detectors has a different procedure to identify hits from the same particle. The hit information is finally combined to reconstruct the particle track. The procedures are described in the following subsections for each detector.

Calorimeter (SEC)

An electromagnetic shower is produced when γ or $e^{\pm}$ is incident on the calorimeter. The number of crystals responding within the shower depends on the initial energy of the photon and the properties of the crystal material. The shower and hence the incident photon is reconstructed by identifying the crystals, where the shower belongs, via the nearest neighbor search.

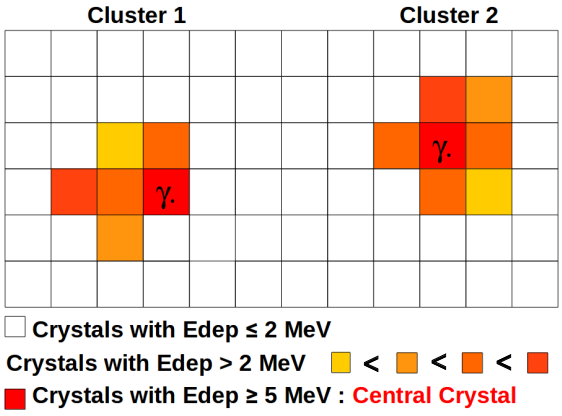

Figure 3.5.: A schematic drawing of the cluster finding algorithm of the SEC. The boxes represent the individual SEC modules. The white boxes are the SEC elements with the energy deposit less than 2 MeV while the colored boxes are the crystals with an energy deposit larger than 2 MeV. The two areas formed by colored boxes represent two reconstructed clusters formed when two photons hit the calorimeter. These two clusters are separated by a minimum distance of four elements from each other.

The cluster finding algorithm, as elaborated in Ref. [111], loops over all hits in the calorimeter to reconstruct the photon cluster. A single cluster is defined as a group of hits that surrounds at least one non-hit element. The hit with the maximum energy deposit, above 5 MeV, is assigned as the central hit. The hits in any neighboring crystal having a time difference smaller than 50ns with respect to the central hit and with a minimum energy of 2MeV are assigned to the cluster [111]. A simplified version of the cluster finding algorithm in the calorimeter is illustrated in Fig. 3.5. The sum of the energy deposited by each hit defines the energy of the cluster. A cluster above 20 MeV is considered for track reconstruction. This is necessary to reject the low-energy background. The position of a cluster is determined by the weighted sum of the position of each element, which is estimated using Equation 3.1 and Equation 3.2 [111, 112, 113]. It is for this reason that the position resolution of the reconstructed cluster has better precision than the SEC element granularity. 5 degrees in θ and 7.5 degrees in ϕ is the geometrical coverage for a single element of the SEC. The position resolution for the photon in SEC varies with cluster energy and position. It has an average 2° standard deviation in θ and ϕ with respect to the true value. The cluster position is defined by taking the mean value of the individual positions

$$\vec{X} = \frac{\sum_i w_i \vec{x_i}}{\sum_i w_i}, \tag{3.1}$$

where the weights depend on the deposited energy

$$w_i = \text{MAX}\,\{0, W_0 + ln\frac{E_i}{\sum_i E_i}\}, \tag{3.2}$$

where $\vec{x_i}$ is the position vector from the origin to the center of the crystal i and E_i is the energy of i^{th} cluster. The parameter W_0 has the value 5 [111].

Plastic Scintillator Barrel (PSB)

The cluster finding algorithm in the PSB assigns a new cluster for the highest energetic hit above the minimum energy deposited E_{min} = 0.5 MeV. It further searches for a suitable hit above E_{min} but less than the highest energetic hit within 10 ns time difference [72]. This process continues until another hit with higher energy deposit is found. This is repeated until all hits in the PSB are considered. The hit in the cluster with the highest energy deposit is the central hit. The time information is calculated as an average of the contributing hits. The energy of the central hit is assigned as the energy deposit of the cluster. Each plane of PSB has a single value for the polar angle θ, which is 30° for the forward part, 90° for the central part, and 140° for the backward part. The azimuthal angle ϕ of a cluster is an average of the ϕ of constituent elements. Clusters with not more than three elements are considered and saved into the cluster bank, which will later be used during the track finding routine.

Mini Drift Chamber (MDC)

The track reconstruction involves the reconstruction of the momentum and direction of the charged particles. The charged particles in MDC follow the helical path under the influence of the magnetic field ($\tilde{\mathbf{B}}$) by SCS, as shown in Fig. 3.6. The angles θ and Φ_0, and the momentum ($\tilde{\mathbf{P}}$) are obtained from the direction of the helical path using the Lorentz relation. The helical trajectories of a charged particle in the MDC are reconstructed in two steps, Pattern Recognition (PR) and Track Fitting (TF) [80].

The helix recognition is done by identifying the hit pattern, assuming that the MDC has

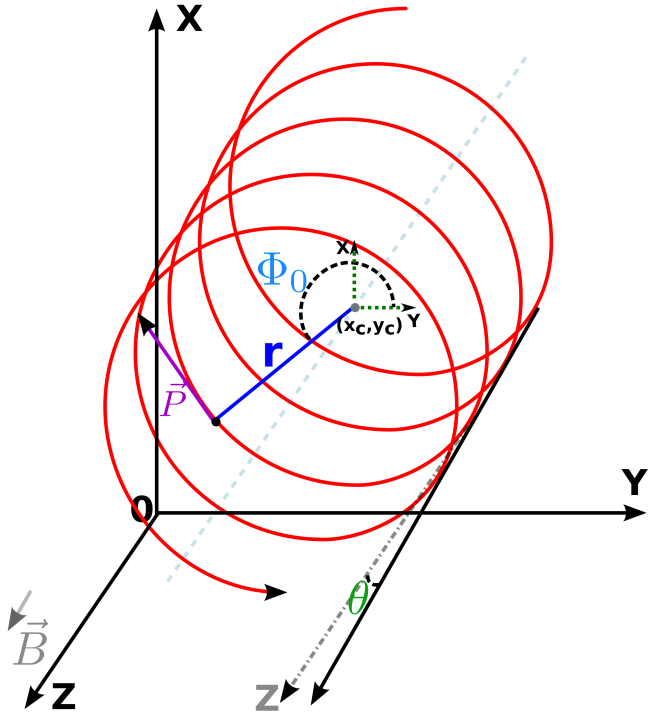

Figure 3.6.: A schematic drawing of the trajectory of the charged particle reconstructed by the pattern recognition as a helix (arbitrarily chosen) with axis parallel to the Z-axis of the WASA coordinate system. The radius **r** of the helix and the transverse momentum $\tilde{\mathbf{P}}$ of the particle in the X-Y-plane is shown as the blue line and purple arrow, respectively. The polar angle Φ_0 describes the relative orientation of the helix center (x_c, y_c) and coordinate center. The angle θ is the angle between a vector tangent to the helix and the z-axis. These parameters are determined by MDC during helix reconstruction.

a homogeneous magnetic field along the z-direction. The hit straws belonging to the same helix are grouped together, and the first step estimation of helix parameters is done. The detailed description of the helix parameterization can be found in Refs. [80, 84]. The PR method is based on a global minimization procedure, which is done in two stages. The first stage forms the axial tracklets by fitting the circles formed by projecting the hit coordinates onto the XY-plane to the hits in the axial MDC tubes. The second stage combines the axial tracklets with the inclined tubes to complete the 3-D helices. The plane of a track is defined by using a combination of the origin and hit in at least two stereo straws. The homogeneous magnetic field assumption helps here to produce a single and smooth helix. The pattern recognition algorithm is attempting to find the best fit for any number of tracks to the array of the MDC hits [114].

A single helix is used for each track in the pattern recognition. The track parameters are calculated from the helix parameters described above. For which the value of the magnetic field is determined from the magnetic field map described in Ref. [68]. Consecutively, the momentum of the charged particle is determined. The magnitude of the momentum is given by the Lorentz relation by using the helix parameters. For a more accurate determination of the track parameters, a Kalman filter [115, 116] is used. The track fitting takes care of the measurement errors and physical effects such as energy loss in the detector material, multiple Coulomb scattering, and the magnetic field inhomogeneity. The tracks are traced back to their origin from the outer layer of MDC by using a full fitting algorithm. This mapping is

done in discrete steps. At each step, the helix parameters are recalculated based on the last step prediction. The errors from the helix and drift distance are taken into account at each step. For the first hit, the helix parameters from the PR are used with estimated errors. Accordingly, with these newly calculated helix parameters, a new helix is constructed. The parameters from this new helix are used as initial parameters for the next step. This process continues until the center point or origin is reached.

In this analysis, the main goal is to distinguish electrons and pions. In the initial stage of the analysis, all particles are identified by default as pions. The tracks belonging to the electrons are re-fitted to achieve the precision in the track parameters after using the particle identification method.

3.2.2.1. Track Assignment

The clusters produced by the same particle in MDC, PSB and SEC are matched and assigned as one track by a track finding algorithm. The track reconstruction algorithm is optimized by taking the combination of the trajectories of the particle in the individual detectors. The combinations are listed in Table 3.1. Eight different categories are contemplated based on the different combinations to identify a particle as charged or neutral. The algorithm is based on the propagation of the reconstructed MDC helix outward through the rest of the detectors.

Charged tracks are assigned by matching the position of the MDC helix with PSB and SEC clusters. To ensure that the SEC and MDC clusters are stemming from the same particles, the maximum matching angle between the SEC clusters and MDC tracklets is 20 in the default setting. A detailed description can be found in Ref. [72]. To have a valid charged track, there must always be a cluster in the MDC with or without including information from one or both of the other two detectors.

Neutral tracks in the central detectors are assigned as the clusters in the SEC, which are not in positional coincidence with the MDC helix, i.e., 20°. The momentum vectors, as defined in Equation 3.1, originate at the primary interaction vertex and point towards the center of the SEC cluster. These vectors are assigned as the photon candidates. Neutrons have a detection efficiency of less than 10% [117].

Based on these algorithms, all possible tracks are identified as charged tracks or neutrals. If the clusters in the calorimeter do not correlate with the MDC and PSB clusters, they are assigned to neutral tracks.

Combination	Track information
MDC, PSB, SEC	charged track, punching through the calorimeter, registered in all detectors
MDC, PSB	charged track, stopped in PSB or the solenoid
MDC, SEC	charged track, not detected in PSB
PSB, SEC	charged track, not detected in MDC
MDC	charged track, stopped in MDC
PSB	charged track, stopped in PSB, not detected in MDC
SEC	neutral track

Table 3.1.: A list of possible hit combinations in the sub-detectors of the Central Detector that result in tracks [72].

3.3. Particle Identification Method

3.3.1. The Forward Detector for ^{3}He Identification

Each detector has a unique method of identifying particles using the characteristic signature left in the passage through the material. For example, charged particles should be discriminated from neutrals. In neutral particles, neutrons and photons should be discriminated. Correspondingly, pion, proton, deuterons, ^{3}He and ^{4}He have to be separated among the charged particles. Although neutrons can be reconstructed by particles from secondary interactions in the FD, it is mainly used to reconstruct charged particles. The FD particle identification procedure used in this analysis is based on the specific energy loss described by the Bethe equation [39, 108]. Due to the different masses of the particles, the deposited energy and stopping power of the detectors allows to clearly separate them. This method is called the $\Delta E-\Delta E$ technique. Fig. 3.7 illustrates the $\Delta E-\Delta E$ technique used in FD for the MC simulation of energetically equally distributed single tracks of various particles. These single track simulations do not include the nuclear interactions of the particles with the passive material of the detector. Consequently, a clear separation between the different charged particles can be identified. A graphical cut can be used to select and separate the individual bands for the desired particle species. It is possible to substantially reduce the background from the other hadronic-nuclear interactions and nuclear losses by using a graphical cut.

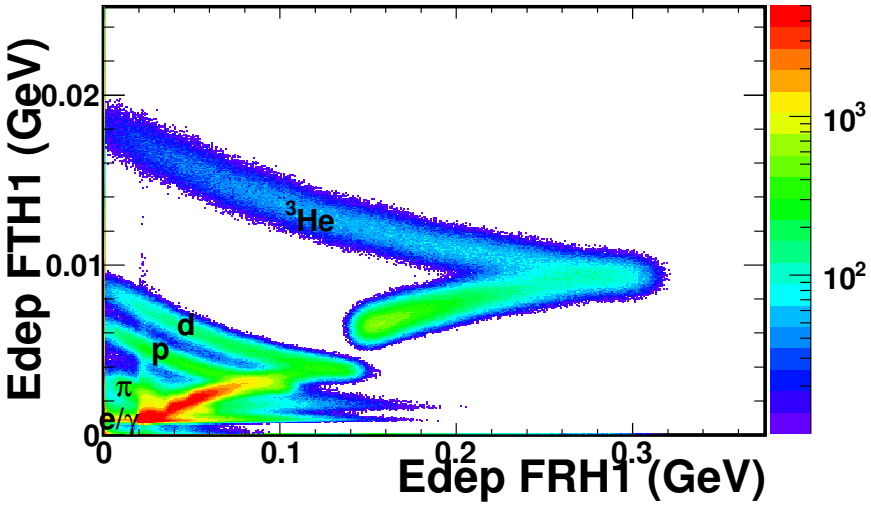

Figure 3.7.: MC simulation showing the $\Delta E-\Delta E$ method used in the FD particle identification. The energy deposited in the first layer of the FTH is plotted as a function of the energy deposited in the first layer of the FRH. The single tracks of the particles isotropically distributed in ϕ within the detector acceptance range for θ from 3° to 18° are shown. The energy range of the generated single tracks of the ^{3}He particles is between 0 and 1000 MeV; positrons and photons between 0 and 100 MeV; deuterons, protons and pions are 0−450 MeV, 0−360 MeV and 0−200 MeV, respectively. Each particle type has a characteristic band.

3.3.2. The Central Detector for $e^{\pm}$, $\pi^{\pm}$ and γ Identification

The neutral particles in the CD are reconstructed and treated as photons. For the charged particles, two different correlations are used to separate leptons, pions, and protons, as demonstrated in Fig. 3.8. A good discrimination between the electrons and pions as well as between the negative and positive charged particles are seen. Both the PSB and SEC information can be used for particle identification.

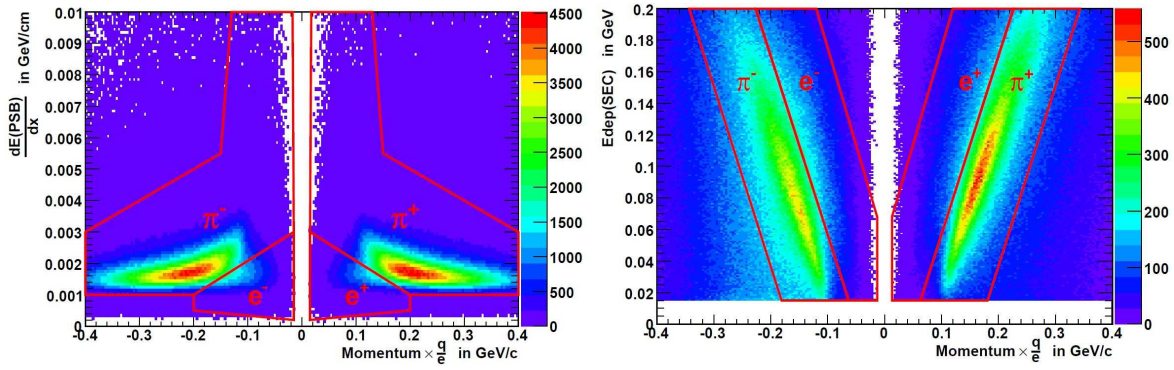

(a) (b)

Figure 3.8.: (a) is the Energy loss in the PSB as a function of the signed momentum from the MDC. However, the energy deposited in the SEC as a function of signed momentum from the MDC has been shown in (b). The plots are taken from Refs. [72, 84]. Both histograms are the simulation of the isotropic single tracks of $e^{\pm}$ and $\pi^{\pm}$.

3.4. Preselection

Preselection is a set of conditions employed to reduce to a subset of relevant events from the raw data using the reaction and the decay specific conditions. Even though the majority of the background is filtered out at the trigger level, these background contributions are still present in a large amount. The goal of the preselection is to decrease file size and computing time. The preselection is done by using the distinctive features of the ^{3}He particles identified in the forward direction. To select ^{3}He particles, the ΔE-ΔE method described in Section 3.3.1 is used. The events with one ^{3}He track are saved as a subset of the initial data set and are the relevant candidates for the pd→^{3}He X reaction [110]. The reconstruction efficiency of the selection criteria is 94%, which includes the detector acceptance discussed in Section 3.1.1 and the track reconstruction efficiency in the forward detector. The preselection suppressed the backgrounds from protons and deuterons in the forward detector. The presorted data are almost 15% of the initial data. After preselection, the process of the detector calibration is described in the subsequent section.

3.5. Energy Calibration

3.5.1. Scintillating Electromagnetic Calorimeter

The calibration procedure of the SEC is to optimize the reconstruction of photons. The initial calibration constants, carried out after the detector was brought from Uppsala, are obtained from the study of cosmic ray μ [83]. The existing calibration constants are obtained from the previous η meson beam time, and are derived using the photons from the neutral pion decay $\pi^0 \rightarrow \gamma\gamma$. The calibration data are a dedicated data set collected for the reaction $pp \rightarrow pp\pi^0$ at 400 MeV beam kinetic energy. This is the energy near π^0 production threshold and is the ideal candidate for the calibration purposes. At this energy: 1. a clean π^0 peak is obtained, 2. photons will be distributed isotropically and offer better statistics in all modules, 3. because of the high pion rate, a few hours of data taking is sufficient.

The energy calibration constants k_is are generated for each module i^{th} by selecting two

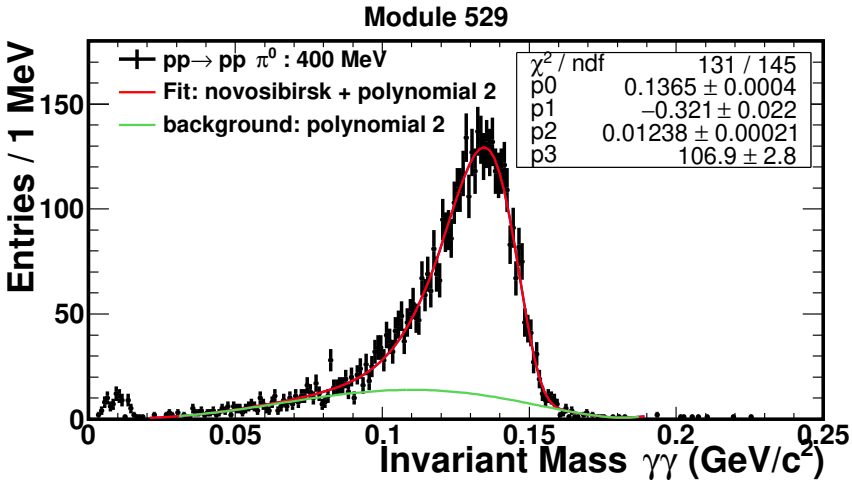

Figure 3.9.: The black histogram represents the invariant mass of two neutral crystals in the SEC for module 529 after deploying existing calibration constants. The small hump around 0.010 MeV/c^2 is the consequence of the combinations where both SEC clusters are the wrongly reconstructed low energy photons called split-offs, which will be discussed in Section 4.2.1. The data are fitted with the combined function of asymmetric Gaussian (Novosibirsk) and a polynomial. The combinatorics in addition to the π^0 peak are fitted with the green polynomial. These combinatorics are coming from the combinations of wrongly reconstructed photons that do not belong to the same event. p0 and p2 are the peak position and σ obtained from the fit.

neutral clusters in the SEC under the clean condition of the π^0 production data. These constants lead to an energy correction per element as $E_i \rightarrow E_i.k_i$. The 2γ invariant mass, which is used as the monitoring spectra and for the gain correction, has been assigned to the central crystal. The invariant mass is

$$M_{\gamma_1\gamma_2} = \sqrt{(E_{\gamma_1}+E_{\gamma_2})^2 - |(\vec{P}_{\gamma_1}+\vec{P}_{\gamma_2})|^2} = \sqrt{2E_{\gamma_1}E_{\gamma_2}(1-cos\theta_{1,2})} \sim \sqrt{E_{\gamma_1}E_{\gamma_2}} \tag{3.3}$$

where $E_{\gamma_1}, E_{\gamma_2}$ and $\vec{P}_{\gamma_1}, \vec{P}_{\gamma_2}$ are the energies and momenta of the photons. $\theta_{1,2}$ is the opening angle between γ_1 and γ_2. As an example, the invariant mass $M_{\gamma_1\gamma_2}$ for one of the modules is shown in Fig. 3.9. $M_{\gamma_1\gamma_2}$ distribution is fitted with a combined Novosibirsk and polynomial function to extract the peak position. The Novosibirsk function $N(x)$ is a Gaussian with a logarithmic tail providing a good description of the 2γ invariant mass distribution [118],

$$\begin{aligned} N(x) &= A\ exp\left[\frac{-(\beta)^2}{\tau^2} - \frac{\tau^2}{2}\right] \\ \text{where, } \beta &= ln\left(1+\Lambda\tau\left(x-x_0\right)\right);\ \ \Lambda = \frac{sinh\left(\tau\sqrt{ln4}\right)}{\Sigma\tau\sqrt{ln4}}. \end{aligned} \tag{3.4}$$

The function has four free parameters: 'A' is the amplitude, 'τ' is the tail parameter, 'Σ' is the width, and 'x_0' is the peak position. The tail for the π^0 distribution is negative. The Novosibirsk function fitted in the peak range characterizes the peak shape. However, the polynomial describes the background.

The peak position of the fitted function is at (0.1365 $\pm$ 0.0004) GeV/c^2, i.e., not at the correct pion mass 0.135 GeV/c^2. Simultaneously, the peak positions for all modules are de-

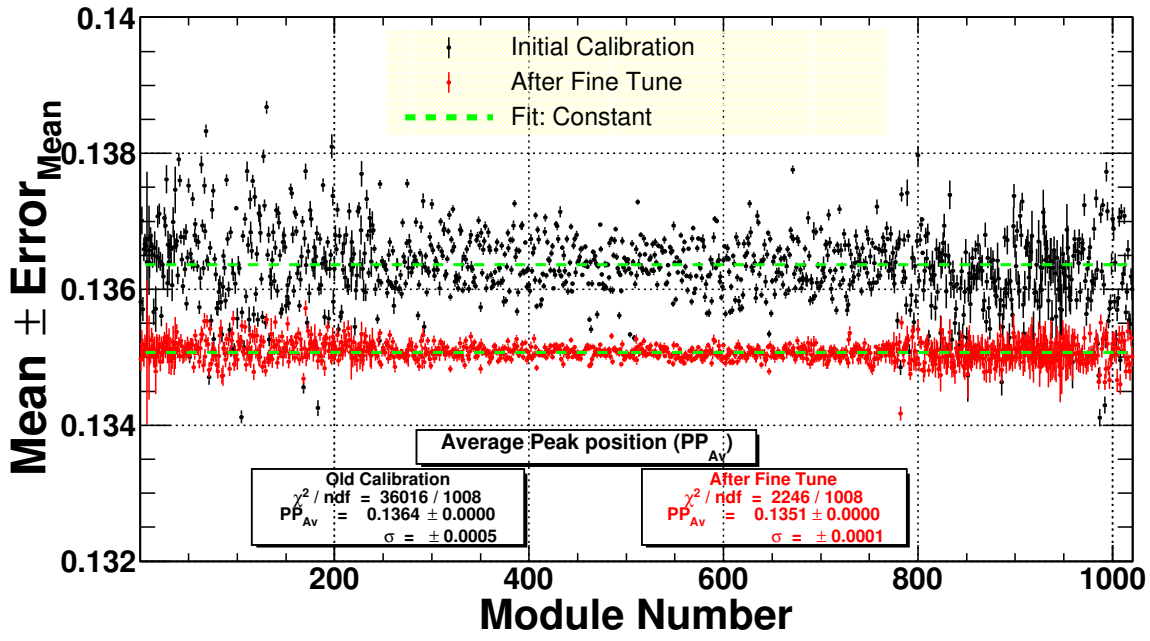

Figure 3.10.: The peak positions from the fitted function for all modules are plotted for the $pp \rightarrow pp\pi^0$ data at 400 MeV. The y-axis represents the peak position and the x-axis is the SEC module number. The black points are the peak positions using initial calibration constants and the red points are the peak positions using updated calibration constants. The green line is the constant fit. The fit parameters (average values) are listed in the legends in the respective colors. The standard deviations (σ) are estimated with Equation 3.5, as $\chi^2/ndf >> 1$.

termined and plotted as black points in Fig. 3.10. The crystals from the left, middle and right regions of the histogram belong to the backward, central and forward part of the SEC. The spread in the peak positions is larger in the backward and the forward part of the calorimeter. This is related to the detector geometry as well as to the statistics in those parts. The different crystal sizes in these parts, the lower granularity of the calorimeter crystals in the back part, and an exit cone in the forward part significantly worsen the accuracy of the reconstruction. Moreover, the insufficient statistics in the forward and the backward part makes it more uncertain to determine the peak position in these parts. However, the situation is worse in the backward part due to the forward boost. The larger fit error in these parts is the consequence of the low statistics.

The average peak position obtained by a constant fit to the distribution in Fig. 3.10 is 0.1364 GeV/c^2. $\chi^2/ndf >> 1$ indicates that the fit error does not represent the actual uncertainty in the distribution, but it is underestimated. Therefore, the uncertainty of the fit parameter is estimated as the standard deviation (σ) of the distribution

$$\sigma = \sqrt{\frac{1}{N-1}\sum_{i=1}^{N}(X(i)-p0)^2}, \tag{3.5}$$

where N is the total number of measurements. The σ of the black distribution is 0.0005 GeV/c^2, as listed in Fig. 3.10. This average peak position (0.1364 $\pm$0.0005) GeV/c^2 indicates that the 2γ invariant mass with existing calibration is off from the π^0 meson mass. Consequently, a global calibration correction factor κ_g, global for all detectors, is introduced for gain correction. Wherein it is assumed that for each module the influence of

the other 1019 modules to the invariant mass of that module is leveling out [119]. The factor κ_g is

$$\kappa_g = \frac{M_{\pi^0}}{M_{\gamma\gamma}^{Avg}} , \tag{3.6}$$

where $M_{\gamma\gamma}^{Avg}$ is the peak position of the 2 photon invariant mass integrated over all 1020 modules. The difference between the real π^0 mass and the actual one is assigned solely to the particular i^{th} detector module, for which the 2γ invariant mass is plotted. In this case, the gain is corrected according to

$$k_i = k_i^0 \times \left(\frac{M_{\pi^0}}{M_{\gamma\gamma}^i} \right)^n \times \kappa_g , \tag{3.7}$$

where k_i^0 is old gain constant and k_i is the new gain constant for i^{th} module. n is the order of the M_{π^0} and $M_{\gamma\gamma}^i$ function. Considering the invariant mass is proportional to the square root of the energy of each photon, a quadratic function is used in the first place followed by a linear hypothesis. This is done to avoid gain overcorrection (biased) in one direction. The gain correction is done iteratively, until a stable and precise peak position is obtained at the correct π^0 mass. The final results of updated calibration constants are illustrated as the red points in Fig. 3.10. Evidently, the precision of measurement is improved and the peak position is stabilized, i.e., the spread over the crystals is reduced. The average peak position (0.1351 ± 0.0001) GeV/c^2, as shown in the legend, is at the correct π^0 mass. The error σ in the peak position is determined using Equation 3.5 as the fit error is underestimated, i.e., $\chi^2/ndf >> 1$.

The peak position and the precision are cross checked for the higher energetic photons in the $pd \rightarrow {}^3$He ω ($pd\omega$) beam time, where the π^0 distribution integrated over modules is studied run wise under the $pd \rightarrow {}^3$He $\pi^+\pi^-\pi^0$ hypothesis. This is done because it is one of the prominent background reactions for the proton-deuteron collision at the current energies (Appendix C.1). Moreover, it has a single π^0 in the final state. Resultantly, this reaction will have the cleanest π^0 distribution. The resolution (FWHM) and peak position of the fitted function for the $pd\omega$ beam time are plotted in the top and bottom panels of Fig. 3.11, respectively.

The percentage gain in resolution over peak position (σ/peak-position) is 12% for the $pd\omega$ data. In this case, the peak position is shifted at the smaller value (0.1295 ± 0.0012) GeV/c^2 with the updated constants. These shifts arise because higher energetic photons in the $pd\omega$ data have different energy distribution than the 400 MeV $pp \rightarrow pp\pi^0$ data. Which implies that the approximation $M_{\gamma 1\gamma 2} \sim \sqrt{E_{\gamma 1} E_{\gamma 2}}$ of the algorithm does work differently. Additionally, the time-dependent inconsistencies, mainly due to the temperature dependent long-term drifts of the gain, can also be seen over the run period. Both the incorrect position of the π^0 peak and the time dependent fluctuations are corrected by applying the run wise global correction factor.

The correction is named global because the gain in each run period is corrected by employing a single constant for all 1020 elements. The global correction factor k_G is extracted for each run as a ratio of the 2γ invariant mass $M_{\gamma\gamma}$ peak position and the π^0 rest mass M_{π^0}. k_G for r^{th} run is

$$k_G^r = \frac{M_{\gamma\gamma}{}^r}{M_{\pi^0}} \tag{3.8}$$

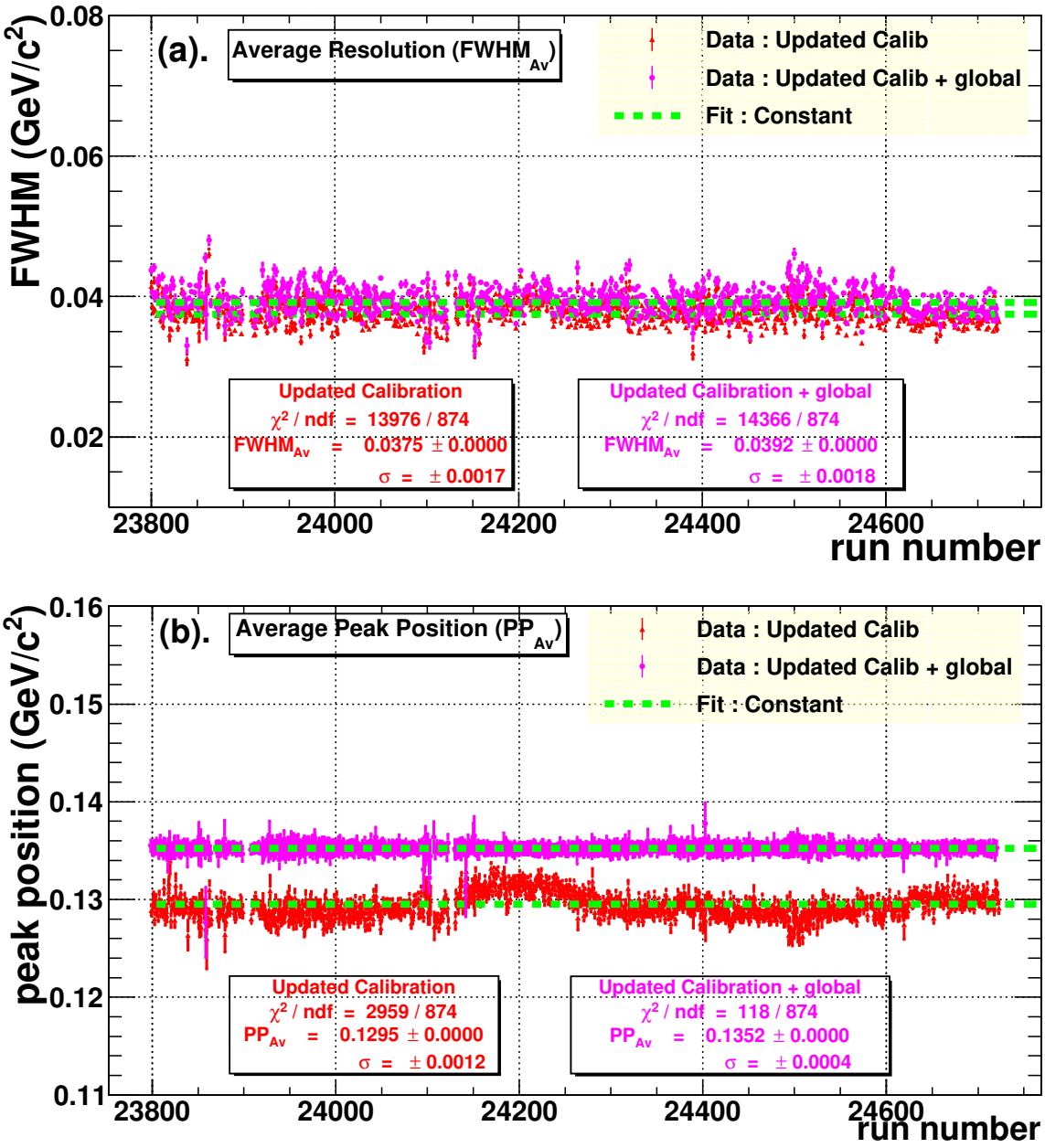

Figure 3.11.: The y-axis of (a) represents the full width half maximum (FWHM) obtained from the fit with the fit error. The x-axis is the run number. The variation of the peak position with the fit error over the run period is shown in (b). The magenta and the red distributions are the comparisons between updated calibration constants and updated calibration constants with global correction, respectively. The green lines are the constant fits. The fit parameters are tabulated in the legends and highlighted in the respective colors. Considering $\chi^2/ndf >> 1$ and $<< 1$, the standard deviation (σ) is the estimated uncertainty from Equation 3.5.

k_Gs for all runs are extracted with the updated calibration constants. The data after global corrections are plotted as magenta points in Fig. 3.11. The average peak position (0.1352 ± 0.0004) GeV/c^2 is at the correct π^0 mass and time dependent inconsistencies are substantially improved after global corrections. The average value for the FWHM is (39.2±1.8) MeV. However, the percentage gain in resolution remained unchanged

12%. Nevertheless, the aim to obtain a stable and precise peak position at π^0 rest mass is achieved.

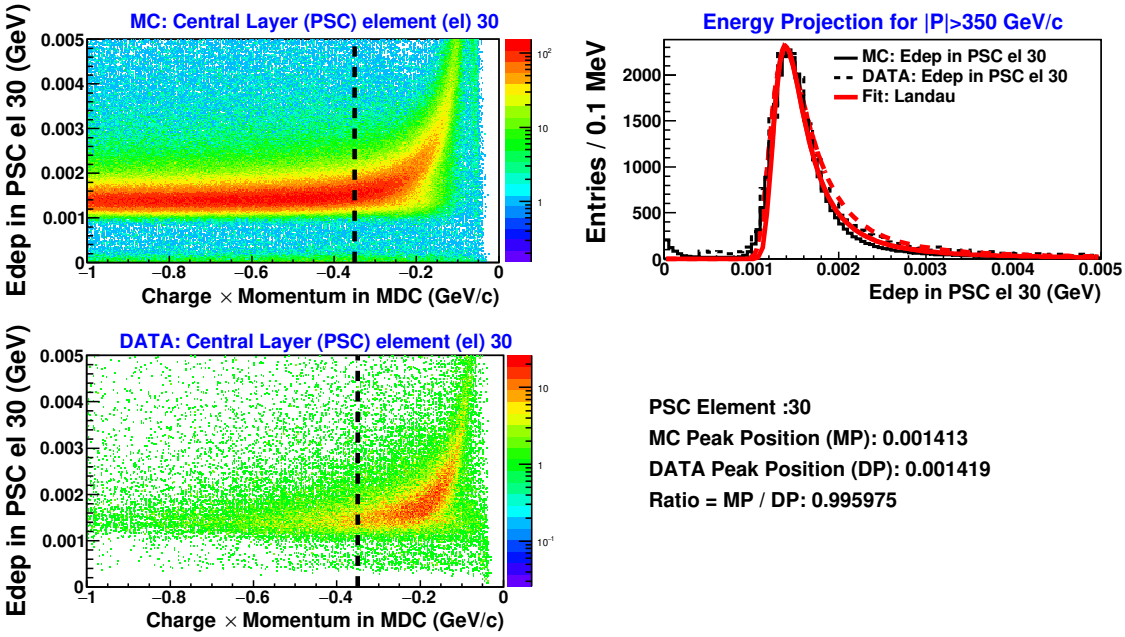

Figure 3.12.: The x-axis of the left column represents the signed momentum (Momentum×Charge) and the y-axis is the deposited energy in the Plastic Scintillator. The total energy deposited in the 30^{th} element of the central layer, by the homogeneously distributed isotropic single track of π^-, is shown in the top left panel. The corresponding data distribution with updated calibration constants is plotted in the bottom left panel. The projections of both histograms for the minimum ionizing pion, below the black dashed line at -350 MeV/c momentum, are plotted in the top right panel. The solid histogram is the Monte Carlo and dashed is the data. The red curve is the Landau function fitted to the projections. The peak positions for the two histograms are listed in the bottom right panel. The ratio of two, as listed in the bottom right panel, is nearly 1. Which is an indication of a reasonable calibration.

3.5.2. Plastic Scintillators

The calibration procedure for the PSB consists of two steps: energy calibration and non-uniformity correction. The description of the plastic scintillator calibration can be found in Ref. [72] and Ref. [84]. As a first step, the constants to convert the measured energy deposited from the QDC units to MeV are determined. The energy loss of a charged particle in a thin plastic scintillator is described by the Bethe-Bloch-Equation, which is a function of the incident kinetic energy of the particle, the path length of the particle through the material, and the properties of the scintillating material. The fluctuations of the energy loss by the ionization of a charged particle were theoretically described by Landau [120]. This description ends with a universal asymmetric probability density function. Considering the dependence of the path length of a particle on the scattering angle theta, the deposited energy by the minimum ionizing particles (MIPs) is corrected for the path length for all theta values in the second step. This step is called the non-uniformity correction.

The path length correction is necessary as the signal generated by the particle has to propagate through the elements to the light-guides at the upstream end. Correspondingly, the

signal is attenuated by the time it arrives to the readout end. The deposited energy of such particles have been rectified for the path length for all values of θ and calibrated deposited energy. The change in the peak position is related to the polar angle by an exponential form $E_{corrected} = E_{original}.exp[-(\theta-\theta_r)/C]$, where C is the non-uniformity correction constant and θ_r is a constant reference angle. These constants are determined by fitting the exponential function to the deposited energy of minimum-ionizing pions versus the polar angle distribution of the data. The non-uniformity correction and the initial calibration constants employed in this study are determined in Ref. [84].

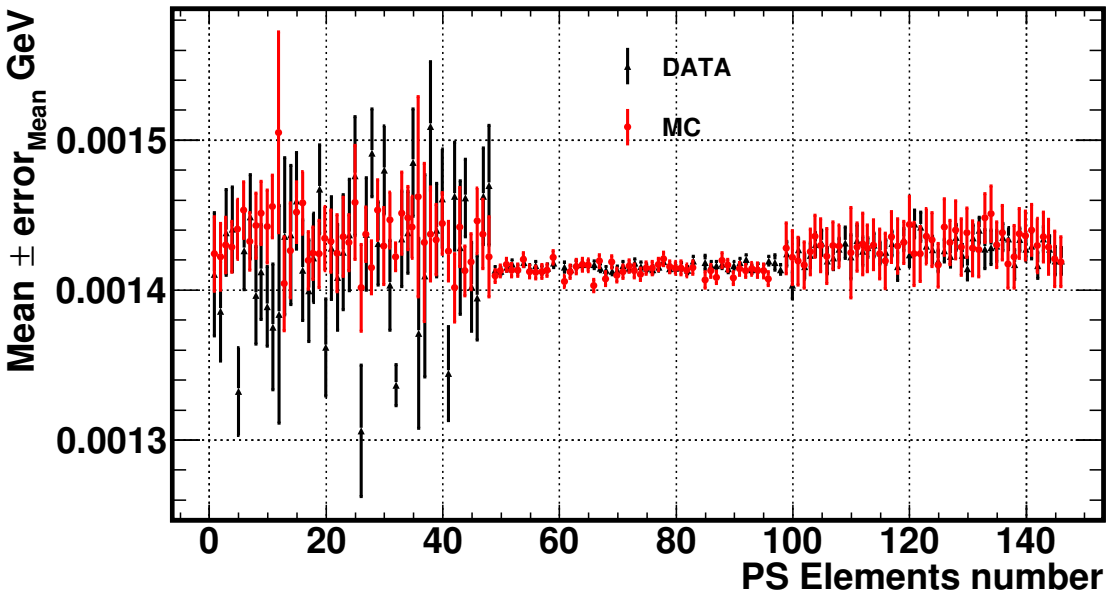

Figure 3.13.: An illustration of the mean of the deposited energy as a function of the PSB elements. The mean values are the peak positions of the Landau fits. The errors shown are statistical obtained from the fit. The black points are the data after new calibration and the red points are the Monte Carlo results. The mean values of the Monte Carlo simulation and data are in agreement.

The process of calibration for this work demanded a fine tuning of the initial calibration constants with the goal of having the peak positions for the data and MC simulation at the same point. This is accomplished by comparing the energy deposit in the PSB for each reconstructed MDC signed momentum (momentum×charged) of the data and Monte Carlo, as shown in Fig. 3.12. The data distribution represents the path length corrected energy loss per unit path length in the PSB. Clearly, the distribution is dominated by the pions, as only a single band is visible. Simultaneously, the Monte Carlo simulated isotropic π^- tracks with the kinetic energy ranged from 10 MeV to 1000 MeV are utilized as a reference for the calibration fine tuning. The π-mesons are MIPs and lose a constant amount of energy above 250 MeV/c. Subsequently, the projection of energy deposited in the PSB, left from the black dashed line at -350 MeV/c signed momentum, is plotted in the upper right panel of Fig. 3.12 for the data and simulations. Both the distributions are fitted with a Landau function [120] to extract the peak positions and resolutions.

The updated calibration constants are determined to match the position of the data peak with simulations. The updated calibration constant $C_i^{updated}$ for i^{th} element is derived from

the initial constant C_i^{initial} for the same i^{th} element as

$$C_i^{\text{updated}} = C_i^{\text{initial}} \times \frac{P_i^{\text{MC}}}{P_i^{\text{data}}}, \tag{3.9}$$

where P_i^{data} and P_i^{MC} are the peak positions for i^{th} element in the data and Monte Carlo, respectively. An illustrative plot to demonstrate the calibration of element 30 in the central layer of the PSB is presented in the top right panel of Fig. 3.12. A comparison between the peak positions of the simulation and the calibrated data is shown. The ratio of two peak positions ($\frac{\text{MP}}{\text{DP}} = \frac{P_i^{MC}}{P_i^{data}}$), as shown in the bottom right panel of Fig. 3.12, is nearly 1. This is an indication of a stable calibration. Similarly, the peak positions for all 150 PSB elements are extracted and populated in Fig 3.13. The errors shown are from the fits. The black points are the calibrated data and the red points are simulations. The large spread in the backward part is due to the lack of statistics, which makes it more difficult to locate the peak position. Moreover, most of the decay products in the data have the forward boost and pass through the central and the forward part of the PSB. The Monte Carlo distribution in these parts has been populated by simulating the isotropic single tracks. Regardless, the peak positions for the data and Monte Carlo are in agreement within errors for all elements of the PSB. Hence, the goal of the calibration is achieved.

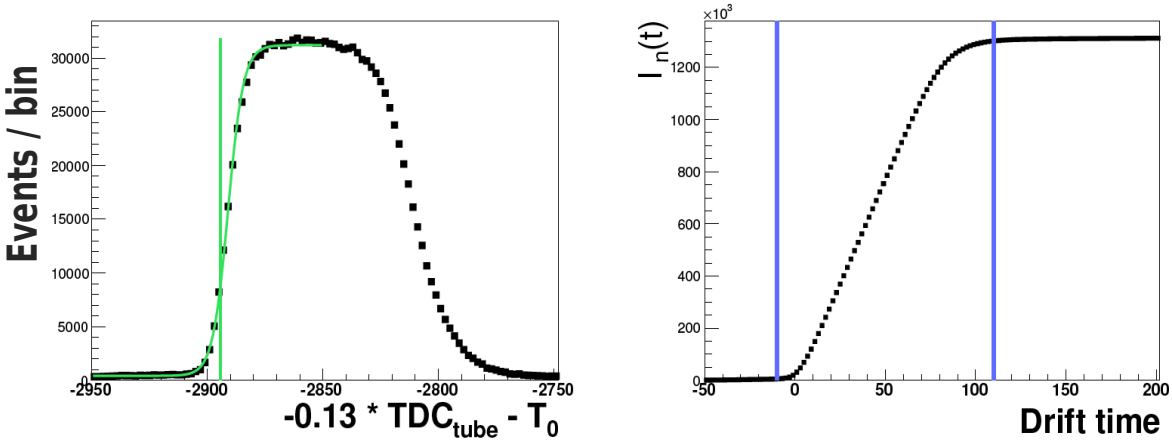

Figure 3.14.: Example distributions for the drift time calibration for one layer in MDC. The figure is taken from Ref. [110]. The distribution of -0.13.TDC$_{tube}$-T$_0$ for data is shown as black points in the left panel. The data are fitted with a Fermi function to the determined offset. The right spectrum is the integral of the left spectrum along with the range indicated by the vertical lines [110].

3.5.3. Mini Drift Chamber

The calibration of the MDC improves the positional information called drift distance by using the time information called drift time. The time taken by the cascade to reach the anode wire is called the drift time. Which is about 100-200 ns depending on the radius of the straw [84]. The time from the PSB is used as the start time for the drift time calculation. The closest approach of a cascade to reach the wire within the drift time is called the drift distance. It is determined by measuring the drift time using distance-time relation. The MDC calibration, which consists of two steps, is performed before the helix reconstruction.

As a first step, the relative offsets between various straws and between times from different TDC modules are corrected. This is done by determining the position of the rising edge of the hit distribution with respect to the PSB time when the cascade reaches the anode of each straw, as shown in the left panel of Fig. 3.14 [109]. In the second step, a range around the distribution is defined, corresponding to the range of the possible drift times. Such a range is shown as a blue window in the right panel of Fig. 3.14 for respective time values shown on the left panel [109]. The smallest time belongs to the particle passing near the anode while the largest time belongs to the particle passing near the tube surface. This time window is mapped to the possible drift distance values. This information is used in the calibration routine on the hit level. The detailed description of the calibration procedure for MDC is discussed in Ref. [84]. The MDC calibration for this data set is done and can be found in Refs. [109, 110].

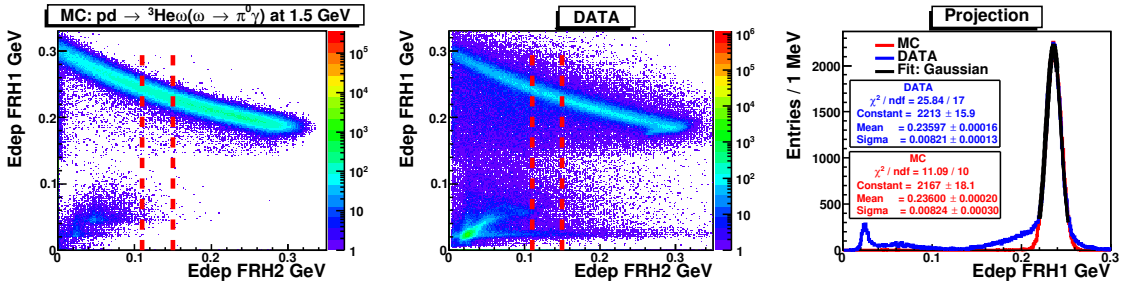

Figure 3.15.: Deposited energy in the first layer of FRH as a function of the deposited energy in the second layer of FRH is shown in the left and middle panels. The simulations after matching to the data are plotted in the left panel. The middle panel represents the measured data. The red dashed lines indicate the range in the second layer of FRH (0.11 GeV−0.15 GeV), for which the deposited energy in the first layer of FRH is projected. The projection for the Monte Carlo simulation and the experimental measurement is plotted in the right panel as blue and red histograms, respectively. The black distribution is the Gaussian function fitted to projections. The fit parameters are arranged in the legends highlighted in the respective colors.

3.6. Data and Monte Carlo matching

To compare simulated events with the experimental data and have optimized efficiencies, the simulated events must show the same performance for each detector component as for the data. The data and the Monte Carlo (MC) simulation are matched using a procedure developed for WASA. This package provides means to modify the detector response in the Monte Carlo according to the experimental data. The procedure of matching the Monte Carlo response to the data is referred to as smearing in this thesis and the related parameters as smearing parameters. Each detector has a separate smearing parameter that defines the detector behavior, describing the particle properties such as energy and time on the hit level. Both the peak position and width of the particle property can be varied.

The Monte Carlo resolution of the energy deposit in each layer of the forward detector is matched with the measurement by employing the relative Gaussian smearing to the deposited energy E as

$$E = E \times Random\ Gauss(1, \sigma_{smear-rel}), \tag{3.10}$$

where *Random Gauss* is a random generator, which samples a random number from the

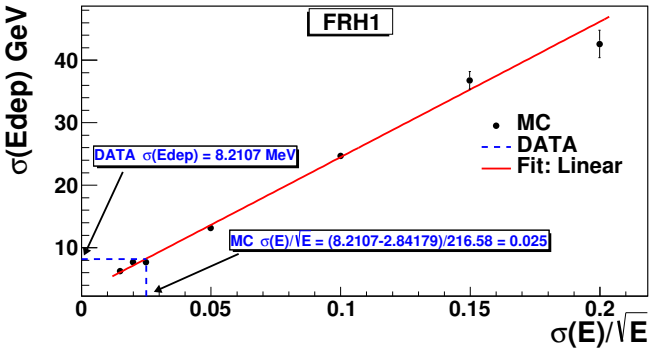

Figure 3.16.: The black points represent the resolution of the energy deposit $\sigma(Edep)$ in the first layer of FRH as a function of the smearing parameters $\sigma(E)/\sqrt{E}$ for the energy deposit in FRH 2 between 0.11 GeV and 0.15 GeV. The Monte Carlo simulations for the pd$\rightarrow$ ^{3}He$\omega \rightarrow$ ^{3}He$\pi^0\gamma$ reaction have been used to generate the distribution. The red curve represents a linear fit to the black points. The y-intercept of the blue horizontal line represents the resolution of experimental measurement ($\sigma = 0.0082$ GeV). The corresponding parameter $\sigma(E)/\sqrt{E} = 0.025$ is shown as the x-intercept of the blue vertical line.

Layer	**Resolution**	
	σ_{data} (MeV)	σ_{MC} (MeV)
FWC1	0.7344 ± 0.0068	0.6812 ± 0.0024
FWC2	0.6463 ± 0.0040	0.6545 ± 0.0020
FTH1	0.8903 ± 0.0047	0.8606 ± 0.0029
FTH2	1.7323 ± 0.0120	1.6673 ± 0.0110
FTH3	1.9859 ± 0.0186	1.8557 ± 0.0162
FRH1	8.2107 ± 0.1253	8.2403 ± 0.2978
FRH2	18.9576 ± 0.1171	18.6171 ± 0.1370

Table 3.2.: The σ of the energy deposit for the data and simulation in different layers of the forward detector are listed after relative smearing.

standard Gaussian Distribution with mean value 1 and resolution $\sigma_{smear-rel}$. The user controlled parameter $\sigma_{smear-rel}$ is tuned to smear the Monte Carlo simulation for a detector component. The parameter $\sigma_{smear-rel}$ is the relative energy resolution $\sigma(E)/\sqrt{E}$. The different resolution of the corresponding detector layer is achieved for different $\sigma_{smear-rel}$ values. To identify the $\sigma_{smear-rel}$ value corresponding to the resolution of the experimental data, the resolution for a range of $\sigma_{smear-rel}$ is determined. For which the deposited energies of simulated and measured ^{3}He particles in various FD layers are plotted as a function of the deposited energy in the consecutive layer. Subsequently, the projection over the energy deposited in one layer for the different energy ranges of the other layer is fitted with the Gaussian function and σ is determined. One such illustration for the first layer of FRH is shown in Fig. 3.15, where the simulation is plotted after applying the final smearing parameter $\sigma(E)/\sqrt{E}$. This is accomplished by fitting the resolution of the Gaussian fit for different values of the parameter $\sigma(E)/\sqrt{E}$, as illustrated in Fig. 3.16. The accurate value for the smearing parameter $\sigma(E)/\sqrt{E}$ corresponding the measured data, as highlighted in Fig. 3.16, is 0.025. The effect of the obtained smearing parameter is demonstrated in Fig. 3.15, where Monte Carlo has a resolution close to the measurement. Likewise, the smearing parame-

ters for other layers of FD are obtained. The σ for the simulation is in agreement with the measurement for all layers of the forward detector, as evidenced in Table 3.2.

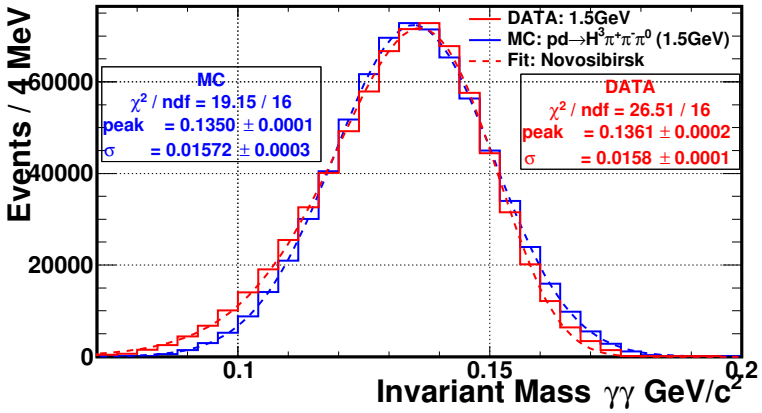

Figure 3.17.: The background-subtracted distribution of the 2γ invariant mass is shown. The red histogram is the data at 1.50 GeV. The blue histogram is the Monte Carlo simulation using pd→ ^{3}He$\pi^+\pi^-\pi^0$ reaction. The simulation shown is the result after the matching procedure. The dashed distributions are the asymmetric Gaussian (Novosibirsk) fit. The fit parameters are shown in the legends.

The calibrated data and the simulation are matched for the SEC using the combined performance and acceptance of all subsystems. Wherein, a single smearing parameter is used for all detectors of the calorimeter. The resolution of the π^0 peak in the Monte Carlo simulation is modified using a relative Gaussian smearing, as described for the FD. The desired value of the smearing parameter $\sigma(E)/\sqrt{E}$ corresponding to the resolution in the measurement is obtained. The simulated data for the reaction $pd \rightarrow {}^3\mathrm{He}\,\pi^+\pi^-\pi^0$ describe the measurement in terms of peak position and resolution, as shown in Fig. 3.17. Minor discrepancies in the line shape around the tails are due to the background subtraction. In a nutshell, the peak positions and resolutions of the data and Monte Carlo are close to each other.

The smearing of the PSB is done iteratively following the same procedure as described for the FD. Where the relative root mean square value of the energy resolution is provided as input. Herein each of the 150 PSB elements has a separate smearing parameter. The σ of the smearing result is shown in Fig. 3.18a. Evidently, the simulation describes well the data within errors.

The simulation of MDC is conformed with the data according to the time resolution of a single drift tube, that is accomplished by smearing the spatial resolution for drift distance on the hit level. The residuals of the drift distance are used as a monitoring parameter. The residual is the difference between the fitted and measured distance. Ideally, the residuals should be zero if there are no systematic shifts, which is observed in the form of a prominent peak near zero. 17 different parameters are deployed to match the Monte Carlo simulations of 17 MDC layers with the data. These parameters are derived iteratively as obtained for FD. The width of the residual of the drift distance for the smeared Monte Carlo and data is extracted and compared in Fig. 3.18b for all layers. The comparison is quantified in terms of the absolute difference between the resolution of the smeared Monte Carlo simulations and measurements $|\sigma_{MC} - \sigma_{DATA}|$, as demonstrated in Fig. 3.18b. Furthermore, $|\sigma_{MC} - \sigma_{DATA}|$ distribution is fitted with a constant function. The uncertainty in the fit parameter is estimated from Equation 3.5 as $\chi^2/ndf >> 1$. The attained value of the fit parameter (0.06±0.05) is close to 0. This indicates that the peak widths of the smeared Monte Carlo are in good agreement with the calibrated data for all the MDC layers.

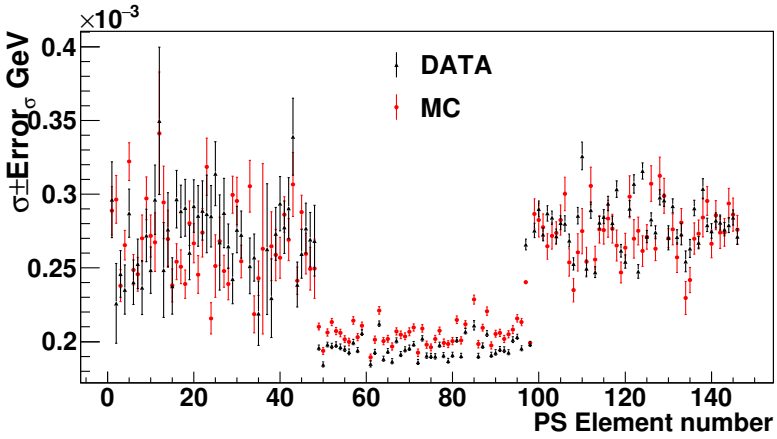

(a)

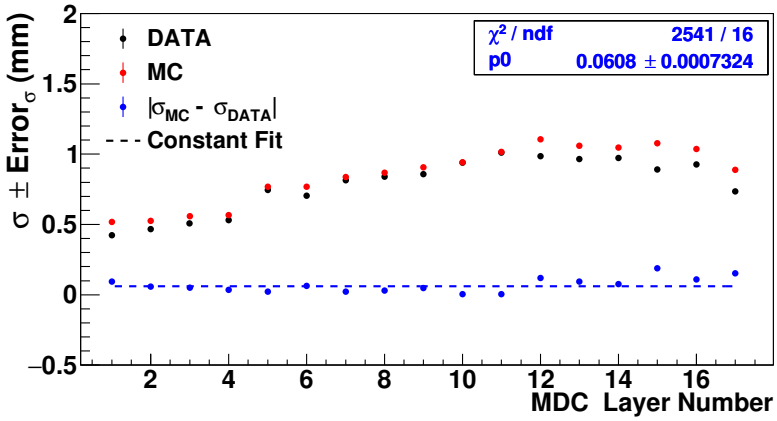

(b)

Figure 3.18.: The mean and σ of the Landau fit for different PSB elements are plotted in (a). However, (b) represents the σ of the Lorentzian peak as a function of the MDC layer number. The black points are the data after applying updated calibration constants and the red points are Monte Carlo simulation after the matching procedure. The absolute difference in the data and the Monte Carlo resolutions ($|\sigma_{MC} - \sigma_{DATA}|$) in the MDC is plotted as blue points. The absolute difference is fitted with the blue dashed constant function. The parameter of the constant fit, as listed in the legend, is valued at 0.

3.7. Run Information

The $pd \rightarrow {}^3\mathrm{He}\,\omega$ experiment was run with 126 s long cycle structure. In the 126 s cycle, the data is accepted only in the flat top period. When the beam is accelerated to the desired energy and stored in the ring, the flat top period starts. 1.4 s after beam acceleration, the high voltages of the detectors (CD, FD, MDC and FPC) are ramped up to the normal operation level. At the cycle time of 5.5 s, the pellet vacuum shutters open and the data acquisition starts. The pellet vacuum shutters closed at 116 s to block the pellet, till the flat top of the next cycle is reached. The high voltages ramp down at 116 s, before the beam is dumped, to protect the wire chamber and photomultiplier tubes from high current. Fig. 3.19 is an illustration of the scaler readout for a cycle during data collection. A detailed graphical description of a single cycle structure can be found in Fig. 3.20. The duty cycle of DAQ is around 88.5%. However, the average livetime of the data acquisition is estimated to be 82%. That is the ratio of input trigger and accepted trigger signals (DAQ livetime =

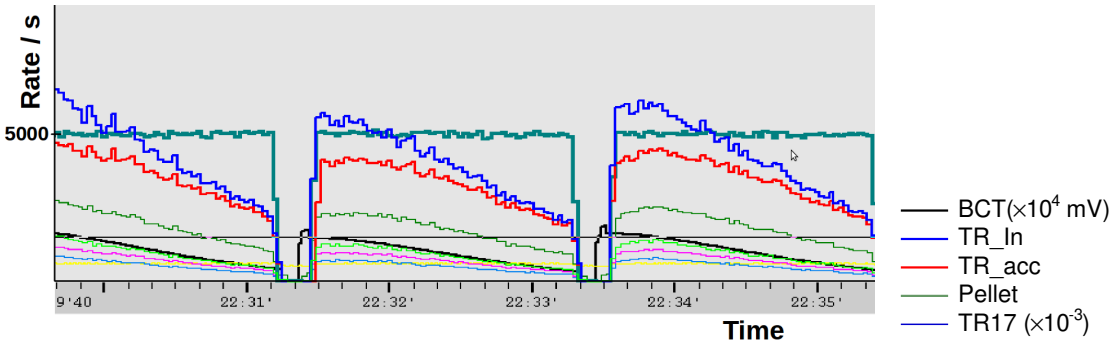

Figure 3.19.: Scaler display for several cycles of the experiment. The x-axis is the clock time during a run. The time for each of the three cycles shown in the plot is 126 seconds. The black curve is beam intensity provided by a beam current transformer (BCT), downscaled by a factor of 10000. The castleton green line is the pellet rate. The blue curve is the rate of the experimental trigger called input trigger (`TR_In`) which includes all triggers shown on the display except black, castleton green, and red lines. The red curve is the trigger accepted by the data acquisition called trigger accepted (`TR_acc`). The sky blue curve is trigger 17, which is a measure of the luminosity. Other curves are the rates for the other input triggers, which will not be discussed here. The rate of all trigger rates is given in s^{-1}.

TR_In/TR_acc) measured at different time instances during the data taking.

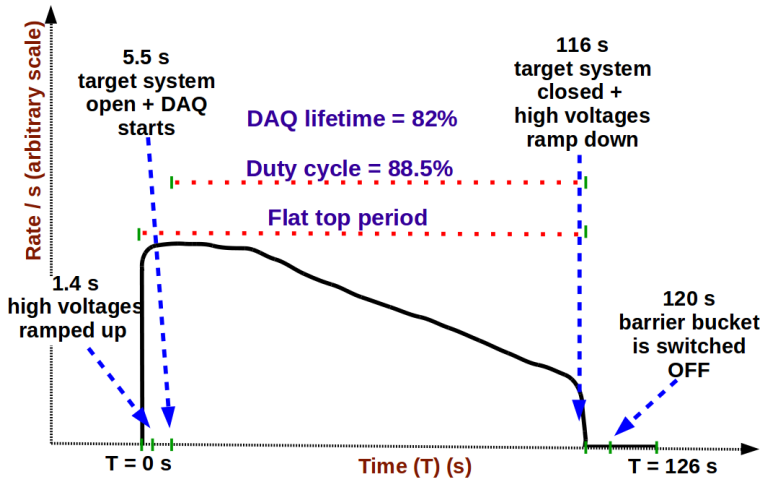

Figure 3.20.: The detailed structure of a cycle during the $pd \rightarrow {}^3\mathrm{He}\,\omega$ beam time.

The total run time for the full beam is the sum of the time of individual runs, which is estimated to be 205.1 hours. The values are arranged in Table 3.3. Considering the duty cycle of 88.5% and DAQ lifetime of 82.0%, the effective time for data taking (T_R) is 148.83 hours, as shown in Table 3.3. The effective time of the run (T_R) is used to estimate the average luminosity and will be discussed in Section 4.1.2.

The luminosity is an important feature and must be studied in an experiment given how it affects the data analysis at higher values, which will be discussed in a systematic way in Section 5.2.2. The luminosity achieved can be monitored via Trigger 17 called “luminosity trigger”. Trigger 17 is a measure of the pd scattering events during the experiment. It

	1.45 GeV	1.50 GeV	Entire data
Total Time of data taking	105.08 hours	100 hours	205.08 hours
Duty Cycle			88.5%
DAQ life time			82%
Time of data taking T_R	76.26 hours	72.57 hours	148.83 hours

Table 3.3.: An estimation of the effective time of the data taking.

sends a signal if both the central and forward layers of PSB have at least one hit above thresholds. This trigger gives the luminosity measure in terms of the total event rate per second. However, the events are not distributed uniformly but appear in discrete spikes whenever individual pellets are passing through the proton beam, as demonstrated in Fig. 2.3. In addition, the pellet rate fluctuates throughout the beam time with an average value between 2,000 and 8,000 pellets per second. To account for these effects, an instantaneous event rate is derived when the pellet traverses the beam. This instantaneous rate is the ratio of the luminosity rate to the pellet rate "TR17/Pellet rate". More details about this factor can be found in Ref. [84].

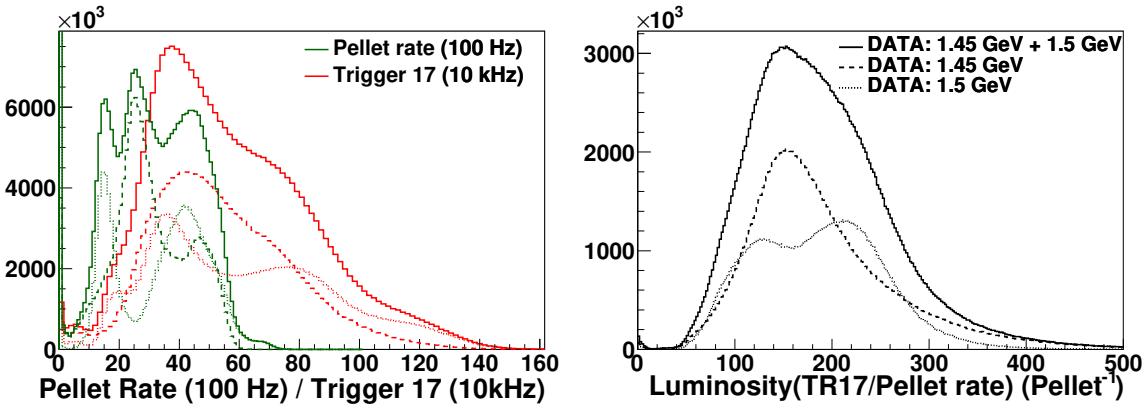

Figure 3.21.: The pellet rate and the Trigger 17 rate are plotted in the **left panel** as red and dark green histograms, respectively. The dashed, dotted and the solid lines are the corresponding distributions for the rates averaged over the runs at 1.45 GeV, 1.50 GeV and for the combined data set. The **right panel** represents the instantaneous luminosity factor "TR17/Pellet rate" combined for all the runs.

The factor "TR17/Pellet rate", which is the relative measure of the instantaneous luminosity, is used for this work. The instantaneous luminosity can be estimated by combining the relative measure with a conversion factor, which is derived from the trigger simulations and known attributes of the pellet target. It is clearly seen in Fig. 3.19 that the trigger rates and hence the relative measure of the luminosity vary over the cycle. The luminosity is varied due to various factors, such as the fractional fluctuations in the beam current and the pellet target variations due to the temperature. The luminosity trigger, pellet rate, and the instantaneous luminosity measure have been averaged over the beam time and plotted in Fig. 3.21. Clearly, the values of the most probable instantaneous luminosities measure are $\approx$150 $pellet^{-1}$ for 1.45 GeV, $\approx$130 $pellet^{-1}$ and $\approx$220 $pellet^{-1}$ for 1.50 GeV and $\approx$150 $pellet^{-1}$ for the entire data set.

4. Data Analysis and Signal Extraction

The analysis starts with selecting the $pd \rightarrow {}^3\mathrm{He}\,\omega$ final state by identifying ^{3}He particles using the particle identification method described in the previous chapter. Followed by the selection of the Central Detector tracks specific to the ω decay. Specific conditions are used to suppress the background coming from different reactions and other ω decays.

In the reaction $pd \rightarrow {}^3\mathrm{He}\,\omega$, the ω meson is tagged via the missing mass derived from the initial and final state particles p, d and ^{3}He. The missing mass, which is the effective mass of the system, is the difference of the square of the missing energy and the missing momentum of the system. The missing mass ($MM_{^3\mathrm{He}}$), which is used to tag the ω meson, is derived from the scattered ^{3}He particle and can be expressed as

$$MM^2_{^3\mathrm{He}} = \left(E_p + E_d - E_{^3\mathrm{He}}\right)^2 - \left(\vec{\mathbf{P}}_p + \vec{\mathbf{P}}_d - \vec{\mathbf{P}}_{^3\mathrm{He}}\right)^2 , \tag{4.1}$$

where E_p, E_d and $E_{^3\mathrm{He}}$ are the energies of the proton beam, target deuteron and the ^{3}He and $\vec{\mathbf{P}}_p$, $\vec{\mathbf{P}}_d$ and $\vec{\mathbf{P}}_{^3\mathrm{He}}$ are their momenta, respectively. In an event where an ω meson is produced, $MM_{^3\mathrm{He}}$ should correspond to the ω meson mass. This missing mass is independent of the decay mode of the ω and depends only on the measurement of the ^{3}He particles. The missing mass without a decay specific selection in the Central Detector is called inclusive for this study. As an example, in the final state $pd \rightarrow {}^3\mathrm{He}\,\omega$, the ω meson is reconstructed inclusively. Whereas, when the ω meson is tagged with additional decay specific constraints in the Central Detector, the missing mass is called exclusive. For instance, the decays $\omega \rightarrow \pi^0\gamma$ and $\omega \rightarrow e^+e^-\pi^0$ are the candidates of the exclusive final state. In the following sections, the analysis steps used to select ω decay channels are presented.

4.1. $pd \rightarrow {}^3\mathrm{He}\;\omega$ Final State Reconstruction

In order to reconstruct the $pd \rightarrow {}^3\mathrm{He}\,\omega$ inclusive final state, the ^{3}He track in the forward direction is identified using the method described in Section 3.3.1.

4.1.1. ^{3}He Selection

The initial selection of the ^{3}He candidates starts from the threshold-based trigger level and further selection is made during the preselection, as discussed in Section 3.4. The dedicated calibration constants are mentioned in [110]. In order to have a realistic Monte Carlo efficiency, the threshold and the trigger conditions used during the experiment are mimicked and applied to the simulated data.

The ΔE-ΔE distributions, as used for the preselection in Section 3.4, are plotted for the Monte Carlo simulation of the $pd \rightarrow {}^3\mathrm{He}\,\omega(\omega \rightarrow \pi^0\gamma)$ reaction and preselected data in Fig. 4.1a and Fig. 4.1b, respectively. In the data distribution, a ^{3}He band is seen along with residual background contributions. This background mostly constitutes of protons and

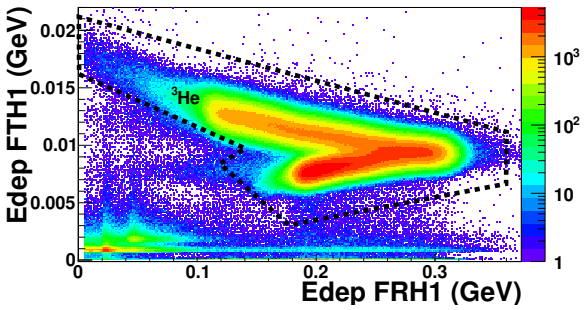

(a) Simulation using the $pd \rightarrow {}^3\mathrm{He}\ \omega(\omega \rightarrow \pi^0\gamma)$ reaction.

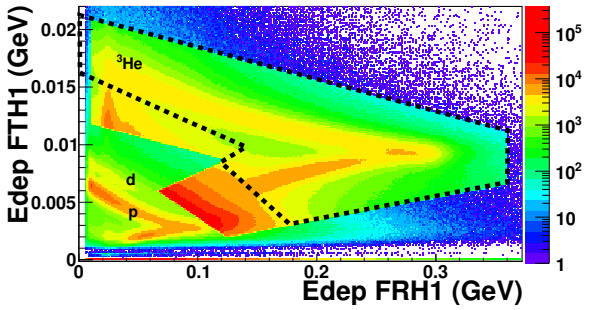

(b) Preselected data.

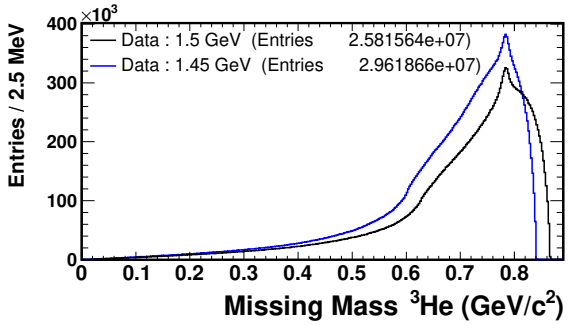

(c) Missing mass of ^{3}He particles using data: including all ω decays and non-resonant background.

Figure 4.1.: Particle identification plot for ^{3}He particles. The energy deposited in the first layer of the forward range hodoscope (FRH1) as a function of energy deposited in the first layer of forward trigger hodoscope (FTH1) is plotted in the top row. **(a)** represent the Monte Carlo simulations and **(b)** is data. The missing mass of ^{3}He particles using Equation 4.1 is plotted in **(c)** for two energies. The peak at the ω meson mass 0.7827 GeV/c^2 sitting on top of a continuous background.

deuterons originating from the elastic scattering, quasi-elastic scattering and breakup reactions. The boundary around the ^{3}He band is enhanced due to the graphical cut used during preselection (Section 3.4). The loci around the deposited energy of 0.015 GeV in FTH 1 and 0.02 GeV in FRH1, and the deposited energy of 0.005 GeV in FTH 1 and 0.16 GeV in FRH1 correspond to the minimum ionizing protons and deuterons that fall into the graphical cut implemented for the preselection. Although, the latter structure includes contributions from the low energy protons and deuterons satisfying the preselection condition. It has been observed in simulations that the high energy ^{3}He particles lose a remarkable amount of energy due to nuclear interactions with the detector material.

The graphical cut to select ^{3}He particles is optimized by choosing the best cut window from the available selection choices. The cut optimization aims to achieve the maximum possible signal and minimum possible background content. For this purpose, a quantity called significance (S) is defined. S gives the measure of the statistical power to observe the signal and provides the number of standard deviations the signal is away from zero [121].

$$S = \frac{N_s}{\sigma(N_s)} = \frac{N_s}{\sqrt{N_s + N_b}}, \tag{4.2}$$

where N_s is the number of observed signal events in the ω peak, $\sigma(N_s)$ is the uncertainty in

N_s, and N_b is the number of events in the remaining background. The numbers N_s and N_b have been obtained by fitting the ^{3}He particles missing mass distribution (Equation 4.1). The fitting procedure will be discussed later in Section 4.1.2.

Significance less than 3 means that the statistical power is not sufficient to observe the signal. On the other hand, significance between 3 and 5 means that the signal is close to be observed, while its value larger than 5 would mean that signal will be observed. In a nutshell, the significance is a qualitative instrument that allows to monitor and quantify the signal quality.

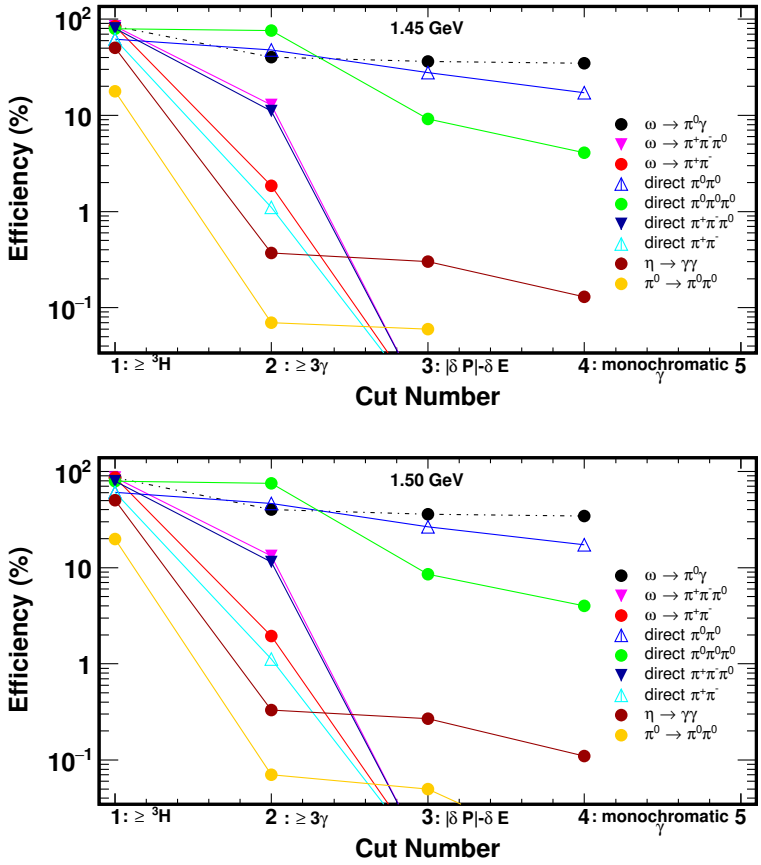

Figure 4.2.: A comparison between the efficiencies of the signal decay $\omega \to \pi^0\gamma$ and the backgrounds at each step of the analysis. The labels on the x-axis are various analysis conditions and the y-axis represents the corresponding efficiency. The explicit values for each cut are listed in Appendix. E.1. Evidently, the signal to background ratio has improved significantly at each step of the analysis.

For cut optimization, the significance and the overall reconstruction efficiency (ε) are optimized simultaneously, as explained in Appendix B.1. The reconstruction efficiency (ε) is defined as,

$$\varepsilon = \frac{\text{Numbers of events survived the selection criteria}}{\text{Total number of simulated events}} = \frac{N}{N_0}. \tag{4.3}$$

The overall reconstruction efficiency is the product of the geometric acceptance, the intrinsic efficiency of the detector and the reconstruction efficiency of the analysis algorithms. The intrinsic efficiency is defined as the fraction of particles impinging on the detector that interacts

with it to produce detector signals. The geometric limitation of the detector is determined from the output of the event generator, as discussed in Section 3.1.

The selection to choose ^{3}He particles for this analysis is indicated on the Monte Carlo and data distributions in Fig. 4.1. The corresponding reconstruction efficiency ε_{inc} is 84.65% for 1.45 GeV and 86.71% for 1.50 GeV beam energy, as shown in Fig. 4.2. The selection has the statistical significance value of 61 and 66 for 1.45 GeV and 1.50 GeV, respectively. Further details are given in Appendix B.1. The smaller significance for 1.45 GeV data set as compared to 1.50 GeV can be explained with the fact that the cross section for ω production is comparable at both energies, while the multi pion production cross section is larger at 1.45 GeV [90, 99]. The events from the residual background contributions will be rejected at the later stages of the analysis.

The kinetic energy of the ^{3}He particle is reconstructed using the scattering angle θ and the deposited energy, as described in Section 3.2.1. The back to back decay of the two-body ^{3}He-ω final state in the center of mass frame is no longer the same in the lab frame. The trajectories and energies of ^{3}He particles and ω mesons are correlated in the lab frame. In order to see this correlation for ^{3}He particle, the scattering angle as a function of the kinetic energy is plotted in Fig. 4.3. Owing to the kinematic constraint, the ^{3}He particles from the ω production lie on the arc as seen in the simulation.

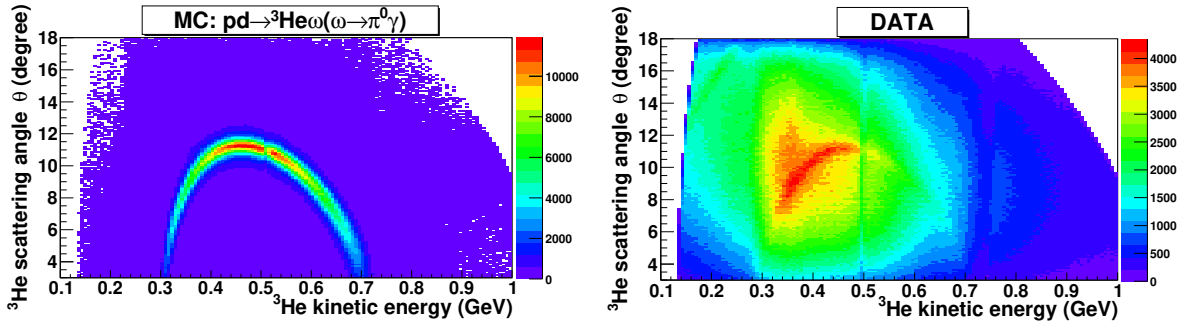

(a) Simulation of the $pd \rightarrow {}^3He\ \omega(\omega \rightarrow \pi^0\gamma)$ reaction for 1.50 GeV beam kinetic energy

(b) Data for 1.50 GeV beam kinetic energy

Figure 4.3.: Correlation between the polar angle θ and the kinetic energy of the ^{3}He particles. The distribution of the Monte Carlo simulation using the $pd \rightarrow {}^3He\ \omega(\omega \rightarrow \pi^0\gamma)$ reaction is shown in (a), and for the data is plotted in (b). The kinetic energy and θ values are kinematically restricted to the curvature, clearly visible in the simulation spectrum. The similar curvature is seen in the data, but in coincidence with the background from the non-resonant multi pion production. The simulation shows the ^{3}He particles from the ω meson production is within the geometric acceptance of the WASA detector.

The ^{3}He particles from non-resonant direct pion production and the mis-reconstructed tracks account for large background contributions in the data. Resultantly, the maxima of the ω meson curvature in the data shift to the lower energy as compared to the simulation. The maxima of the curvature is defined as the position on the ω arc with the maximum number of entries. These maxima can be seen as the red portion of the arc in both histograms of Fig. 4.3. The maxima are subsequently comparable when the background contribution in the data is reduced at the later stage of the analysis, as shown in Fig 4.15. The gaps at 0.5 GeV and 0.7 GeV kinetic energies are due to the separation between the individual layers of FRH. Due to these gaps the energy information in the material between the layers is lost.

The missing mass distributions $MM_{^3\mathrm{He}}$ for two beam energies are shown in Fig. 4.1c. Evidently, the missing mass distributions for two energies have peaks at the ω meson mass 0.7827 GeV/c^2, on top of a continuous background. The peak positions for two energies are

at the PDG value of the ω meson mass, which indicate the goodness of detector calibration and kinetic energy reconstruction. The background of the missing mass distributions ends at different values because of the different phase space of the two energies. The two phase space distributions are useful for systematic studies of the background subtraction, as discussed in Chapter 5. The steep rise in background continuum, between 0.60 GeV/c^2 and 0.65 GeV/c^2, is due to the geometric acceptance limit of the forward detector for these multipion non-resonant background reaction (refer to Appendix A.3). This in turn enhanced further by the ^{3}He particle identification cut, which makes a different influence on the two types of major reactions (see Appendix A.2). The background of the multi pion production is subtracted to extract the ω meson peak, as discussed in the next section.

4.1.2. Inclusive Missing Mass of the ^{3}He after ^{3}He Selection

The ω meson, including all ω decays, is tagged via the missing mass of the proton, deuteron and ^{3}He system. In order to count the number of ω mesons in the data, the smooth background from the direct pion production must be subtracted. This is achieved via a simultaneous fit of the signal peak and background distribution.

The Monte Carlo simulated phase spaces of the multi pion productions are used to fit background in the data. The Monte Carlo simulation is an isotropic phase space distribution where only resonance production with mass-dependent Breit-Wigner sampling and energy-momentum constraints are included. As the correct phase shape of the background is unknown, the phase space simulations of the most prominent backgrounds are weighted with a polynomial to fit the data. For a comparison with the neutral final state $\omega \to \pi^0\gamma$ at the later stage of the analysis, only neutral multi pion productions ($\pi^0\pi^0$ and $\pi^0\pi^0\pi^0$) are considered. The final combined fit function used to describe the data is given as

$$\text{Fit function} = p_0 \cdot PS_{\omega\to\pi^0\gamma}(x) + (p_1 \cdot PS_{\pi^0\pi^0}(x) + p_2 \cdot PS_{\pi^0\pi^0\pi^0}(x)) \cdot \left(1 + p_3 \cdot x + p_4 \cdot x^2 + \ldots\right), \tag{4.4}$$

where x is the missing mass of ^{3}He estimated using Equation 4.1. p_i are the fit parameters. $PS_{\omega\to\pi^0\gamma}(x)$, $PS_{\pi^0\pi^0\pi^0}(x)$ and $PS_{\pi^0\pi^0}(x)$ are the Monte Carlo phase space (PS) distributions for the $\omega \to \pi^0\gamma$ decay, $pd \to {}^3$He $\pi^0\pi^0\pi^0$ reaction and $pd \to {}^3$He $\pi^0\pi^0$ reaction, respectively, at missing mass x. $(1 + p_3 \cdot\ x + p_4 \cdot x^2 + \ldots)$ represents the polynomial convoluted with the background phase space distributions.

As seen in Fig. 4.1c, the two energies have different kinematic limits and phase space distributions, and therefore the resulting polynomial order and fit ranges are different for two energies. To decide the order of the polynomial and fit range, the goodness-of-fit (calculated using MINUIT minimization routine in root) is monitored for various polynomial orders and the fit ranges. The polynomial of order 5 between fit range $[0.575 - 0.840]$ GeV/c^2 provides the lowest χ^2 value for 1.50 GeV spectrum (see Appendix K for illustration). However, the phase space of the 1.45 GeV beam energy is more sophisticated to fit. In this case, the ω peak is sitting directly on the top of the maximum of the background phase space (compare Fig. 4.1c and Appendix A.3). A higher order (6^{th}) polynomial, and the fit range $[0.575 - 0.855]$ GeV/c^2 provide the minimum value for the χ^2/ndf in 1.45 GeV data (Appendix K).

The final fits are shown in Fig. 4.4. The background-subtracted peak is compared to the Monte Carlo simulation of the $pd \to {}^3$He $\omega(\omega \to \pi^0\gamma)$ reaction. The peak positions for both energies 1.45 GeV and 1.50 GeV are (783.44±0.12) MeV/c^2 and (783.33±0.12) MeV/c^2, respectively, which are near the ω meson mass (782.70±.12) GeV/c^2. The peak widths

are almost double the particle data group value (8.49±0.08) MeV/c^2 [39]. That is (15.36±0.36) MeV/c^2 for 1.45 MeV and (15.71±0.37) MeV/c^2 for 1.50 GeV GeV beam enery. This is due to the fact that the ω line shape is convoluted with the detector resolution. Appendix F can be referred to for ^{3}He resolution.

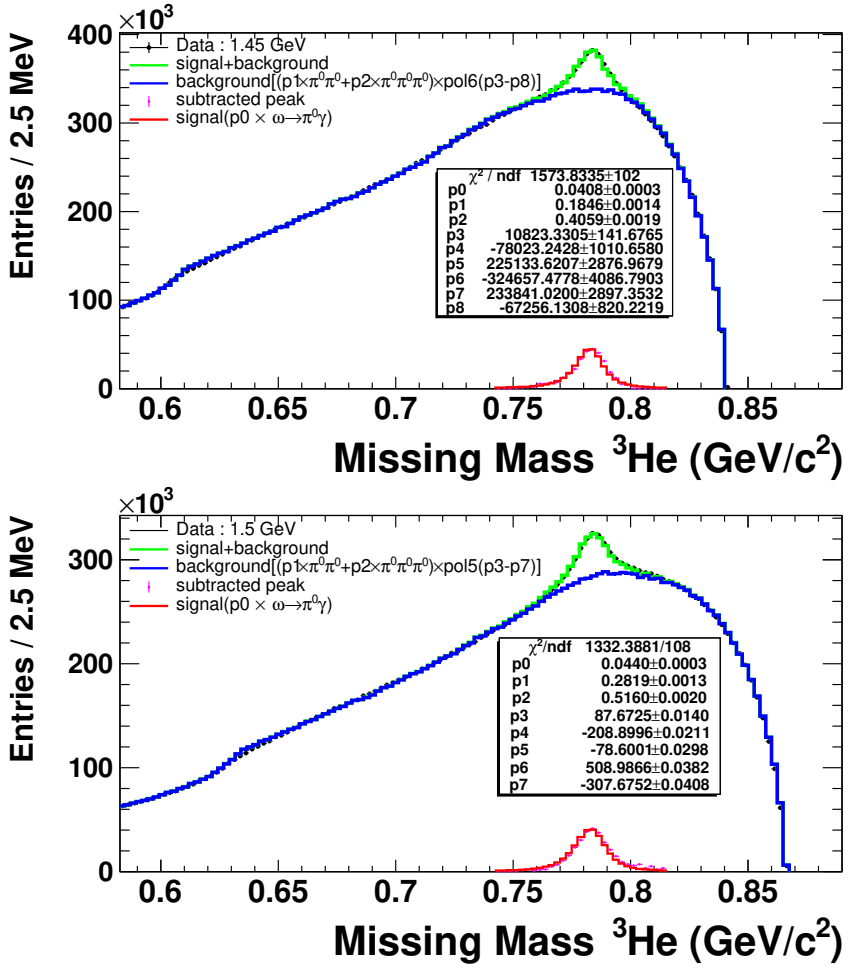

Figure 4.4.: The inclusive missing mass spectrum of ^{3}He particles for the two beam kinetic energies. The black histogram is data, the green curve is the combined fit of the signal (Monte Carlo simulation for the $\omega \rightarrow \pi^0\gamma$ decay) and the background (Monte Carlo simulation for the $pd \rightarrow {}^3\text{He}\ \pi^0\pi^0$ and $pd \rightarrow {}^3\text{He}\ \pi^0\pi^0\pi^0$) convoluted with a polynomial. The background-subtracted data have been plotted as magenta points. The subtracted data is compared to the simulation of the $\omega \rightarrow \pi^0\gamma$ plotted as the red curve. The simulation, in combination with the parameter p0, is sufficient to describe the line-shape of the subtracted data peak.

The events in the background-subtracted peak, which provide an estimated number of ω mesons, are listed in Table 4.1. The errors shown in the ω count are statistical, propagated as, ${}^{stat}\sigma_{signal} = \sqrt{\sigma^2_{data} + \sigma^2_{background}} = \sqrt{N^{count\ range}_{data} + N^{count\ range}_{background}}$. The in-peak signal to background ratio ($N^{count\ range}_{signal}/N^{count\ range}_{background}$) is 0.0325 and 0.0400 at 1.45 GeV and 1.50 GeV, respectively. Which is estimated by dividing the numbers in the peak region ($N^{count\ range}_{sigal}$) to the number in the background distribution ($N^{count\ range}_{background}$) in the peak region. The peak region is the missing mass distribution between 0.736 GeV/c^2 and 0.824 GeV/c^2. As mentioned

	1.45 GeV	**1.50 GeV**	**Entire data set (1.45 GeV+1.50 GeV)**
N_{ω}^{rec}	$(3.15\pm0.04)\times10^5$	$(3.28\pm0.04)\times10^5$	$(6.43\pm0.06)\times10^5$
$N_{\omega}{}^{\circ} = \frac{N_{\omega}^{rec}}{\varepsilon_{inc}}$	$(3.72\pm0.05)\times10^5$	$(3.78\pm0.05)\times10^5$	$(7.50\pm0.07)\times10^5$

Table 4.1.: A list of the number of ω mesons reconstructed N_{ω}^{rec} and the total number of ω mesons $N_{\omega}{}^{\circ}$ produced using the inclusive missing mass. The errors shown here are statistical.

previously, the smaller signal to background ratio at 1.45 GeV is due to the fact that the ω production cross section is comparable at both energies, while the multi pion production cross section is larger at 1.45 GeV [90, 99].

The efficiency corrected numbers are the estimate of the total number of ω mesons produced, as shown in Table 4.1. The sum of the numbers at two energies gives the numbers for the entire data set. The estimated number of ω mesons is around 0.64 million and efficiency corrected number is about 0.75 million. The numbers from Table 4.1 will be used in Chapter 5 to estimate the branching ratio and the number of the $\omega \to e^+e^-\pi^0$ decays.

The total number of ω mesons (N_{ω}°) is used to estimate the average luminosity L_A, which is averaged over the entire beam time as

$$L_A = \frac{N_{\omega}{}^{\circ}}{cs_{\omega} \times T_R} = \left[\frac{(7.50 \pm 0.07) \times 10^5}{(83.6 \pm 1.5) nb \times 148.83\ hours}\right]_{entire\ data} \tag{4.5}$$
$$L_A = (1.67 \pm 0.04) \times 10^{31} cm^{-2} s^{-1},$$

where T_R is the total run time from Table 3.3 and the cross section cs_{ω} is (83.6±1.5)nb at 1.45 GeV beam kinetic energy [90]. The known cross section at 1.45 GeV is used for the entire data set in the calculations because the cross section at 1.5 GeV range is negligibly different [90]. The luminosity is comparable to the luminosities in previous $pd \to {}^3\mathrm{He}\ \eta$ experiments [72, 84]. The order of the instantaneous luminosity is known from the estimated average luminosity L_A, as the instantaneous luminosity dependence branching ratio of $\omega \to \pi^0\gamma$ will be studied is Section 5.2.2.

4.2. $pd \to {}^3\mathrm{He}\ \omega(\omega \to \pi^0\gamma)$ Final State Reconstruction

The study of the $\omega \to \pi^0\gamma$ decay is presented below. This decay serves as one of the reference channel of the $\omega \to e^+e^-\pi^0$ decay. The three neutral tracks in the Central Detector for the $\pi^0\gamma \to \gamma\gamma\gamma$ final state are selected in addition to the ^{3}He particles in the forward direction. The following discussion describes the routine used to reconstruct the $\pi^0\gamma$ final state.

4.2.1. γ Identification

Three or more neutral tracks having energy deposit above 20 MeV are identified in the SEC, assuming that the track has no corresponding hits in the PSB and MDC. No explicit condition is added on the track multiplicity in the Central Detector because it will filter out good event candidates due to chance coincidences and neutral split-offs.

The chance coincidence may lead to the inclusion of tracks from background events within time conditions and/or drop the efficiency at higher luminosities, due to the long

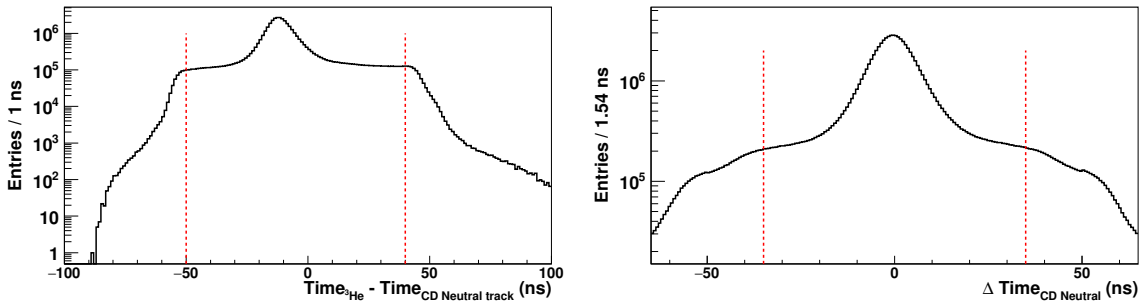

(a) Time difference between neutral tracks in CD and the selected ^{3}He.

(b) Time difference between two neutral tracks in CD.

Figure 4.5.: Time coincidence plots to select the three photons final state of the ω decay. The black distributions represent the time differences in data. The events within the red dashed lines have been selected.

SEC signals and correspondingly long integration times. The wrongly reconstructed tracks due to these effects violate the principle of energy-momentum conservation. These effects have been studied in detail in Ref. [84]. However, in this work, the first effect is taken care of by applying strict Kinematic conditions and the second effect will later be studied in Section 5.2.2.

Split-offs are wrongly reconstructed low energetic fake photon tracks. As stated in the previous chapter, a cluster in the SEC is reconstructed by looking for a continuous spread of energy deposited by the particle into neighboring elements. The average cluster size is a few crystals surrounded by a border of empty crystals, as shown in Fig. 3.5. There is a possibility that one of the elements from the same cluster does not fire, thus creating a hole. As a result of this gap, the same cluster may be split into two different clusters very close to each other. One of the two clusters has very low energy. Therefore, an event with one photon can be reconstructed as two tracks. The low energetic cluster is called split-off. These split-offs can be seen in any kind of shower in the SEC: the electromagnetic shower of photons, the electromagnetic shower of $e^{\pm}$ and the hadronic shower of $\pi^{\pm}$. A detailed description about split-off can be found in Ref [122].

The γ identification in the Central Detector starts with checking the time coincidence of the neutral track with the selected ^{3}He particles. The time of ^{3}He tracks is taken from FTH, while for the neutral tracks it is provided by SEC cluster. As different detectors have different resolution, it is necessary to use different time cut for charged and neutral particles. The time difference distributions used to monitor the chosen time window are presented in Fig. 4.5. The optimal time windows are indicated. Neutral tracks with time coincidences of (-50 ns−40 ns) with the ^{3}He particles and (-35 ns−35 ns) with other neutral tracks are considered. The presence of some background cannot be ruled out despite using a narrower time cut. The cut windows are chosen in such a way that the region of maximum density of the signal is included and the background from events like pile up or spurious tracks is excluded from the selection. The remaining physical background, which cannot be eliminated by the time cut, will be highly suppressed by applying the decay specific kinematic conditions.

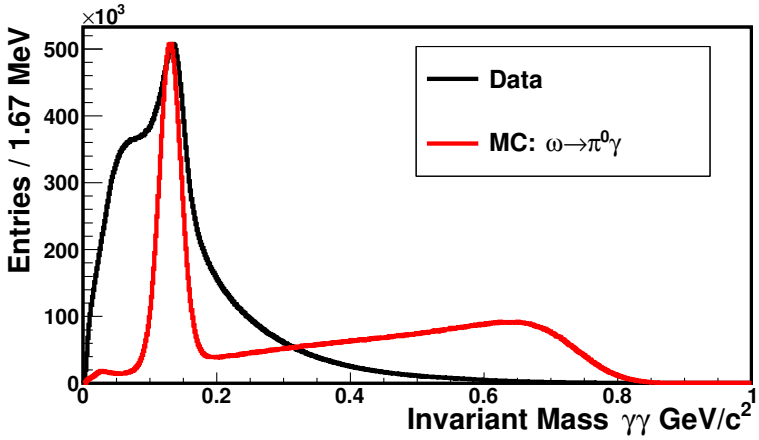

Figure 4.6.: The invariant mass distributions of any two neutral tracks in the Central Detector within the time window shown in Fig. 4.5. The black curve is data and the red curve is Monte Carlo simulation for the $\omega \to \pi^0\gamma$ decay. The simulation is scaled to the data with respect to the maximum height of the spectra. A peak is observed at the π^0 meson mass 0.135 GeV/c^2, in both distributions.

4.2.2. π^0 Reconstruction

The π^0 meson in the $\omega \to \pi^0\gamma$ decay channel is reconstructed by investigating the invariant mass of two neutral tracks for all possible combinations. The two γ invariant mass ($M_{\gamma_1\gamma_2}$) in the Central Detector is calculated from the reconstructed energies ($E_{\gamma 1}$,$E_{\gamma 2}$) and momenta ($P_{\gamma 1}$,$P_{\gamma 2}$), using Equation 3.3.

Fig. 4.6 shows the invariant mass of any two reconstructed photons in data and Monte Carlo of the $pd \to {}^3\mathrm{He}\,\omega(\omega \to \pi^0\gamma \to \gamma\gamma\gamma)$ reaction. In both cases a peak is seen on top of a continuous background. The enhancement of the spectra at low energy ((0.01-0.02) GeV/c^2) is mainly from the split-offs. The rest of the background shape is a result of the combinations where one of the γ is not from the π^0 meson. The broad hump around 0.7 GeV/c^2 in the combinatorics of the Monte Carlo simulation is seen due to the fact that the three photons invariant mass in the $\omega \to \pi^0\gamma$ decay must peak at the ω meson mass 0.7827 GeV/c^2. When the single photon combines with one of the photons from the $\pi^0 \to \gamma\gamma$ decay, the invariant mass must not be at the ω meson mass but close to it. This projection is not very prominently seen in the data, since at this stage of the analysis a large contribution of background is coming from the other ω decays and direct multi pion productions. The peak position for Monte Carlo and data is at the correct pion mass 0.135 GeV/c^2. In order to select the events from the $\omega \to \pi^0\gamma$ decay, more specific cuts dedicated to choosing the $\pi^0\gamma$ final state have been used.

4.2.3. $\omega \to \pi^0\gamma \to \gamma\gamma\gamma$ Final State Selection

The $\omega \to \pi^0\gamma \to \gamma\gamma\gamma$ final state is fully reconstructed with one ^{3}He track reconstructed in the Forward Detector and at least three neutral tracks in the electromagnetic calorimeter. The next step is to check the overall kinematic balance of the reaction.

4.2.3.1. Overall Kinematic Check

The energy and momentum balance, which are the differences of the energy sum and momentum sum of the incoming ($\mathbf{E_{in}}$, $\vec{\mathbf{P}}_{\mathbf{in}}$) and outgoing particles ($\mathbf{E_{out}}$, $\vec{\mathbf{P}}_{\mathbf{out}}$), respectively, are checked for the reaction hypothesis $pd \to {}^3\mathrm{He}\ \omega(\omega \to \pi^0\gamma \to \gamma\gamma\gamma)$. The overall missing energy δE and absolute value of the overall missing momentum $|\delta\vec{\mathbf{P}}|$ of the p, d, ^{3}He and 3γ system are used as a measure of the overall kinematic of the system.

$$\begin{aligned} \delta\mathbf{E} &= (\mathbf{E}_{in} - \mathbf{E}_{out}) = (\mathbf{E}_{beam} + \mathbf{E}_{target}) - \left(\mathbf{E}_{^3\mathrm{He}} + \mathbf{E}_{\gamma_1} + \mathbf{E}_{\gamma_2} + \mathbf{E}_{\gamma_3}\right), \\ \delta\vec{\mathbf{P}} &= \left(\vec{\mathbf{P}}_{in} - \vec{\mathbf{P}}_{out}\right) = \left(\vec{\mathbf{P}}_{beam} + \vec{\mathbf{P}}_{target}\right) - \left(\vec{\mathbf{P}}_{^3\mathrm{He}} + \vec{\mathbf{P}}_{\gamma_1} + \vec{\mathbf{P}}_{\gamma_2} + \vec{\mathbf{P}}_{\gamma_3}\right), \end{aligned} \tag{4.6}$$

where E and $\vec{\mathbf{P}}$ are the energies and momenta of the particle mentioned in the subscripts.

For the reaction of interest and the reactions with same topology, the δE and δP are connected via the overall missing mass (δM) as, $\delta E^2 = |\delta P|^2 + \delta M^2$. However, for the

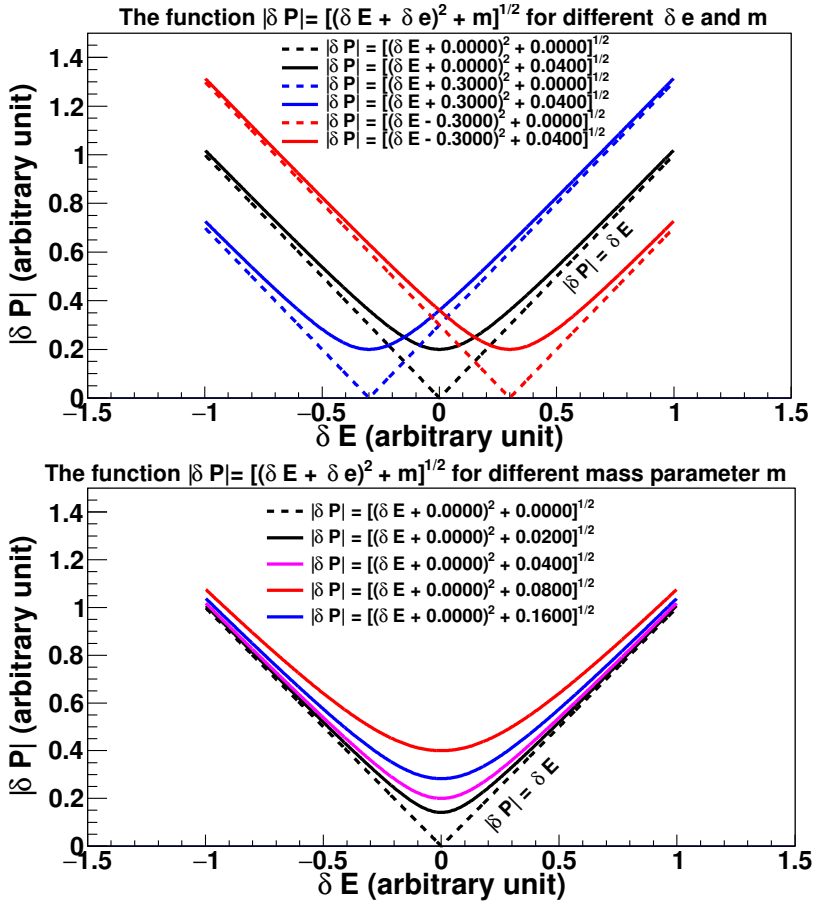

Figure 4.7.: The top panel shows the calculated overall missing momentum as a function of the overall missing energy for different energy shift (δe) and mass parameter m. The energy-momentum balance calculations for no energy shift ($\delta e = 0$) and different mass parameter m are plotted in the bottom panel (inspired by Ref. [122]).

reactions having a different number of particles and/or particle masses than the reaction of interest, a constant shift in the overall missing energy will be observed. This shift depends upon the energy of the missing or additional particles. In these cases, the δE and δP will be correlated via another consideration, $|\delta\vec{\mathbf{P}}| = \delta P = \sqrt{(|\delta E| + \delta e)^2 + m}$ where δe and m are

the shift parameter and mass parameter, respectively [122]. This correlation might follow different distributions depending upon different scenarios of particle numbers and particle type.

For better understanding, $|\delta P|$ is calculated as a function of δE and plotted in Fig. 4.7. The plot explains the following scenarios:
Scenario I: ($\delta E = |\delta P| = m = \delta e = 0$), where all entries are localized at (0,0) in Fig. 4.7. When energy, momentum and mass are conserved.
Scenario II: ($\delta e \neq 0$), where a shift in the energy axis is seen, shown as a red and blue curve in the top panel of Fig. 4.7. These situations will be followed by the reactions having a different topology or particle masses.
Scenario III: ($\delta E = |\delta P| \neq 0$ but $m = 0$), which is illustrated by the dashed lines in Fig. 4.7. Here the reactions differ by the number of photons only and the massive particles remain same, i.e., the energy and momentum are conserved for massive particles only.
Scenario IV: ($m \neq 0$), which is shown by solid histograms in Fig. 4.7. The value of the mass parameter m will determine the shift in the momentum axis as well as the curvature of the hyperbola, as illustrated in the bottom panel of Fig. 4.7.

Distributions of the overall missing momentum and overall missing energy are plotted in Fig. 4.8 for the Monte Carlo simulation of the signal decay $\omega \to \pi^0\gamma$ and possible background reactions, and the data.

The energy, momentum and mass are conserved and all events should lie at (0,0) for an ideal case of the $\omega \to \pi^0\gamma$ decay. However, due to the detector response and wrongly reconstructed particles, δE and $|\delta P|$ values are smeared and acquire non zero values around (0,0). The asymmetric distribution of the $\omega \to \pi^0\gamma$ decay around (0,0), as shown in Fig. 4.8b, is due to underestimation of the photon momentum. The blue arm towards the negative energy axis is due to the wrongly reconstructed photons, which are mainly split-offs. A parallel hyperbolic structure, which is having a vertex shifted towards the positive energy axis, is formed due to the combinations of the fake photons.

In case of data, the hyperbolic structure corresponding to the $\pi^0\gamma$ decay is not clearly visible and is rather dominated by the continuous distributions of the δe and m values. The largest contribution is originated from the direct neutral pion productions $\pi^0\pi^0$ and $\pi^0\pi^0\pi^0$, which lead to scenario II. The number of photons in these reactions is larger than $\pi^0\gamma$ decay. A shift, as compared to the $\pi^0\gamma$ decay, towards the positive energy values near (0,0) is seen and the positive values of the missing energy are preferred (Fig. 4.8c and Fig. 4.8d). The blue arm from the parallel hyperbolic structure is more intense due to split-offs, which result in an increase of photons in the final state.

In addition to the neutral pions, the background from the direct charged pion production and contribution from the pionic ω decays (mostly $\omega \to \pi^+\pi^-\pi^0$) is present in the data. These multi pion final states follow the scenario IV. Resultantly, a shift in the energy axis is seen (Fig. 4.8e-h). The missing energy values are always positive in this case, as two charged pions are missing to balance out the energy and momentum. Besides, the condition of the neutral track multiplicity is fulfilled by the low energetic split-offs created in the hadronic shower.

The residues from the decays $\eta \to \gamma\gamma$ and $\pi^0 \to \gamma\gamma$ persist in the selection (see Fig. 4.2 for the reconstruction efficiencies). The criterion of the three photon final state is fulfilled by one or more split-offs, which are the contributions due to scenario II. Wherein the low energetic fake photon makes a negligible change in the missing energy. The distributions from these contributions are localized around (0,0), as seen in Fig. 4.8i-j. The preferred orientation towards the positive values of the missing energy is an indication that photon

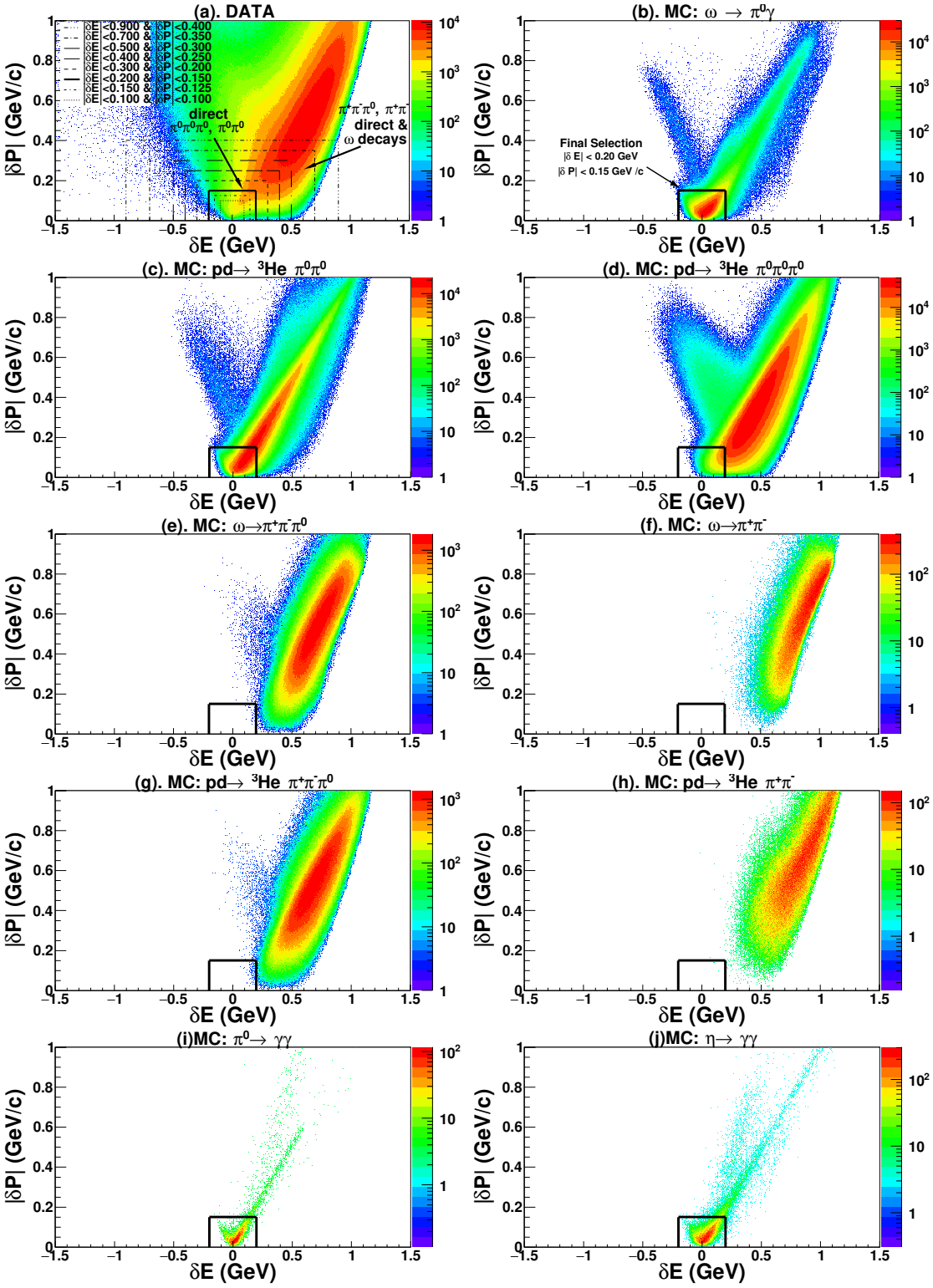

Figure 4.8.: The absolute value of the overall missing momentum |δP| vs overall missing energy δE of the ^{3}He particles and 3γ system is shown for 1.5 GeV beam energy. **a** represents the data, **b** is the simulated signal, and the simulated backgrounds are shown from **c** to **j**. Various δE-|δP| constraints used for purity check are indicated on the data. The solid black box shows the selection boundaries for the relevant event candidates.

four-momenta is underestimated.

A constraint on the overall missing energy and overall missing momentum is used to refine the event selection. As discussed previously, the sample is contaminated with the in-peak backgrounds $\omega \to \pi^+\pi^-\pi^0$ and $\omega \to \pi^+\pi^-$, and these contributions cannot be subtracted from the missing mass spectrum. Resultantly, the signal and backgrounds cannot be distinguished on an event-by-event basis, but only in a "statistical" sense. In this case, the cut optimization is done by evaluating the probability from the Monte Carlo simulations that a given event is a signal event. This probability, estimated using the Bayes theorem [121], can be regarded as a purity of the sample and is given as [121]

$$\pi = \frac{N_s}{N_s + \sum_i N_{bi}} = \frac{1}{1 + \sum_i \frac{\varepsilon_{bi}}{\varepsilon_s} w_i} = \frac{1}{1 + \sum_i \frac{N_{bi}}{N_{bi}^0} \frac{N_s^0}{N_s} w_i} = \frac{1}{1 + \sum_i \frac{N_{bi}}{N_s} w_i}, \tag{4.7}$$

where N_s and N_{bi} are the number of events in the MC simulation of the signal and in the i^{th} background contribution out of various decays and reactions, respectively. The superscript 0 refers to the total events simulated for the signal and the backgrounds. For this analysis, an equal number of events are simulated for the signal and all backgrounds, i.e., $N_{bi}^0 = N_s^0$. The efficiencies of the signal ε_s and i^{th} background ε_{bi} are the likelihoods that a signal event is identified as signal and i^{th} background event is identified as the signal. w is a weighting factor depending on the relative cross-sections and branching fractions

$$\mathbf{w} = \frac{cs_b \times BR_b}{cs_s \times BR_s}, \tag{4.8}$$

where cs and BR are the cross sections and the branching ratios of the given subscripts, respectively, which are listed in Appendix C.1 for the signal and backgrounds. These cross-sections and the branching ratios are the so-called prior probabilities of the signal and backgrounds. A modification of Equation 4.7 for j^{th} background gives the probability $\mathbf{P}(b)$ of j^{th} background to appear in an event as the signal.

$$\mathbf{P}_j(b) = \frac{\frac{\varepsilon_{bj}}{\varepsilon_s} w j}{1 + \sum_i \frac{\varepsilon_{bi}}{\varepsilon_s} w_i}. \tag{4.9}$$

Furthermore, the contribution (events) of j^{th} background for a single event of the signal is

$$\frac{\varepsilon_{bj}}{\varepsilon_s} w = j^{th} \text{ background events per event of the signal.} \tag{4.10}$$

The expected statistical error ($< \delta M_{meas} >$) in any measurement ($< M_{meas} >$) is related to the quantity $\varepsilon \times \pi$ as [123]

$$\frac{< \delta M_{meas} >}{< M_{meas} >} = \frac{C}{\sqrt{\varepsilon \times \pi}}, \tag{4.11}$$

where C is a constant term. Equation 4.11 shows that the expected statistical error is minimal if the event selection maximizes the quality $\varepsilon \times \pi$ ("efficiency $\times$ purity"). A way to optimize the statistical significance in Equation 4.2 is to optimize the quantity $\varepsilon \times \pi$ [123].

The quantities ε, π and $\varepsilon \times \pi$ as a function of different energy-momentum constraints are shown in Fig. 4.9 for 1.5 GeV beam energy. The $|\delta P| - \delta E$ cuts used in this study are

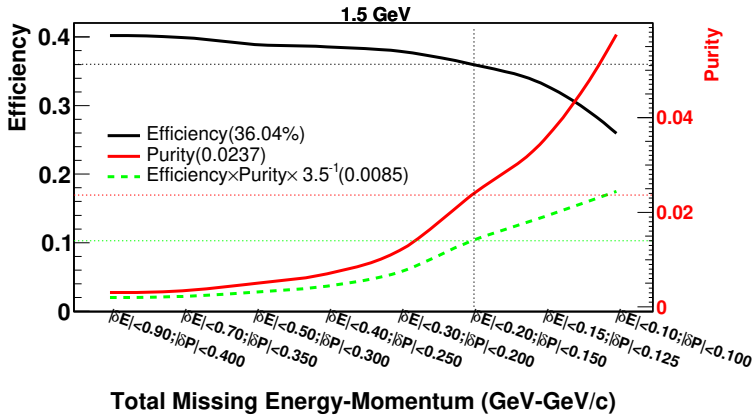

Figure 4.9.: The efficiency (black), purity (red) and the quantity purity×efficiency (green dashed) are plotted as a function of the different $\delta E - |\delta P|$ selection criteria. The left axis with black labels represents the efficiency and the right axis highlighted with red labels is purity. The quantity purity×efficiency, when downscaled by a factor 3.5, is plotted using the purity axis. The final selection and the corresponding variables are indicated by the straight dashed lines. The variable values are listed in the legends.

shown in Fig. 4.8a. Clearly, a larger value of $\varepsilon \times \pi$ may be achieved as the cut window approached close to (0,0), see Fig. 4.9. This reduction is due to the suppression of background contributions in the vicinity of (0,0). However, at the same time the signal is reduced too, as evident in the efficiency distribution shown in Fig. 4.9. Thus, a compensation in purity is made to achieve better efficiency. Finally, a cut rejecting all in-peak backgrounds and the charged pion productions, as illustrated in Fig. 4.8 with solid boxes, is used for the analysis. The background from the neutral pion will be dealt with later using more specific kinematic conditions. The remnant of the resonance production will be subtracted by fitting the missing mass.

As observed in Fig. 4.8, the majority ($\approx$90%) of the signal events are localized below 0.15 GeV missing momentum. Moreover, almost all the events from the decays/reactions having charged pions in the final state lie below 0.20 GeV missing energy. The rectangular enclosure formed by $|\delta E| \leq 0.2\ GeV$ and $|\delta P| \leq 0.15\ GeV/c$ is considered as the final constraint to select 3γ as coming from the $\pi^0\gamma$ decay. The effect of the energy-momentum conservation condition on the measured branching ratio has been explored in the next chapter.

The condition rejects approximately 88% of the events from the direct $\pi^0\pi^0\pi^0$ production. However, roughly 58% for the events from the $\pi^0\pi^0$ production passed this constraint, as most of the events fall over the hyperbolic structure near (0,0) due to the reaction kinematics. Moreover, almost 81% of the remnant events of the $\eta \rightarrow \gamma\gamma$ decay and 85% of the $\pi^0 \rightarrow \gamma\gamma$ decay fall under this box. The reconstruction efficiencies of the signal and backgrounds are plotted in Fig. 4.2.

The optimal value of the quantity $\varepsilon \times \pi$ for the final selection is $0.3642 \times 0.0228 = 0.0083$ in 1.45 GeV data. Similarly, $\varepsilon \times \pi = 0.3604 \times 0.0237 = 0.0085$ for 1.50 GeV. The statistical significance of the selection for 1.45 GeV and 1.50 GeV is 15 and 16, respectively. Clearly, the signal to background ratio is being improved as compared to the inclusive final state, which is evident from efficiencies in Fig. 4.2.

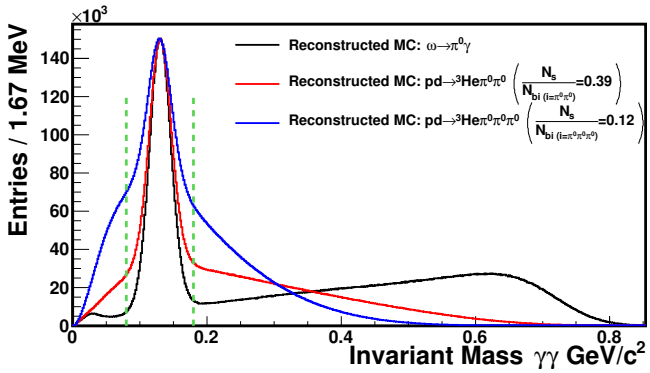

Figure 4.10.: The invariant mass of any two neutral tracks for the reconstructed Monte Carlo simulations of the $\omega \to \pi^0\gamma$ decay (black), the direct $\pi^0\pi^0$ production (red), and the direct $\pi^0\pi^0\pi^0$ production (blue). The green lines are the narrow selection around the π^0 peak used for the purity test. N_s/N_{bi} values are listed in the legend.

4.2.3.2. Monochromatic γ Selection Criterion

In addition to using the overall kinematic constraint, another condition, called "Monochromatic γ" in this study, is used to refine the selection. This condition is essentially used for two reasons. Firstly, it reduces the background coming from direct neutral pion productions. Secondly, it is a better way to distinguish the single photon from the photon coming from the π^0 meson decay.

The separation of the single γ from other two photons is also possible by using a mass window over the invariant mass of two photons. However, most of the events from the background productions, $\pi^0\pi^0$ and $\pi^0\pi^0\pi^0$, are localized in the π^0 peak region, as shown in Fig. 4.10. Therefore, the cut on the invariant mass of two photons is not very effective in reducing background contribution. Which is clearly demonstrated from the values of the function N_s/N_{bi} in the denominator of the Equation 4.7. N_s/N_{bi} value for the $\pi^0\pi^0$ and $\pi^0\pi^0\pi^0$ productions are 0.39 and 0.12, respectively. In order to reach high purity, N_s/N_{bi} should be as large as possible. It is therefore better to use a cut on a variable that distributes the signal and backgrounds in different kinematical regions, such as the "Monochromatic γ".

Let's first understand the kinematics behind the selection criterion. In the ω-rest system (CM), π^0 and γ decay back to back and have equal and opposite 3-momenta. The kinematics of the $\omega \to \pi^0\gamma$ decay are presented in Appendix D. The single γ, specified by the subscript 'm' (γ_m), is monochromatic in the rest frame of the ω meson with energy $P^{CM}_{\gamma_m} = E^{CM}_{\gamma_m} = 0.38\ GeV$. Whereas, the energy $E^{CM}_{\pi^0} = 0.40\ GeV$ and momentum $P^{CM}_{\pi^0} = 0.38\ GeV$ of π^0 are distributed among the two photons from the π^0 meson decay. The opening angle between the γ_m and π^0 is 180°. The angle between the γ_m and the two photons from π^0 decay is distributed between 0° to 180°, with most of the entries localized close to its maximum at 168.50° (details are in Appendix D). The angle between the two γ from π^0 decay in the CM system lies between 39.14° and 180°, where the maximum contribution is at 39.14° and most of the entries are localized towards the maximum (Appendix D).

In order to study these kinematic variables, the angle between the first two photons $\angle(\gamma_1,\gamma_2)^{CM}$ and the energy of the third photon $E^{CM}_{\gamma 3}$ in the ω rest frame are plotted for all photon combinations. The one-dimensional spectra of these variables are presented in Fig. 4.11a for the true Monte Carlo (PLUTO) and the true Monte Carlo (GEANT) simu-

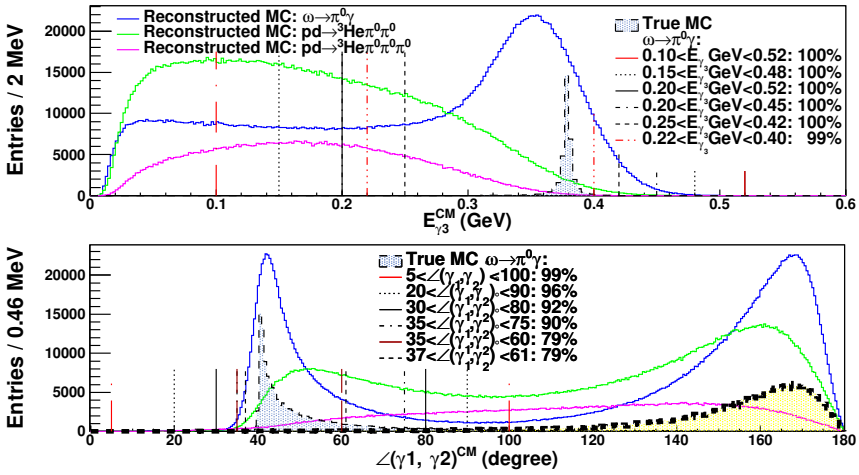

(a) The true MC simulations for the $\omega \rightarrow \pi^0\gamma$ decay (filled area), the reconstructed MC simulations for the $\omega \rightarrow \pi^0\gamma$ decay (blue), $\pi^0\pi^0$ production (green), and $\pi^0\pi^0\pi^0$ production (magenta) are compared at 1.50 GeV.

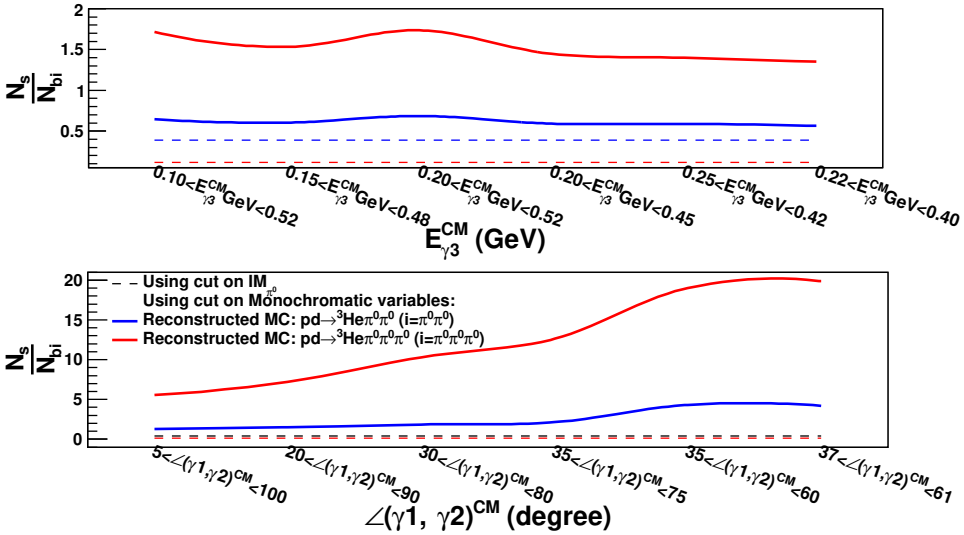

(b) The reconstructed MC for the $\pi^0\pi^0$ production (blue) and $\pi^0\pi^0\pi^0$ production (red) are shown at 1.50 GeV.

Figure 4.11.: **(a)** is the distributions of the angle between two photons $\angle(\gamma 1, \gamma 2)^{CM}$ and the energy of third photon $E^{CM}_{\gamma 3}$ in the ω rest frame. The similar lines represent the energy and angle window used to study the function N_s/N_{bi}. **(b)** represents values of N_s/N_{bi} as a function of the cut window. The function N_s/N_{bi} obtained by using the π^0 mass window in Fig. 4.10 is shown as dashed lines for a comparison.

lations of signal and backgrounds. For these tests, the two types of cuts $\angle(\gamma_1, \gamma_2)^{CM}$ and $E^{CM}_{\gamma 3}$ are uncorrelated. Fig. 4.11b shows a comparison between the quantity N_s/N_{bi} for different energy and angular windows (solid lines) and the π^0 mass cut (dashed lines) for two major backgrounds. It is observed that N_s/N_{bi} is larger if cuts on these kinematic variables are used, as compared to the cut on π^0 mass shown in Fig. 4.10. This indicates that the "Monochromatic γ" selection has better sensitivity as compared to π^0 mass cut. A cut on the monochromatic energy between 0.20 and 0.52 GeV yields the best sensitivity. For the opening angle between two photons, it seems that the sensitivity increases as the cut becomes tighter around the maximum point. However, at the same time, the efficiency de-

creases. The efficiency, signal phase space and the statistical significance of the different combinations of energy and angular constraints are studied for cut optimization. Related details can be found in Appendix B.3.

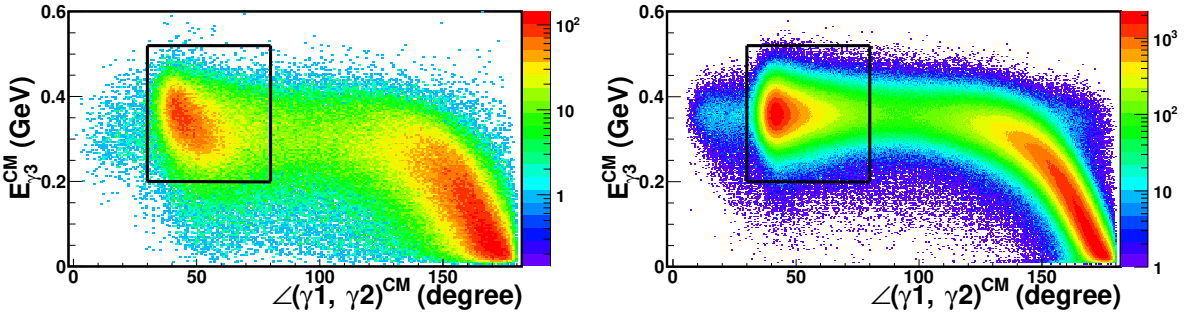

(a) Data at 1.50 GeV.

(b) MC simulation for the $pd \rightarrow {}^3\mathrm{He}\,\omega(\omega \rightarrow \pi^0\gamma)$ reaction at 1.50 GeV.

Figure 4.12.: **(a)** and **(b)** are the monochromatic γ plot for data and Monte Carlo, respectively. The x-axis represents the angle between the photons decaying from the π^0 in the ω-rest frame ($\angle(\gamma 1,\gamma 2)^{CM}$). Two photons coming from π^0 are considered as first and second, in three photon combinations. The y-axis represents the energy distribution of the third γ in the ω-rest frame ($E^{CM}_{\gamma 3}$). The distributions are plotted for all possible combinations of three photons. The used optimum cut to select events for the correct $\pi^0\gamma$ combinations are shown as the black boxes.

The distribution of $E^{CM}_{\gamma 3}$ as a function of $\angle(\gamma 1,\gamma 2)^{CM}$ is plotted for all combinations in Fig. 4.12. The structure on the right side of these plots originates when the single γ and a γ from the π^0 decay are combined. The prominent region on the left side corresponds to the π^0. An optimal selection of 0.20 GeV$<E^{CM}_{\gamma 3}<$0.52 GeV and $30^\circ < \angle(\gamma 1,\gamma 2)^{CM} < 80^\circ$ is shown. The achieved statistical significance for the optimal selection is 17.97 and 20.60 for 1.45 GeV and 1.50 GeV, respectively. The respective reconstruction efficiency is 34.74% and 34.35%. The phase space acceptance is 92% for both cases. The efficiencies in Fig. 4.2 convey that the monochromatic condition is not affecting the signal statistics by a great amount, as the signal efficiency has been reduced by only $\approx$2%. However, this cut is showing a significant influence on the dominant backgrounds, since the $\pi^0\pi^0$ production is reduced by $\approx$11% and $\pi^0\pi^0\pi^0$ by $\approx$5%.

4.2.4. Influence of the $\omega \rightarrow \pi^0\gamma$ Final State Selection on the Decay Kinematics

The quantitative influence of the final selection for the $\omega \rightarrow \pi^0\gamma$ decay is seen in terms of the exclusive efficiency ε_{exc}, as listed in Fig. 4.2. The detector's total acceptance after $\pi^0\gamma$ selection is 34.74% for 1.45 GeV and 34.35% for 1.50 GeV. It has been observed that the $\pi^0\pi^0$ direct production has the largest probability ($\mathbf{P}(b)$=89%) to appear in an event. The probability $\mathbf{P}_j(b)$ has been evaluated using Equation 4.9. There is a chance that about 7% of the event is a direct $\pi^0\pi^0\pi^0$ production. The probability of existence of other contributions, $\omega \rightarrow \pi^+\pi^-\pi^0$, $\omega \rightarrow \pi^+\pi^-$, $\eta \rightarrow \gamma\gamma$ and $\pi 0 \rightarrow \gamma\gamma$ decays, direct $\pi^+\pi^-\pi^0$ and $\pi^+\pi^-$ productions, is almost 0. The absence of any in-peak background contribution makes it easier to deal with the background situation and measure the absolute branching fraction. The multi pion background contributions are subtracted by fitting the missing

mass distribution. The influence of the final state selection criteria on the kinematics of the phase space is visualized in terms of control spectra in the following subsections.

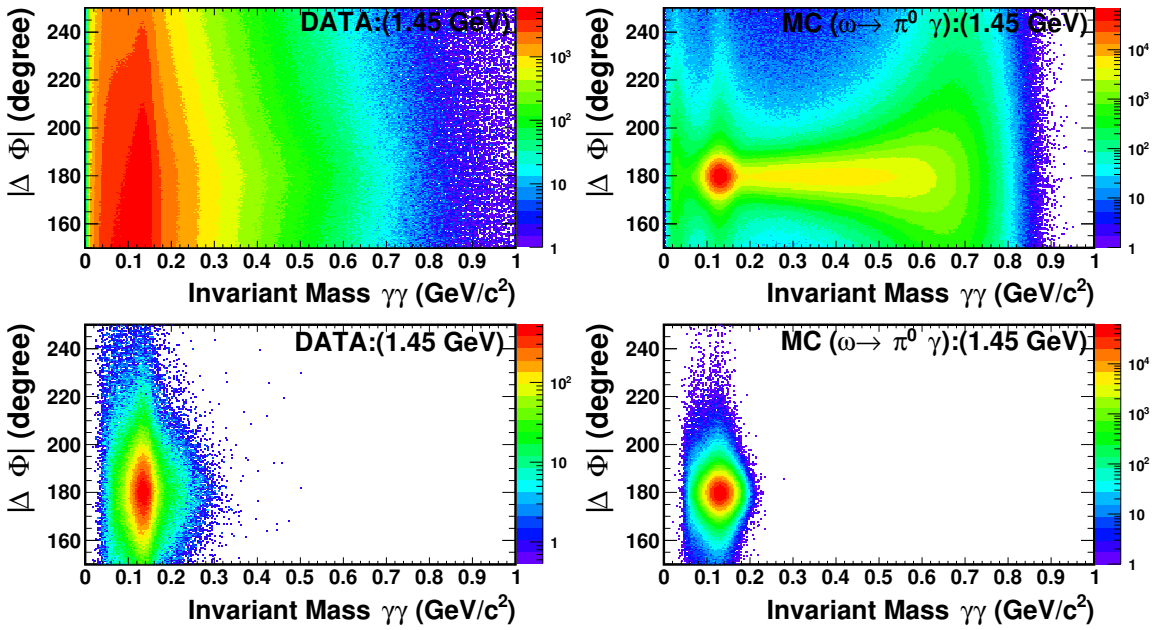

Figure 4.13.: The co-planarity angle $\Delta\Phi$ is plotted as a function of two photon invariant mass from the π^0 decay. The top and bottom row represent the distributions with and without $\pi^0\gamma$ selection criteria, respectively. The left and right distributions represent the data and the Monte Carlo simulation of the signal, respectively.

4.2.4.1. The Co-planarity Angle ($|\Delta\Phi|$)

As discussed in Section 4.2.3.2, the π^0 meson and the single γ of the $\omega \rightarrow \pi^0\gamma$ decay fly back-to-back in the ω rest frame. A detailed kinematics have been provided in Appendix. D. This feature effectively separated the two photons from the π^0 decay and reduced the background from the multi pion production.

The effect of the cut is observed on the co-planarity angle $\Delta\Phi$, as an illustration. Which is an absolute difference in the azimuthal angle of the π^0 meson and the single γ in the center of mass frame of ω meson, $\Delta\Phi = |\phi^{CM}_{\pi^0} - \phi^{CM}_{\gamma}|$. The four-momentum of the π^0 meson is reconstructed based on the four-momentum vectors of two γ identified as coming from the $\pi^0 \rightarrow \gamma\gamma$ decay. In an ideal case, $\Delta\Phi$ should be 180°. The invariant mass of two γ decaying from the π^0 meson as a function of $\Delta\Phi$ is shown in Fig. 4.13, before and after $\omega \rightarrow \pi^0\gamma$ final selection. As photons from the π^0 were indistinguishable before the selection criteria, all photon combinations are seen in the upper row. After the final selection criteria, the data and Monte Carlo distributions are predominantly localized near $\Delta\Phi = 180^\circ$. A separate region of the two photon combinations from the π^0 meson decaying back to the single γ is seen in the vicinity of 180° and π^0 meson mass. The data have a broader distribution around $\Delta\Phi = 180^\circ$ due to the presence of contribution from the direct pion productions. Nevertheless, both distributions become cleaner after the selection criteria.

4.2.4.2. The 2γ Invariant Mass

The distribution of the two photon invariant mass is a powerful kinematic observable for the $\omega \rightarrow \pi^0\gamma$ decay. The invariant mass of two γ is used as a monitoring spectrum to check the effect of the kinematic cuts. The invariant mass of 2 neutral tracks in the SEC

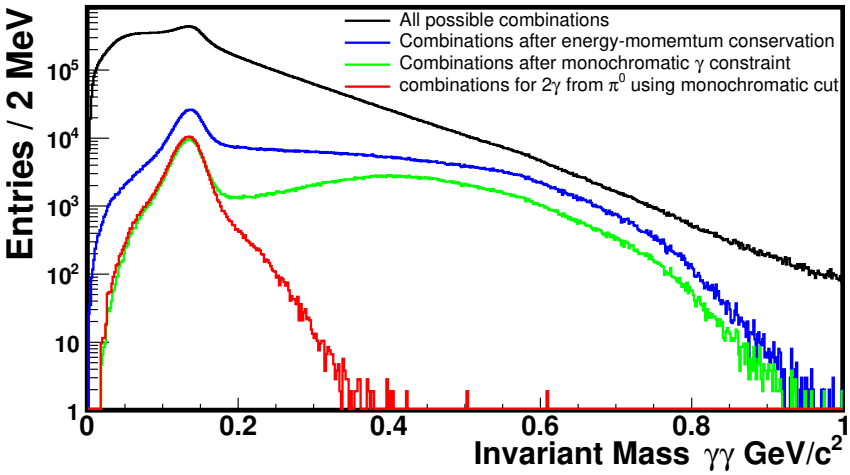

Figure 4.14.: The black line is the two γ invariant mass distribution for all combinations. The blue curve is the histogram after the overall kinematic check. The green curve is the distribution after the monochromatic γ selection criterion for all combinations. The red curve is the distribution for the 2γ decaying from the π^0, after the monochromatic γ cut. A cleaner π^0 peak is seen after each condition.

for the data is shown in Fig. 4.14 after different conditions. The distribution after selecting three γ in the Central Detector shows a peak at the π^0 rest mass (m_{π^0} =0.135 GeV/c^2) on the top of large background from combinatorics and other background reactions. The distribution after using the constraint on the energy and momentum conservation shows that the background from other reaction channels is suppressed to a great extent. Although, the combinatorics are still seen in the distribution, as shown in Fig. 4.14. The invariant mass of 2γ from the π^0 decay can be seen with a cleaner π^0 peak after passing through the monochromatic criterion. The peak position of the final π^0 distribution (red curve) obtained by fitting a combined Novosibirsk and polynomial function is at (135.01$\pm$0.10) MeV/c^2 and (134.82$\pm$0.11) MeV/c^2 for 1.45 GeV and 1.50 GeV beam energies, respectively. The FWHM of the π^0 peak is (35.19$\pm$0.12) MeV and (35.93$\pm$0.11) MeV for 1.45 GeV and 1.50 GeV beam energies, respectively.

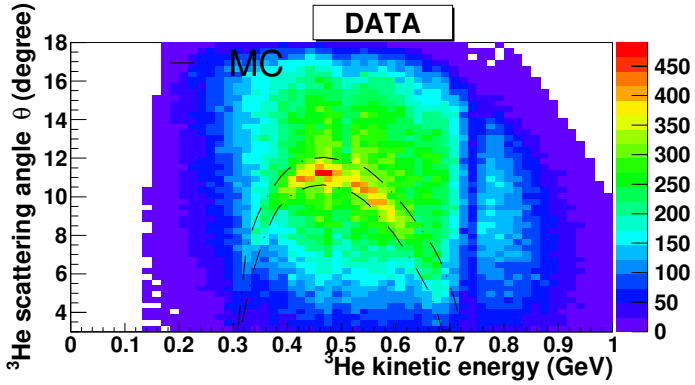

Figure 4.15.: The kinetic energy correlation with the polar angle after $\pi^0\gamma$ final selection is shown for data. The background from the multi pion production is reduced substantially as compared to the inclusive final state shown in Fig 4.3b. The position of the arc in simulated data is drawn as the black dashed enclosure.

4.2.4.3. The Kinetic Energy and the θ Correlation of ^{3}He Particles

A considerable effect is seen on the kinetic energy vs θ plot of ^{3}He particles after the $\pi^0\gamma$ selection criteria. The ^{3}He arc from the ω production was obscured by the background in the inclusive final state, as shown in Fig. 4.3. The situation is improved and a cleaner ^{3}He arc is seen in Fig. 4.15 along with the substantially reduced background from multi pion production. A reference arc of Monte Carlo simulation is drawn for comparison. The maximum of the curvature in the data, which was shifted towards the lower kinetic energy, is now positioned at the same energy as that of the simulation given in Fig. 4.3. The data and the simulation look comparable. The background in data is reduced substantially and a clean signal is seen.

4.2.4.4. The Exclusive Missing Mass of the ^{3}He Particles after $\omega \rightarrow \pi^0\gamma$ Final State Selection

The energy resolution of the Forward Detector is better than the Electromagnetic Calorimeter. This is evident from the FWHM value of the average true and reconstructed kinetic energy difference relative to the true kinetic energy distributions. FWHM distributions have been illustrated in Appendix F. The FWHM is around (37.22±0.35) MeV for the ^{3}He particles and approximately (197.26±1.57) MeV for photons. Therefore, the missing mass spectrum is used to monitor this analysis and to obtain results. A one-dimensional spectrum of the ^{3}He particles missing mass after $\pi^0\gamma$ final state selection is shown in Fig. 4.16. The missing mass is exclusive, as all final state products are reconstructed. An enhancement at the ω meson mass (0.7827 GeV/c^2) is seen on a smooth background from direct pion production. The background is considerably reduced and a cleaner peak is seen at the ω mass, as compared with the inclusive missing mass shown in Fig. 4.4. In order to count for the signal and background separately, the background is fitted and subtracted from the data.

The best fitted range and polynomial order in this case are $[0.575-0.84]$ and 5 for 1.45 GeV, while $[0.575-0.855]$ and 4 for 1.50 GeV. $N_{signal}^{count\ range}/N_{background}^{count\ range}$ has improved to 0.0984 and 0.1120 for 1.45 GeV and 1.50 GeV, respectively, as against 0.0325 and 0.0400 in the inclusive final state. The peak position of the extracted data, (782.70±0.32) MeV/c^2 for 1.45 GeV and (783.09±0.33) MeV/c^2 for 1.50 GeV, is at the correct ω meson mass 0.7827 GeV/c^2. The resolution (FWHM) of the background-subtracted data peak is (14.78±1.14) MeV for 1.45 GeV and (14.77±1.21) MeV for 1.50 GeV. Within errors, these values are in agreement with each other. The systematic effect due to the fit function will be discussed in the next chapter.

The number in the background-subtracted peak gives the number of the $\omega \rightarrow \pi^0\gamma$ decays in data. The yield for two energies is listed in Table 4.2. The error shown are statistical. The number of the reconstructed $\omega \rightarrow \pi^0\gamma$ decays when corrected by the Monte Carlo efficiency yields the total number of $\omega \rightarrow \pi^0\gamma$ decays. The numbers for the entire data set, estimated as the sum of the numbers for two energies, are shown in Table 4.2. These numbers will later be used to estimate the branching ratio of the $\omega \rightarrow \pi^0\gamma$ decay.

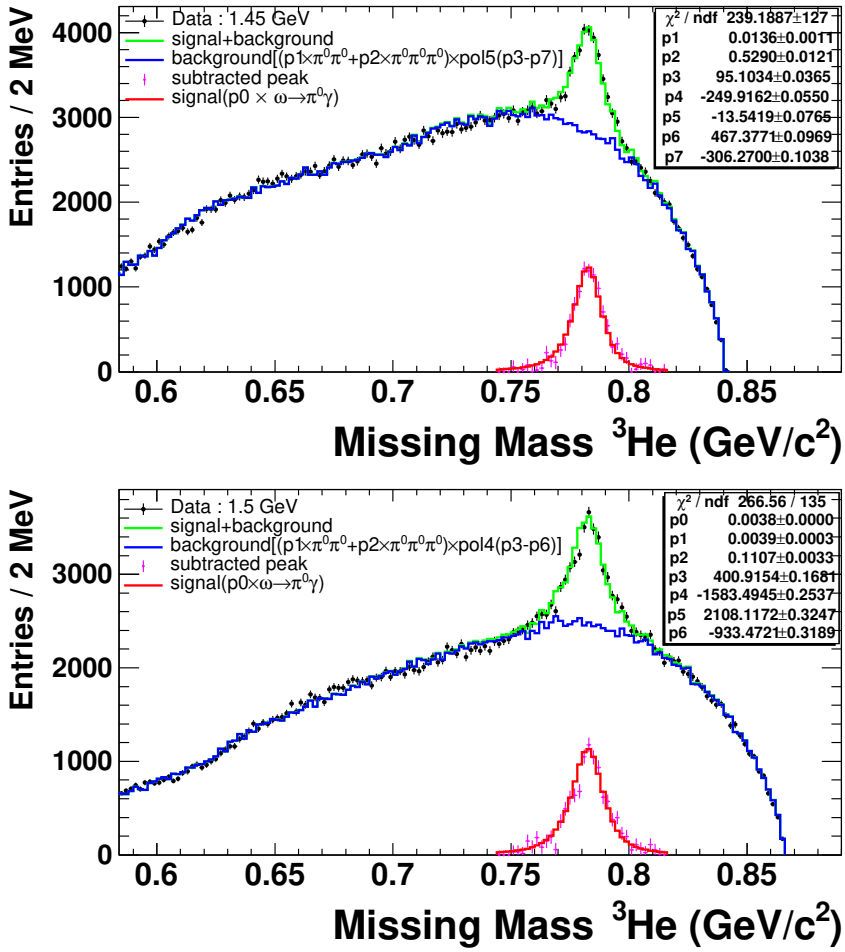

Figure 4.16.: The exclusive missing mass of ^{3}He particles after final $\pi^0\gamma$ selection is shown. The smooth phase space background from the multi pion production has been reduced substantially. The black histogram corresponds to data, the green histogram is a combined fit of the signal and the background. The continuous background from multi pion production is described by the background simulations convoluted with polynomial, shown as the blue histogram. The fit parameters are shown. The background-subtracted data have been plotted as a magenta histogram at the bottom of the figure. The subtracted data is consistent with the simulation of $\omega \to \pi^0\gamma$ along with the fit parameter p0.

$(X(f))$	**1.45 GeV**	**1.50 GeV**	**Entire data set (1.45 GeV+1.50 GeV)**
total number of $\omega \to \pi^0\gamma$ *decays reconstructed* $N^{rec}_{\omega\to\pi^0\gamma}$	$(1.08\pm0.05)\times10^4$	$(1.08\pm0.04)\times10^4$	$(2.16\pm0.06)\times10^4$
total number of $\omega \to \pi^0\gamma$ *decays* $N^{\circ}_{\omega\to\pi^0\gamma} = \frac{N^{rec}_{\omega\to\pi^0\gamma}}{\varepsilon_{exc}}$	$(3.11\pm0.13)\times10^4$	$(3.14\pm0.13)\times10^4$	$(6.25\pm0.18)\times10^4$

Table 4.2.: The number of the $\omega \to \pi^0\gamma$ decays estimated from the exclusive missing mass.

4.3. $pd \to {}^3\mathrm{He}\,\omega(\omega \to e^+e^-\pi^0)$ Final State Reconstruction

To analyze the reaction $pd \to {}^3\mathrm{He}\,\omega \to {}^3\mathrm{He}\;\; e^+e^-\pi^0$, the charged particles e^+e^- in the Central Detector are identified along with the ^{3}He particle and π^0. The method used to identify the final decay products e^+, e^- and π^0 in the Central Detector is explained in the following subsections.

4.3.1. γ Identification

Two or more neutral tracks above 20 MeV energy deposit in the Central Detector are identified as two gamma candidates. The neutral tracks which are in a time coincidence between -50 ns and 40 ns with ^{3}He particle are considered. The identified neutral tracks are in a time coincidence of -35 ns to 35 ns. These time coincidence plots for neutral tracks are shown in Fig. 4.5.

4.3.2. e^+e^- Identification

Reference Name	Decay/Reaction	Weighting Factor w_i	1.5 GeV	
			$\varepsilon_i(\%)$	$w_i \times \varepsilon_i$
$\omega \to \pi^0e^+e^-$	$pd \to {}^3\mathrm{He}\,\omega(\omega \to \pi^0e^+e^-)$	1	11.3100	
$\omega \to \pi^+\pi^-\pi^0$	$pd \to {}^3\mathrm{He}\,\omega(\omega \to \pi^+\pi^-\pi^0)$	1158±91	14.9000	172.5420±13.5590
$\omega \to \pi^0\gamma$	$pd \to {}^3\mathrm{He}\,\omega(\omega \to \pi^0\gamma)$	109±9	0.0610	0.0664±0.0055
$\omega \to \pi^+\pi^-$	$pd \to {}^3\mathrm{He}\,\omega(\omega \to \pi^+\pi^-)$	20±2	1.7800	0.3560±0.0356
$\omega \to \eta\gamma$	$pd \to {}^3\mathrm{He}\,\omega(\omega \to \eta\gamma)$	1±0	0.0793	0.0008±0.0000
$\pi^+\pi^-\pi^0$	$pd \to {}^3\mathrm{He}\,\pi^+\pi^-\pi^0$	14137±1136	12.4400	1758.6428±141.3184
$\pi^0\pi^0\pi^0$	$pd \to {}^3\mathrm{He}\,\pi^0\pi^0\pi^0$	1787±150	0.1400	2.5018±0.2100
$\pi^+\pi^-$	$pd \to {}^3\mathrm{He}\,\pi^+\pi^-$	932±74*	0.9900	9.2268±0.7326
$\pi^0\pi^0$	$pd \to {}^3\mathrm{He}\,\pi^0\pi^0$	3216±261	0.0600	1.9296±0.1566
$\rho \to \pi^+\pi^-$	$pd \to {}^3\mathrm{He}\,\rho(\rho \to \pi^+\pi^-)$	155347±1242*	1.5684	2436.4624±19.4795
$\eta \to \gamma\gamma$	$pd \to {}^3\mathrm{He}\,\eta(\eta \to \gamma\gamma)$	495±45	0.0004	0.0012±0.0002
$\eta \to \pi^+\pi^-\pi^0$	$pd \to {}^3\mathrm{He}\,\eta(\eta \to \pi^+\pi^-\pi^0)$	288±27	7.9890	23.0083±2.1570
$\eta \to \gamma\pi^+\pi^-$	$pd \to {}^3\mathrm{He}\,\eta(\eta \to \gamma\pi^+\pi^-)$	53±5	1.5040	0.7971±0.0752
$\pi^0 \to \gamma\gamma$	$pd \to {}^3\mathrm{He}\,\pi^0(\pi^0 \to \gamma\gamma)$	3070±246	0.0004	0.0123±0.0010
*: extrapolations				

Table 4.3.: The weighting factors w_i are listed for the probable background contributions with respect to the signal decay $\omega \to e^+e^-\pi^0$. w_i is estimated by applying Equation 4.8. The corresponding efficiency ε_i and the quantity $w_i \times \varepsilon_i$ after the selection of at least a pair of oppositely charged tracks and at least two neutral tracks are shown for 1.5 GeV beam energy. The numbers for 1.45 GeV can be found in Appendix G.1.

The next step in the reconstruction of the $e^+e^-\pi^0$ final state is to identify the lepton pair in the Central Detector. The e^+e^- pair selection is aimed at reducing the most prominent background from the reactions having the same topology, but with charged pions. For instance, the $\omega \to \pi^+\pi^-\pi^0$ decay and the $\pi^+\pi^-\pi^0$ direct production.

To ensure that tracks from the oppositely charged particles are coming from the same event, their time coincidence with the ^{3}He particles, two photons, and with each other must

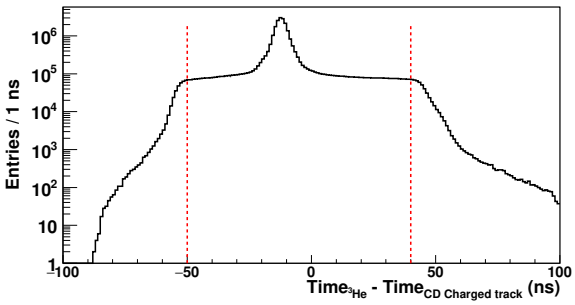

(a) The time difference between the ^{3}He particles and the charged particles (from PSB).

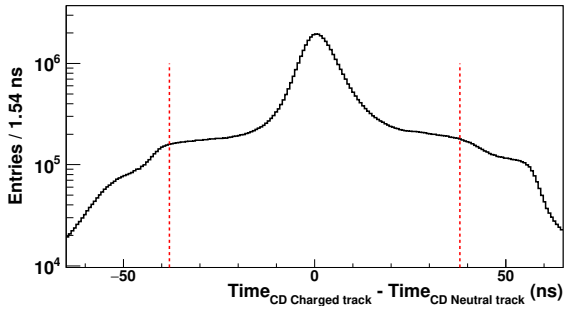

(b) The time difference of the charged tracks with the neutral tracks (from SEC).

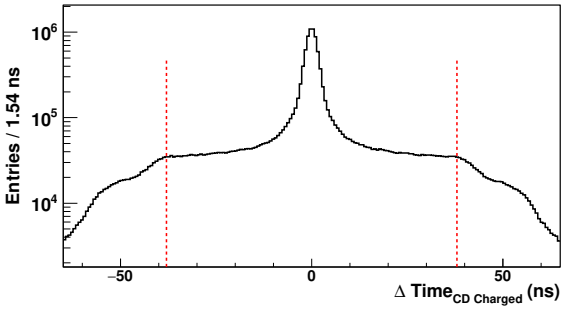

(c) The time difference between two charged tracks.

Figure 4.17.: **(a)**, **(b)** and **(c)** are the time coincidence plots to select the two charged particles and two photons in the final state of the $\omega \to e^+e^-\pi^0$ decay. The time information of the charged and neutral particles comes from the plastic scintillator barrel and electromagnetic scintillating calorimeter, respectively. The time coincidence of the neutral tracks with the ^{3}He particles and between the neutral tracks is shown in Fig. 4.5. The red dashed lines illustrate the cuts used for the time coincidence. The two charged tracks above 20 MeV energy deposit have a time coincidence with ^{3}He particle from -50 ns to 40 ns and with the photons between -38 ns and 38 ns are chosen. The time coincidence between two charged tracks is constrained between -38 ns and 38 ns. Wider time cuts are used to avoid the systematic effects from different shapes of the time spectra in data and simulations. Moreover, to select any slow ^{3}He particle, which may fall in the extended tail on the right-hand side.

be affirmed. The time coincidence for the three cases is shown in Fig. 4.17. It is observed in the plots that the time selection spectra for charged tracks are narrower than that of the neutral tracks, as shown in Fig. 4.5 and Fig. 4.17. This is because the time resolution of the plastic scintillator detectors (5 ns) is significantly better than that of the calorimeter (40 ns) [68]. The corresponding time cuts are shown. The background from the chance coincidences will later be suppressed by applying decay specific kinematic constraints.

The pattern recognition in the MDC has an efficiency of about 80% for a single charged track [72]. The reconstruction efficiencies to select two charged tracks, as plotted in Fig. 4.18, are 22.42% and 22.47% for 1.45 GeV and 1.50 GeV beam energy, respectively. It should be noted here that the reconstruction efficiency includes the efficiency of the track fitting algorithm. This further reduced by 56% and 54% for 1.45 GeV and 1.50 GeV beam energy, respectively, when the condition of at least two neutral tracks in the CD is added.

The reconstruction efficiency of the signal, after selecting at least a pair of oppositely

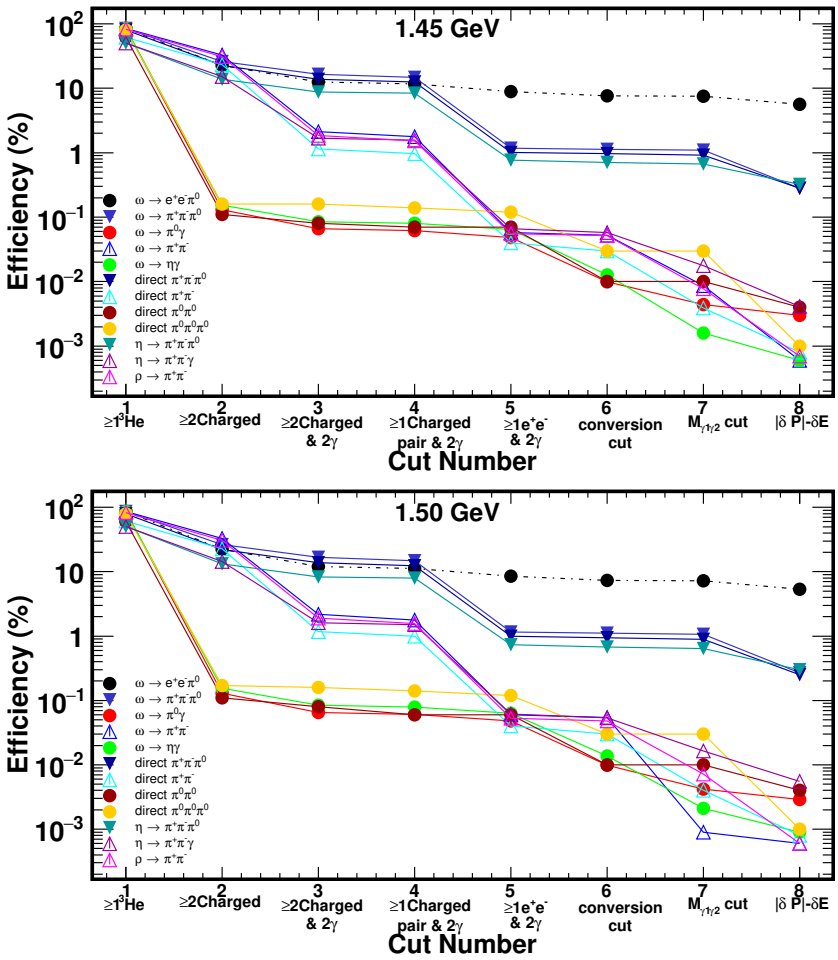

Figure 4.18.: The efficiencies of the signal decay $\omega \rightarrow e^+e^-\pi^0$ and the backgrounds are plotted as a function of the analysis steps. The labels on the x-axis represent the selection criterion and the y-axis is efficiency. The values of reconstruction efficiencies are listed in Appendix H.1. Clearly, an improvement in the signal to background ratio is observed with each condition.

charged tracks and at least two neutral tracks, is reduced by 87% from the inclusive final state. Which can be verified from Fig 4.18. The reconstruction efficiencies of signal and backgrounds after selecting at least a pair of oppositely charged tracks and at least two neutral tracks are listed in Table 4.3. The efficiency of the most abundant in-peak background, $\omega \rightarrow \pi^+\pi^-\pi^0$, is reduced by 83%. Whereas, the reconstruction efficiency of the decay $\omega \rightarrow \pi^0\gamma$ is dropped to 0.06%. This is one of the potential in-peak backgrounds because of its branching ratio relative to the signal, $BR_{\omega\rightarrow\pi^0\gamma}/BR_{\omega\rightarrow\, e^+e^-\pi^0}$=109, please refer to Appendix C.1 for explicit branching ratios. The final states like the $\omega \rightarrow \pi^0\gamma$ decay, which have topology different than the signal decay $\omega \rightarrow e^+e^-\pi^0$, have survived mainly due to the effects from the detector response. For instance, the conversion electrons at the beam pipe are responsible for the survival of the final states $\omega \rightarrow \pi^0\gamma$, $\omega \rightarrow \eta\gamma$, $\pi^0\pi^0$, $\pi^0\pi^0\pi^0$, $\eta \rightarrow \gamma\gamma$ and $\pi^0 \rightarrow \gamma\gamma$. However, the backgrounds $\omega \rightarrow \pi^+\pi^-$, $\pi^+\pi^-$, $\eta \rightarrow \pi^+\pi^-\gamma$, $\rho \rightarrow \pi^+\pi^-$, $\eta \rightarrow \gamma\gamma$ and $\pi^0 \rightarrow \gamma\gamma$ are there due to the split-offs. These effects will be dealt with later in this analysis. The in-peak background contribution from the $\omega \rightarrow \pi^+\pi^-$ shows a reduction of 98%. The decay $\omega \rightarrow \eta\gamma$ is suppressed up to 0.08%. Considering the relative decay probabilities $BR_{\omega\rightarrow\eta\gamma}/BR_{\omega\rightarrow\, e^+e^-\pi^0}$ $\sim$1.0 and efficiency $<<$ 1%, it is not one of the prominent

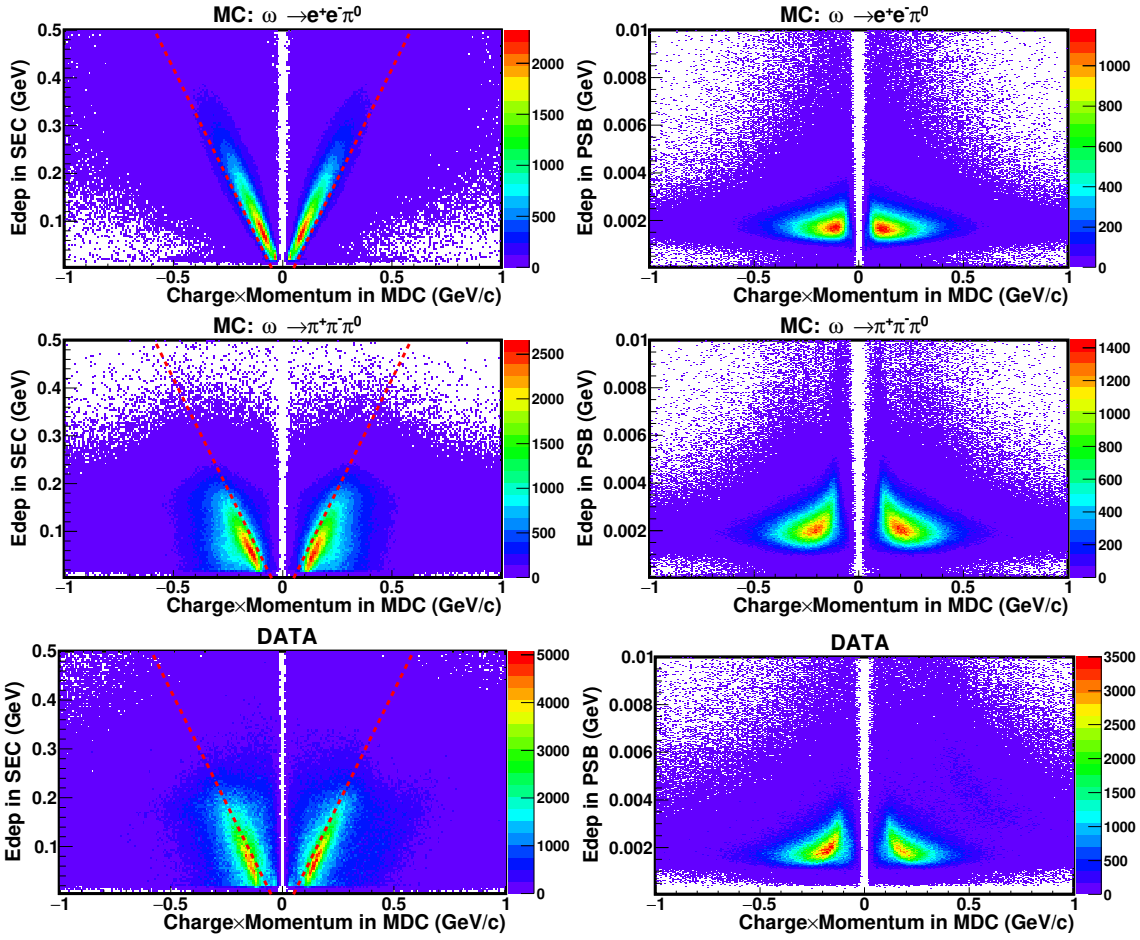

Figure 4.19.: Particle identification (PID) plots for the charged particles in the CD. The first column is the $\Delta E - P$ plot of the energy deposit in the SEC versus charged momentum [Charged×Momentum] reconstructed in the MDC. The energy deposited in the PSB as a function of the charged momentum is plotted in the second column. The first and the second rows are the MC simulations of $\omega \to e^+e^-\pi^0$ and $\omega \to \pi^+\pi^-\pi^0$, respectively. The third row is data. The events above the optimal selection, shown as red lines, are identified as electrons.

in-peak backgrounds. The branching fractions of different decays and the reconstruction efficiencies are listed in Appendix C.1 and Appendix H.1, respectively. The most abundant multi-pion production $\pi^+\pi^-\pi^0$ is reduced by 85% and the direct $\pi^+\pi^-$ production by 99%. The efficiency of the direct $\pi^0\pi^0$ production is reduced up to 0.06-0.07%. For the $\pi^0\pi^0\pi^0$ production reaction, the efficiency is reduced to 0.14%. The decays $\eta \to \pi^+\pi^-\pi^0$, $\eta \to \pi^+\pi^-\gamma$, and $\rho \to \pi^+\pi^-$ have been reduced by 84%, 97%, and 98%, respectively. The decay modes $\eta \to \gamma\gamma$ and $\pi^0 \to \gamma\gamma$ have reduced close to 0 and they are not the potential background candidates. However, considering their weighting factors w_i, as listed in Table. 4.3, their contribution for each $\omega \to e^+e^-\pi^0$ event will be monitored, until suppressed completely.

As the next step, the electrons are separated from the pions by using the particle identification method (PID) described in Section 3.3.2. The particle identification plots are shown in Fig. 4.19. The distributions for the $\omega \to e^+e^-\pi^0$ and $\omega \to \pi^+\pi^-\pi^0$ decays illustrate the position of the electron and pion pairs. As observed in Table 4.3, a large contribution from

the pions is present in the data in comparison to electrons. Consequently, the electrons and pions cannot be separately seen by naked eyes. An optimum graphical selection is used to select electrons, as shown by the red dashed lines. Appendix B.4 can be referred to for details on cut optimization. The signal purity of the selected data sample is around 0.04%. The selection has an efficiency of 8.87% and 8.58% for 1.45 GeV and 1.50 GeV, respectively. The overall reconstruction efficiency of the cut has been plotted in Fig 4.18. Almost 76% of the electrons from the $\omega \to e^+e^-\pi^0$ decay have been selected. However, only 8% pions from each the decay $\omega \to \pi^+\pi^-\pi^0$ and the direct $\pi^+\pi^-\pi^0$ production have survived the selection. In addition, selection includes around 3% pions from the decays $\omega \to \pi^+\pi^-$ and $\rho \to \pi^+\pi^-$, around 4% pions from the $\eta \to \pi^+\pi^-\gamma$ and direct $\pi^+\pi^-$ production, and 9% pions from the $\eta \to \pi^+\pi^-\pi^0$ decay.

The remnant background contributions, when normalized to the signal using Equation 4.8, show up in large quantities. The normalized background contributions can be seen in the form of weighting factors w_i listed in Table 4.3. w_i basically represent the number of the $pd \to {}^3\text{He}\ X(X \to Y)$ reactions produced with every $\omega \to e^+e^-\pi^0$ decay. In addition, the measure of the background contributions per $\omega \to e^+e^-\pi^0$ event, i.e., $\frac{\varepsilon_{bj}}{\varepsilon_s}w$, is obtained from Equation 4.10 for the present analysis condition. The relative reconstruction efficiencies have been taken into account accordingly. $\frac{\varepsilon_{bj}}{\varepsilon_s}w$ values are plotted in Fig. 4.25 for different contributions. The explicit $\frac{\varepsilon_{bj}}{\varepsilon_s}w$ values and the probability $\mathbf{P}_j(b)$ that a given event is j^{th} background contribution can be found in Appendix I. $\mathbf{P}_j(b)$ has been evaluated from Equation 4.9. As seen in Fig. 4.25 that the background contributions $\omega \to \pi^+\pi^-\pi^0$ and direct $\pi^+\pi^-\pi^0$ production is present in most abundance. In addition, the contributions from other pionic final states are present in a large amount. The contribution per $\omega \to e^+e^-\pi^0$ event for the decay $\eta \to \pi^+\pi^-\gamma$ will add up to a considerable amount, when scaled for more events of the $\omega \to e^+e^-\pi^0$ decay. Contributions from the neutral reactions, direct $\pi^0\pi^0$ and $\pi^0\pi^0\pi^0$ productions persist in the event sample. The fractions of the decays $\eta \to \gamma\gamma$ (0.05) and $\pi^0 \to \gamma\gamma$ (0.20) per $\omega \to e^+e^-\pi^0$ decay have survived. The contributions $\omega \to \pi^+\pi^-$ and $\omega \to \eta\gamma$ are completely suppressed.

4.3.3. The $\omega \to e^+e^-\pi^0(\pi^0 \to \gamma\gamma)$ Final State

Hitherto in order to fully reconstruct the $\omega \to e^+e^-\pi^0 \to e^+e^-\gamma\gamma$ final state, one ^{3}He particle in the Forward Detector in time coincidence with at least one, e^+e^- pair and at least two neutral tracks in the Central Detector are identified. The event selection is further refined by using additional constraints over the detector responses and reaction kinematics, as discussed in the following.

4.3.3.1. Effects from External Conversion

Dilepton pairs created in the material of the beam pipe are mis-reconstructed as coming from the vertex, as shown in Fig. 4.20. The vertex of the electron and positron for the conversion pair is determined by calculating the point of the closest distance between the reconstructed MDC helices of the dilepton. The distance between the conversion vertex and the beam-target interaction point (0,0) in the xy-plane is equal to the radius (R) of the beam pipe, as shown in Fig. 4.20. However, the vertex of the reconstructed electron-positron pair (non-conversion event) is close to the primary vertex. This implies that the distance between the non-conversion vertex and the primary vertex point is close to zero. As discussed previously, the opening angle between two particles influences their invariant mass. Correspondingly, the method to reduce the events from external conversion in the beam pipe is

monitored by the invariant mass of the lepton pair calculation at the beam pipe [124].

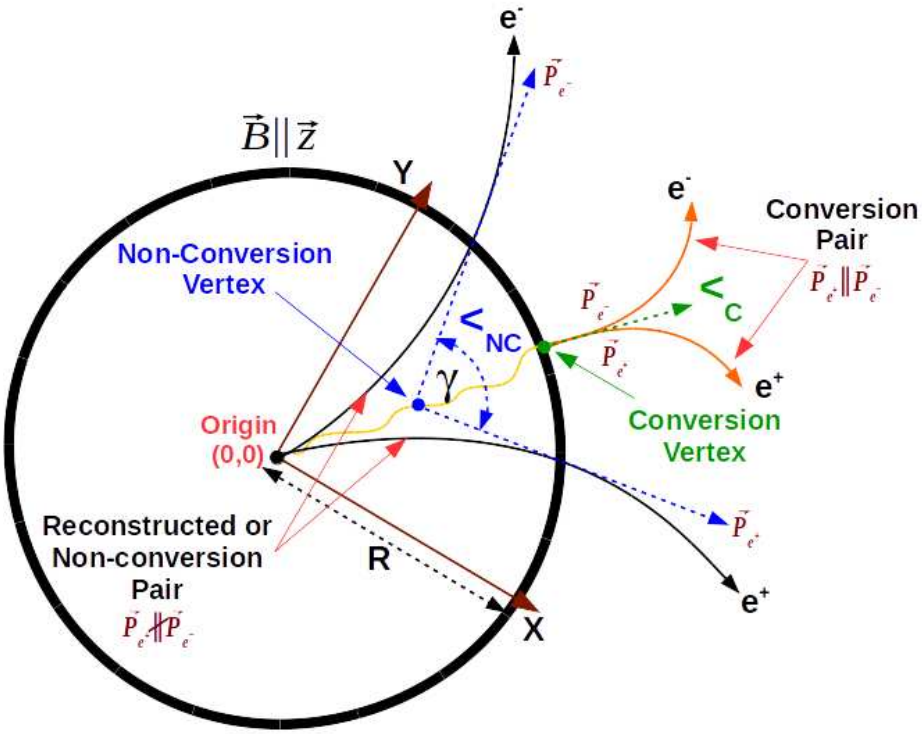

Figure 4.20.: Schematic view of the mis-reconstruction of conversion e^+ and e^- at the beam pipe. The curved arrows denote the momenta of the e^+ and the e^-. The black and orange arrows are the vectors for the reconstructed and conversion pairs, respectively. The momenta are parallel for the conversion pair and opening angle between them is close to zero at the beam pipe radius.

The dilepton invariant mass is calculated by first evaluating the azimuthal angle of the particles at the beam pipe using the MDC helix parameters. Which is then used to determine the momenta of particles. The four vectors of the dilepton pair are reconstructed at the beam pipe by assigning the electron mass. The four vectors of the conversion dielectron are added to calculate the invariant mass of the created pair. The momenta of e^+ and e^- from the conversion events are parallel to each other at the point of conversion at the beam pipe. Moreover, the opening angle between their trajectories at the beam pipe is close to zero, i.e., $\angle_C \approx 0$ (see Fig. 4.20). It is at this point that the photon which creates the conversion dilepton pair intersects the beam pipe. The invariant mass of the conversion electron pair evaluated via the energy-momentum four-vectors at the beam pipe is around twice the electron mass. The electron and positron pair coming from the non-conversion events have a large opening angle, i.e., $\angle_{NC} >> 0$, and correspondingly the values of their invariant mass at the beam pipe are larger than their true invariant mass. As electron and positron pairs traverse the beam pipe after their flight through the magnetic field, the opening angle increases during the flight and so does the invariant mass. The conversion and non-conversion events are monitored by the two-dimensional histogram where the radius of the closest approach as a function of the invariant mass of the lepton pair at the beam pipe is plotted, as shown in Fig. 4.21.

The $\omega \to \pi^0\gamma$ decay is the most influential background due to the conversion events. As this decay mode differs from the signal decay by only a virtual photon, i.e., $\omega \to e^+e^-\pi^0 \to$

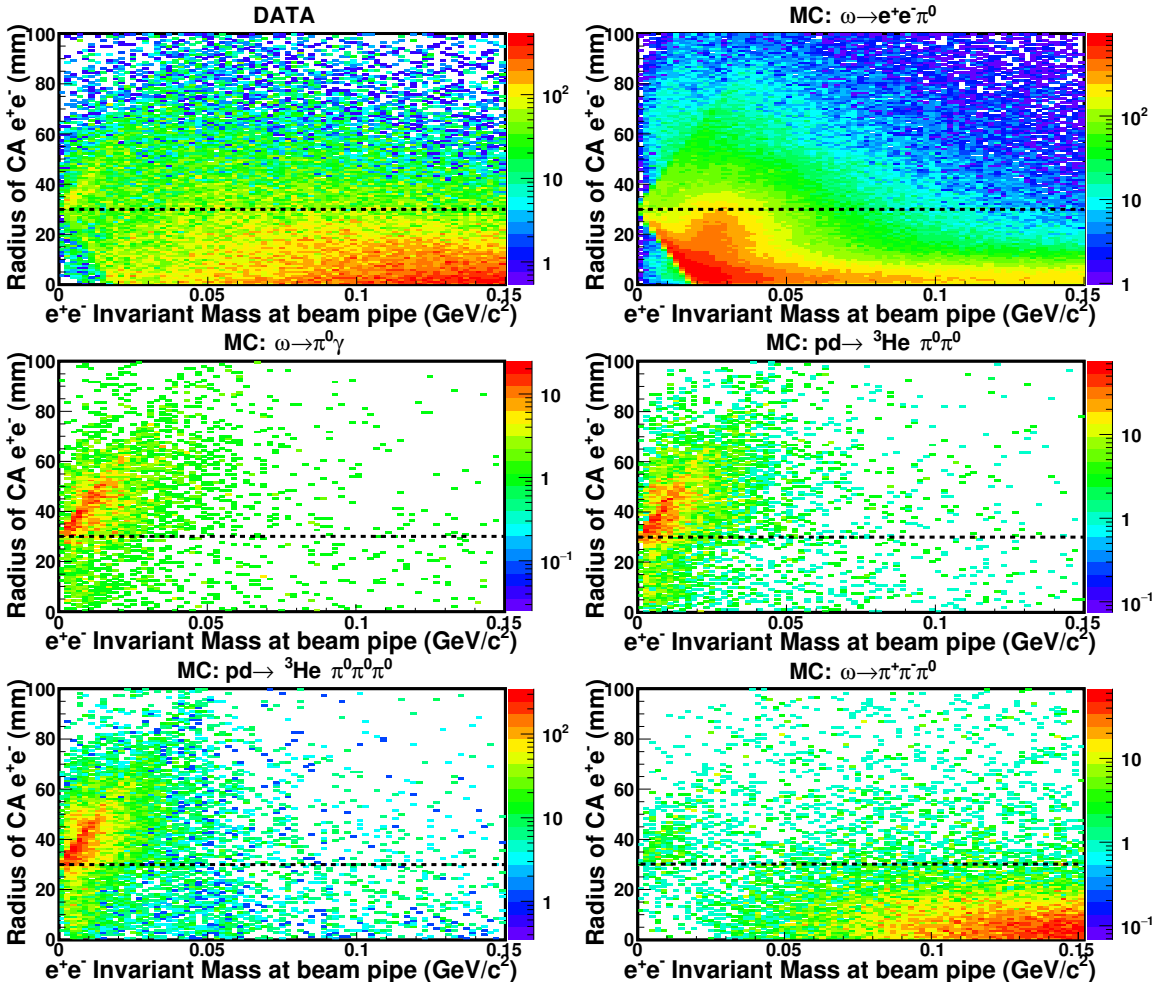

Figure 4.21.: Radius of the closest approach (CA) e^+e^- or the radius of vertex as a function of the e^+e^- invariant mass at the beam pipe. The top left panel is data. The top right panel is the Monte Carlo simulation of the signal, $\omega \to e^+e^-\pi^0$ decay. The second left panel is the Monte Carlo simulation of the $\omega \to \pi^0\gamma$ decay. The distributions for the direct $\pi^0\pi^0$ and $\pi^0\pi^0\pi^0$ production are presented in the second right and the bottom left panels, respectively. The Monte Carlo simulation of the $\omega \to \pi^+\pi^-\pi^0$ decay is shown in the bottom right panel. The conversion events are seen as a red diagonal structure starting from around 30 mm radius of CA in Monte Carlo. This structure is not prominent in the data. The combinations above black dashed line are rejected.

$\pi^0\gamma^*$. The final states with at least four γ in the final state, i.e., direct $\pi^0\pi^0$ and $\pi^0\pi^0\pi^0$ productions, might behave like the $e^+e^-\pi^0$ final state, if one of the photons produced a dilepton pair via the internal conversion. The conversion dilepton in combination with two photons might pass the selection criteria in these final states. Decays with two photons in the final state such as $\pi^0 \to \gamma\gamma$ and $\eta \to \gamma\gamma$ could have ended up being the same topology, if one of the photons produces a conversion dielectron pair and other photons produce an extra photon due to neutral split-off. As mentioned already, these are not one of the most abundant background candidates, but their contributions for each $\omega \to e^+e^-\pi^0$ decay event is monitored. In order to compare the characteristic features of the data and Monte Carlo, the Monte Carlo simulation of the decay $\omega \to \pi^+\pi^-\pi^0$ is shown. The events above the invariant mass 0.08 GeV/c^2 in data distribution is mainly coming from the decays and reactions having at least one pion pair in the final state. The invariant mass of pions at the beam pipe is much

higher than the invariant mass of the dilepton pair. The possibility that they contribute to the conversion events is very low, as hardly any conversion event is seen in the histogram.

The internal conversion of photons are seen as the events above the radius of the beam pipe (30 mm) and at the lowest dilepton invariant masses in the data, as seen for the Monte Carlo. The cut shown in Fig. 4.21 is used to suppress the conversion electrons. The combinations below this line are considered as combinations not coming from external conversions.

The influence of the conversion cut is quantitatively seen in terms of the reconstruction efficiencies, as plotted in Fig 4.18. Almost 80% of the $\omega \to \pi^0\gamma$ decays are rejected. 85% of the events from the direct $\pi^0\pi^0$ production and 75% of the $\pi^0\pi^0\pi^0$ production is lost due to this condition. Whereas, only 14% of the signal ($\omega \to e^+e^-\pi^0$) events are rejected, which is 1.2% of the overall reconstruction efficiency.

The signal purity of the selected sample is not affected, as the background is much larger than the signal. The neutral backgrounds are suppressed significantly. $\frac{\varepsilon_{bj}}{\varepsilon_s}w_j$ values in Fig. 4.25 show that the decay $\omega \to \pi^0\gamma$, direct $\pi^0\pi^0$ and $\pi^0\pi^0\pi^0$ productions for a single event of the $\omega \to e^+e^-\pi^0$ decay is reduced to around 0.14, 7 and 7 from 0.60, 42 and 24, respectively. Moreover, for the $\eta \to \gamma\gamma$ and $\pi^0 \to \gamma\gamma$ decays $\frac{\varepsilon_{bj}}{\varepsilon_s}w_j$ is suppressed to 0.01 from 0.05 and 0.20, respectively. These backgrounds will further be reduced later when the specific constraint over the decay kinematics is used.

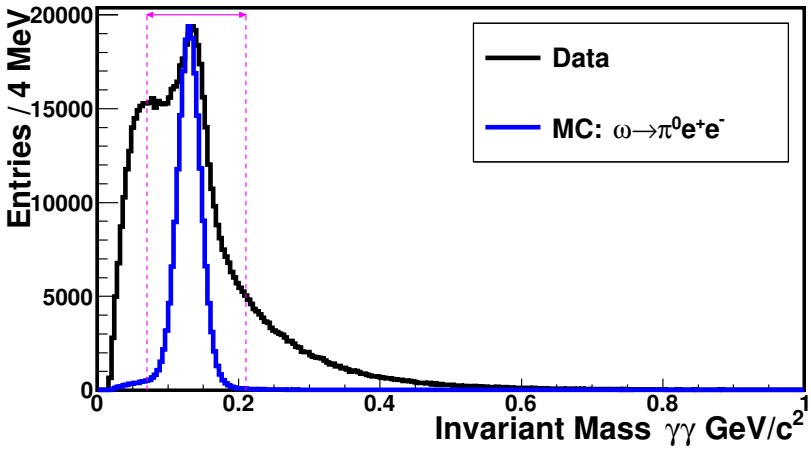

Figure 4.22.: The black curve is the invariant mass of any two neutral tracks in the central detector for data. The blue curve is Monte Carlo simulations for the $\omega \to e^+e^-\pi^0$ decay scaled to the data with respect to the maximum intensity. A peak at the π^0 meson mass (0.135 GeV/c^2) is observed in both spectra. The data has a huge combinatorics background coming from the multi-pion productions. The invariant mass window shown with magenta lines is used to select π^0 candidates.

4.3.3.2. π^0 Candidates Selection

The π^0 meson in the $e^+e^-\pi^0$ final state is reconstructed using the invariant mass ($M_{\gamma_1\gamma_2}$) of two neutral tracks identified in the Central Detector, as shown in Equation 3.3. The two photon invariant mass distribution of the data and Monte Carlo of the $\omega \to e^+e^-\pi^0$ decay are shown in Fig. 4.22. A peak near the π^0 mass 0.135 GeV/c^2 is sitting on top of the background coming from combinatorics and background reactions. The FWHM of the π^0 peak in data is 39 MeV. In order to restrict the two photons coming from π^0 a mass window

of 0.070 GeV/c^2−0.210 GeV/c^2 is used. The two neutral tracks within this window are selected as decay photons from π^0.

The backgrounds having only two charged pions in the final state ($\pi^+\pi^-$) are mostly survived due to the split-offs from the hadronic shower. A cut on the two photons invariant mass will take care of all kinds of split-offs, which can be seen as a hump at low invariant masses.

The condition on the two photon invariant mass covered almost 98% of the signal events, as shown in Fig 4.18. However, an efficiency reduction of only 3-4% is seen for the decays $\omega \rightarrow \pi^+\pi^-\pi^0$, direct $\pi^+\pi^-\pi^0$ production and $\eta \rightarrow \pi^+\pi^-\pi^0$ decay. The direct $\pi^+\pi^-$ production, the decays $\eta \rightarrow \pi^+\pi^-\gamma$ and $\rho \rightarrow \pi^+\pi^-$ have been reduced by 87%, 70% and 85%, respectively.

The evaluated $\frac{\varepsilon_{bj}}{\varepsilon_s} w_j$ values in Fig. 4.25 show that the decays $\eta \rightarrow \gamma\gamma$ and $\pi^0 \rightarrow \gamma\gamma$ have zero contributions for each event of the $\omega \rightarrow e^+e^-\pi^0$ decay. However, the direct $\pi^+\pi^-$ production, the decay $\rho \rightarrow \pi^+\pi^-$ and the decay $\eta \rightarrow \pi^+\pi^-\gamma$ is reduced to 81.00, 0.96 and 0.03 from 613.00, 6.00 and 0.12, respectively, for every signal event. An improvement from 0.04% to 0.05% is seen in signal purity π, as shown in Fig. 4.25.

The purity of 0.05% is significantly low and indicates that the additional kinematic constraint is required. The next step towards the final state reconstruction is to monitor the overall kinematics of the reaction $pd \rightarrow {}^3\text{He}\ \omega \rightarrow {}^3\text{He}\ \ e^+e^-\pi^0$.

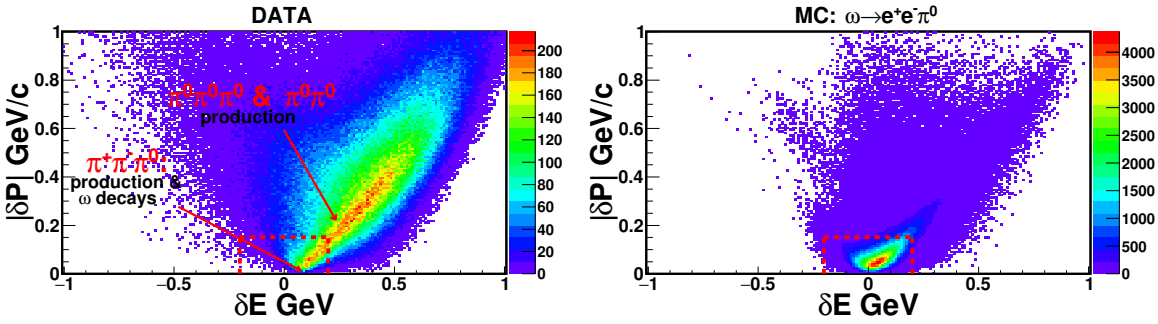

Figure 4.23.: The overall missing momentum (δP) has been plotted against the overall missing energy (δE) of the ^{3}He particle and $\gamma\gamma e^+e^-$ system. The distributions represent the data (left) and the Monte Carlo simulation of the signal (right). The $\omega \rightarrow e^+e^-\pi^0$ events near the vertex (0,0) is hidden under the enormous background in the data. The individual background contributions are shown in Fig. 4.24. The red rectangular enclosure in both plots shows the optimal area selected as $\omega \rightarrow e^+e^-\pi^0$ decay.

4.3.3.3. Overall Kinematic Check

The overall missing momentum $|\delta P|$ and the overall missing energy δE for the Monte Carlo simulation of signal decay $\omega \rightarrow e^+e^-\pi^0$ and the data is plotted in Fig. 4.23. The Monte Carlo simulations of the possible background contributions are shown in Fig. 4.24. The $|\delta P|$ and δE are evaluated using Equation 4.6.

The structure corresponding to the signal $\omega \rightarrow e^+e^-\pi^0$ is hidden underneath large background contributions in data. Which is evident from the $\frac{\varepsilon_{bj}}{\varepsilon_s} w_j$ values. $\frac{\varepsilon_{bj}}{\varepsilon_s} w_j$ after reconstruction of the e^+, e^- and π^0 particles is 1700, 170, 81, 25, 7 and 7 for the direct $\pi^+\pi^-\pi^0$ production, $\omega \rightarrow \pi^+\pi^-\pi^0$ decay, direct $\pi^+\pi^-$ production, $\eta \rightarrow \pi^+\pi^-$ decay, $\pi^0\pi^0$ production and $\pi^0\pi^0\pi^0$ production, respectively. These background contributions lead to continuous δe

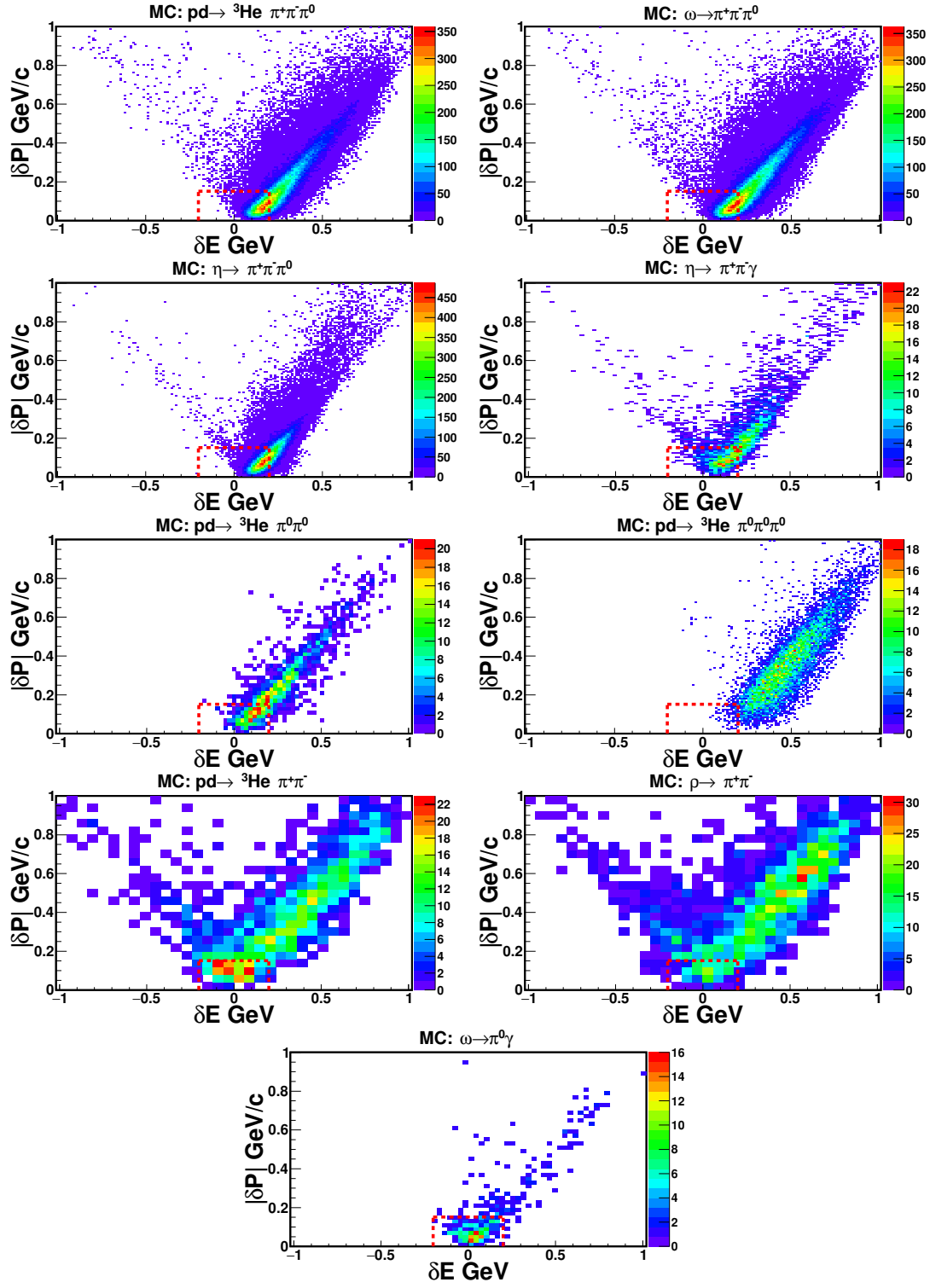

Figure 4.24.: The distributions of the overall missing momentum (δP) as a function of the overall missing energy (δE) are shown for the background contributions. The Monte Carlo simulation of the direct $\pi^+\pi^-\pi^0$ production, the decays $\omega \to \pi^+\pi^-\pi^0$, $\eta \to \pi^+\pi^-\pi^0$ and $\eta \to \pi^+\pi^-\gamma$, the direct $\pi^0\pi^0$, $\pi^0\pi^0\pi^0$ and $\pi^+\pi^-$ productions, the decays $\rho \to \pi^+\pi^-$ and $\omega \to \pi^0\gamma$ are plotted from the top left to the bottom panel, respectively.

and m values, resulting in the data distribution shown in Fig. 4.23. The parameters δe and m are defined in Section 4.2.3.1.

The prominent structure around (0.1,0) in the data distribution, mainly originates from the decay $\omega \to \pi^+\pi^-\pi^0$ and direct $\pi^+\pi^-\pi^0$ production due to scenario ii, as discussed in Section 4.2.3.1. Correspondingly, the events from the $\eta \to \pi^+\pi^-\pi^0$ decay lie in the same region. A similar structure for the decay $\eta \to \pi^+\pi^-\gamma$ is seen on account of scenario iv. As one photon is missing, the structure for the decay $\eta \to \pi^+\pi^-\gamma$ is slightly shifted towards the origin as compared to the $\pi^+\pi^-\pi^0$ final state. $\frac{\varepsilon_{bj}}{\varepsilon_s}w_j$ value for the $\eta \to \pi^+\pi^-\gamma$ at this stage is 0.03 and this may end up to a significant count when scaled for more events of the $\omega \to e^+e^-\pi^0$ decay.

The direct $\pi^0\pi^0$ and $\pi^0\pi^0\pi^0$ productions and the $\omega \to \pi^0\gamma$ decay acquire the same topology as that of the signal if conversion lepton survives the conversion cut. At this point, the fraction $\frac{\varepsilon_{bj}}{\varepsilon_s}w_j$ for the $\omega \to \pi^0\gamma$ decay is 0.06. Which mostly lie over the hyperbolic structure close to (0,0). Whereas, the direct neutral pions will follow scenario ii and have an energy shift towards the positive energy axis, with most of the entries preferably towards the positive energy axis.

The decay $\rho \to \pi^+\pi^-$ and direct $\pi^+\pi^-$ production are following scenario iv, where neither of energy, momentum and mass is conserved. Among them, the contribution from the direct $\pi^+\pi^-$ production is not negligible, firstly, due to the expectedly high cross section [90, 99, 101], and secondly, more events in this reaction are localized near (0,0) and have maximum chances to survive.

The event selection is refined by using an additional constraint over the energy and momentum balance. The restriction on energy and momentum is optimized by studying the efficiency, purity and the quantity efficiency×purity for different cuts. The details are provided in Appendix B.5. It is seen that the combination of $-0.2\ GeV \geq \delta E \leq 0.2\ GeV$ and $|\delta P| \leq 0.18\ GeV/c$, as indicated by the red lines in Fig. 4.23 and Fig. 4.24, is the optimal selection window. The reconstruction efficiency of this selection, as shown in Fig. 4.18, is 5.59% and 5.33% for 1.45 GeV and 1.50 GeV, respectively. An improvement in purity is achieved. The purity, as plotted in Fig. 4.25, has been enhanced to 0.12% and 0.13% from 0.05% in 1.45 GeV and 1.5 GeV data sets, respectively.

Fig. 4.18 shows that the restriction selects almost 75% of the signal events passing through the selection. Approximately 75%, 70%, 50% and 70% of events had been rejected from the $\omega \to \pi^+\pi^-\pi^0$ decay, direct $\pi^+\pi^-\pi^0$ production, $\eta \to \pi^+\pi^-\pi^0$ decay and $\eta \to \pi^+\pi^-\gamma$ decay, respectively. The direct $\pi^0\pi^0$ and $\pi^0\pi^0\pi^0$ productions are further reduced by 60% and 97%, respectively. Almost 80% and 91% of the residuals from the direct $\pi^+\pi^-$ production and the $\rho \to \pi^+\pi^-$ decay has been rejected. Around 68% of the traces from the $\omega \to \pi^0\gamma$ decay have still passed the cut.

The fractional contributions per $\omega \to e^+e^-\pi^0$ decay ($\frac{\varepsilon_{bj}}{\varepsilon_s}w_j$) in Fig. 4.25 suggest that most abundant background contributions which passed the selection criteria are direct $\pi^+\pi^-\pi^0$ production ($>$700) and $\omega \to \pi^+\pi^-\pi^0$ decay ($\simeq$58). The second strong contributions are coming from the direct $\pi^+\pi^-$ production ($>$23) and the $\eta \to \pi^+\pi^-\pi^0$ decay ($\simeq$16). The contribution from the $\eta \to \pi^+\pi^-\gamma$ decay is 0, i.e., suppressed completely. Clearly, the signal to background ratio has improved significantly.

4.3.4. Influence of the $\omega \to e^+e^-\pi^0$ Exclusive Final State Selection on the Decay Kinematics

The impact of the $\omega \to e^+e^-\pi^0$ final state selection criteria can be seen in the form of the exclusive efficiency (ε_{exc}) plotted in Fig. 4.18. 5.59% of the total detector acceptance for 1.45 GeV beam kinetic energy indicates that almost 8.25% of the geometrically ac-

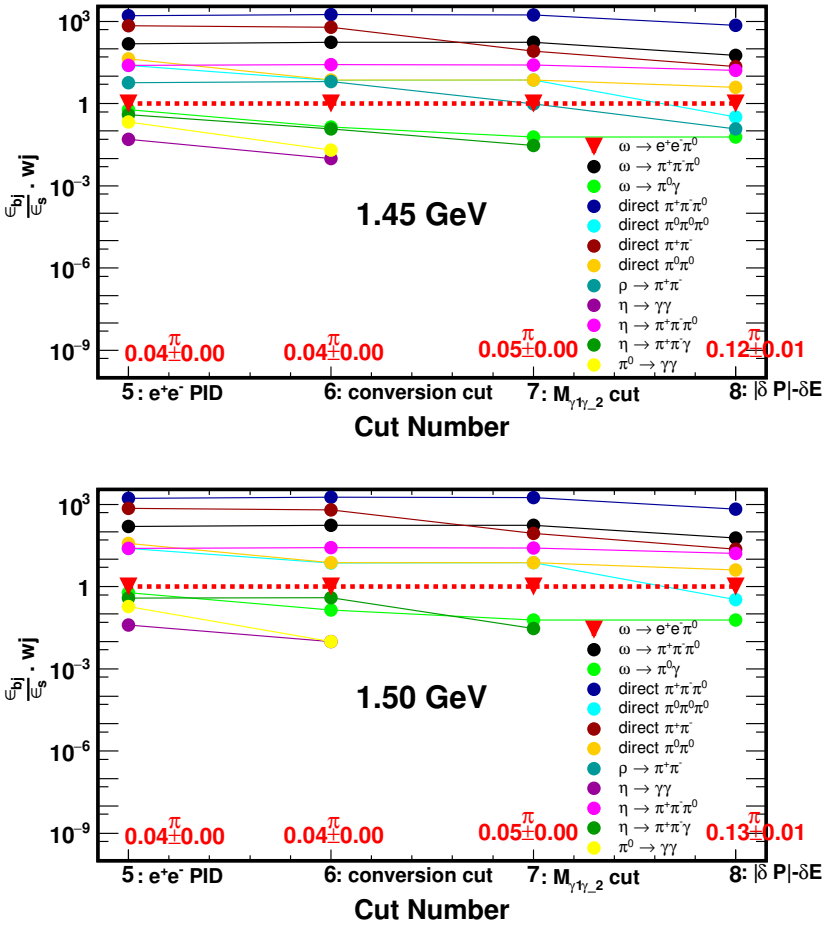

Figure 4.25.: The background contributions for a single event of the $\omega \to e^+e^-\pi^0$ decay ($\frac{\varepsilon_{bj}}{\varepsilon_s} w_j$) are plotted as a function of analysis conditions. $\frac{\varepsilon_{bj}}{\varepsilon_s} w_j$ has been evaluated from Equation 4.10 using w_js from Table 4.3. $\frac{\varepsilon_{bj}}{\varepsilon_s} w_j$ values and the corresponding background probabilities $\mathbf{P}_j(b)$, as discussed in Equation 4.9, can be found in Appendix I. The purity π at each step, estimated using Equation 4.7, is given as the red text.

cepted phase space (see Section 3.1) survived. Similarly, almost 7.78% of the geometrically accepted phase space for 1.50 GeV beam Kinetic energy persists. The overall detector acceptance for 1.50 GeV beam energy has turned out to 5.33%.

The total reconstruction efficiency for the $e^+e^-\pi^0$ final state is used to estimate the number of the $\omega \to e^+e^-\pi^0$ events that should be found in the data. The expected numbers will be useful to judge the quality of the data and the analysis. The expected number of $\omega \to e^+e^-\pi^0$ decays in-data ($N^{expected}_{\omega \to e^+e^-\pi^0}$) is calculated as $N^{expected}_{\omega \to e^+e^-\pi^0} = N^{\circ}_{\omega} \times \varepsilon_{exc} \times BR^{PDG}_{\omega \to e^+e^-\pi^0}$, where N°_{ω} is the total number of ω mesons in the data for two beam energies listed in Table 4.1. $BR_{\omega \to e^+e^-\pi^0} = (7.7 \pm 0.6).10^{-4}$ is the branching ratio of the $\omega \to e^+e^-\pi^0$ decay [39]. A total of $(16\pm4)_{1.45\ GeV}$ + $(16\pm4)_{1.50\ GeV}$ = (32 ± 6) $\omega \to e^+e^-\pi^0$ events is expected in the entire data set.

In addition to this, a significant difference is the seen in the fractional contribution of the backgrounds per signal event $\frac{\varepsilon_{bj}}{\varepsilon_s} w_j$, the probability $\mathbf{P}_j(b)$ of backgrounds to appear in a signal and the sample purity π. $\frac{\varepsilon_{bj}}{\varepsilon_s} w_j$ and π for each step has been plotted in Fig. 4.25. Correspondingly, $\mathbf{P}_j(b)$ is listed in Appendix I for the reference. More impor-

tantly, a perceptible influence is observed in the kinematic phase space of the data. The effect of the final selection is monitored by checking the following quantities.

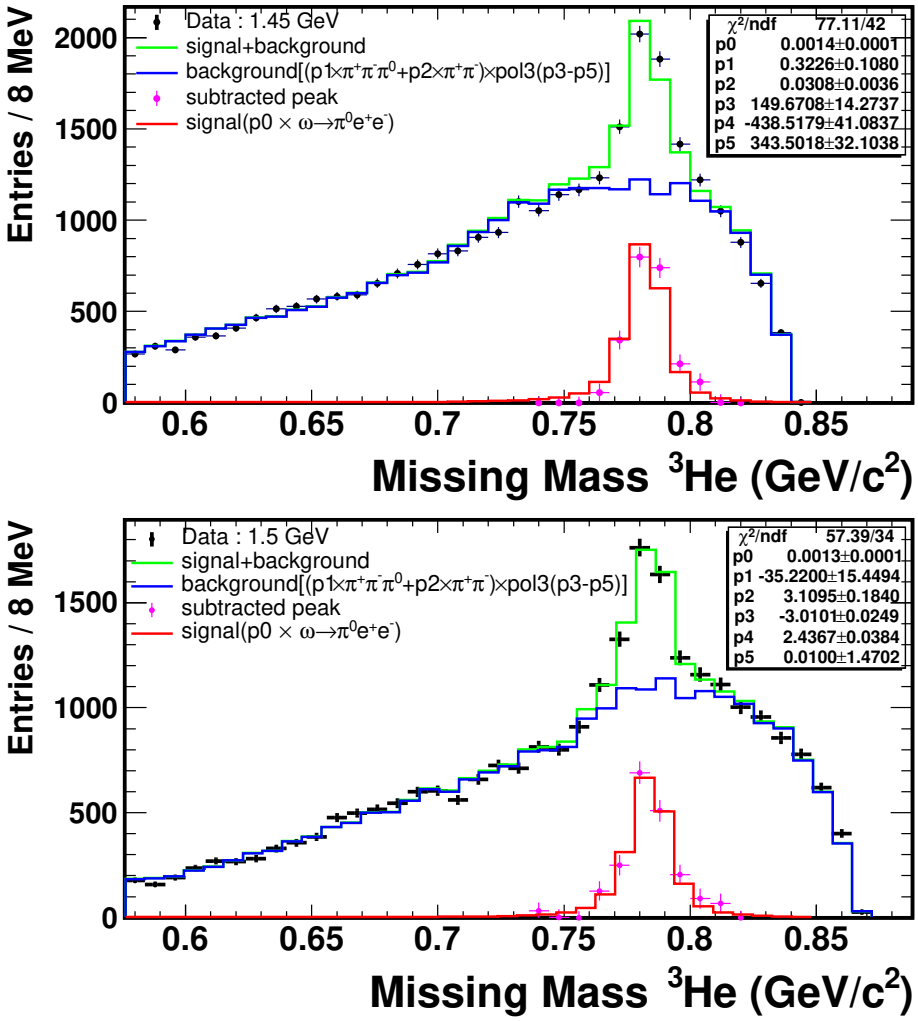

Figure 4.26.: Missing mass spectra are shown after the $e^+e^-\pi^0$ final state selection. The upper panel is the plot for 1.45 GeV and the lower panel is for 1.50 GeV beam energy. The black histograms in the plots are the data. The green histogram is the combined fit of the signal ($\omega \to e^+e^-\pi^0$) and backgrounds ($\pi^+\pi^-\pi^0$ and $\pi^+\pi^-$) convoluted with a polynomial. The background shape is described by the $\pi^+\pi^-\pi^0$ and $\pi^+\pi^-$ phase space simulations convoluted with the polynomial of order 3. The magenta points are the background-subtracted ω peak, which is well explained with the simulation of the $\omega \to e^+e^-\pi^0$ decay convoluted with parameter p0.

4.3.4.1. Missing Mass of ^{3}He after $\omega \to e^+e^-\pi^0$ Exclusive Final State Selection

The exclusive missing mass of ^{3}He particle is plotted in Fig. 4.26 after the ^{3}He and exclusive $\omega \to e^+e^-\pi^0$ final state selection. The two spectra in Fig. 4.26 show a comparison between two energies. A cleaner peak at the ω mass 0.7827 GeV/c^2 is seen on top of the multi pion background as compared to the inclusive missing mass in Fig. 4.4. The direct $\pi^+\pi^-\pi^0$ has largest probability $\mathbf{P}_j(b)$ (=87.00%) to present in the event sample (Appendix I). The in-peak background from the $\omega \to \pi^+\pi^-\pi^0$ decay is the second most abundant background and has $\mathbf{P}_j(b)$=7.00%. The backgrounds from the direct $\pi^+\pi^-$, $\pi^0\pi^0$ and $\pi^0\pi^0$ productions and the decay $\eta \to \pi^+\pi^-\pi^0$ have probability of 3.00%, 0.50%, 0.04% and 2.00% respec-

tively, to be seen as a signal. The contribution from the $\omega \to \pi^0\gamma$ decay, which is 0.06 for each $\omega \to e^+e^-\pi^0$ decay ($\frac{\varepsilon_{bj}}{\varepsilon_s}w_j$), is rounded up to 2 when scaled to the 32 events of the $\omega \to e^+e^-\pi^0$ decay expected in the data.

The background from all multi-pion background productions and the decay $\eta \to \pi^+\pi^-\pi^0$ have been subtracted from the data by fitting the missing mass spectra, as shown in Fig. 4.26. The extracted number of the reconstructed $\omega \to e^+e^-\pi^0$ decays has been listed in Table 4.4 and compared with the expected number.

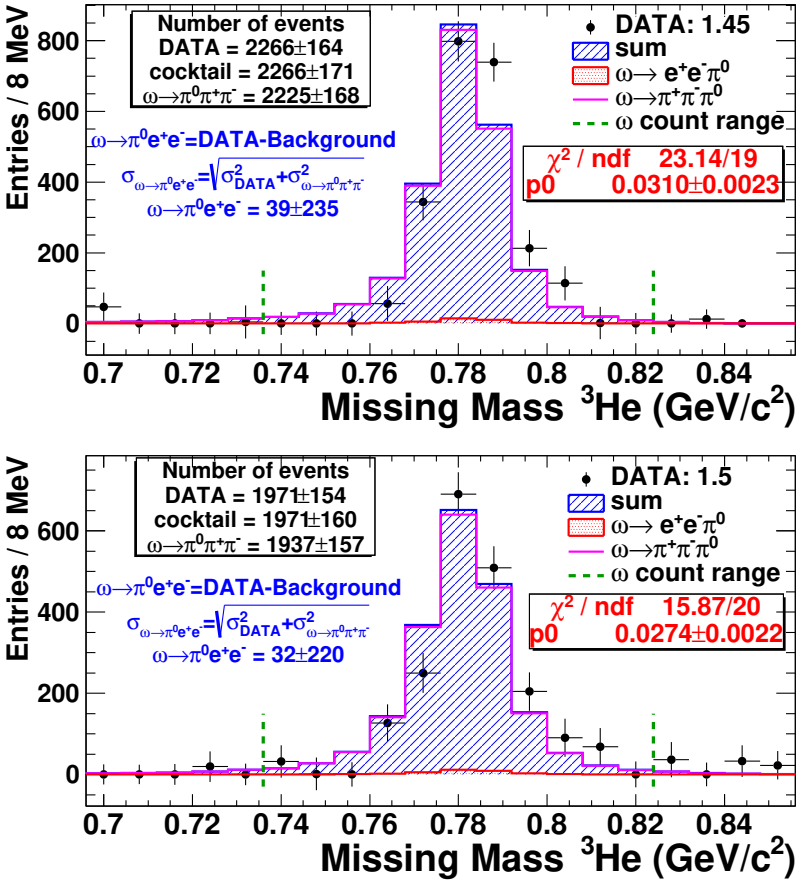

Figure 4.27.: The background-subtracted data peaks from the ^{3}He missing mass distributions in Fig. 4.26 are plotted as black points. The blue filled area is the cocktail sum of the $\omega \to e^+e^-\pi^0$ and $\omega \to \pi^+\pi^-\pi^0$. The contributions from other ω decays are negligible. The red area at the bottom is the signal $\omega \to e^+e^-\pi^0$. The magenta histogram is the contribution from the $\omega \to \pi^+\pi^-\pi^0$ decay. The dark green dashed lines represent the range used to estimate the number of ω mesons in the peak.

As mentioned already, the in-peak background from the $\omega \to \pi^+\pi^-\pi^0$ decay is the second most abundant contribution. This is reflected in the counts under the background-subtracted ω peak. The extracted number is 100 times larger than the expected $\omega \to e^+e^-\pi^0$ events. Thus, the subtracted data peak must be explained by the superposition of signal and backgrounds, and further the backgrounds must be subtracted from the peak. A superposition fit of the signal and the background ω decays is plotted in Fig. 4.27. The superposition fit is created using

$$\text{Superposition Fit} = \text{p0} \times \text{Superposition} = \text{p0} \times \sum_X (PS_X \times cs_X \times BR_X) \tag{4.12}$$

where PS_X, cs_X and BR_X are the Monte Carlo simulation phase space, cross section and branching ratio for the X^{th} contribution, respectively. As $X \in [\omega \to e^+e^-\pi^0, \omega \to \pi^+\pi^-\pi^0, \omega \to \pi^0\gamma]$, the common coefficient cs_ω will be taken care in parameter p0. The value of cs_ω is equated as 1. The coefficient BR_X of each X is well known, and hence, all the contributions in this case are called as "fixed species". p0, which is used to scale the superposition of Monte Carlo to the data, is a free parameter in the fit function. The covariance matrix is calculated by the fit routine from the known attributes of the "fixed species"and unknown parameter p0. The superposition fit function takes care of the error arises due to the background subtraction. This is well evident in the parameter value p0. The errors are propagated throughout in a systematic way. The errors of the branching fractions and the parameter p0 are taken into account, accordingly. The error of the X^{th} decay (σ_X) is estimated as

$$\sigma_X = (\mathrm{p0} \times cs_X \times PS_X \times BR_X) \times \sqrt{(\frac{\sigma_{\mathrm{p0}}}{\mathrm{p0}})^2 + (\frac{\sigma_{PS_X}}{PS_X})^2 + (\frac{\sigma_{BR_X}}{BR_X})^2 + (\frac{\sigma_{cs_X}}{cs_X})^2}. \tag{4.13}$$

As no separate cross section coefficient is used, i.e., $cs_X = 1$, the error in cross section σ_{cs_X} is 0 for this fit. Whereas, the error of the Monte Carlo superposition ($\sigma_{\mathrm{Superposition}}$) is

$$\sigma_{\mathrm{Superposition}} = \left(\mathrm{p0} \times \sum_X (cs_X \times PS_X \times BR_X)\right) \times \sqrt{(\frac{\sigma_{\mathrm{p0}}}{\mathrm{p0}})^2 + \frac{\sum_X \left((\frac{\sigma_{PS_X}}{PS_X})^2 + (\frac{\sigma_{BR_X}}{BR_X})^2 + (\frac{\sigma_{cs_X}}{cs_X})^2\right) \times (cs_X \times PS_X \times BR_X)^2}{\left(\sum_X (cs_X \times PS_X \times BR_X)\right)^2}}, \tag{4.14}$$

The area under the sum and the background-subtracted data peak between the mass range of 0.736 GeV/c^2 – 0.824 GeV/c^2, which is same as used for the inclusive final state and the $\omega \to \pi^0\gamma$ exclusive final state, is in agreement within the errors. The range chosen is 5σ on left and 4σ on the right side of the ω peak. The background contribution from the $\omega \to \pi^+\pi^-\pi^0$ decay is estimated and listed in Table 4.4.

	1.45 GeV	**1.50 GeV**	**Entire data**
$\omega \to e^+e^-\pi^0$ *expected* ($N^{expected}_{\omega \to e^+e^-\pi^0}$)	(16±4)	(16±4)	(32±6)
Number of events in the continuous background subtracted peak	(2266±164)	(1971±154)	(4237±225)
in-peak background $\omega \to \pi^+\pi^-\pi^0$	(2225±168)	(1937±157)	(4162±230)
$\omega \to e^+e^-\pi^0$ *reconstructed in data* ($N^{rec}_{\omega \to e^+e^-\pi^0}$)	(39±235)	(32±220)	(71±322)
overall purity (%)	0.14%	0.13%	0.14%
overall significance	0.24	0.20	0.31
in-peak purity (%)	1.72%	1.62%	1.66%
in-peak significance	0.82	0.72	1.10

Table 4.4.: The number of reconstructed $\omega \to e^+e^-\pi^0$ decays, overall purity, overall significance, in-peak purity, and the in-peak significance are presented. For overall purity and significance, all background contributions have been taken into consideration. However, for in-peak purity and significance, only in-peak backgrounds are used.

The most abundant in-peak background contribution from the $\omega \to \pi^+\pi^-\pi^0$ decay is subtracted from the data peak to have an estimate of the number of the $\omega \to e^+e^-\pi^0$ decays in data.

$$N_{\omega\to e^+e^-\pi^0} = N_{DATA\ peak} - N_{background} = N_{DATA\ peak} - N_{\omega\to \pi^+\pi^-\pi^0} = 71_{Entire\ data} \quad (4.15)$$

The errors are propagated systematically for two energies, as,

$$\sigma_{\omega\to e^+e^-\pi^0} = \pm\sqrt{\sigma^2_{data} + \sigma^2_{\omega\to \pi^+\pi^-\pi^0}} = \pm\sqrt{225^2 + 230^2} = \pm 322_{Entire\ data} \quad (4.16)$$

The resulting number, as listed in Table 4.4, is estimated to be (39±235) and (32±220) for 1.45 GeV and 1.50 GeV, respectively. The in-peak signal to background ratio, which was 0.0325 and 0.0400 in the inclusive final state for 1.45 GeV and 1.50 GeV, respectively, turns out to be 26.61×10^{-4} for 1.45 GeV and 24.90×10^{-4} for the respective energies. The number of reconstructed $\omega \to e^+e^-\pi^0$ decay is nearly two times the expected number (32±6). This is an indication that there are still remnants of the background from the $\omega \to \pi^+\pi^-\pi^0$ decay, which is almost 50% of the current yield. One of the reasons for this discrepancy may be the background contributions that are not accurately estimated from the Monte Carlo simulations. However, the estimated errors are large enough to accommodate for this inaccuracy. Therefore, within errors, the numbers extracted and the numbers expected for two energies are in agreement. The large error bars are due to the presence of huge background contributions in the event sample and the background subtractions.

The overall purity and in-peak purity of the sample listed in Table 4.4 are consistent with previous numbers listed in Fig. 4.25. The statistical significance indicates that with existing statistics it is unrealistic to find a selection capable of allowing the observation of the signal [121]. In order to observe a signal, the significance of at least 3 should be needed. The achieved yield for the $\omega \to e^+e^-\pi^0$ decay is supporting the previous statement. (71±322) reconstructed events basically mean 0 events, i.e., $\omega \to e^+e^-\pi^0$ decay is not found in the data. The result will be discussed later in Chapter 5.

4.3.4.2. Invariant Mass of e^+e^- after $\omega \to e^+e^-\pi^0$ Exclusive Final State Selection

As discussed in Chapter 1, the main focus of this work is to check for the feasibility of measuring the $\omega - \pi$ transition form factor. The reconstructed e^+e^- pair is giving an access to the full range of virtual photon mass (q^2) shown in Fig. 1.6. The dilepton invariant mass, which is evaluated from Equation 1.6, is plotted in Fig. 4.28 for both energies. In order to compare data with Monte Carlo, a superposition histogram of signal ($\omega \to e^+e^-\pi^0$) and all possible backgrounds is created as

$$\mathrm{Fit}_{\mathrm{superposition}} = \mathrm{p2} \times (.\mathrm{p0} \times PS_{\pi^+\pi^-} + \mathrm{p1} \times BR_{\rho\to\pi^+\pi^-} \times PS_{\rho\to\pi^+\pi^-} + \sum_X (PS_X \times cs_X \times BR_X)), \quad (4.17)$$

where *cs*, *BR* and *PS* are the cross section, branching ratio and the simulated phase space of the X^{th} decay/reaction. The subscript X varies over the set $\left[\omega \to e^+e^-\pi^0,\ \omega \to \pi^+\pi^-\pi^0,\ \omega \to \pi^0\gamma,\ \pi^+\pi^-\pi^0,\ \pi^0\pi^0,\ \pi^0\pi^0\pi^0,\ \eta \to \pi^+\pi^-\pi^0\right]$. The free parameter p2 is the scaling parameter, which normalizes the Monte Carlo sum to the data. The signal and the backgrounds in Equation 4.17 are the fixed species, whose attributes (*cs* and *BR*) are known, as listed in Appendix C.1. The parameters p0 and p1 are the unknown coefficients of the direct $\pi^+\pi^-$ production and the ρ meson production. As these

attributes are unknown at the current energies. For convenience, parameters p0 and p1 are named as "variable species ", in this document.

In order to fit a combination of fixed species and variable species to the fixed data yield, the variable species must be normalized appropriately. So that true marginal distribution is reproduced. The plot technique is influenced by Ref. [125]. Wherein, firstly the covariance matrix of Equation 4.17 is calculated from fixed species only, i.e., fixing variable species to 0. In the next step, for fixed attributes of the fixed species, the obtained covariance matrix of Equation 4.17 is modified by allowing variable species to be varied freely.

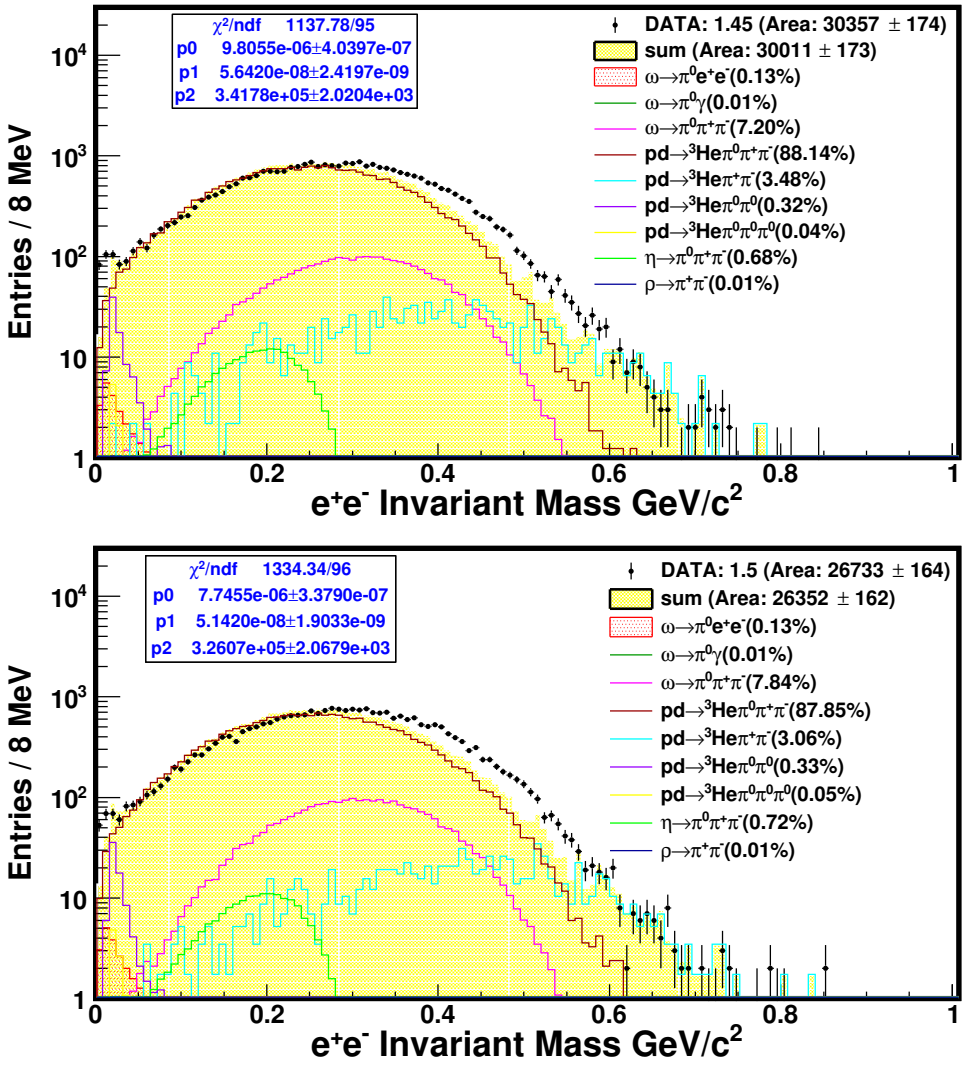

Figure 4.28.: The e^+e^- invariant mass distributions after the $\omega \to e^+e^-\pi^0$ final state selection are shown for 1.45 GeV (top) and 1.50 GeV (bottom) beam energies. The black points represent the data distribution. Which is compared with the superposition histogram of the Monte Carlo signal and backgrounds, highlighted as the yellow area. The individual signal and background contributions are plotted. The respective percentage contributions are given in the legend.

The final superposition histogram and the contributing backgrounds are plotted in Fig. 4.28 with data. The parameter values are listed in Fig. 4.28. The value of the parameter p0, which is $(9.81\pm0.40)\times10^{-6}$ b for 1.45 GeV and $(7.75\pm0.34)\times10^{-6}$ b for 1.5 GeV, anticipates the cross section of the $\pi^+\pi^-$ production to be significantly larger. Which is ap-

proximately two orders of magnitude higher than the ω meson production. In contrast, the values of parameter p1 are (56.42±0.24)×10^{-9} b and (51.42±0.19)×10^{-9} b for 1.45 GeV and 1.50 GeV, respectively. This indicates that the cross-section of the ρ meson production is expected to be comparable to the ω meson cross-section. The ∼100% decay width of the $\rho \to \pi^+\pi^-$ makes it a probable background candidate for the rare $\omega \to e^+e^-\pi^0$ decay (refer to Appendix C.1 for branching fractions). The weighting factors w_i for the direct $\pi^+\pi^-$ production and the decay $\rho \to \pi^+\pi^-$ are re-evaluated from Equation 4.8, by equating $cs_{\pi^+\pi^-}$ and $cs_{\rho\to\pi^+\pi^-}$ with the p0 and p1 values, respectively. The new w_i for the direct $\pi^+\pi^-$ production is (153679±13811) and (116277±9298) for 1.45 GeV and 1.50 GeV, respectively. Similarly, for the decay $\rho \to \pi^+\pi^-$, the re-estimate of w_i turns out to be (877±80) for 1.45 GeV and (799±70) for 1.50 GeV. Accordingly, $\frac{\varepsilon_b}{\varepsilon_s}w$ values for the direct $\pi^+\pi^-$ production are (22±2) and (18±2) in 1.45 GeV data and 1.50 GeV data, respectively. Whereas, $\frac{\varepsilon_b}{\varepsilon_s}w$ of the $\rho \to \pi^+\pi^-$ decay is (0.11±0.01) for 1.45 GeV and (0.09±0.01) for 1.50 GeV. Traces of these contributions survived the split-off cut are scaled up to a significant amount, due to the large values of parameters p0 and p1. The contribution from $\rho \to \pi^+\pi^-$ decay impacts the quality of the final sample, as the masses of the ρ and ω mesons are comparable [39].

Moreover, the distributions in Fig. 4.28 suggest that the entries in the data and the Monte Carlo simulations are localized within the physically allowed regions (refer to Ref. [126] for kinematic limit details). Furthermore, the line shape of the superposition and data are comparable. Conclusively, Within errors, the Monte Carlo simulation is in agreement with the expectations. However, the discrepancy between data and Monte Carlo for the higher invariant masses might be due to the unknown production mechanisms of the direct processes, given an isotropic phase space population has been assumed for the simulations. In addition, the statistical fluctuations are contributing to this discrepancy.

Contribution	**1.45 GeV**			**1.50 GeV**		
	Events	σ_{stat}	σ_{fit}	Events	σ_{stat}	σ_{fit}
DATA	30357 ±	174		26733 ±	164	
MC:						
SUM	30011 ±	173	126	26352±	162	107
$\omega \to e^+e^-\pi^0$	37 ±	6	1	34±	6	1
$\omega \to \pi^0\gamma$	3 ±	2	0	3 ±	2	0
$\omega \to \pi^+\pi^-\pi^0$	2161 ±	47	10	2066±	46	10
$\pi^+\pi^-\pi^0$	26452 ±	163	100	23150 ±	152	88
$\pi^+\pi^-$	1044 ±	33	80	806±	28	60
$\pi^0\pi^0$	96 ±	10	3	87±	9	3
$\pi^0\pi^0\pi^0$	12 ±	4	1	13±	4	1
$\eta \to \pi^+\pi^-\pi^0$	204 ±	14	2	190±	14	2
$\rho \to \pi^+\pi^-$	3 ±	2	0	3±	2	0
overall purity (%)	0.12%			0.13%		
overall significance	0.21			0.21		
in-peak purity (%)	1.68%			1.62%		
in-peak significance	0.79			0.74		

Table 4.5.: The number of events in the superposition histogram and in the individual contributions is shown for two energies. The statistical and fit errors are given.

An estimate for the number of the signal and background events to be found in data is obtained from the superposition histogram and compared with the estimates from the

missing mass spectra. The counts for the superposition histogram and for each contribution are listed in Table 4.5. The statistical errors and errors due to fit are shown. The errors due to fit are propagated bin wise in a systematic way, as shown in Equation 4.13 and Equation 4.14. BR_X for the direct production is taken as 1 and its error σ_{BR_X}=0. The cross section cs_X for the direct $\pi^+\pi^-$ production and the ρ meson production are unknown, and hence the parameter values p0, p1 and the corresponding errors are used.

The number of $\omega \rightarrow e^+e^-\pi^0$ decay is estimated to be $(37\pm6\pm1)_{1.45GeV}$ and $(34\pm6\pm1)_{1.5GeV}$ for two energies. This estimate agrees well with the signal yield in data obtained from the missing mass spectra, as listed in Table 4.4. The yield of each background contribution for a single event of the $\omega \rightarrow e^+e^-\pi^0$ decay ($\frac{\varepsilon_b}{\varepsilon_s}w$), as listed in Fig. 4.25, is in agreement with the current yield shown in Table 4.5. Provided, the current yield is extrapolated for (37±6±1) and (34±6±1) events of the $\omega \rightarrow e^+e^-\pi^0$ decays in 1.45 GeV and 1.5 GeV data, respectively.

The statistical significance and purity, as listed in Table 4.5, are consistent with the previously obtained values in Fig. 4.25 and Table 4.4. The small value of the statistical significance supports the statement that event selection does not have enough statistical power to observe the signal.

5. Results and Discussions

5.1. The Inclusive Missing Mass of ^{3}He: $pd \rightarrow {}^3\mathrm{He}\ \omega$

The inclusive missing mass distributions are used to estimate the total number of ω mesons, as discussed in the previous chapter. The Monte Carlo simulation of the $\omega \rightarrow \pi^0\gamma$ channel has been combined with the neutral multi-pion productions, which are the most prominent backgrounds for the $\omega \rightarrow \pi^0\gamma$ final state, to fit the data.

The statistical significance of the event selection, 61 for 1.45 GeV and 66 for 1.50 GeV, is large enough (>>5) to observe the ω meson in data. The signal to background ratio for the inclusive missing mass spectrum in the peak region is 3% for 1.45 GeV and 4% for 1.50 GeV. The situation is improved after $\pi^0\gamma$ final state selection and a better precision in the fits is obtained. The background-subtracted data distribution is described by the simulations. The peak positions and the resolution obtained for two energies are listed in Table 5.1. The peak positions obtained from data for both energies are close to the particle data group value (0.7827±0.0001) GeV/c^2. The number of ω mesons extracted from the background-subtracted peak is presented in Table 4.1 of the previous chapter.

	peak position (MeV)		FWHM (MeV)	
	MC	data	MC	data
	Inclusive final state			
1.45 GeV	782.34±0.02	783.44±0.12	15.40±0.06	15.36±0.36
1.50 GeV	782.49±0.02	783.33±0.12	15.75±0.08	15.71±0.37
	$\omega \rightarrow \pi^0\gamma$ final state			
1.45 GeV	782.36±0.10	782.70±0.32	14.13±0.36	14.78±1.14
1.50 GeV	782.39±0.12	783.09±0.33	15.52±0.47	14.77±1.21

Table 5.1.: The peak position and resolution (FWHM) of the background-subtracted peak for two beam energies at different stages of the analysis.

The total number of ω mesons N_{ω° in data is estimated as

$$\begin{aligned} N_{\omega}{}^{\circ} = \frac{N_{\omega}^{rec}}{\varepsilon_{inc}} &= \left[\frac{(3.15 \pm 0.04) \times 10^5}{0.8465}\right]_{1.45\ GeV} + \left[\frac{(3.28 \pm 0.04) \times 10^5}{0.8671}\right]_{1.50\ GeV} \\ &= \left[(3.72 \pm 0.05) \times 10^5\right]_{1.45\ GeV} + \left[(3.78 \pm 0.05) \times 10^5\right]_{1.50\ GeV} \\ N_{\omega}{}^{\circ} &= \left[(7.50 \pm 0.07) \times 10^5\right]_{entire\ data}, \end{aligned} \tag{5.1}$$

where N_{ω}^{rec} is the number of reconstructed ω mesons obtained from the background subtracted peak. The ε_{inc} is the Monte Carlo efficiency of the selection criteria. The errors shown are the propagated statistical errors. The numbers are used to evaluate the average luminosity ($L_A = (1.67 \pm 0.04) \times 10^{31} cm^{-2} s^{-1}$) during the beam time, as shown in Equation 4.5, and the branching ratio. Which is evaluated later in this chapter.

5.2. The Exclusive Missing Mass of ^{3}He: $pd \to {}^3\mathrm{He}\ \omega\ (\omega \to \pi^0\gamma)$

The signal to background ratio after implying the exclusive final state is improved to 0.0984 for 1.45 GeV and 0.1120 for 1.50 GeV as compared to the inclusive final state. The significance values of 17.97 (1.45 Gev) and 20.60 (1.50 GeV) are sufficient to detect the $\omega \to \pi^0\gamma$ decay in data. The missing mass distributions after exclusive selection are used to estimate the total number of ω mesons decaying into $\pi^0\gamma$. The total number $N^{\circ}_{\omega\to\pi^0\gamma}$ of $\omega \to \pi^0\gamma$ decays during the full beam time is calculated as

$$\begin{aligned} N^{\circ}_{\omega\to\pi^0\gamma} = \frac{N^{rec}_{\omega\to\pi^0\gamma}}{\varepsilon_{exc}} &= \left[\frac{(1.08\pm0.05)\times10^4}{0.3474}\right]_{1.45\ GeV} + \left[\frac{(1.08\pm0.04)\times10^4}{0.3435}\right]_{1.50\ GeV} \\ &= \left[(3.11\pm0.13)\times10^4\right]_{1.45\ GeV} + \left[(3.14\pm0.13)\times10^4\right]_{1.50\ GeV} \\ N^{\circ}_{\omega\to\pi^0\gamma} &= \left[(6.25\pm0.18)\times10^4\right]_{entire\ data}, \end{aligned} \tag{5.2}$$

where $N^{rec}_{\omega\to\pi^0\gamma}$ is the number of $\omega \to \pi^0\gamma$ decays in the background subtracted data peak and ε_{exc} is the reconstruction efficiency. These numbers can be referred from Table 4.2. The total number of $\omega \to \pi^0\gamma$ decays will be used to determine the branching ratio of the $\omega \to \pi^0\gamma$ decay, as discussed in the upcoming section.

Branching ratio of the $\omega \to \pi^0\gamma$ decay ($BR^{measured}_{\omega\to\pi^0\gamma}$)			
	1.45 GeV	**1.50 GeV**	**Entire data (1.45+1.5) GeV**
$BR^{measured}_{\omega\to\pi^0\gamma} = \frac{N^{\circ}_{\omega\to\pi^0\gamma}}{N^{\circ}_{\omega}}$	$\frac{(3.11\pm0.13)\times10^4}{(3.72\pm0.05)\times10^5}$	$\frac{(3.14\pm0.13)\times10^4}{(3.78\pm0.05)\times10^5}$	$\frac{(6.25\pm0.18)\times10^4}{(7.50\pm0.07)\times10^5}$
BR_f	$= (8.36\pm0.37)\%$	$= (8.31\pm0.34)\%$	$= (8.33\pm0.25)\%$

Table 5.2.: The measured branching ratio $BR^{measured}_{\omega\to\pi^0\gamma}$ for 1.45 GeV beam energy, 1.5 GeV beam energy and the combined data set are given in the second, the third and fourth columns, respectively. N°_{ω} and $N^{\circ}_{\omega\to\pi^0\gamma}$ are listed in Table 4.1 and Table 4.2, respectively. The values shown here are the final branching ratios BR_f.

5.2.1. Branching Ratio of the $\omega \to \pi^0\gamma$ Decay

The average branching fraction of the $\omega \to \pi^0\gamma$ decay calculated for the average luminosity is expressed as

$$\begin{aligned} BR^{measured}_{\omega\to\pi^0\gamma} = \frac{N^{\circ}_{\omega\to\pi^0\gamma}}{N^{\circ}_{\omega}} &= \frac{\left[(6.25\pm0.18)\times10^4\right]_{entire\ data}}{\left[(7.50\pm0.07)\times10^5\right]_{entire\ data}} \\ BR^{measured}_{\omega\to\pi^0\gamma} &= (8.33\pm0.25)\%, \end{aligned} \tag{5.3}$$

where N°_{ω} and $N^{\circ}_{\omega\to\pi^0\gamma}$ are taken from Equation 5.1 and Equation 5.2, respectively. The measured branching ratio in three cases, as listed in Table 5.2, are found close to the particle data group $(8.40\pm0.22)\%$ [39]. The errors shown here are statistical. The systematic errors

are estimated by exploring the systematic effect coming from the background subtraction and the analysis procedure. Which will be presented in Section 5.2.3.

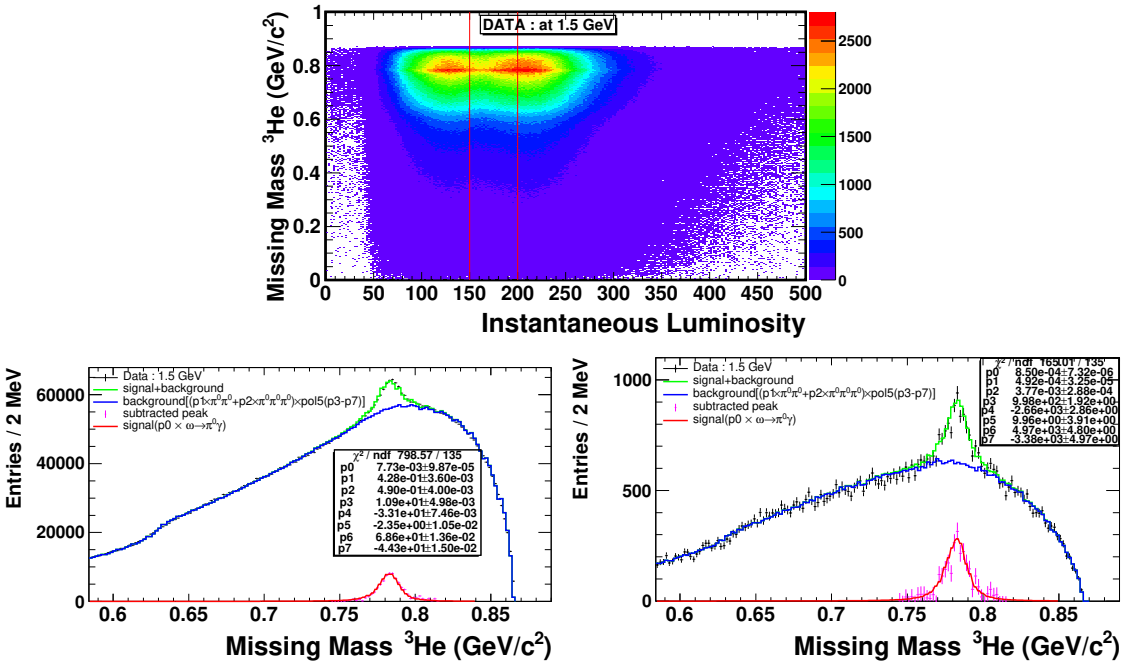

Figure 5.1.: The inclusive missing mass of ^{3}He particles as a function of luminosity measure "TR17/Pellet rate" is plotted in the top panel for 1.50 GeV beam energy. As an illustration, the bin in the luminosity range of (150 - 200) $pellet^{-1}$ has been projected as black histogram in the bottom left panel. The luminosity range of the missing mass projection is indicated by two red lines. To extract the number of ω mesons, the missing mass spectrum is fitted. The bottom right panel represents the missing mass projection and the fit for the same luminosity range after the $\pi^0\gamma$ final state. The number of the $\omega \to \pi^0\gamma$ decays is extracted.

5.2.2. Luminosity Dependence of the Measured Branching Ratio of the $\omega \to \pi^0\gamma$ Decay

The instantaneous luminosity for the ω production is the ratio of the total number of ω mesons to the interaction cross-section with an average of one pellet in the beam. The missing mass of ^{3}He is plotted as a function of the instantaneous luminosity factor "TR17/Pellet rate" in the top panel of Fig. 5.1. Which is a relative measure for the instantaneous luminosity,

$$\text{Instantaneous Luminosity} = \frac{\text{TR17}}{\text{Pellet rate}} \tag{5.4}$$

where trigger 17 represents a measure of the luminosity described in Section 3.7.

The instantaneous luminosity factor, in combination with a conversion factor derived from the known attributes of the pellet target and the trigger simulations, would be the instantaneous luminosity. In the following sections, the instantaneous luminosity factor is referred to as luminosity.

Large luminosities could cause pileups from chance coincidences, possibly affecting the results. The trigger used during the *pd* beam time, based on the unique signature of ^{3}He particle, effectively suppresses background from elastic, quasi-elastic and breakup reactions. These backgrounds, around one million times larger than the ω production [90, 127], constitute the majority of the total cross section of the *pd* collision. Owing to the high cross-section, there is a possibility that these background events survive the trigger conditions at high rates in the form of event pileup.

The pileup from the background might coincide in time with the long SEC signals, named as coincidences, and are mostly considered as a signal or part of the actual event. These chance coincidences create an imbalance in energy and momentum and cause a reduction in efficiency. Which further becomes pronounced at higher luminosities. The effect is scaled up depending on the number of γ in the event. As a consequence, the branching ratio would decrease with increasing luminosity. For detailed description of the luminosity effects please refer to Ref. [84].

In order to see this effect, the branching fraction with respect to luminosity is studied. To accomplish this, the inclusive missing mass of ^{3}He is plotted as a function of the instantaneous luminosity in the upper panels of Fig. 5.1 for 1.5 GeV. It can be seen from the plot that most of the time the luminosity lies between 100 $pellet^{-1}$ and 250 $pellet^{-1}$. The ^{3}He missing mass for different luminosity ranges are fitted and a number of ω mesons extracted. One of such missing mass fits for the luminosity range (150 - 200) $pellet^{-1}$ is shown in the bottom left panel of Fig. 5.1 for 1.5 GeV beam energy. The number of ω meson extracted in 1.50 GeV data set is $(7.77\pm0.20)\times10^4$. Correspondingly, the projection onto the missing

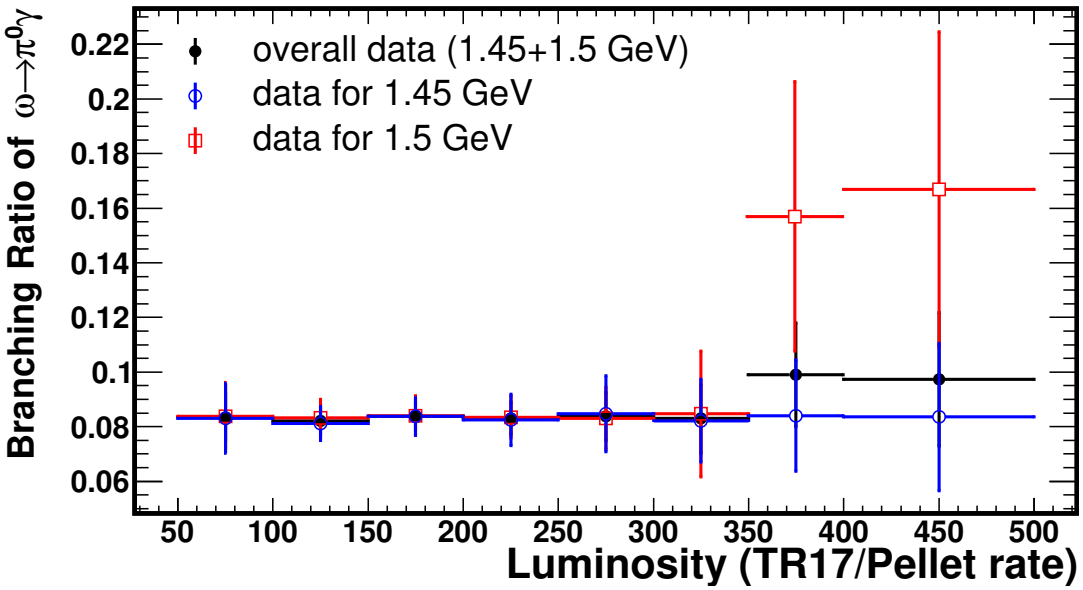

Figure 5.2.: The measured branching ratio of the $\omega \rightarrow \pi^0\gamma$ decay is plotted as a function of the different luminosity values. The blue, red and black points are the data at 1.45 GeV, 1.5 GeV and the combined data for both energies, respectively. The branching ratios for three data sets are in agreement within error.

mass after $\omega \rightarrow \pi^0\gamma$ final state is fitted and the peak is extracted for different luminosity bins. As an example, the fit for the range (150 - 200) $pellet^{-1}$ is shown in the right panel of Fig. 5.1. The number extracted from the data is $(2.59\pm0.21)\times10^3$ for $\omega \rightarrow \pi^0\gamma$ final state at

1.50 GeV beam energy. The errors shown are the propagated statistical errors. The extracted numbers for both energies and each bin are presented in Appendix J for two final states.

The branching ratio of the decay mode $\omega \to \pi^0\gamma$ is obtained using Equation 5.3. Where the total number of the $\omega \to \pi^0\gamma$ decays is divided with the total number of ω mesons for corresponding luminosity bins. The evaluated branching ratio for different bins is plotted in Fig. 5.2. The overall data are obtained by adding the individual contributions of two beam energies, as shown in Equation 5.1 and Equation 5.2. The branching ratio for the combined data set is estimated for each bin, as shown previously in Equation 5.3. The errors shown here are statistical. It can be seen in Fig. 5.2 that the branching ratio is not changing significantly and is consistent within uncertainties. The branching ratios in different luminosity range for three data sets are in agreement within errors with the particle data group (8.40±0.22)% [39]. The branching ratios are comparably larger for the last two higher luminosity bins. This jump might arise due to the statistical fluctuations and systematics in the fitting procedure, as the statistics in these bins is low. The fits for the last two bins are presented in Appendix J. The last two bins may have an influence on the branching ratio to some extent. Therefore, it is significant to do a systematic check of the branching ratio measurement for luminosity. Which is presented in the following.

5.2.3. Systematical Uncertainties

Systematic uncertainties are often of comparable size to the statistical uncertainties in the measurement of a physical quantity. Consequently, they play a key role in the measurement. Some common examples of systematic uncertainty include uncertainties that arise from the detector calibration, detector acceptance, parameters of the model used to make inferences that are not known precisely, physical/detector related background which cannot be separated from the signal and signal selection bias in the analysis.

Two types of systematic effects have been explored for this study [128]. In the first type, the systematic study is performed using a selection of different sets of events, which are a subset of the final analysis sample. In particular, the luminosity dependent effect is a candidates for this type of test. In this case, two variables σ_Δ and λ are tested to determine if the branching ratio value for the selected subset, BR_i, deviate systematically from the final branching ratio, BR_f [129],

$$\begin{aligned} \sigma_\Delta &= \sqrt{|\sigma_i^2 - \sigma_f^2|} \\ \lambda &= \frac{BR_f - BR_i}{\sigma_\Delta}. \end{aligned} \tag{5.5}$$

The $|\lambda| > 2$ for a particular test indicates the presence of a systematic effect that is not understood properly. The systematical deviation that arises due to this effect has to be accounted for as the difference in the branching ratios, $BR_f - BR_i$.

The second type of systematic study is independent of the selected data set. For instance, the systematic effect arises due to background subtraction and different types of cuts used for the final event selection. In this case, the difference between the final branching ratio, BR_f, and the branching ratio from the cross check, BR_i, is given in terms of the uncertainty

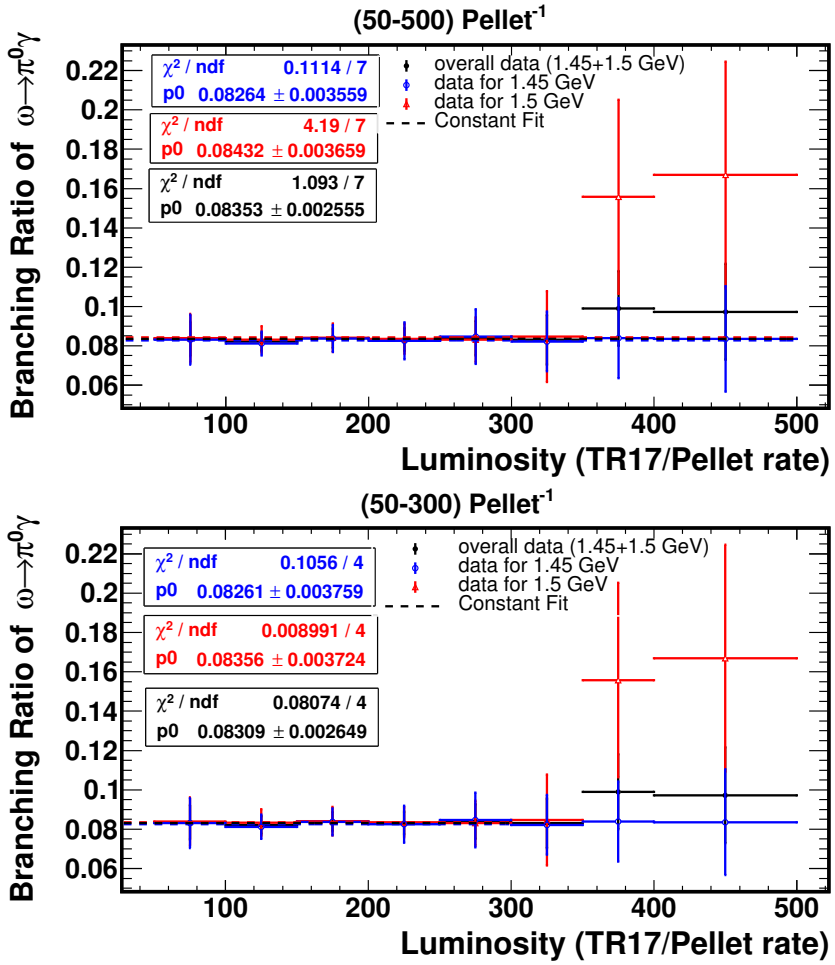

Figure 5.3.: The branching ratios as a function of luminosity are fitted for the different luminosity ranges, as indicated on the top legends. The blue, red and black markers represent the 1.45 GeV, 1.50 GeV and the combined data set, respectively. The constant fits for different ranges are plotted as dashed lines. The fit parameters and χ^2/ndf are listed in legends.

of the standard analysis [129],

$$\Delta BR = \frac{BR_f - BR_i}{\sigma_{BR_f}}. \tag{5.6}$$

If an effect is greater than one standard deviation, i.e., $|\Delta BR| > 1$, then this systematic effect should be considered as $BR_f - BR_i$.

5.2.3.1. Systematic Uncertainty due to Luminosity

The systematic effect on the branching ratio from the last three luminosity bins is understood and presented here. The branching ratio is estimated by fitting three histograms in Fig. 5.2 with a constant fit. The fits for two extreme luminosity ranges (50 - 500) $pellet^{-1}$ and (50 - 300) $pellet^{-1}$ are shown in Fig. 5.3. The $\chi^2/ndf << 1$ indicates that the error estimated by the fit routine is not the true error of distribution. Rather, there is an overestimation of errors. In this particular case, where each measurement has different error (σ_i) and hence different weight ($w_i = \frac{1}{\sigma_i^2}$), the uncertainty is estimated as the weighted standard deviation

Luminosity $pellet^{-1}$	**1.45 GeV**		**1.5 GeV**		**Entire data (1.45+1.50) GeV**	
	BR_i	λ	BR_i	λ	BR_i	λ
(50−500)	8.26±0.13	0.29	8.43±0.80	-0.17	8.35±0.29	-0.14
(50−400)	8.26±0.13	0.29	8.40±0.58	-0.19	8.34±0.24	-0.14
(50−350)	8.26±0.13	0.29	8.36±0.04	-0.15	8.31±0.08	0.08
(50−300)	8.26±0.14	0.29	8.36±0.04	-0.15	8.31±0.08	0.08

Table 5.3.: The branching ratio values obtained in the systematical tests for luminosity are listed for three data sets. The corresponding systematical check variable λ is presented.

σ_w of the parameter p0 from the data points $X(i)$ [130].

$$\sigma_w = \sqrt{\frac{N \sum_{i=1}^{N} w_i \left(X(i) - p0\right)^2}{N-1 \sum_{i=1}^{N} w_i}}, \tag{5.7}$$

where N is the total number of measurements. The parameter p0 and the estimated uncertainty are listed in Table 5.3. Likewise, the branching fraction estimates for other luminosity ranges are tabulated in Table 5.3. It is observed that the branching ratio for 1.45 GeV is consistent in each luminosity range. Moreover, the uncertainties in 1.45 GeV data are similar for all luminosities. However, for 1.5 GeV the branching ratios and uncertainties are consistent for the lower and medium luminosities (50-350) $pellet^{-1}$. The deviation of the branching ratio from its final value and its error increases when higher luminosity bins (350-500) $pellet^{-1}$ are included. It should be noted here that the branching ratios for a full luminosity range (50-500) $pellet^{-1}$ are the same as that of the branching ratios listed in Table 5.2, however, using a different method. The branching ratios, within errors, are in agreement for both cases.

The systematic effect is studied using the first type of test, as explained in Equation 5.5. Clearly, none of the three data sets have λ value greater than 2, as shown in Table 5.3. This implies that the luminosity does not have any systematical deviation which is not taken care of by the statistical error.

5.2.3.2. Systematic Effect due to the Fitting Procedure

The branching fraction is obtained by dividing the two numbers extracted by fitting two missing mass distributions. The systematic effect, in the branching ratio, would get canceled if both distributions had similar phase spaces because the fits would also be comparable. However, the inclusive and exclusive missing mass distributions in the present data have different phase spaces. Consequently, their fits are different. This implies that the systematic effect due to the fitting procedure is not canceled, and accordingly it has been tested in the following.

The fit range and polynomial order are altered in order to study this effect. Only the converging fits from various combinations are considered. As an illustration, the extracted numbers N_{ω}^{rec} and $N_{\omega\to\pi^0\gamma}^{rec}$, and the branching ratio estimate $BR_{\omega\to\pi^0\gamma}^{measured}$ are plotted in Fig. 5.4 for different combinations in 1.45 GeV data. The corresponding distributions for 1.5 GeV beam energy and explicit values for both energies can be found in Appendix L.1 for reference.

The second type of systematic check is applicable in this case because the same data set is used for all tests. The results from the systematic check have been presented in Table 5.4. It

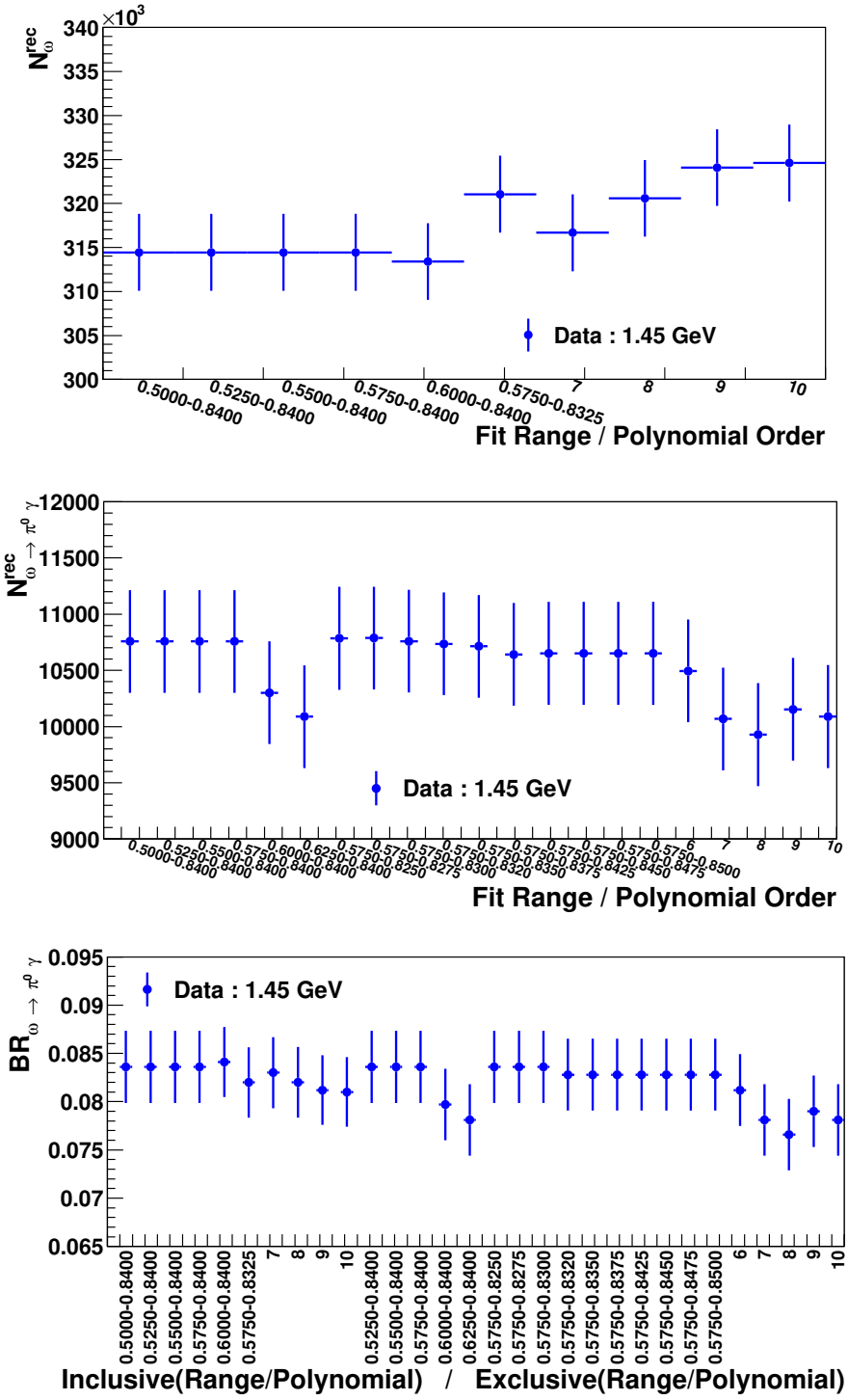

Figure 5.4.: The **top panel** represents the number of reconstructed ω mesons (N_ω^{rec}) and the **middle panel** is the number of reconstructed $\omega \rightarrow \pi^0\gamma$ events ($N_{\omega\rightarrow\pi^0\gamma}^{rec}$) for different combinations of fit ranges and polynomial orders in 1.45 GeV data. The left parts of both histograms represent the varied fit range for the fixed polynomial order, same as used for the final fits shown in Fig. 4.4. The vice-versa is represented by the right portion of both histograms. The branching fraction $BR_{\omega\rightarrow\pi^0\gamma}^{measured}$ for different combinations of the fit ranges and polynomial orders of the inclusive and exclusive missing mass is plotted in the **bottom panel** for 1.45 GeV data. The errors shown are statistical.

is clear from the table that $|\Delta B|$ is greater than 1 only for 1.45 GeV data. The systematical uncertainty, which is the difference of test value with respect to the final branching ratio value, is taken into account as

$$\sigma(1.45\ GeV)_{fit-sys} = {}^{+0.70}_{-0.05}. \tag{5.8}$$

$|\Delta B| < 1$ in the 1.5 GeV data set suggests that there is no systematic effect that arises due to background subtraction in this data. The error is propagated to estimate the systematic uncertainty in the combined data as

$$\sigma(1.45\ GeV + 1.50\ GeV)_{fit-sys} = {}^{+0.70}_{-0.05}. \tag{5.9}$$

5.2.3.3. Systematic Effect due to ^{3}He Identification

The systematic effect due to the ^{3}He identification is studied and presented in this section. Various selections considered for the cut optimization in Section 4.1.1 are used here. These graphical cuts are illustrated in Fig. 5.5. The name and description of various

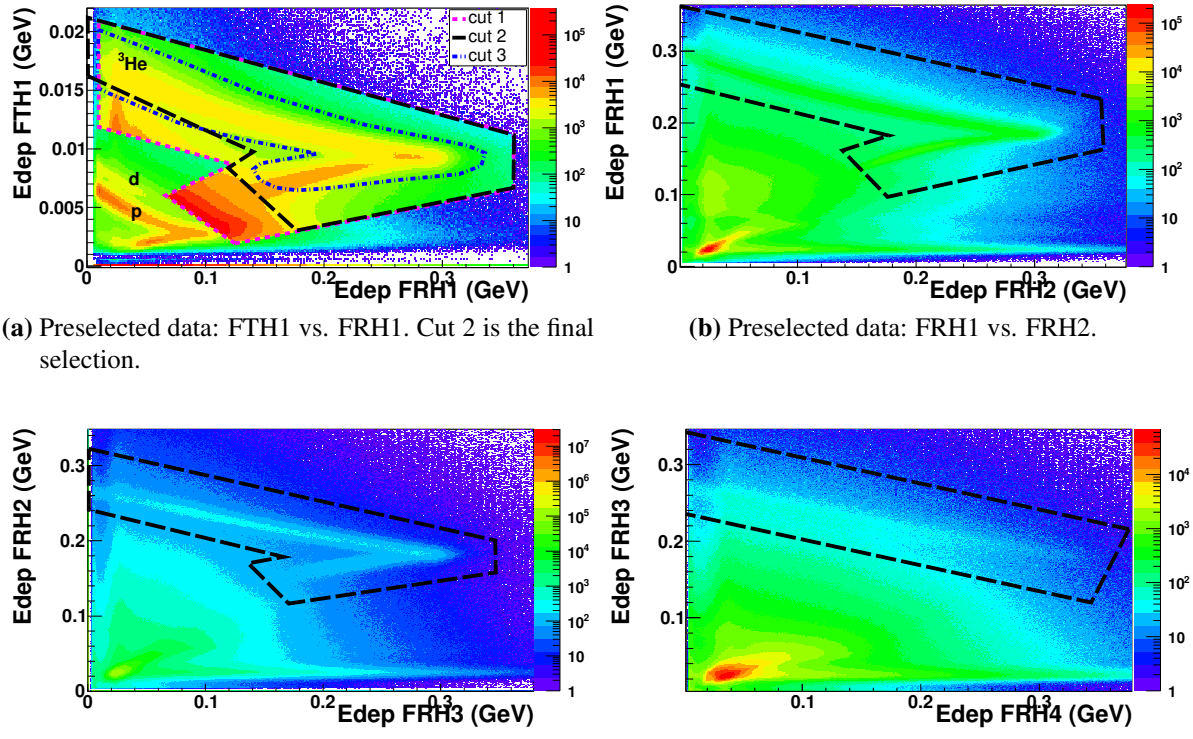

(a) Preselected data: FTH1 vs. FRH1. Cut 2 is the final selection.

(b) Preselected data: FRH1 vs. FRH2.

(c) Preselected data: FRH2 vs. FRH3.

(d) Preselected data: FRH3 vs. FRH4

Figure 5.5.: Particle identification (PID) plot for ^{3}He particles. The enclosures formed by the same types of lines are various conditions on the energy loss patterns used for the consistency check and cut optimization. 'Cut 2' on the FTH1 vs. FRH1 is the criterion used for final analysis.

cuts used are listed in Table 5.5. All aspects of the selection criterion are considered for this study, i.e., if the selection is too wide **'FTH1 vs FRH1 (Cut 1)'**, optimum **'FTH1 vs FRH1 (Cut 2)'** and too narrow **'FTH1 vs FRH1 (Cut 3)'**. Additionally, the Monte Carlo study indicates that most of the ^{3}He is stopped in the FRH2. However, very few ^{3}He acquire

Range/Pol	1.45 GeV		Range/Pol	1.5 GeV	
	$BR_f - BR_i$	ΔBR		$BR_f - BR_i$	ΔBR
(0.5000-0.8400)/6_{inc}	0.00	0.00	(0.5000-0.8550)/5_{inc}	0.00	0.00
(0.5250-0.8400)/6_{inc}	0.00	0.00	(0.5250-0.8550)/5_{inc}	0.00	0.00
(0.5500-0.8400)/6_{inc}	0.00	0.00	(0.5500-0.8550)/5_{inc}	0.00	0.00
(0.6000-0.8400)/6_{inc}	-0.05	-0.14	(0.6000-0.8550)/5_{inc}	0.00	0.00
(0.5750-0.8325)/6_{inc}	+0.16	+0.43	(0.6250-0.8550)/5_{inc}	+0.21	+0.62
(0.5750-0.8400)/7_{inc}	+0.06	+0.16	(0.6500-0.8550)/5_{inc}	+0.21	+0.62
(0.5750-0.8400)/8_{inc}	+0.16	+0.43	(0.5750-0.8450)/5_{inc}	+0.21	+0.62
(0.5750-0.8400)/9_{inc}	+0.24	+0.65	(0.5750-0.8475)/5_{inc}	+0.21	+0.62
(0.5750-0.8400)/10_{inc}	+0.26	+0.70	(0.5750-0.8500)/5_{inc}	+0.21	+0.62
(0.5000-0.8400)/5_{exc}	0.00	0.00	(0.5750-0.8525)/5_{inc}	+0.07	+0.21
(0.5250-0.8400)/5_{exc}	0.00	0.00	(0.5750-0.8575)/5_{inc}	+0.10	0.29
(0.5500-0.8400)/5_{exc}	0.00	0.00	(0.5750-0.8550)/6_{inc}	-0.08	-0.24
(0.6000-0.8400)/5_{exc}	+0.39	+1.05	(0.5750-0.8550)/7_{inc}	-0.13	-0.38
(0.6250-0.8400)/5_{exc}	+0.55	+1.49	(0.5750-0.8550)/8_{inc}	-0.10	-0.29
(0.5750-0.8250)/5_{exc}	0.00	0.00	(0.5750-0.8550)/9_{inc}	-0.13	-0.38
(0.5750-0.8275)/5_{exc}	0.00	0.00	(0.5750-0.8550)/10_{inc}	-0.05	-0.15
(0.5750-0.8300)/5_{exc}	0.00	0.00	(0.5000-0.8550)/4_{exc}	0.00	0.00
(0.5750-0.8325)/5_{exc}	+0.08	+0.22	(0.5250-0.8550)/4_{exc}	0.00	0.00
(0.5750-0.8350)/5_{exc}	+0.08	+0.22	(0.5500-0.8550)/4_{exc}	0.00	0.00
(0.5750-0.8375)/5_{exc}	+0.08	+0.22	(0.6000-0.8550)/4_{exc}	+0.08	+0.24
(0.5750-0.8425)/5_{exc}	+0.08	+0.22	(0.5750-0.8450)/4_{exc}	-0.23	-0.68
(0.5750-0.8450)/5_{exc}	+0.08	+0.22	(0.5750-0.8475)/4_{exc}	-0.16	-0.47
(0.5750-0.8475)/5_{exc}	+0.08	+0.22	(0.5750-0.8500)/4_{exc}	-0.08	-0.24
(0.5750-0.8500)/5_{exc}	+0.08	+0.22	(0.5750-0.8525)/4_{exc}	0.00	0.00
(0.5750-0.8400)/6_{exc}	+0.24	+0.65	(0.5750-0.8575)/4_{exc}	0.00	0.00
(0.5750-0.8400)/7_{exc}	+0.55	+1.46	(0.6000-0.8600)/4_{exc}	+0.08	+0.24
(0.5750-0.8400)/8_{exc}	+0.70	+1.89	(0.6000-0.8625)/4_{exc}	+0.15	+0.44
(0.5750-0.8400)/9_{exc}	+0.46	+1.24	(0.6000-0.8650)/4_{exc}	+0.15	+0.44
(0.5750-0.8400)/10_{exc}	+0.55	+1.49	(0.5750-0.8550)/6_{exc}	+0.08	+0.24
			(0.5750-0.8550)/7_{exc}	+0.31	+0.91
			(0.5750-0.8550)/8_{exc}	+0.31	+0.91
			(0.5750-0.8550)/9_{exc}	+0.31	+0.91
			(0.5750-0.8550)/10_{exc}	+0.22	+0.65

Table 5.4.: The systematical checks for the background subtraction using different combinations of fit range and polynomial orders are presented. The deviations of the test values from the final branching ratio value ($B_f - B_i$) and the estimates of the test variable ΔBR are shown. The tests for which ΔBR is greater than 1 are highlighted in red.

enough energy to reach FRH4 (see Appendix A.1 for illustration). As a result, another combination of graphical cut, named **'Combined'**, is included in this study. Wherein, the ^{3}He are forced to additionally pass the conditions on energy loss patterns of the subsequent FRH layers. These additional selection criteria are shown in Fig. 5.5. The ^{3}He structure, along with associated protons and deuterons and the minimum ionizing protons and deuterons, is seen coming from various scatterings and breakup reactions. Imposing additional conditions for each layer rejects ^{3}He that loses energy via scattering with a nucleus in the detector

	Cut Name	Cut Description
1.	**'Combined':** [FTH1 vs FRH1 (Cut 2)]+[FRH1 vs FRH2] +[FRH2 vs FRH3]+[FRH3 vs FRH4]	Events within the black enclosure in Fig. 5.5a must additionally pass the conditions indicated by the black enclosures in Fig. 5.5b, Fig. 5.5c and Fig. 5.5d
2.	Widest Selection window: **'FTH1 vs FRH1 (Cut 1)'**	Events within the magenta enclosure in Fig. 5.5a (equivalent to the preselection PID)
3.	Optimum Selection window: **'FTH1 vs FRH1 (Cut 2)'** Optimized selection, used for the final analysis	Events within the black enclosure in Fig. 5.5a
4.	Narrow Selection window: **'FTH1 vs FRH1 (Cut 3)'**	Events within the blue enclosure in Fig. 5.5a

Table 5.5.: The second column represents the name and the third column is the description of the different graphical cuts used for the cut optimization and systematic studies.

material in a further downstream layer.

The branching ratio estimates as a function of the ^{3}He PID cuts have been presented in Fig. 5.6 for three data sets. The efficiency of the cut increases from left to right on the x-axis. The missing mass spectra, efficiencies, the numbers, and the branching ratio estimate $BR^{measured}_{\omega\to\pi^0\gamma}$ for each cut can be found in Appendix M.

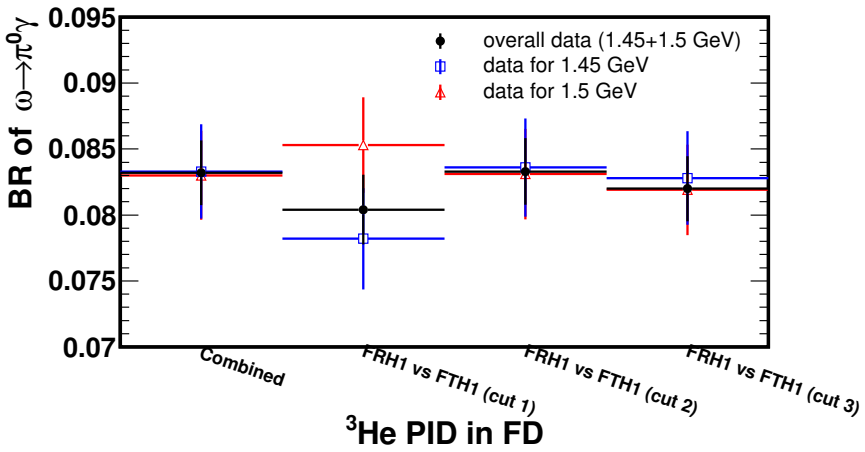

Figure 5.6.: An illustration of the systematic effect on the branching ratio measurement due to the ^{3}He particle identification (PID) method. The x-axis of distribution represents different ^{3}He PID cuts. Whereas, the y-axis corresponds to the branching ratio value for each cut. The blue, red and black points are the 1.45 GeV, 1.50 GeV and combined data set, respectively. The errors are propagated statistical errors.

The second type of check is performed to ascertain the uncertainty estimate present in the distributions. The ΔBR values (>1) for ^{3}He PID, as shown in Table 5.6, indicate that 1.45 GeV data have systematical deviation arising due to particle identification which has not been explained by the statistical uncertainty. This systematic effect is accounted as the

deviation of test value from the final branching ratio,

$$\sigma(1.45\ GeV)_{^3\mathrm{He\ pid}} = {}^{+0.55}_{0}. \tag{5.10}$$

However, no systematic effect has been observed in 1.5 GeV and combined data sets, which is arising because of ^{3}He identification.

	1.45 GeV		**1.50 GeV**		**Entire data (1.45+1.50) GeV**	
	$B_f - B_i$	ΔBR	$B_f - B_i$	ΔBR	$B_f - B_i$	ΔBR
^{3}He PID:						
1. Combined	+0.03	+0.08	+0.01	+0.03	+0.05	+0.20
2. FRH1 vs FTH1 (cut1)	+0.55	+1.53	-0.22	-0.65	+0.14	+0.56
3. FRH1 vs FTH1 (cut3)	+0.08	+0.22	+0.12	+0.35	+0.13	+0.52
$\lvert\delta P\rvert - \lvert\delta E\rvert$ test:						
1. $\lvert\delta E\rvert < 0.50; \lvert\delta P\rvert < 0.300$	-6.43	-17.38	-3.54	-10.41	-4.98	-19.92
2. $\lvert\delta E\rvert < 0.40; \lvert\delta P\rvert < 0.250$	-3.27	-8.84	-2.91	-8.56	-3.10	-12.40
3. $\lvert\delta E\rvert < 0.30; \lvert\delta P\rvert < 0.200$	-1.02	-2.76	-0.77	-2.27	-0.90	-3.60
4. $\lvert\delta E\rvert < 0.15; \lvert\delta P\rvert < 0.125$	+0.05	+0.14	-0.09	-0.27	-0.03	-0.12
5. $\lvert\delta E\rvert < 0.10; \lvert\delta P\rvert < 0.100$	+0.05	+0.14	+0.07	+0.21	+0.05	0.20
Mono. γ test:						
1. 0.10< E <0.52; 5< θ <100	-0.13	-0.35	+0.24	+0.71	+0.05	+0.20
2. 0.20< E <0.52; 5< θ <100	0.00	0.00	+0.09	+0.27	+0.04	+0.16
3. 0.20< E <0.52; 35< θ <60	-0.05	-0.14	+0.09	+0.27	+0.01	+0.25
4. 0.15< E <0.48; 20< θ <90	+0.16	+0.43	-0.02	-0.06	-0.04	-0.16
5. 0.20< E <0.45; 35< θ <75	-0.03	-0.08	+0.19	+0.56	+0.08	+0.32
6. 0.25< E <0.42; 37< θ <61	+0.03	+0.08	0.00	0.00	0.00	0.00
7. 0.22< E <0.40; 30< θ <80	+0.03	+0.08	+0.45	+1.32	+0.24	+0.96
8. 0.22< E <0.40; 35< θ <60	+0.21	+0.57	+0.16	+0.47	+0.19	0.76

Table 5.6.: The systematic checks for the ^{3}He identification, $|\delta P| - |\delta E|$ and monochromatic γ cuts. Different combinations of cuts are used as mentioned in the first column. The difference between the final branching ratio and the test values ($B_f - B_i$) and the estimates of the test variable ΔBR are presented. The tests for which ΔBR is greater than 1 are marked in red.

5.2.3.4. Systematic Effect due to $|\delta P| - \delta E$ cut

The energy-momentum ($|\delta P| - \delta E$) conservation constraint is one of the key conditions which plays an important role in selecting the $\omega \rightarrow \pi^0\gamma$ final state. The quantitative effect of the constraint is already seen in Fig. 4.2, where almost 3.91% of the signal events in 1.45 GeV data set and 4.24% in 1.50 GeV is rejected by this condition. The influence of this restriction on the result is presented in this section.

The systematic check is done by varying the $|\delta P| - \delta E$ constraints and fixing all the other analysis conditions to same as described in Section 4.2. The different constraints which are illustrated in Fig. 4.8 have been used for systematic study. The same constraints are used for cut optimization in Section 4.2.3.1. The constraints vary from a subset of the final cut to its superset, as shown in Fig. 4.8. The corresponding missing mass spectra, counts in the background-subtracted peak, efficiencies and the branching ratio $BR^{measured}_{\omega\rightarrow\pi^0\gamma}$ estimate

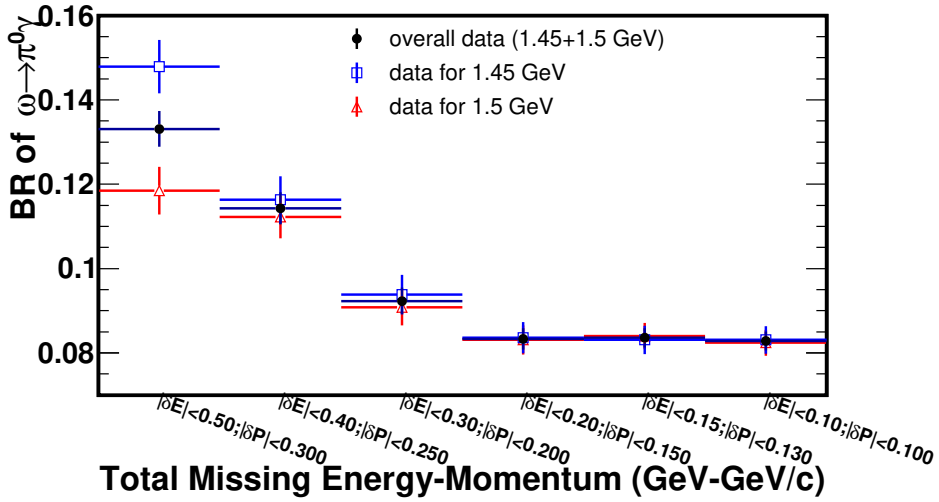

Figure 5.7.: The systematic effect on the measured branching ratio due to the energy-momentum constraint is illustrated for three data sets. Various energy-momentum conservation constraint is presented on the x-axis and the measured branching ratio with statistical errors for each constraint is shown on the y-axis. The blue, red and black markers are the points for the 1.45 GeV, 1.50 GeV, and combined data set, respectively.

have been presented in Appendix N. The $BR^{measured}_{\omega\to\pi^0\gamma}$ for various constraints are plotted in Fig. 5.7. The points are arranged from left to right in the decreasing order of efficiency.

It has been observed that the branching ratio below the absolute missing energy of 0.20 GeV is consistent within the error. However, a jump is observed for the cuts above 0.20 GeV missing energy. This is because the in-peak pion background from the decay $\omega \to \pi^+\pi^-\pi^0$ starts contributing above 0.20 GeV missing energy. Which is evident from Fig. 4.8. The jump, for the points above 0.40 GeV, is even higher on account of another in-peak contribution from the $\omega \to \pi^+\pi^-$ decay. This leads to an overestimation of the reconstructed number of $\omega \to \pi^0\gamma$ decays and henceforth, the branching ratio. Consequently, the inclusion of measurements above ($|\delta E| >$)0.20 GeV is responsible for the large systematic errors. Furthermore, in order to achieve an accurate error estimate after including the points with $|\delta E| >$0.20 GeV, the number of in-peak background decays must be subtracted from the ω peak. However, this will require the branching ratio of the $\omega \to \pi^0\gamma$ decay as an input parameter, which is an observable here. Consequently, to correctly estimate the systematic uncertainty, it would be justified to restrict the fit up to $|\delta E|$ = 0.20 GeV. The fourth point from the right in Fig. 4.8 is the cut used in the final analysis, i.e., $|\delta E| <$0.20 GeV;$|\delta P| <$0.150 GeV. This cut has been excluded from the systematic check. The second kind of systematic check has been performed. The results are listed in Table 5.6 for various tests. The ΔBR values for the most appropriate tests, which are $|\delta P| - |\delta E|$ **test** 4. and 5. in Table 5.6, are not greater than 1 ($\Delta BR \not> 1$). This indicates that the deviations of the test values from the final branching ratio have been taken care of by the statistical uncertainties. There is no systematic effect that arises due to energy momentum constraint.

5.2.3.5. Systematic Effect due to "Monochromatic γ" Criteria

The "monochromatic γ" selection criterion is another kinematic restriction that is influential in selecting a cleaner $\omega \to \pi^0\gamma$ final state, as discussed in Section 4.2.3. It is seen in

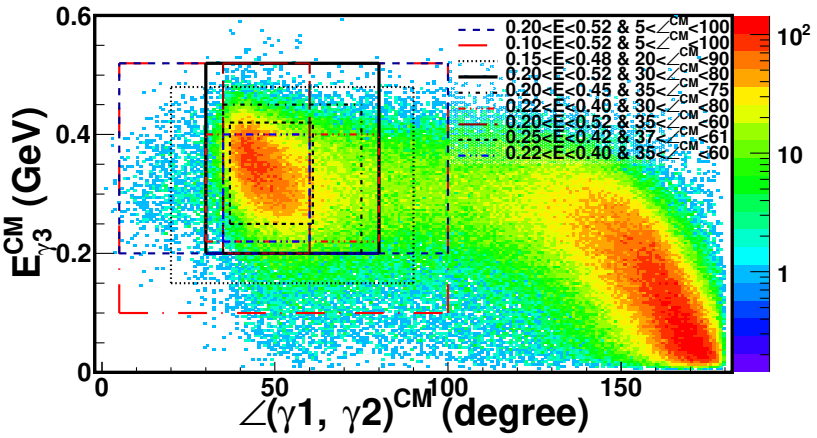

Figure 5.8.: Various combinations of the energy and angular windows used for the cut optimization and systematic studies are plotted on data distribution. The energy and angular ranges are the same as shown in Fig. 4.11. The final cut to select events for the correct $\pi^0\gamma$ combinations are shown as the solid black box.

Fig. 4.14 that the monochromatic constraint is proven to be an effective tool to separate the π^0 from other combinatorics. The investigation to explore the systematic effect is done by studying the number $N^{rec}_{\omega\rightarrow\pi^0\gamma}$ and branching ratio $BR^{measured}_{\omega\rightarrow\pi^0\gamma}$ for varied monochromatic γ selections. The conditions used for cut optimization in Section 4.2.3.2 are considered for this systematic study. The illustration and the description of different monochromatic cuts are given in Fig. 5.8. This exercise improved the present understanding of the result. The missing mass spectra, efficiencies, the number of reconstructed $\omega \rightarrow \pi^0\gamma$ decays, and the measured $BR^{measured}_{\omega\rightarrow\pi^0\gamma}$ for different monochromatic cuts have been presented in Appendix O. The estimated $BR^{measured}_{\omega\rightarrow\pi^0\gamma}$ for each cut is plotted in Fig. 5.9. The points in Fig. 5.9 are organized in decreasing order of efficiency from left to right.

The fluctuations seen in the branching ratio are not significant and measured values are in agreement within errors. Moreover, there is no dependency seen in the branching ratio. In order to quantify the systematic effect, the second type of systematic check has been performed. The results have been presented in Table 5.6 in the form of variable ΔBR. The ΔBR values for 1.45 GeV data and combined data suggest that there is no significant effect is seen due to the monochromatic γ criterion in these data sets. On the contrary, for 1.50 GeV data, a significant deviation in branching ratio is seen which cannot be explained with statistical uncertainty (as $\Delta BR > 1$). The systematical uncertainty is accounted for as the difference of test value with respect to the final value as

$$\sigma(1.50\ GeV)_{mono-sys} = {}^{+0.45}_{-0.02}. \tag{5.11}$$

5.2.4. Results

The systematic effects due to the luminosity effects, fitting procedure, and different analysis conditions have so far been explicitly discussed. The systematical uncertainties in different data sets are summarized in Table 5.7. The results from the systematical studies have shown that there is no effect seen due to luminosity which changes the branching ratio values beyond what cannot be explained by the statistical uncertainties. It is observed that the background subtraction procedure introduces an effect greater than one standard deviation

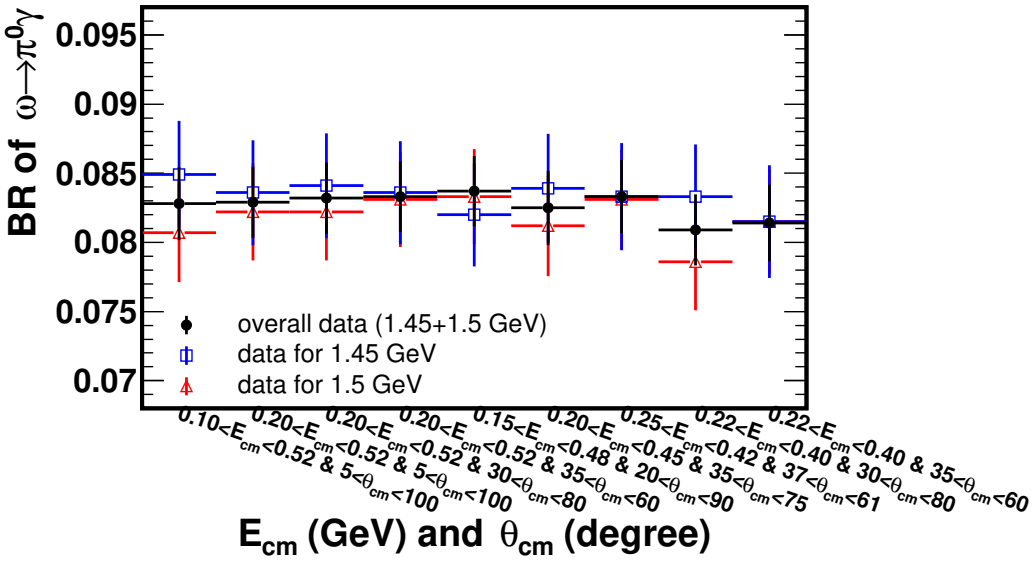

Figure 5.9.: The systematic effect on the branching ratio due to the monochromatic γ criterion is demonstrated in this distribution. The monochromatic γ cuts and the corresponding branching ratios are the x-axis and the y-axis of the distribution, respectively. The propagated statistical errors are shown. The blue, red and black markers are the points for 1.45 GeV, 1.50 GeV and combined data set, respectively. The final value BR_f is plotted on the fourth bin named 0.2< E_{cm} <0.52&30< θ_{cm} <80, which is the final cut used.

	1.45 GeV		**1.5 GeV**		**(1.45+1.5) GeV**	
	σ_{BR}	ΔBR	σ_{BR}	ΔBR	σ_{BR}	ΔBR
luminosity	-	-	-	-	-	-
$fit-sys$	$^{+0.70}_{-0.05}$	$^{+1.89}_{-0.14}$	-	-	$^{+0.70}_{-0.05}$	$^{+1.89}_{-0.14}$
^{3}He pid	$^{+0.55}_{0}$	$^{+1.53}_{0}$	-	-	-	-
$\lvert\delta P\rvert-\delta E$	-	-	-	-	-	-
mono−γ	-	-	$^{+0.45}_{-0.02}$	$^{+1.32}_{-0.06}$	-	-

Table 5.7.: The systematical uncertainties in the $BR^{measured}_{\omega\to\pi^0\gamma}$ are presented for three data sets.

in 1.45 GeV and combined data sets. However, 1.5 GeV data have no significant systematic effect due to the background subtraction procedure. In addition, 1.45 GeV data have a considerable systematic effect that arises due to ^{3}He PID condition. Which has not been observed in 1.5 GeV and combined data sets. Moreover, a significant systematic effect that arises due to the monochromatic γ selection criterion is observed in the 1.50 GeV data. Conversely, for 1.45 GeV and combined data, this effect is not seen. The final values of the branching ratio with statistical and systematical uncertainties are given as,

$$\begin{aligned} BR^{measured}_{\omega\to\pi^0\gamma}(1.45\ GeV) &= 8.36(\pm 0.37 stat)^{(+0.70)}_{(-0.05)} fit-sys^{(+0.55)}_{(0)}{}^3\text{He pid}\%, \\ BR^{measured}_{\omega\to\pi^0\gamma}(1.50\ GeV) &= 8.31(\pm 0.34 stat)\pm^{(+0.45)}_{(-0.02)} mon-sys\%, \\ BR^{measured}_{\omega\to\pi^0\gamma} &= 8.33(\pm 0.25 stat)^{(+0.70)}_{(-0.05)} fit-sys\%. \end{aligned} \tag{5.12}$$

The results obtained are consistent within errors in three data sets. Furthermore, the evaluated branching ratios for the entire data set are in agreement with the particle data group

value $(8.40 \pm 0.22)\%$. However, the branching ratio value has significant systematic uncertainty.

5.3. Analysis of the Missing Mass of ^{3}He after $\omega \to e^+e^-\pi^0$ Final State Selection: Exclusive

It is expected from Section 4.3 that a total of (16±4) events should be found in 1.45 GeV, (16±4) in 1.50 GeV and (32±6) in the entire data set. The expectations are a few orders less than what is seen in the data peaks. This is due to the contributions from other decays of the ω meson. The in-peak background contributions, as discussed in Section 4.3, must be subtracted from the data peak. Correspondingly, the data peak has been explained with a superposition of the Monte Carlo simulations using the branching ratios. The superposition plot of the signal and all background ω decays is plotted in Fig. 4.27. The area under the sum histogram within the mass range of 0.740 GeV/c^2 − 0.816 GeV/c^2 is in agreement with the area under the data peak. 98% area of the superposition histogram is the contribution from the $\omega \to \pi^+\pi^-\pi^0$ decay. The number of $\omega \to e^+e^-\pi^0$ candidates are estimated to be (39±235) and (32±220) for 1.45 GeV and 1.50 GeV, respectively. The difference in the estimated numbers for the two energies is due to the different continuous background shapes and the different efficiencies for the two energies. The total number of reconstructed Dalitz decay candidates is (71±322) in the entire data set. The numbers for all cases are tabulated in Table 5.8. Furthermore, these (71±322) events are extracted and cross-validated from the superposition histogram of the e^+e^- invariant mass distributions, as shown in Fig. 4.28.

	1.45 GeV	**1.50 GeV**	**Entire data set**
$\omega \to e^+e^-\pi^0$ *expected*	(16±4)	(16±4)	(32±6)
$\omega \to e^+e^-\pi^0$ *reconstructed*	(39±235)	(32±220)	(71±322)

Table 5.8.: The number of the $\omega \to e^+e^-\pi^0$ events expected and reconstructed from the superposition histogram, as shown in Fig. 4.27, are shown for three data sets.

The reconstructed $\omega \to e^+e^-\pi^0$ decays (71±322) are almost two times of the events expected (32±6). Firstly, this indicates that despite using particle identification, the extracted event sample still has at least 50% background contribution from the decay $\omega \to \pi^+\pi^-\pi^0$. Which could not be eliminated at this point with the current approach. The second reason for this discrepancy might be that the Monte Carlo simulation is not able to give an accurate background estimate. This implies that a different physics model might be useful.

Nevertheless, the persisting discrepancy is covered under the large errors in the yield. Within errors, the reconstructed and the expected yield show an agreement. However, the large error indicates that in principle 0 signal could be found in the data. Considering no signal is found in the data, it is infeasible to determine the transition form factor in the existing $pd \to {}^3$He ω data set with the current approach.

In order to obtain a reasonable form factor distribution with the *pd* collision, the statistical power must be improved either by increasing the signal statistics and/or by reducing the background, mainly the in-peak contributions. Increasing the signal yield could only be possible if the time of the run is increased, as the current reconstruction efficiency, luminosity, and the cross section are already at the limits (see their relation in Equation 4.5). However, firstly, any such possibility has been ruled out as WASA-at-COSY is no longer functional, and secondly, it was unreasonable to run the experiment for so long when another

alternative approach that has a comparably larger cross section is available with the pp collision. Correspondingly, the test beam time data for the pp collision had already been acquired for the feasibility test. The only way to attempt a reasonable form factor distribution with the existing pd data is to reduce the contribution from the $\omega \to \pi^+\pi^-\pi^0$ decay to nearly 0. Such that the error is substantially suppressed and comes closer to zero. The background situation is expected to improve by using a kinematic fit procedure for the $\omega \to e^+e^-\pi^0$ decay hypothesis, and other machine learning and deep learning approach, such as the neural network, decision tree, random forest, support vector machine, genetic algorithm, etc.

6. Conclusions and Outlook

The branching ratio of the $\omega \to \pi^0\gamma$ decay has been measured in the *pd* data set. The results are listed in Table 6.1. The branching ratio $BR^{measured}_{\omega\to\pi^0\gamma}$ measured in the overall data is

$$BR^{measured}_{\omega\to\pi^0\gamma} = 8.33(\pm 0.25)\text{stat}^{(+0.70)}_{(-0.05)}\text{sys}\%; \tag{6.1}$$

The branching ratios measured in three data sets are in agreement within errors with the PDG value $(8.40 \pm 0.22)\%$ [39]. However, it has significant systematic uncertainty. It has also been realized that using two different beam energies is helpful to have insights about the systematic effects arising due to the background subtraction method. Furthermore, it is recommended that the branching ratios relative to one of the prominent ω decays, such as $\omega \to \pi^+\pi^-\pi^0$, are determined in a manner where explicit exclusive yield is possible. For relative branching ratios, numbers obtained from the inclusive missing mass are not required and that results in more precise measurement. However, the analysis of the most prominent ω decay $\omega \to \pi^+\pi^-\pi^0$ had been the subject of a different thesis [110]. The current result is an indication that the procedure to extract the signal for $\pi^0\gamma$ as one of the reference decay for $\omega \to e^+e^-\pi^0$ is well established.

$BR^{measured}_{\omega\to\pi^0\gamma}(\%)$		
1.45 GeV	**1.50 GeV**	**combined data**
$8.36(\pm 0.37)\text{stat}^{(+0.70)\text{sys}(+0.55)\text{ sys}}_{(-0.05)\text{fit }(0)^3\text{He pid}}$	$8.31(\pm 0.34)\text{stat}^{(+0.45)\text{sys}}_{(-0.02)\text{mono}}$	$8.33(\pm 0.25)\text{stat}^{(+0.70)\text{sys}}_{(-0.05)\text{fit}}$

Table 6.1.: The final values of the branching ratio of the $\omega \to \pi^0\gamma$ decay mode for three data sets.

Concurrently, a total of (39±235) events of the $\omega \to e^+e^-\pi^0$ decay is reconstructed in 1.45 GeV data, and (32±220) in 1.5 GeV data. The extracted (71±322) events in the entire data set turn out to be almost double the yield expected from the inclusive final state. The event sample at this stage has impurities from the in-peak $\omega \to \pi^+\pi^-\pi^0$ contributions. Considering the large errors, the estimated numbers are in agreement with the expectations. Although, the reconstructed events are equivalent to zero as large errors outsize the statistics.

In a nutshell, the feasibility study of the $\omega - \pi$ transition form factor with the WASA-at-COSY *pd* collision data has been conducted successfully. Conclusively, a high precision measurement of the transition form factor could not be obtained with the existing $pd \to {}^3He\,\omega$ data set and current analysis approach. This is because, firstly, there are not enough signal events present in the data, and secondly, the large errors are leading the effective signal yield close to '0'. The large error bars are the consequence of the subtraction of a huge amount of background events. The majority of background consists of pions in the final state. As the inseparable pions fall under the graphical cut and kinematic constraints and survived till the end. These events, in combination with the cross section and branching ratios, become significant.

Simultaneously, a successful establishment of the branching fraction for the $\omega \to \pi^0\gamma$ decay and its agreement with the world average is an indication that the WASA apparatus with

its simulation and analysis techniques are on the right track. The $\omega - \pi$ transition form factor is not feasible only due to the lack of statistics obtained in the current experiment. There is no issue with the WASA-at-COSY apparatus or its technique, if this experiment would have been run for the sufficient time it might have detected a significant signal with the existing analysis methods.

However, in order to achieve a reasonable form factor distribution from the existing *pd* data set, the background contributions having pions in the final state must be reduced. Specifically, the contribution from the $\omega \to \pi^+\pi^-\pi^0$ decay has to be suppressed close to 0. Which is not attainable with the current analysis approach. Presumably, the background situation and the signal purity are expected to improve by implying the alternative approaches based on machine learning methods or using the kinematic fitting procedure for the analysis chain or using both. However, the extent of improvement by these alternatives is limited. Nevertheless, exploration of these methods could be the potential outlook for this study.

Alternatively, the data for a test beam time using the $pp \to pp\omega$ reaction, where the cross section is comparably larger, had already been collected. Which could be a promising substitute to improve the statistical significance. An exploration of pp test beam data is another potential outlook for this study.

Appendix

A. $\Delta E - \Delta E$ Distributions of the Monte Carlo Simulations of the Backgrounds

Fig. A.1 shows the $\Delta E - \Delta E$ distributions of the Monte Carlo simulations of the signal and backgrounds for the energy loss pattern in various layers of the Forward Detector. The distributions are shown in support of the cut optimization discussed in Section 4.1.1. Evidently, a few ^{3}He particles from the ω production acquire enough energy and reach the FRH4. While a large number of the ^{3}He particles from the direct $\pi^0\pi^0$ production are stopped in the FRH4. Moreover, a significant number of the ^{3}He particles from the direct $\pi^0\pi^0\pi^0$ production are able to reach the FRH4. Graphical cuts used in Fig 5.5 for cut optimization are illustrated in Fig. A.1. The graphical cut selects almost all the ^{3}He particles from the ω production.

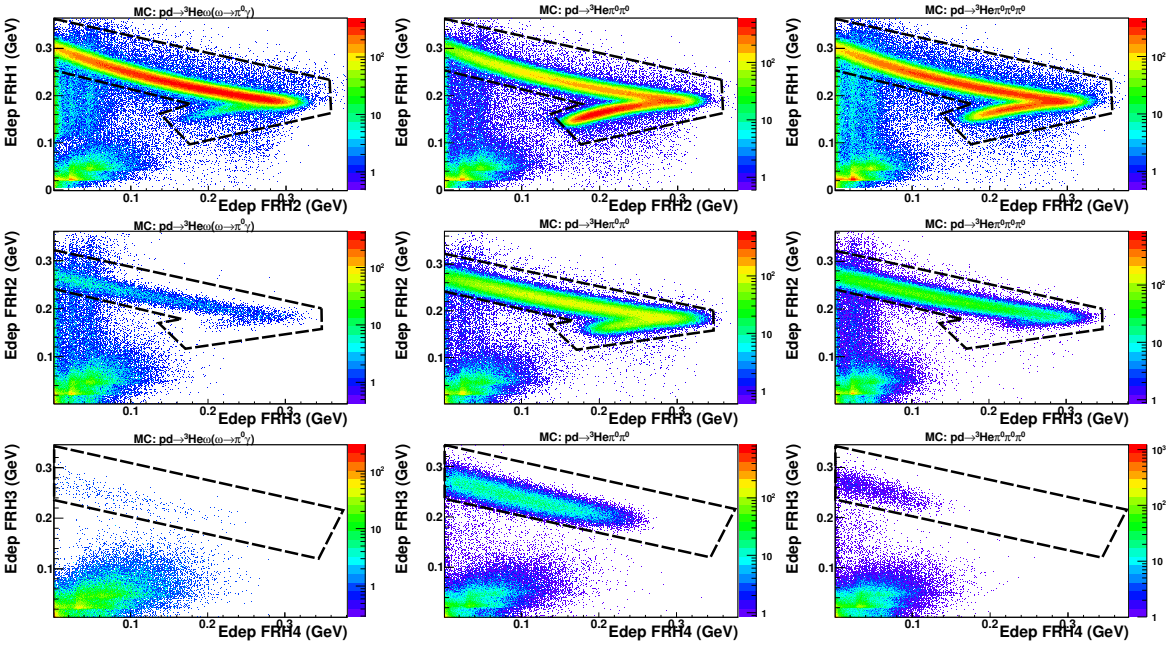

Figure A.1.: The particle identification plots for ^{3}He particles for the Monte Carlo simulations of the signal and background reactions. The first, second and third rows are the respective FRH1 vs. FRH2, FRH2 vs. FRH3 and FRH3 vs. FRH4 distributions. The left, middle and right columns are the Monte Carlo simulations of the $\omega \to \pi^0\gamma$ decay, direct $\pi^0\pi^0$ and direct $\pi^0\pi^0\pi^0$ productions, respectively.

The $\Delta E - E$ plot for the multi pion background production $\pi^0\pi^0$ and $\pi^0\pi^0\pi^0$, as shown in Fig. A.2, has been compared with the signal shown in Fig. 4.1a. Evidently, the graphical cut used to select ^{3}He is differently influencing the two background phase spaces. A consequence of this influence is seen in the background line shape of the ^{3}He missing mass spectra of data, as seen in Fig. 4.1c. Which is more explicitly visible in the individual phase spaces for the direct multi-pion production presented in Fig. A.3. This is because no physics spe-

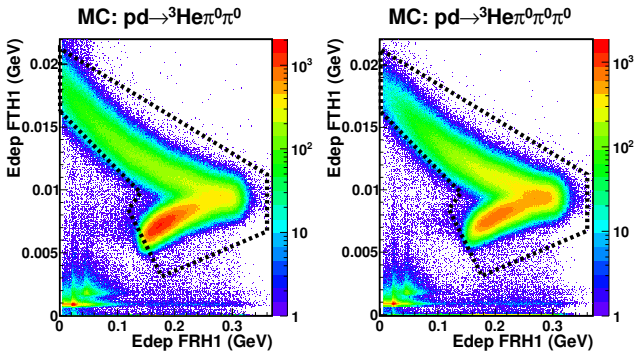

Figure A.2.: The energy deposited in the forward range hodoscope (FRH1) is shown as a function of energy deposited in the forward trigger hodoscope (FTH1). The left panel is the Monte Carlo simulation for the $pd \rightarrow {}^3\mathrm{He}\,\pi^0\pi^0$ reaction and the right panel is the Monte Carlo simulation for $pd \rightarrow {}^3\mathrm{He}\,\pi^0\pi^0\pi^0$ reaction. The effect of the ^{3}He identification cut, which is chosen using the signal distribution, can be seen as the black dashed lines.

cific process and interactions are implemented in PLUTO to simulate the multi pion phase space.

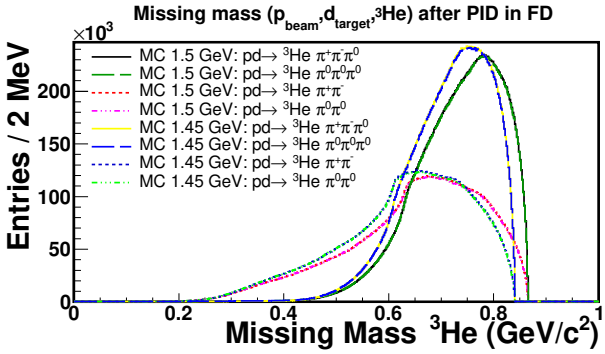

Figure A.3.: The effect of ^{3}He identification cuts on the missing mass phase space of the multi pion productions is illustrated. The black, dark green, red and magenta histograms are the Monte Carlo simulation for the $pd \rightarrow {}^3\mathrm{He}\,\pi^+\pi^-\pi^0$, $pd \rightarrow {}^3\mathrm{He}\,\pi^0\pi^0\pi^0$, $pd \rightarrow {}^3\mathrm{He}\,\pi^+\pi^-$ and $pd \rightarrow {}^3\mathrm{He}\,\pi^0\pi^0$ reactions, respectively, for 1.50 GeV beam energy. Similarly, the Monte Carlo simulations of the same reactions using 1.45 GeV are plotted as the yellow, blue, dark blue and bright green histograms, respectively.

The phase spaces of the double and triple pion productions, as shown in Fig. A.3, explain the line shape of the data in Fig. 4.1c. This justifies that the use of a combined phase space of the double and triple pion production is more accurate for fitting. Therefore, Equation 4.4 is a better representation of the fitting function than folding one of multi-pion phase space with a polynomial.

It can be seen in Fig. A.3 that the maxima of the background phase space in 1.45 GeV fall at the ω meson mass (0.7827±0.0001) GeV/c^2. However, the position of ω meson peak lies on the left edge of the 1.50 GeV multi pion phase space.

Regardless of simulating an equal number of events, the phase spaces of 1.45 GeV turned out to be higher in amplitude as compared to 1.50 GeV. Which further illustrates the fact that the multi pion production cross section is comparably larger in 1.45 GeV as compared to 1.50 GeV (see Table C.1).

B. Cut Optimization

B.1. $\Delta E - \Delta E$ Cut for ^{3}He Selection

The graphical cut to select ^{3}He particles, as discussed in Section 4.1.1, is optimized by selecting the best cut window out of the various selection choices. The name and description of various cuts used are listed in Table 5.5, while their illustration is shown in Fig. 5.5. The fitted spectra are presented in Appendix M.1. The efficiencies and the reconstructed numbers for each cut are listed in Table M.1. The estimated statistical significance and the overall reconstruction efficiency (ε) of the signal are plotted in Fig. B.1 for two energies. The optimized cut has a statistical significance value of 61 and 66 for 1.45 GeV and 1.50 GeV, respectively, as indicated in Fig. 4.1a. The reconstruction efficiency ε_{inc} corresponding to the optimum cut is 84.65% for 1.45 GeV and 86.71% for 1.50 GeV beam energy.

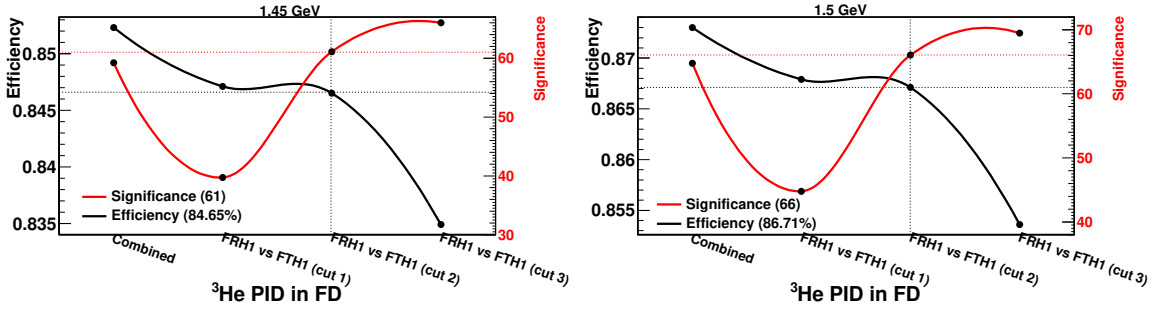

Figure B.1.: The Monte Carlo efficiency (black) and the statistical significance (red) of various particle identification conditions are plotted in the left and right columns for 1.45 GeV and 1.50 GeV, respectively. 'Cut 2' on the FTH1 vs. FRH1 is the criterion used for the final analysis.

B.2. $\delta E - \delta P$ Cut for the $\omega \to \pi^0\gamma$ Decay

Cut optimization plot, as discussed in Section 4.2.3.1 for 1.5 GeV, is shown in Fig. B.2 for 1.45 GeV beam energy. The final selection is indicated by the dashed lines. The optimal value of the quantity $\varepsilon.\pi$ is $0.3642 \times 0.0228 = 0.0083$. The obtained statistical significance of the selection is 15.

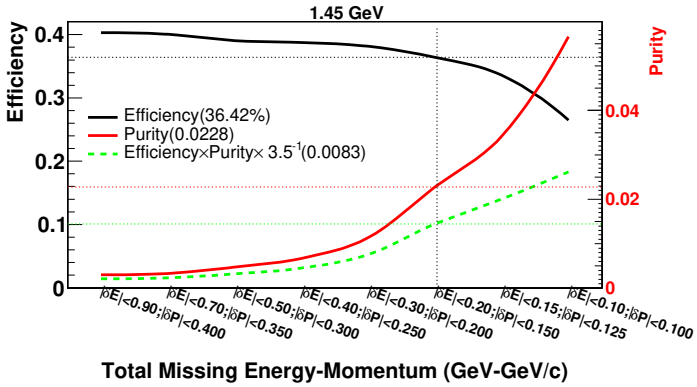

Figure B.2.: The efficiency (ε), purity (π) and the purity×efficiency (ε × π) as a function of the different δE-δP selection criteria for 1.45 GeV beam energy are shown. The black, red and green distributions represent the ε, π and ε × π, respectively. The final selection is indicated by the straight dashed lines. The variable values are listed in the legend.

B.3. Monochromatic γ Selection Cut for the $\omega \to \pi^0\gamma$ Decay

Plots to support the "cut optimization"for monochromatic γ selection discussed in Section 4.2.3.2 are presented in Fig. B.3. The efficiency and signal phase space along with the statistical significance, for various combinations of the energy and angular constraints shown in Fig. 5.8, are presented. The resulting Monte Carlo efficiencies, PLUTO phase space, and

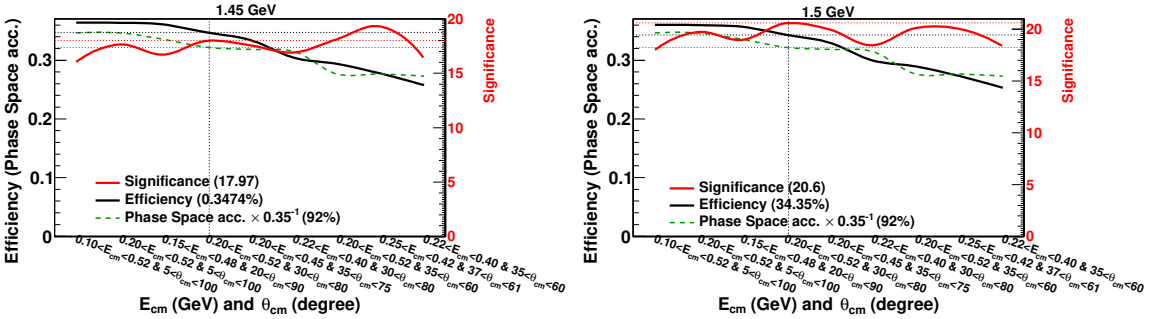

Figure B.3.: The resulting phase space acceptance, efficiency and statistical significance, for different combinations of the energy and angular windows, as shown in Fig. 5.8, are plotted for two energies. An optimum cut is chosen, shown as dashed straight lines.

statistical significance are plotted in Fig. B.3. Which shows that 1.45 GeV data has the maximum significance for the energy and angular values closer to the maximum of distribution in Fig. 4.11a. Since the maximum significance is reached at the cost of reconstruction efficiency and phase space, the selection of events very close to the maximum of energy and angular distributions is avoided. Thus, an optimal selection of 0.20 GeV$<E_{\gamma 3}^{CM}<$0.52 GeV and $30^\circ < \angle(\gamma 1,\gamma 2)^{CM} < 80^\circ$ is used instead. Furthermore, the maximum significance for 1.50 GeV is reached by using the optimal selection similar to that of 1.45 GeV, as shown in Fig. B.3. The significance of the narrow selection (right bump) in 1.45 GeV is larger than optimal selection (middle bump). Whereas, in 1.50 GeV it is slightly lower than optimal selection. The change in significance is due to the difference in the center of mass energy of the systems, at the two energies. This further leads to a different angular and energy distribution of photons in direct pion productions at two energies. Consequently, a relatively

larger amount of background events is rejected towards narrower selection in 1.45 GeV, as compared to 1.50 GeV. The achieved statistical significances for the optimal selection are 17.97 and 20.60 for 1.45 GeV and 1.50 GeV, respectively. The overall reconstruction efficiencies, for 1.45 GeV and 1.50 GeV beam energies, are 34.74% and 34.35% respectively. While the phase space acceptance is 92% in both cases.

B.4. e^+e^- Identification Cut for the $\omega \to e^+e^-\pi^0$ Decay

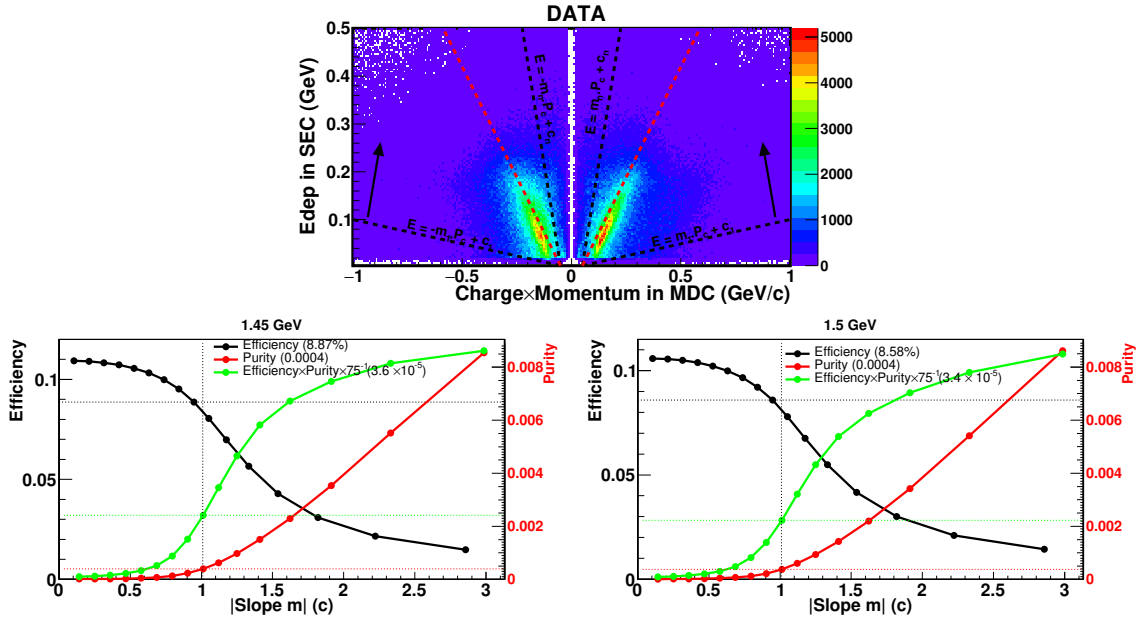

Figure B.4.: The top panel is the $\Delta E - P$ plot of the energy deposit in the SEC (Edep_{SE}) versus charged momentum [Charged×Momentum] (P_{MDC}) reconstructed in the MDC for data. The linear relation between Edep_{SE} and P_{MDC}, used to separate the $e^{\pm}$ from the $\pi^{\pm}$, are shown as black distribution for slopes m_1 and m_n. Where m_1.....m_n are various slopes considered for the study. The conditions are varied in the direction of the arrow, by varying the slopes from m_1 to m_n. The bottom row represents the distributions of the quantities: efficiency (solid black), purity (solid red), and efficiency×purity (solid green), for various slope parameters. The optimal quantities for the chosen condition, as indicated by dashed lines, are listed in legends. The events above the red lines (optimal selection) on $\Delta E - P$ plots are identified as electrons.

The optimization of the particle identification (PID) cut, as discussed in Section 4.3.2, is presented here. The PID plot to separate the electrons from the pions is shown in Fig. B.4. The deposited energy in the electromagnetic scintillating calorimeter (Edep_{SE}) as a function of the signed momentum (Charge×Momentum) (P_{MDC}) in the mini drift chamber is plotted in the top panel of Fig. B.4. A graphical correlation between energy Edep_{SE} and momentum P_{MDC}: Edep_{SE}=m.P_{MDC}+c, is used to separate electrons from pions. Where c is the energy Edep_{SE} intercept and m is the slope - a quantity that defines graphical correlation. The correlation is optimized by studying the efficiency, purity and efficiency×purity ($\varepsilon \times \pi$) for different |m| values in [$|\text{m}_1|$.....$|\text{m}_n|$]. Fig. B.4 shows that the sample with a high $\varepsilon \times \pi$ value is obtained at larger slopes, i.e., nearly vertical lines, where almost all the electrons are outside the selection. This is reflected in the efficiency of selection which is close to

zero at large slopes. Compensation between two quantities is made and an optimum correlation is considered as indicated by dashed lines. This optimum correlation selects most of the electron and rejects as many pions as possible. The optimum selection Edep_{SE}=0.94.P_{MDC}+c has an efficiency of 8.87% and 8.58% for 1.45 GeV and 1.50 GeV, respectively. The signal purity of the selected data sample is 0.04% at both energies.

B.5. $\delta E - \delta P$ Cut for the $\omega \to e^+e^-\pi^0$ Decay

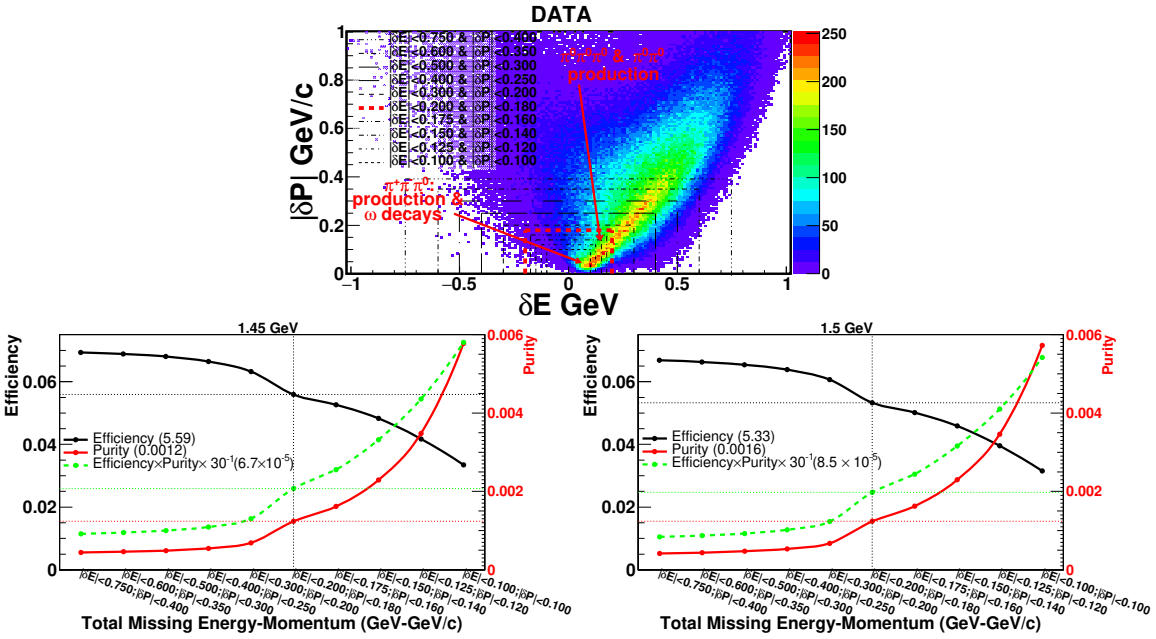

Figure B.5.: Top panel is the overall missing momentum (δP) against the overall missing energy (δE) of the ^{3}He particle and $\gamma\gamma e^+e^-$ system for data. Various energy-momentum conservation constraints chosen for "cut optimization " are shown with the same types of lines. The efficiency (black), purity (red) and efficiency×purity (green) for different cuts are shown in the bottom row. The optimal cut, considered in this analysis, is indicated by straight (dashed) lines. The values are listed in legends. The area enclosed by the red rectangle in data is the optimal cut to select events as $\omega \to e^+e^-\pi^0$ decay.

The event selection is refined by using an additional constraint over the energy and momentum balance. The restriction on energy and momentum, as discussed in Section 4.3.3.3, is optimized by studying the efficiency, purity and quantity efficiency×purity for different cuts. The "cut optimization" plots, in Fig. B.5, shows that the maximum value for the quantity efficiency×purity is obtained from the window closer to (0,0). The efficiencies for these selections are reduced tremendously, i.e., close to 0. Compensation between two quantities is made and an optimal selection shown as dashed straight lines is considered. The combination of $-0.2\ GeV \geq \delta E \leq 0.2\ GeV$ and $|\delta P| \leq 0.18\ GeV/c$ is the optimal selection window. The efficiencies of this selection are 5.59% and 5.33% for 1.45 GeV and 1.50 GeV, respectively. An improvement in purity is achieved for both energies - from 0.05% to 0.12% and 0.13% for 1.45 GeV and 1.50 GeV, respectively.

C. Production Cross Sections and Branching Fractions of the Signal and Backgrounds

The production cross sections and the branching fractions employed to estimate the weighting factors **w** listed in Table 4.3 are shown in Table C.1. These value have been used in the superposition fit in Section 4.3.4.1 and Section 4.3.4.2 to estimate the number of the $\omega \to e^+e^-\pi^0$ decay in data.

Decay Branching Ratio (BR [39])	**Reaction Cross Section (σ) at 1.45 GeV**
$pd \to {}^3$**He** ω $BR_{\omega\to\pi^+\pi^-\pi^0}$=(89.3±0.6)% $BR_{\omega\to\pi^0\gamma}$=(8.40±0.22)% $BR_{\omega\to\pi^+\pi^-}$=(1.53±0.06)% $BR_{\omega\to\pi^0e^+e^-}$=(7.7±0.6)×$10^{-4}$ $BR_{\omega\to\eta\gamma}$=(4.5±0.4)×10^{-4}	(83.6±1.5±2.27) nb [90]
$pd \to {}^3$**He** $\pi^+\pi^-\pi^0$	(910±7±80) nb [99]
$pd \to {}^3$**He** $\pi^0\pi^0\pi^0$	(115±3±23) nb [99]
$pd \to {}^3$**He** $\pi^+\pi^-$	Unknown extrapolated to 10μb from [101, 102, 103]
$pd \to {}^3$**He** $\pi^0\pi^0$	(207±3±8) nb [100]
$pd \to {}^3$**He** ρ $BR_{\rho\to\pi^+\pi^-}$≈100%	Unknown extrapolated to 60 nb from ω cross section
$pd \to {}^3$**He** η $BR_{\eta\to\gamma\gamma}$=(39.41±0.20)% $BR_{\eta\to\pi^+\pi^-\pi^0}$=(22.92±0.28)% $BR_{\eta\to\gamma\pi^+\pi^-}$=(4.22±0.08)%	(80.8±3.6±43.1) nb [99]
$pd \to {}^3$**He** π^0 $BR_{\pi^0\to\gamma\gamma}$=(98.823±0.034)%	0.50 nb extrapolated from [101, 104]

Table C.1.: Cross section table for the $pd \to {}^3$He X reactions. The branching fractions for the relevant decays are given.

D. Kinematics of the $\omega \rightarrow \pi^0\gamma$ Decay and it's Monochromatic γ Property

This section presents a detailed description of the kinematics of the $\omega \rightarrow \pi^0\gamma$ decays and monochromatic γ, as discussed in Section 4.2.3.2.

In the ω-rest system (CM), π^0 and γ will decay back to back and will have equal and opposite 3-momenta, as shown in the top left panel of Fig. D.1. The single γ, specified by the subscript 'm' γ_m, will be monochromatic in the rest frame of the ω meson, with energy

$$P^{CM}_{\gamma_m} = E^{CM}_{\gamma_m} = \left[\left(m^2_{\omega} - m^2_{\pi^0}\right) / \left(2 \times m_{\omega}\right)\right] = 0.38\ GeV. \tag{D.1}$$

Whereas, the energy and momentum of π^0,

$$\begin{aligned} E^{CM}_{\pi^0} &= \left[\left(m^2_{\omega} + m^2_{\pi^0}\right) / \left(2 \times m_{\omega}\right)\right] = 0.40\ GeV, \\ P^{CM}_{\pi^0} &= \left[\left(m^2_{\omega} - m^2_{\pi^0}\right) / \left(2 \times m_{\omega}\right)\right] = 0.38\ GeV, \end{aligned} \tag{D.2}$$

are distributed among the two photons decaying from the π^0 meson.

In the center of mass system of the π^0 meson (CM_{π^0}), as shown in the top right panel of Fig. D.1, the energy and momenta of the secondary photons are unique and depend only on the mass of the π^0 meson, i.e., $E^*_{\gamma_1} = P^*_{\gamma_1} = E^*_{\gamma_2} = P^*_{\gamma_2} = m_{\pi^0}/2$. The π^0 meson in the center of mass frame of the ω meson acquire a velocity, defined by its energy and momentum. Due to the motion of the π^0 meson in the CM system, the energies and angles of the secondary photons will have some distribution in the CM system. As they are emitted over a range of angles in the CM_{π^0} system, the energy and momentum of the secondary photons in the CM system depend on the CM_{π^0} system decay angle relative to the direction of motion of the parent π^0 meson. The energy and momentum of the secondary photons can be transformed from the CM_{π^0} system to the CM system in terms of the decay angles as

$$\begin{aligned} E_{\gamma_1} &= b(E^*_{\gamma_1} + \beta P^*_{\gamma_1} cos\theta^*_1), & E_{\gamma_2} &= b(E^*_{\gamma_2} - \beta P^*_{\gamma_2} cos\theta^*_2), \\ P_{\gamma_1} &= b(\beta E^*_{\gamma_1} + P^*_{\gamma_1} cos\theta^*_1), & P_{\gamma_2} &= b(\beta E^*_{\gamma_2} - P^*_{\gamma_2} cos\theta^*_2), \\ P_{\gamma_1} sin\theta_1 &= P^*_{\gamma_1} sin^*\theta_1, & P_{\gamma_2} sin\theta_2 &= P^*_{\gamma_2} sin^*\theta_2, \end{aligned} \tag{D.3}$$

where β is the constant velocity of the CM_{π^0} system, if seen from the CM system of the ω meson and b is the Lorentz boost factor. According to the relativistic kinematics, $\beta = P^{CM}_{\pi^0}/E^{CM}_{\pi^0} = 0.38/0.40 = 0.94/c$, correspondingly, $b = E^{CM}_{\pi^0}/m_{\pi^0} = 0.40/m_{\pi^0} = 2.99c^2$. Equation D.3 is the relation between the angles in CM system and angles in the CM_{π^0} system. Using the Lorentz transformations in Equation D.3, the CM angular distribution $S(\theta) = d(cos\theta^*)/d(cos\theta)$ is given as

$$S(\theta_1) = \frac{sin\theta_1}{2b^2(1 - \beta cos\theta_1)^2}, \qquad S(\theta_2) = \frac{sin\theta_2}{2b^2(\beta cos\theta_2 - 1)^2}, \tag{D.4}$$

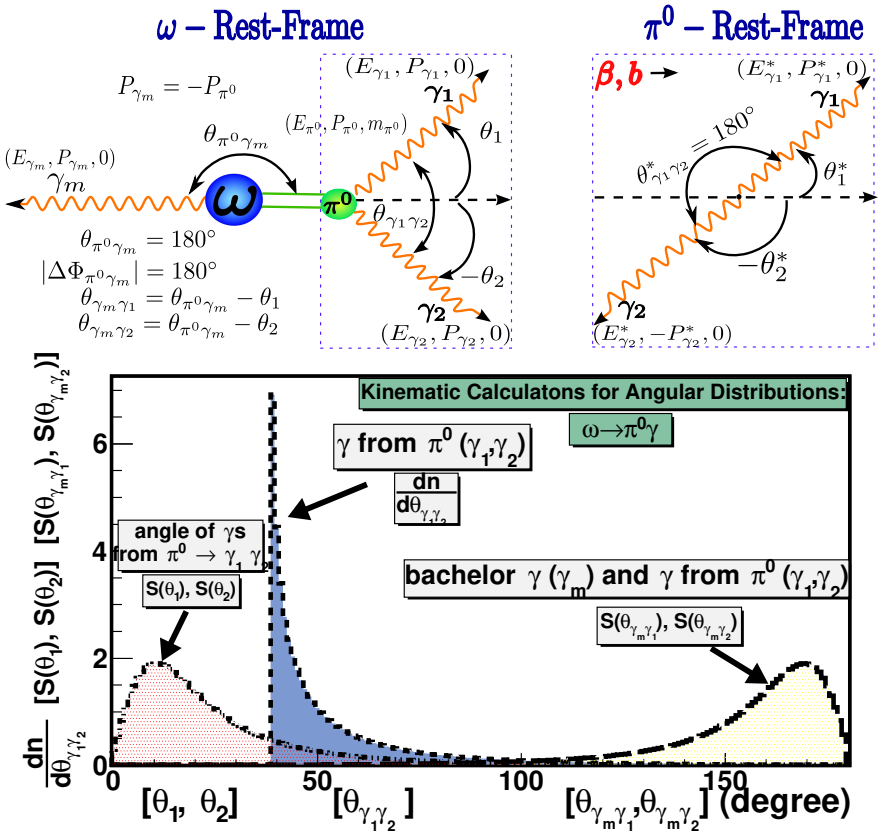

Figure D.1.: Kinematical diagram: **Top Left:** Rest frame of ω meson (CM); **Top Right:** Rest frame of π^0 meson (CM_{π^0}). The CM_{π^0} system quantities have been denoted by an asterisk. β refer to the velocity of the CM_{π^0} system as seen from the CM; b is $1/\sqrt{1-\beta^2}$. **Bottom:** Calculation of the angular distributions using relativistic kinematics. The distribution $(S(\theta_1), S(\theta_2))$ of the angle $(\theta_{\gamma_1}, \theta_{\gamma_2})$ between the momenta the decaying π^0 and its decay products is shown as red filled area. The yellow filled area corresponds to the calculated distribution $(S(d\theta_{\gamma_m\gamma_1}), S(d\theta_{\gamma_m\gamma_2}))$ of angle $(\theta_{\gamma_m\gamma_1}, \theta_{\gamma_m\gamma_2})$ between the photon from the π^0 and single photon γ_m. The blue filled area is $dn/d\theta_{\gamma_1\gamma_2}$, the distribution of the angle $(\theta_{\gamma_1\gamma_2})$ between photons coming from the π^0 in the CM system.

see Refs. [126, 131] for the derivation. The distribution for Equation D.4 is calculated and plotted as the red filled area in the bottom panel of Fig. D.1. This shows that the angular distribution of the secondary photons with respect to their parent π^0 meson is distributed between 0° to 180°. Furthermore, it is maximum at 11.50° in the CM frame with most of the entries concentrated towards the lower angles.

As shown in the top left panel of Fig. D.1, the γ_m and π^0 decay back to back, thus, the opening angle between them $(\theta_{\gamma_m\pi^0})$ is 180°. This means that the number of events within a $\theta_{\gamma_m\gamma_1}$ or $\theta_{\gamma_m\gamma_2}$ interval is equal to the number of events within the corresponding θ_1 or θ_2 interval, provided the following relation is satisfied

$$d\theta_{\gamma_m\gamma_1} = d\theta_{\gamma_m\pi^0} - d\theta_1 = 180^\circ - d\theta_1, \qquad d\theta_{\gamma_m\gamma_2} = d\theta_{\gamma_m\pi^0} - d\theta_2 = 180^\circ - d\theta_2. \quad \text{(D.5)}$$

Thus, the angular distribution for a $\theta_{\gamma_m\gamma_1}$ and $\theta_{\gamma_m\gamma_2}$ interval for the θ_1 or θ_2 interval, satisfying Equation D.5, will be

$$S(\theta_{\gamma_m\gamma_1})d\theta_{\gamma_m\gamma_1} = S(\theta_1)d\theta_1, \qquad S(\theta_{\gamma_m\gamma_2})d\theta_{\gamma_m\gamma_2} = S(\theta_2)d\theta_2. \quad \text{(D.6)}$$

The calculated $S(\theta_{\gamma_m\gamma_1})$ ($S(\theta_{\gamma_m\gamma_2})$) distribution is plotted as yellow filled area in the bottom panel of Fig. D.1, which shows that the angle between the monochromatic γ and the two γs from π^0 decay are distributed between 0° to 180° with most of the entries localized close to its maximum at 168.50°.

The distribution of the opening angle, $\theta_{\gamma_1\gamma_2}$, between two secondary photons from the decaying π^0 meson in the CM system is [131]

$$\frac{dn}{d\theta_{\gamma_1\gamma_2}} = \frac{1}{2\beta b} \frac{cos\frac{\theta_{\gamma_1\gamma_2}}{2}}{sin^2\frac{\theta_{\gamma_1\gamma_2}}{2}\sqrt{b^2 sin^2\frac{\theta_{\gamma_1\gamma_2}}{2} - 1}}. \tag{D.7}$$

The minimum value of $\theta_{\gamma_1\gamma_2}$ is when $sin\frac{\theta^{min}_{\gamma_1\gamma_2}}{2} = 1/b = E^{CM}_{\pi^0}/m_{\pi^0}$, implies $\theta^{min}_{\gamma_1\gamma_2} = 39.14°$. The distribution for different $\theta_{\gamma_1\gamma_2}$ range calculated from Equation D.7 is shown in the bottom panel of Fig. D.1 as the blue area, which shows that the angle between the two γ from π^0 decay in the CM system has a range from 39.14° to 180°. Wherein the maximum contribution is at 39.14° and most of the entries are localized towards the maximum.

E. Reconstruction Efficiencies for the $\omega \to \pi^0\gamma$ Final State

The reconstruction efficiencies of the signal decay $\omega \to \pi^0\gamma$ and the probable backgrounds, as discussed in Section 4.2, are presented in Table E.1.

	$\varepsilon_{\omega\to\pi^0\gamma}$ (%)	$\varepsilon_{\omega\to\pi^+\pi^0\pi^0}$ (%)	$\varepsilon_{\omega\to\pi^+\pi^-}$ (%)	$\varepsilon_{\pi^0\pi^0}$ (%)	$\varepsilon_{\pi^0\pi^0\pi^0}$ (%)	$\varepsilon_{\pi^+\pi^-\pi^0}$ (%)	$\varepsilon_{\pi^+\pi^-}$ (%)	$\varepsilon_{\eta\to\gamma\gamma}$ (%)	$\varepsilon_{\pi^0\to\gamma\gamma}$ (%)
Cut	**1.45 GeV**								
I		84.65		61.59	79.70	79.80	61.80	50.12	17.79
II	40.33	12.76	1.85	47.60	75.99	11.11	1.1	0.37	0.07
III	36.42	0.00	0.00	27.80	9.16	0.00	0.00	0.30	0.06
IV	34.74	0.00	0.00	17.24	4.07	0.00	0.00	0.13	0.00
	1.50 GeV								
I		86.71		60.62	79.05	79.16	60.81	50.12	19.77
II	40.28	13.29	1.95	46.35	75.25	11.48	1.12	0.33	0.07
III	36.04	0.00	0.00	26.54	8.54	0.00	0.00	0.27	0.05
IV	34.35	0.00	0.00	17.25	3.99	0.00	0.00	0.11	0.00
I ε_{inc} : 1 ^{3}He , **II**: $\geq 3\gamma$, **III**: $\delta\|P\| - \delta E$, **IV**: ε_{exc} : mono-γ									

Table E.1.: A comparison between the efficiencies of the signal decay $\omega \to \pi^0\gamma$ and the backgrounds (the decay $\omega \to \pi^+\pi^-\pi^0$, the decay $\omega \to \pi^+\pi^-$, $\pi^0\pi^0$ production, $\pi^0\pi^0\pi^0$ production, $\pi^+\pi^-\pi^0$ production, $\pi^+\pi^-$ production, $\eta \to \gamma\gamma$ decay and $\pi^0 \to \gamma\gamma$ decay) is shown at each analysis step.

F. Resolution of the ^{3}He and γ

The sample resolution distributions for the ^{3}He and γ particles, as discussed in Section 4.2.4.4, are presented in this section. Fig F.1 represents the true and reconstructed kinetic energy difference relative to the true kinetic energy of the two particles averaged over all θ and ϕ ranges.

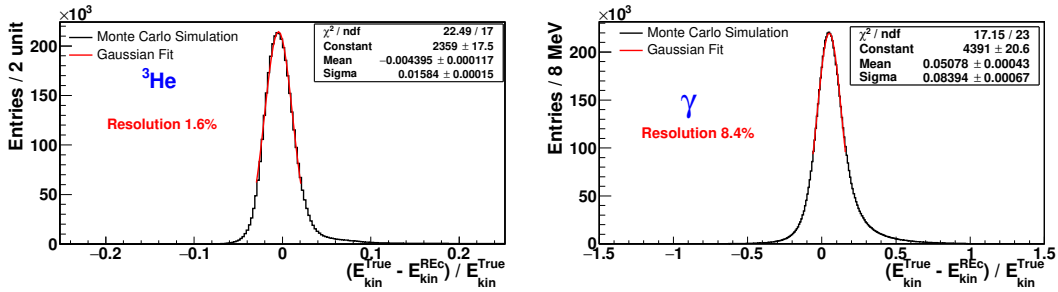

(a) The resolution of ^{3}He. **(b)** The resolution of γ.

Figure F.1.: The true and reconstructed kinetic energy difference relative to the true kinetic energy.

G. The Weighting Factor w_i of Backgrounds Relative to Signal Decay $\omega \to e^+e^-\pi^0$

Table G.1 lists the weighting factor w_i values for signal and backgrounds for 1.45 GeV beam energy. The reconstruction efficiencies (ε_i), after selecting at least a pair of charged particles and at least a pair of oppositely charged tracks and at least two neutral tracks, and their products with the weighting factors ($\varepsilon_i \times w_i$) are shown in Table G.1. These parameters have been discussed in Subsection 4.3.2 for 1.5 GeV. The w_i values have been discussed in Section 4.3 at different analysis steps.

Reference Name	**Decay/Reaction**	**Weighting Factor** w_i	**1.45 GeV**	
			ε_i(%)	$w_i \times \varepsilon_i$
$\omega \to \pi^0 e^+ e^-$	$pd \to {}^3\mathrm{He}\ \omega(\omega \to \pi^0 e^+ e^-)$	1	11.6500	
$\omega \to \pi^+\pi^-\pi^0$	$pd \to {}^3\mathrm{He}\ \omega(\omega \to \pi^+\pi^-\pi^0)$	1158±91	14.6800	169.9944±13.3558
$\omega \to \pi^0\gamma$	$pd \to {}^3\mathrm{He}\ \omega(\omega \to \pi^0\gamma)$	109±9	0.0617	0.0700±0.0055
$\omega \to \pi^+\pi^-$	$pd \to {}^3\mathrm{He}\ \omega(\omega \to \pi^+\pi^-)$	20±2	1.7600	0.3520±0.0352
$\omega \to \eta\gamma$	$pd \to {}^3\mathrm{He}\ \omega(\omega \to \eta\gamma)$	1±0	0.0805	0.0008±0.0000
$\pi^+\pi^-\pi^0$	$pd \to {}^3\mathrm{He}\ \pi^+\pi^-\pi^0$	14137±1136	12.3900	1751.5743±140.7504
$\pi^0\pi^0\pi^0$	$pd \to {}^3\mathrm{He}\ \pi^0\pi^0\pi^0$	1787±150	0.1400	2.5018±0.2100
$\pi^+\pi^-$	$pd \to {}^3\mathrm{He}\ \pi^+\pi^-$	932±74*	0.9600	8.9472±0.7104
$\pi^0\pi^0$	$pd \to {}^3\mathrm{He}\ \pi^0\pi^0$	3216±261	0.0700	2.2512±0.1827
$\rho \to \pi^+\pi^-$	$pd \to {}^3\mathrm{He}\ \rho(\rho \to \pi^+\pi^-)$	155347±1242*	1.5288	2374.9450±18.9877
$\eta \to \gamma\gamma$	$pd \to {}^3\mathrm{He}\ \eta(\eta \to \gamma\gamma)$	495±45	0.0009	0.0045±0.0004
$\eta \to \pi^+\pi^-\pi^0$	$pd \to {}^3\mathrm{He}\ \eta(\eta \to \pi^+\pi^-\pi^0)$	288±27	8.3308	2.3993±0.2250
$\eta \to \gamma\pi^+\pi^-$	$pd \to {}^3\mathrm{He}\ \eta(\eta \to \gamma\pi^+\pi^-)$	53±5	1.5603	0.8270±0.0780
$\pi^0 \to \gamma\gamma$	$pd \to {}^3\mathrm{He}\ \pi^0(\pi^0 \to \gamma\gamma)$	3070±246	0.0006	0.0184±0.0015
*: extrapolations				

Table G.1.: The weighting factors w_i, estimated by using Equation 4.8, are listed for the probable background contributions with respect to the signal $\omega \to e^+e^-\pi^0$. The efficiency ε_i and the quantity $w_i \times \varepsilon_i$ of the signal and backgrounds are listed for 1.45 GeV beam energy.

H. Reconstruction Efficiencies for the $\omega \to e^+e^-\pi^0$ Final State

Table H.1 presents the reconstruction efficiencies of the $\omega \to e^+e^-\pi^0$ decay and background reaction at each step of the analysis. These efficiencies have frequently been discussed in Section 4.3.

	I	II	III	IV	V	VI	VII	VIII
1.45 GeV $\varepsilon(\%)$								
S	84.6500	22.4200	12.4600	11.6500	8.8700	7.6000	7.4500	5.5900
B1	84.6500	25.9200	16.4900	14.6800	1.1700	1.1300	1.0900	0.2800
B2	84.6500	0.1300	0.0659	0.0617	0.0482	0.0099	0.0044	0.0030
B3	84.6500	32.5500	2.1200	1.7600	0.0575	0.0522	0.0087	0.0006
B4	84.6500	0.1541	0.0850	0.0805	0.0647	0.0128	0.0016	0.0006
B5	79.8000	22.6300	13.7500	12.3900	1.0100	0.9600	0.9100	0.2800
B6	61.8000	23.0400	1.1400	0.9600	0.0400	0.0300	0.0039	0.0008
B7	61.5900	0.1100	0.0800	0.0700	0.0700	0.0100	0.0100	0.0040
B8	79.7000	0.1600	0.1600	0.1400	0.1200	0.0300	0.0300	0.0010
B9	50.1200	13.7824	8.7165	8.3308	0.7643	0.7027	0.6658	0.3200
B10	50.1200	15.2065	1.6853	1.5603	0.0662	0.0576	0.0178	0.0041
B11	82.5300	30.9000	1.8500	1.5288	0.0553	0.0520	0.0077	0.0007
1.50 GeV $\varepsilon(\%)$								
S	86.7100	22.4700	12.1100	11.3100	8.5800	7.3700	7.2100	5.3300
B1	86.7100	26.2900	16.7700	14.9000	1.1500	1.1100	1.0700	0.2700
B2	86.7100	0.1300	0.0653	0.0610	0.0481	0.0098	0.0042	0.0029
B3	86.7100	32.8000	2.1700	1.7800	0.0601	0.0541	0.0090	0.0006
B4	86.7100	0.1550	0.0844	0.0793	0.0636	0.0138	0.0021	0.0009
B5	79.1600	22.0100	13.8700	12.4400	0.9900	0.9400	0.8900	0.2500
B6	60.8100	22.7700	1.1800	0.9900	0.0400	0.0300	0.0040	0.0008
B7	60.6200	0.1100	0.0800	0.0600	0.0600	0.0100	0.0100	0.0040
B8	79.0500	0.1700	0.1600	0.1400	0.1200	0.0300	0.0300	0.0010
B9	50.1200	13.1804	8.3374	7.9890	0.7329	0.6735	0.6371	0.3002
B10	50.1200	14.3605	1.6158	1.5040	0.0614	0.0538	0.0164	0.0055
B11	82.8600	30.8090	1.9125	1.5684	0.0532	0.0479	0.0072	0.0006
S: $\omega \to e^+e^-\pi^0$, B1: $\omega \to \pi^+\pi^-\pi^0$, B2: $\omega \to \pi^0\gamma$, B3: $\omega \to \pi^+\pi^-$, B4: $\omega \to \eta\gamma$, B5: $\pi^+\pi^-\pi^0$, B6: $\pi^+\pi^-$, B7: $\pi^0\pi^0$, B8: $\pi^0\pi^0\pi^0$, B9: $\eta \to \pi^+\pi^-\pi^0$, B10: $\eta \to \pi^+\pi^-\gamma$, and B11: $\rho \to \pi^+\pi^-$								
I ε_{inc} : 1 ^{3}He , **II**: $\geq$ 2C, **III**: $\geq$ 2C2γ, **IV**: $\geq 1C^+C^-2\gamma$, **V**: $\geq 1e^+e^-2\gamma(e^\pm$ *PID)* , **VI**: conversion, **VII**: $\geq 1\ e^+e^-\pi^0$ *(m_{π^0} cut)* and **VIII** ε_{exc} : $\delta E - \delta P$								

Table H.1.: A comparison between the efficiencies of the signal decay $\omega \to e^+e^-\pi^0$ and the backgrounds, after each analysis step.

I. The Purity of $\omega \to e^+e^-\pi^0$ Decay at Different Analysis Stages

Contribution	PID	conversion cut	π^0 cut	$\delta E - \delta P$
$\omega \to \pi^0 e^+ e^-$	1	1	1	1
$\frac{\varepsilon_{bj}}{\varepsilon_s} w_j$:				
$\omega \to \pi^+\pi^-\pi^0$	152.81±11.97	172.24±13.50	169.49±13.27	58.03±4.54
$\omega \to \pi^0\gamma$	0.60±0.05	0.14±0.01	0.06±0.01	0.06±0.01
$\pi^+\pi^-\pi^0$	1609.69±129.31	1785.67±143.44	1726.75±138.71	708.10±56.88
$\pi^0\pi^0\pi^0$	24.17±2.03	7.05±0.59	7.19±0.61	0.32±0.03
$\pi^+\pi^-$	700.55±56.02	613.21±49.03	81.32±6.50	22.23±1.78
$\pi^0\pi^0$	42.91±3.45	7.15±0.58	7.30±0.59	3.89±0.31
$\rho \to \pi^+\pi^-$	5.81±0.47	6.38±0.51	0.96±0.08	0.12±0.01
$\eta \to \gamma\gamma$	0.05± 0.01	0.01±0.00	0.00±0.00	~~0.00±0.00~~
$\eta \to \pi^+\pi^-\pi^0$	24.79±2.29	26.60±2.46	25.71±2.37	16.47±1.52
$\eta \to \gamma\pi^+\pi^-$	0.40 ± 0.00	0.12±0.00	0.03±0.00	~~0.00±0.00~~
$\pi^0 \to \gamma\gamma$	0.21±0.02	0.02±0.00	0.00±0.00	~~0.00±0.00~~

Table I.1.: The fraction $\frac{\varepsilon_{bj}}{\varepsilon_s} w_j$ is listed for the 1.45 GeV data set after various analysis conditions. The first, second, third and fourth column are the $\frac{\varepsilon_{bj}}{\varepsilon_s} w_j$ values after e^+e^- PID, conversion cut, cut on 2 γ invariant mass (π^0 cut) and $\delta E - \delta P$ constraint. w_j are taken from Table 4.3.

Contribution	PID	conversion cut	π^0 cut	$\delta E - \delta P$
$\omega \to \pi^0 e^+ e^-$	1	1	1	1
$\frac{\varepsilon_{bj}}{\varepsilon_s} w_j$:				
$\omega \to \pi^+\pi^-\pi^0$	155.27±12.16	174.47±13.66	171.92±13.46	58.68±4.60
$\omega \to \pi^0\gamma$	0.60±0.05	0.14±0.01	0.06±0.01	0.06±0.01
$\pi^+\pi^-\pi^0$	1631.14±131.03	1803.04±144.84	1745.01±140.18	663.10±53.26
$\pi^0\pi^0\pi^0$	24.99±2.10	7.27±0.61	7.43±0.63	0.34±0.03
$\pi^+\pi^-$	724.23±57.91	632.35±50.56	86.18±6.89	23.32±1.86
$\pi^0\pi^0$	38.02 ± 3.06	7.38±0.59	7.38±0.59	4.10±0.33
$\rho \to \pi^+\pi^-$	5.78±0.46	6.06±0.48	0.93±0.08	0.10±0.01
$\eta \to \gamma\gamma$	0.04±0.0	0.01±0.00	~~0.00±0.00~~	~~0.00±0.00~~
$\eta \to \pi^+\pi^-\pi^0$	24.58±2.27	26.29±2.43	25.42±2.35	16.21±1.50
$\eta \to \gamma\pi^+\pi^-$	0.38 ± 0.00	0.39±0.00	0.03±0.00	~~0.00 ±0.00~~
$\pi^0 \to \gamma\gamma$	0.19±0.02	0.01±0.00	0.01±0.00	~~0.00±0.00~~

Table I.2.: $\frac{\varepsilon_{bj}}{\varepsilon_s} w_j$ values, as shown in Table I.1 for 1.45 GeV, are shown for the 1.5 GeV data.

The contributions of each background for a single event of the $\omega \to e^+e^-\pi^0$ decay $\frac{\varepsilon_{bj}}{\varepsilon_s} w_j$, probability $\mathbf{P}_j(b)$ of occurrence of each background contribution for an event, and purity

π of the signal are presented after various analysis conditions. Equation 4.10, Equation 4.9 and Equation 4.7 is used to estimate $\frac{\varepsilon_{bj}}{\varepsilon_s} w_j$, $\mathbf{P}_j(b)$ and π. The quantities $\frac{\varepsilon_{bj}}{\varepsilon_s} w_j$, $\mathbf{P}_j(b)$ and π have thoroughly discussed in Section 4.3. Table I.1 and Table I.2 represent the $\frac{\varepsilon_{bj}}{\varepsilon_s} w_j$ values in 1.45 GeV and 1.5 GeV data. Whereas, $\mathbf{P}_j(b)$ and π values are given in Table I.3 and Table I.4 for 1.45 GeV and 1.5 GeV beam energy, respectively.

Contribution	**PID**	**conversion cut**	π^0 **cut**	$\delta E - \delta P$
purity (%)				
$\omega \to \pi^0 e^+ e^-$	0.04± 0.00	0.04± 0.00	0.05± 0.00	0.12± 0.01
$\mathbf{P}_j(b)$ (%)				
$\omega \to \pi^+\pi^-\pi^0$	5.96±0.57	6.58±0.64	8.39±0.88	7.16±0.76
$\omega \to \pi^0\gamma$	0.02±0.00	0.01±0.00	0.00±0.00	0.01±0.00
$\pi^+\pi^-\pi^0$	62.81±6.12	68.17±6.76	85.49±9.06	87.40±9.34
$\pi^0\pi^0\pi^0$	0.94±0.10	0.27±0.03	0.36±0.04	0.04±0.01
$\pi^+\pi^-$	27.34±2.66	23.41±2.31	4.03±0.43	2.75±0.29
$\pi^0\pi^0$	1.68±0.16	0.27±0.03	0.36±0.04	0.48±0.05
$\rho \to \pi^+\pi^-$	0.23±0.02	0.24±0.02	0.05±0.01	0.01±0.00
$\eta \to \gamma\gamma$	0.00±0.00	0.00±0.00	0.00±0.00	0.00±0.00
$\eta \to \pi^+\pi^-\pi^0$	0.97±0.11	1.02±0.11	1.27±0.15	2.03±0.24
$\eta \to \gamma\pi^+\pi^-$	0.02±0.00	0.01±0.00	0.00±0.00	0.00±0.00
$\pi^0 \to \gamma\gamma$	0.01±0.00	0.00±0.00	0.00±0.00	0.00±0.00

Table I.3.: The probability $\mathbf{P}_j(b)$ and purity have been given for 1.45 GeV beam energy. The values after e^+e^- PID, conversion cut, cut on 2 γ invariant mass, and $\delta E - \delta P$ constraint has been listed in the second to fourth columns, respectively.

Contribution	**PID**	**conversion cut**	π^0 **cut**	$\delta E - \delta P$
purity (%)				
$\omega \to \pi^0 e^+ e^-$	0.04± 0.00	0.04± 0.00	0.05± 0.00	0.13± 0.01
$\mathbf{P}_j(b)$ (%)				
$\omega \to \pi^+\pi^-\pi^0$	5.96±0.57	6.56±0.64	8.40±0.88	7.65±0.80
$\omega \to \pi^0\gamma$	0.02±0.00	0.01±0.00	0.00±0.00	0.01±0.00
$\pi^+\pi^-\pi^0$	62.60±6.10	67.82±6.72	85.30±9.03	86.46±9.20
$\pi^0\pi^0\pi^0$	0.96±0.10	0.27±0.03	0.36±0.04	0.04±0.01
$\pi^+\pi^-$	27.79±2.70	23.79±2.35	4.21±0.45	3.04±0.32
$\pi^0\pi^0$	1.46±0.14	0.28±0.03	0.28±0.03	0.53±0.06
$\rho \to \pi^+\pi^-$	0.22±0.02	0.23±0.02	0.05±0.01	0.01±0.00
$\eta \to \gamma\gamma$	0.00±0.00	0.00±0.00	0.00±0.00	0.00±0.00
$\eta \to \pi^+\pi^-\pi^0$	0.94±0.10	0.99±0.11	1.24±0.14	2.11±0.25
$\eta \to \gamma\pi^+\pi^-$	0.02 ±0.00	0.02±0.00	0.00±0.00	0.00±0.00
$\pi^0 \to \gamma\gamma$	0.01±0.00	0.00±0.00	0.00±0.00	0.00±0.00

Table I.4.: $\mathbf{P}_j(b)$ and purity values for 1.5 GeV are listed in a similar fashion as for 1.45 GeV in Table I.3.

J. Luminosity Dependent Missing Mass Analysis

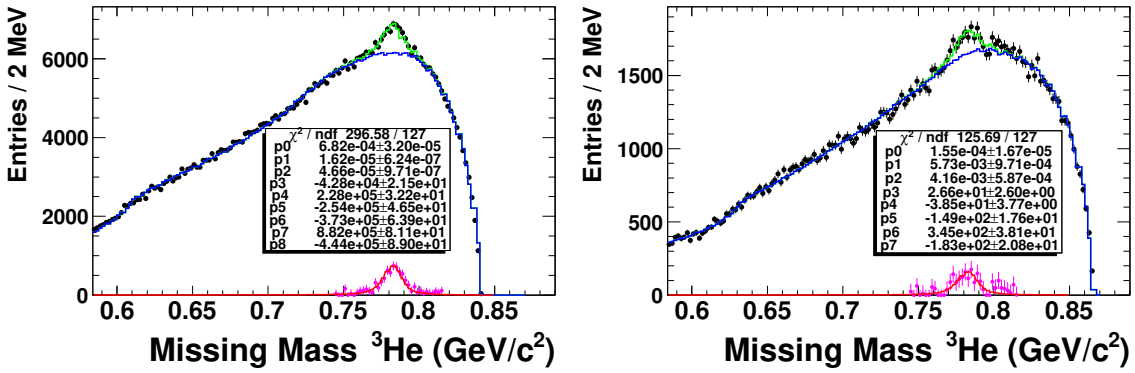

(a) 1.45 GeV: luminosity range: (350−400) *(pellet^{-1})* **(b) 1.50 GeV:** luminosity range: (350−400) *(pellet^{-1})*

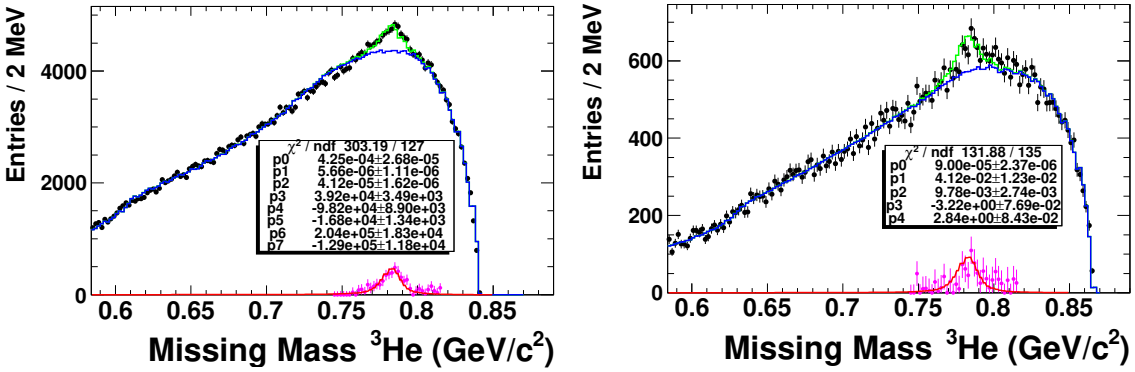

(c) 1.45 GeV: luminosity range: (400−500) *(pellet^{-1})* **(d) 1.50 GeV:** luminosity range: (400−500) *(pellet^{-1})*

Figure J.1.: The inclusive missing mass spectra with the fit functions are presented for last two luminosity bins for two energies.

lum.	1.45 GeV	1.50 GeV	entire data
	N_{ω}^{rec} (N1) ($\times 10^3$)	N_{ω}^{rec} (N2) ($\times 10^3$)	N_{ω}^{rec} (N1+N2) ($\times 10^3$)
(50-100)	(26.07 ± 1.12)	(30.12 ± 1.22)	$(26.07 \pm 1.12) + (30.12 \pm 1.22)$
(100-150)	(101.44 ± 2.23)	(84.96 ± 1.96)	$(101.44 \pm 2.23) + (84.96 \pm 1.96)$
(150-200)	(97.39 ± 2.46)	(77.73 ± 1.99)	$(97.39 \pm 2.46) + (77.73 \pm 1.99)$
(200-250)	(51.67 ± 1.83)	(71.86 ± 1.99)	$(51.67 \pm 1.83) + (71.86 \pm 1.99)$
(250-300)	(24.74 ± 1.31)	(31.18 ± 1.32)	$(24.74 \pm 1.31) + (31.18 \pm 1.32)$
(300-350)	(15.21 ± 0.93)	(7.75 ± 0.67)	$(15.21 \pm 0.93) + (7.75 \pm 0.67)$
(350-400)	(7.47 ± 0.66)	(2.04 ± 0.34)	$(7.47 \pm 0.66) + (2.04 \pm 0.34)$
(400-500)	(5.02 ± 0.55)	(1.01 ± 0.20)	$(5.02 \pm 0.55) + (1.01 \pm 0.20)$

Table J.1.: The number of reconstructed ω mesons is listed for the 1.45 GeV, 1.50 GeV, and combined data set in different luminosity ranges.

lum.	1.45 GeV	1.50 GeV	entire data
	$N^{rec}_{\omega\to\pi^0\gamma}$ (N1) ($\times 10^2$)	$N^{rec}_{\omega\to\pi^0\gamma}$ (N2) ($\times 10^2$)	$N^{rec}_{\omega\to\pi^0\gamma}$ (N1+N2) ($\times 10^2$)
(50-100)	(8.89 ± 1.31)	(10.00 ± 1.41)	$(8.89 \pm 1.31) + (10.00 \pm 1.41)$
(100-150)	(33.80 ± 2.44)	(27.99 ± 2.21)	$(33.80 \pm 2.44) + (27.99 \pm 2.21)$
(150-200)	(33.47 ± 2.59)	(25.86 ± 2.13)	$(33.47 \pm 2.59) + (25.86 \pm 2.13)$
(200-250)	(17.49 ± 1.89)	(23.76 ± 2.05)	$(17.49 \pm 1.89) + (23.76 \pm 2.05)$
(250-300)	(8.60 ± 1.33)	(10.26 ± 1.34)	$(8.60 \pm 1.33) + (10.26 \pm 1.34)$
(300-350)	(5.13 ± 0.89)	(2.60 ± 0.67)	$(5.13 \pm 0.89) + (2.60 \pm 0.67)$
(350-400)	(2.57 ± 0.58)	(1.26 ± 0.34)	$(2.57 \pm 0.58) + (1.26 \pm 0.34)$
(400-500)	(1.72 ± 0.52)	(0.67 ± 0.19)	$(1.72 \pm 0.52) + (0.67 \pm 0.19)$

Table J.2.: The number of the $\omega \to \pi^0\gamma$ decays reconstructed in 1.45 GeV, 1.50 GeV, and combined data are tabulated for different luminosity bins.

The details about the luminosity based systematic effect discussed in Section 5.2.3.1 are presented in this section. Fig. J.1 and Fig. J.2 are illustrations of the inclusive and exclusive missing mass fits for last two luminosity ranges (350−400) $pellet^{-1}$ and (400−500) $pellet^{-1}$. The number of reconstructed ω mesons N^{rec}_{ω} and reconstructed $\omega \to \pi^0\gamma$ decay $N^{rec}_{\omega\to\pi^0\gamma}$, in each luminosity range, are given in Table J.1 and Table J.2, respectively. The branching ratio measured in each bin is listed in Table J.3.

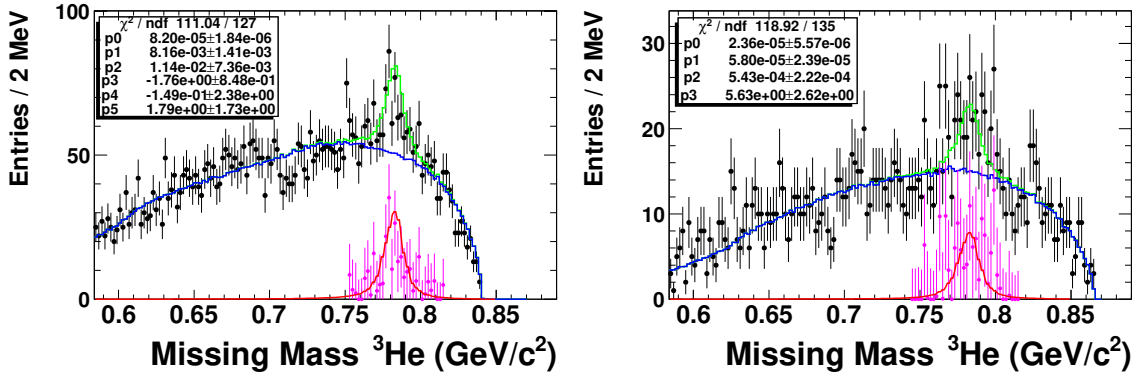

(a) 1.45 GeV: luminosity range: (350−400) $(pellet^{-1})$ **(b) 1.50 GeV:** luminosity range: (350−400) $(pellet^{-1})$

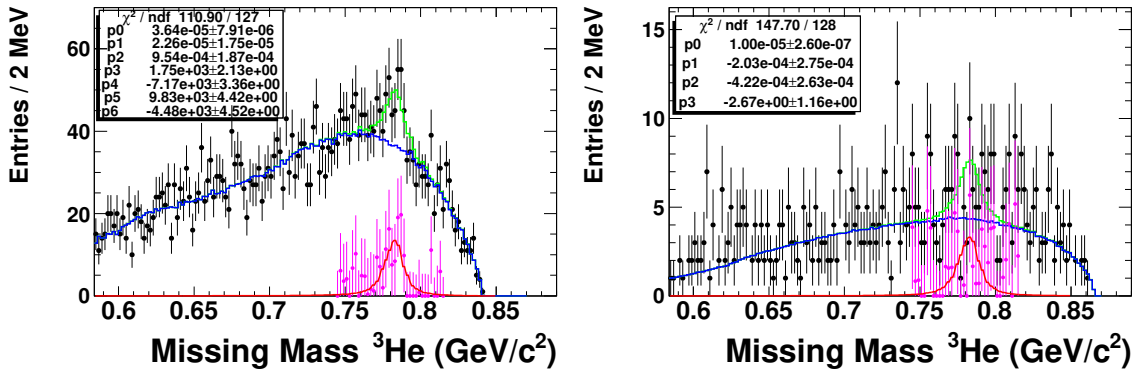

(c) 1.45 GeV: luminosity range: (400−500) $(pellet^{-1})$ **(d) 1.50 GeV:** luminosity range: (400−500) $(pellet^{-1})$

Figure J.2.: The exclusive missing mass in the last two luminosity bins and the fits are presented for two energies.

lum.	1.45 GeV	1.50 GeV	entire data
	$BR_{\omega\to\pi^0\gamma}(\%)$		
(50-100)	(8.31±1.28)	(8.38 ±1.23)	(8.35±0.89)
(100-150)	(8.12±0.61)	(8.32 ±0.69)	(8.21±0.46)
(150-200)	(8.38±0.68)	(8.40 ±0.73)	(8.39±0.50)
(200-250)	(8.25±0.94)	(8.35 ±0.76)	(8.31±0.59)
(250-300)	(8.47±1.39)	(8.31 ±1.14)	(8.38±0.88)
(300-350)	(8.22±1.51)	(8.47 ±2.30)	(8.30±1.27)
(350-400)	(8.38±2.03)	(15.59 ±4.94)	(9.92±1.91)
(400-500)	(8.35±2.69)	(16.75 ±5.78)	(9.74±2.44)

Table J.3.: The branching ratio $BR_{\omega\to\pi^0\gamma}$ of the $\omega \to \pi^0\gamma$ decay is listed for different luminosity ranges. The second, the third and the fourth column represents the results for 1.45 GeV, 1.50 GeV, and for the combined data set, respectively.

K. Reduced χ^2 for Different Fit Ranges and Polynomial Orders

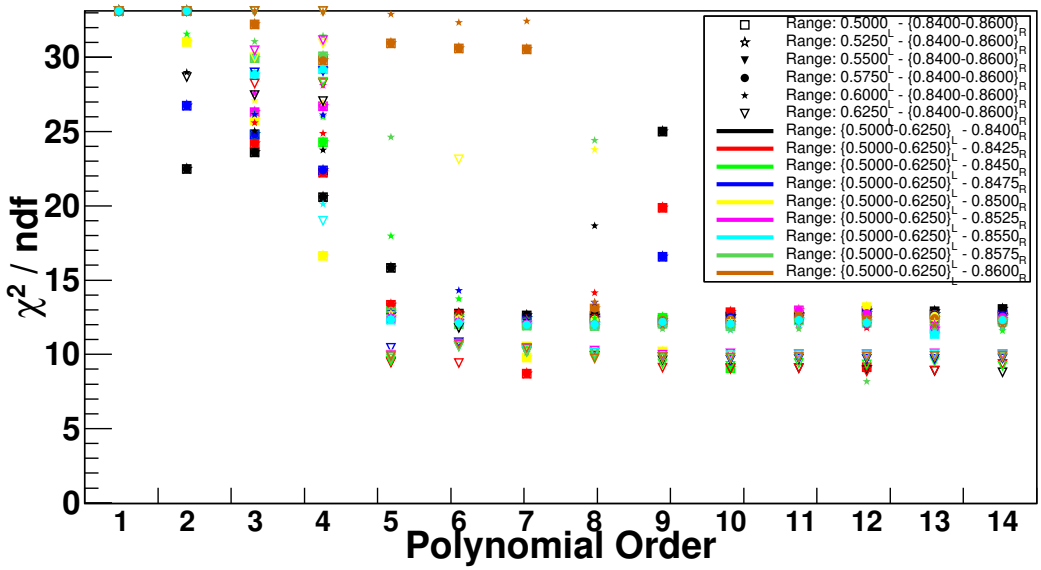

Figure K.1.: χ^2/ndf as a function of the polynomial order is plotted for different fit ranges. The plot is presented for the 1.50 GeV beam energy data. The fit for the various ranges is converging for the polynomial of order 5.

The polynomial's order having the converging fit to the missing mass spectra shown in Fig. 4.1c are diagnosed in this section. Which is achieved by monitoring the minimum value of the function calculated using MINUIT minimization routine in root for various polynomial orders. It is observed that in order to control the background shape, the function has to be fitted to the full phase space of the distribution. The background starts approaching inside the peak when a narrower fit range close to the peak region was selected. The polynomial of order 5 between fit range $[0.575-0.840]$ provides the lowest χ^2/ndf value for the 1.50 GeV, as compared to the lower orders. However, in the case of the 1.45 GeV beam energy, the ω peak is sitting directly on the top of the maximum of the background phase space (compare Fig. 4.1b and Appendix A.3). Which enhanced the sensitivity of the fit. Consequently, 6^{th} order polynomial with fit range $[0.575-0.855]$ provide the minimum value for the χ^2/ndf for 1.45 GeV data. Adequate fits are found in the mentioned fit ranges and polynomial orders.

L. Systematic Effect Due to the Fitting Procedure

The following sections present a detailed description of the systematic studies for the fitting procedure, as discussed in Section 5.2.3.2. The number of the reconstructed ω mesons and the number of the $\omega \to \pi^0\gamma$ decays are given in Table L.1 and Table L.2, for different combinations of the fit ranges and polynomial orders. The fits, which are converging after MINUIT minimization are considered for the systematic studies. The obtained numbers and the branching fractions have been plotted in Fig. L.1 for changing fit ranges and polynomial orders, for 1.5 GeV beam energy.

1.45 GeV			**1.50 GeV**		
For Inclusive Missing Mass Fit					
Fit Range	$N^{rec}(\times 10^5)$	$BR^{measured}_{\omega\to\pi^0\gamma}(\%)$	**Fit Range**	$N^{rec}(\times 10^5)$	$BR^{measured}_{\omega\to\pi^0\gamma}(\%)$
0.5000−0.8400	3.15 ± 0.04	8.36 ± 0.37	0.5000−0.8550	3.28 ± 0.04	8.31 ± 0.34
0.5250−0.8400	3.15 ± 0.04	8.36 ± 0.37	0.5250−0.8550	3.28 ± 0.04	8.31 ± 0.34
0.5500−0.8400	3.15 ± 0.04	8.36 ± 0.37	0.5500−0.8550	3.28 ± 0.04	8.31 ± 0.34
0.5750−0.8400*	3.15 ± 0.04	8.36 ± 0.37	0.5750−0.8550*	3.28 ± 0.04	8.31 ± 0.34
0.6000−0.8400	3.13 ± 0.04	8.41 ± 0.36	0.6000−0.8550	3.28 ± 0.04	8.31 ± 0.34
0.5750−0.8325	3.21 ± 0.04	8.20 ± 0.37	0.6250−0.8550	3.33 ± 0.04	8.19 ± 0.34
			0.6500−0.8550	3.33 ± 0.04	8.19 ± 0.34
			0.5750−0.8450	3.33 ± 0.04	8.19 ± 0.34
			0.5750−0.8475	3.33 ± 0.04	8.19 ± 0.34
			0.5750−0.8500	3.33 ± 0.04	8.19 ± 0.34
			0.5750−0.8525	3.31 ± 0.04	8.24 ± 0.34
			0.5750−0.8575	3.32 ± 0.04	8.21 ± 0.34
Polynomial			**Polynomial**		
6*	3.15 ± 0.04	8.36 ± 0.37	5*	3.28 ± 0.04	8.31 ± 0.34
7	3.17 ± 0.04	8.30 ± 0.37	6	3.25 ± 0.04	8.39 ± 0.35
8	3.21 ± 0.04	8.20 ± 0.37	7	3.23 ± 0.04	8.44 ± 0.35
9	3.24 ± 0.04	8.12 ± 0.36	8	3.24 ± 0.04	8.41 ± 0.35
10	3.25 ± 0.04	8.10 ± 0.36	9	3.23 ± 0.04	8.44 ± 0.34
			10	3.26 ± 0.04	8.36 ± 0.35
(*): final combination of parameters; $N^{rec} = N^{rec}_{\omega}$					

Table L.1.: Tabulation of the number of ω mesons reconstructed (N^{rec}_{ω}) and branching ratio (BR), for different ranges and polynomial orders of the inclusive missing mass fits for two beam energies.

1.45 GeV			1.50 GeV		
For Exclusive Missing Mass Fit					
Fit Range	$N^{rec}(\times 10^4)$	$BR^{measured}_{\omega\to\pi^0\gamma}(\%)$	**Fit Range**	$N^{rec}(\times 10^4)$	$BR^{measured}_{\omega\to\pi^0\gamma}(\%)$
0.5000−0.8400	1.08 ± 0.05	8.36 ± 0.37	0.5000−0.8550	1.08 ± 0.04	8.31 ± 0.34
0.5250−0.8400	1.08 ± 0.05	8.36 ± 0.37	0.5250−0.8550	1.08 ± 0.04	8.31 ± 0.34
0.5500−0.8400	1.08 ± 0.05	8.36 ± 0.37	0.5500−0.8550	1.08 ± 0.04	8.31 ± 0.34
0.5750−0.8400	1.08 ± 0.05	8.36 ± 0.37	0.5750−0.8550	1.08 ± 0.04	8.31 ± 0.34
0.6000−0.8400	1.03 ± 0.05	7.97 ± 0.37	0.6000−0.8550	1.07 ± 0.04	8.23 ± 0.34
0.6250−0.8400	1.01 ± 0.05	7.81 ± 0.37	0.5750−0.8450	1.11 ± 0.04	8.54 ± 0.34
0.5750−0.8250	1.08 ± 0.05	8.36 ± 0.37	0.5750−0.8475	1.10 ± 0.04	8.47 ± 0.34
0.5750−0.8275	1.08 ± 0.05	8.36 ± 0.37	0.5750−0.8500	1.09 ± 0.04	8.39 ± 0.34
0.5750−0.8300	1.08 ± 0.05	8.36 ± 0.37	0.5750−0.8525	1.08 ± 0.04	8.31 ± 0.34
0.5750−0.8325	1.07 ± 0.05	8.28 ± 0.37	0.5750−0.8575	1.08 ± 0.04	8.31 ± 0.34
0.5750−0.8350	1.06 ± 0.05	8.28 ± 0.37	0.5750−0.8600	1.07 ± 0.04	8.23 ± 0.34
0.5750−0.8375	1.06 ± 0.05	8.28 ± 0.37	0.5750−0.8625	1.06 ± 0.04	8.16 ± 0.34
0.5750−0.8425	1.06 ± 0.05	8.28 ± 0.37	0.5750−0.8650	1.06 ± 0.04	8.16 ± 0.34
0.5750−0.8450	1.06 ± 0.05	8.28 ± 0.37			
0.5750−0.8475	1.06 ± 0.05	8.28 ± 0.37			
0.5750−0.8500	1.06 ± 0.05	8.28 ± 0.37			
Polynomial			**Polynomial**		
5*	1.08 ± 0.05	8.36 ± 0.37	4*	1.08 ± 0.04	8.31 ± 0.34
6	1.05 ± 0.05	8.12 ± 0.37	6	1.07 ± 0.04	8.23 ± 0.34
7	1.01 ± 0.05	7.81 ± 0.37	7	1.04 ± 0.04	8.00 ± 0.34
8	0.99 ± 0.05	7.66 ± 0.37	8	1.04 ± 0.04	8.00 ± 0.34
9	1.02 ± 0.05	7.90 ± 0.37	9	1.05 ± 0.05	8.00 ± 0.34
10	1.01 ± 0.05	7.81 ± 0.37	10	1.05 ± 0.05	8.09 ± 0.34

(*): final combination of parameters; $N^{rec} = N^{rec}_{\omega\to\pi^0\gamma}$

Table L.2.: The number of the $\omega \to \pi^0\gamma$ decays reconstructed ($N^{rec}_{\omega\to\pi^0\gamma}$) and branching ratio ($BR$) are listed for two energies, for various fit ranges and polynomial orders of the exclusive missing mass fit.

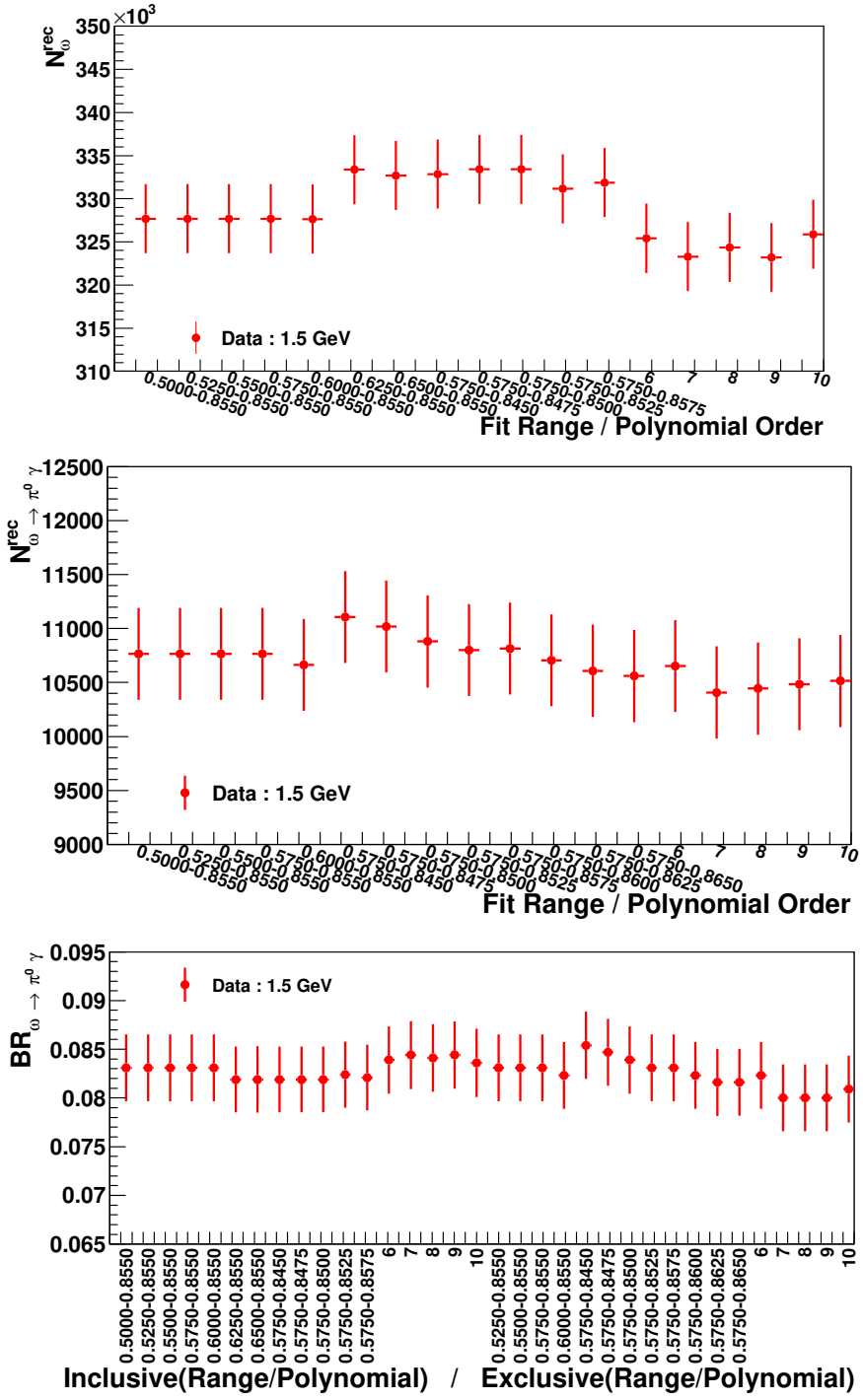

Figure L.1.: N_{ω}^{rec} and $N_{\omega\to\pi^0\gamma}^{rec}$ are presented in the top and middle panels, respectively, for different combinations of fit ranges and polynomial orders for 1.5 GeV beam energy. The varied fit range for the fixed polynomial order same as used for the final fit shown in Fig. 4.4 has been plotted in the left part of both histograms. Whereas the right portion of the histograms presents the vice-versa. The bottom panel illustrates the $BR_{\omega\to\pi^0\gamma}^{measured}$ for different combinations of the fit ranges and polynomial orders for the inclusive and exclusive missing mass in 1.5 GeV data.

M. Systematic Effect Due to the ^{3}He Identification Cut

Forthcoming sections describe the particulars of the systematic studies for the ^{3}He identification cuts considered in Section 5.2.3.3. The sample inclusive and exclusive mass spectra with fits are shown in Fig. M.1. The efficiency ε, number of the ω meson reconstructed N_{ω}^{rec}, the total number of the ω meson N_{ω}°, number of the reconstructed $\omega \to \pi^0\gamma$ decays $N_{\omega\to\pi^0\gamma}^{rec}$, the total number of the $\omega \to \pi^0\gamma$ decays $N_{\omega\to\pi^0\gamma}^{\circ}$ and the measured branching ratio BR have been organized in Table M.1 for different particle identification cuts.

M.1. Missing Mass Spectra for Different Cuts

The representative missing mass spectra for both energies after one of the ^{3}He identification cuts, as discussed in Section 5.2.3.3, are shown in Fig. M.1 for both inclusive and exclusive final states. The missing mass spectra for the final measurement have been demonstrated in Fig. 4.4 and Fig. 4.16 for the respective final states. As established previously in Fig. A.2,

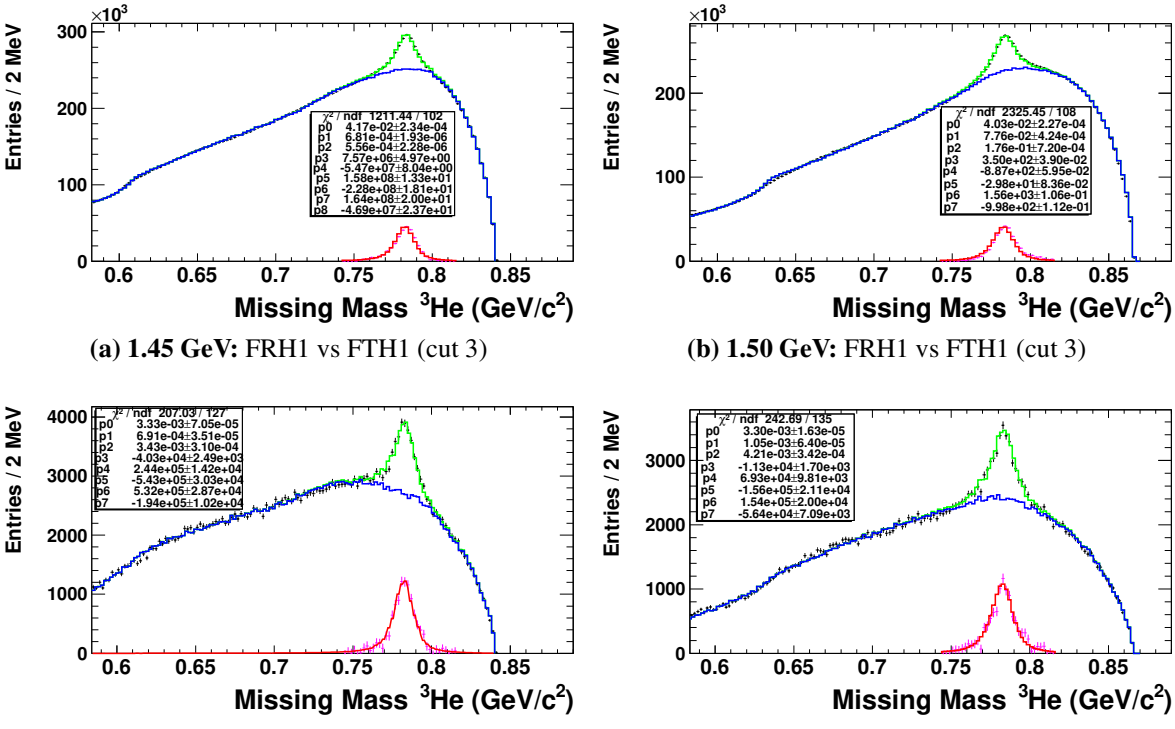

(a) 1.45 GeV: FRH1 vs FTH1 (cut 3)

(b) 1.50 GeV: FRH1 vs FTH1 (cut 3)

(c) 1.45 GeV: FRH1 vs FTH1 (cut 3)

(d) 1.50 GeV: FRH1 vs FTH1 (cut 3)

Figure M.1.: The Missing mass spectra for a particular ^{3}He identification cut are presented for two beam energies. The left and right columns represent the distributions for 1.45 GeV and 1.50 GeV, respectively. The inclusive missing mass is plotted in the top row and exclusive in the bottom row. The best fit functions are plotted on the respective histograms.

the graphical cut for the ^{3}He identification influences the signal and background spaces differently. The effect is prominently seen in the inclusive missing mass spectra. However, the

exclusive missing mass spectra have similar phase space for all cuts with a fractional variation in the statistics. The similar phase space is due to the effective kinematic conditions used to select the $\omega \to \pi^0\gamma$ decay, as discussed in Section 4.2.3. The phase space and $N^{rec}_{\omega\to\pi^0\gamma}$ is significantly influenced by changing the $\omega \to \pi^0\gamma$ final state selection criteria. These effects are illustrated in Appendix N and Appendix O by performing the systematic check for the energy-momentum conservation constraint and monochromatic γ selection criterion, respectively. The influence of the ^{3}He identification cuts is numerically seen in the reconstruction efficiencies for two final states listed in Table M.1. Furthermore, its quantitative effect is translated to N^{rec}_{ω} and $N^{rec}_{\omega\to\pi^0\gamma}$, which can be observed in Table M.1. N^{rec}_{ω} and $N^{rec}_{\omega\to\pi^0\gamma}$ for each cut is used to estimate the N°_{ω} and $N^{\circ}_{\omega\to\pi^0\gamma}$. The numbers, N^{rec}_{ω}, N°_{ω}, $N^{rec}_{\omega\to\pi^0\gamma}$ and $N^{\circ}_{\omega\to\pi^0\gamma}$, for the combined data set (1.45 GeV+1.50 GeV) are estimated by adding the numbers for two energies. The numbers in the table are organized in decreasing order of efficiencies from left to right. The branching ratios tabulated in Table M.1 are estimated using Equation 5.3 for three data sets. The systematic effect due to the particle identification cut for ^{3}He can be seen in Table 5.7.

	combined	**FRH1 vs FTH1 (cut 1)**	**FRH1 vs FTH1 (cut 2)**	**FRH1 vs FTH1 (cut 3)**
$\varepsilon_{inc}(\%)$	85.26	84.71	84.65	83.49
$\varepsilon_{inc}(\%)$	35.02	34.75	34.74	34.30
$N^{rec}_{\omega}(\times10^5)$	3.27±0.04	3.24± 0.06	3.15± 0.04	3.15± 0.04
$N^{\circ}_{\omega}(\times10^5)$	3.84±0.05	3.83± 0.07	3.72± 0.05	3.77± 0.05
$N^{rec}_{\omega\to\pi^0\gamma}(\times10^4)$	1.12±0.05	1.01± 0.05	1.08± 0.05	1.07± 0.04
$N^{\circ}_{\omega\to\pi^0\gamma}(\times10^4)$	3.20± 0.13	2.91±0.14	3.11±0.13	3.12±0.13
BR(%)	8.33±0.36	7.82±0.38	8.36±0.37	8.28±0.36
(1.50 GeV)				
$\varepsilon_{inc}(\%)$	87.33	86.79	86.71	85.36
$\varepsilon_{exc}(\%)$	34.63	34.36	34.35	33.81
$N^{rec}_{\omega}(\times10^5)$	3.34± 0.04	3.25 ± 0.05	3.28± 0.04	3.21±0.04
$N^{\circ}_{\omega}(\times10^5)$	3.83± 0.05	3.75±0.06	3.78± 0.05	3.76± 0.04
$N^{rec}_{\omega\to\pi^0\gamma}(\times10^4)$	1.10±0.04	1.10± 0.04	1.08± 0.04	1.04±0.04
$N^{\circ}_{\omega\to\pi^0\gamma}(\times10^4)$	3.18±0.12	3.20±0.13	3.14±0.12	3.08±0.12
BR(%)	8.30±0.34	8.53±0.36	8.31± 0.34	8.19±0.30
((1.45+1.5) GeV)				
$N^{rec}_{\omega}(\times10^5)$	6.61±0.06	6.49± 0.08	6.43±0.06	6.36± 0.05
$N^{\circ}_{\omega}(\times10^5)$	7.67±0.07	7.58±0.09	7.50± 0.07	7.53± 0.06
$N^{rec}_{\omega\to\pi^0\gamma}(\times10^4)$	2.22± 0.06	2.12 ± 0.06	2.16± 0.06	2.11± 0.06
$N^{\circ}_{\omega\to\pi^0\gamma}(\times10^4)$	6.38± 0.18	6.11± 0.19	6.25 ± 0.18	6.20 ± 0.18
BR(%)	8.32 ±0.25	8.04±0.26	8.33± 0.25	8.20±0.25

Table M.1.: The efficiency ε, N^{rec}_{ω}, N°_{ω}, $N^{rec}_{\omega\to\pi^0\gamma}$, $N^{\circ}_{\omega\to\pi^0\gamma}$ and the measured branching ratio *BR* are organized for different particle identification cuts in three data sets. The blue text represents the values for the final particle identification cut shown in Fig. 5.5.

N. Systematic Effect Due to the Energy-Momentum Constraint

A piece of comprehensive information about the systematic uncertainty due to the energy-momentum conservation constraint, as discussed in Section 5.2.3.4, is demonstrated in this chapter. The missing mass spectra, the number of reconstructed $\omega \to \pi^0\gamma$ decays $N^{rec}_{\omega\to\pi^0\gamma}$, the reconstruction efficiency ε, and the branching ratio estimates $BR^{measured}_{\omega\to\pi^0\gamma}$ for different energy-momentum conservation constraints are discussed in the following.

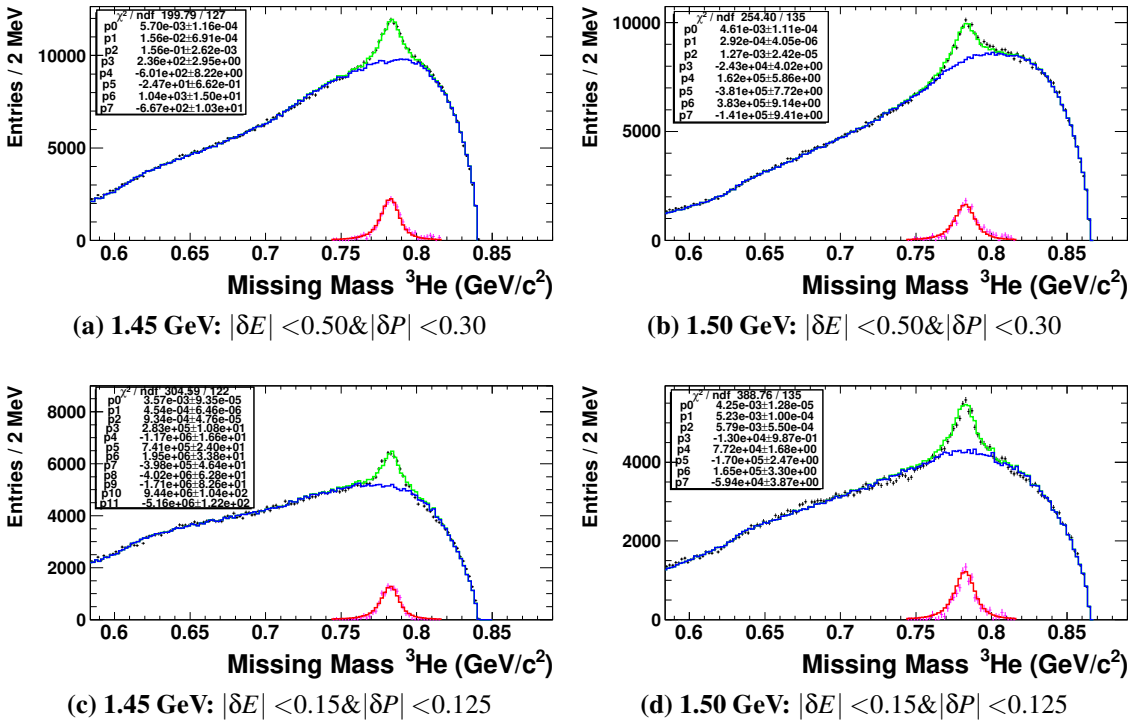

(a) 1.45 GeV: $|\delta E| < 0.50 \& |\delta P| < 0.30$ **(b) 1.50 GeV:** $|\delta E| < 0.50 \& |\delta P| < 0.30$

(c) 1.45 GeV: $|\delta E| < 0.15 \& |\delta P| < 0.125$ **(d) 1.50 GeV:** $|\delta E| < 0.15 \& |\delta P| < 0.125$

Figure N.1.: The exclusive missing mass spectra for two extreme energy-momentum conservation constraints are illustrated for two energies. The left and right columns are 1.45 GeV and 1.50 GeV beam energies, respectively. The number $N^{rec}_{\omega\to\pi^0\gamma}$ extracted using the fit functions is shown.

N.1. Missing Mass Spectra for Different Constraints

The missing mass spectra for the exclusive $\omega \to \pi^0\gamma$ final state are shown in Fig. N.1 for two extreme energy-momentum constraints as an illustration. Evidently, the phase space is changed for different selections. Resultantly, the systematic uncertainty will additionally be influenced by the fitting procedure. To quantize the systematic effect, the number $N^{rec}_{\omega\to\pi^0\gamma}$ for each energy-momentum conservation constraints are extracted and presented in Table N.1. $N^{\circ}_{\omega\to\pi^0\gamma}$ for each cut presented in Table N.1 is estimated from $N^{rec}_{\omega\to\pi^0\gamma}$ and ε. The points in Table N.1 are arranged in decreasing order of efficiency from top to down. The

numbers for the combined data set (1.45 GeV+1.50 GeV) are approximated by adding the numbers for two energies. The measured branching ratio $BR^{measured}_{\omega\to\pi^0\gamma}$ for each cut are listed in Table N.1 for three data sets. Wherein the value of N°_{ω} is the same as for the final measurement in Table 4.1. The systematic effect in the $BR^{measured}_{\omega\to\pi^0\gamma}$ due to energy-momentum conservation constraint has been quantified in Table 5.7.

dE-dP cut	ε_{exc} (%)	$N^{rec}_{\omega\to\pi^0\gamma}(\times10^4)$	$N^{\circ}_{\omega\to\pi^0\gamma}(\times10^4)$	$BR^{measured}_{\omega\to\pi^0\gamma}$(%)
(1.45 GeV)				
($\|\delta E\|$ <0.50&$\|\delta P\|$ <0.300)	37.26	2.05±0.08	5.50±0.22	14.79± 0.64
($\|\delta E\|$ <0.40&$\|\delta P\|$ <0.250)	36.97	1.60±0.07	4.33±0.20	11.63± 0.56
($\|\delta E\|$ <0.30&$\|\delta P\|$ <0.200)	36.40	1.27±0.06	3.49±0.17	9.38± 0.47
($\|\delta E\|$ <0.20&$\|\delta P\|$ <0.150)	34.74	1.08± 0.05	3.11±0.13	8.36± 0.37
($\|\delta E\|$ <0.15&$\|\delta P\|$ <0.125)	32.03	0.99±0.04	3.09±0.12	8.31± 0.34
($\|\delta E\|$ <0.10&$\|\delta P\|$ <0.100)	25.27	0.78±0.03	3.09±0.11	8.31± 0.50
(1.50 GeV)				
($\|\delta E\|$ <0.50&$\|\delta P\|$ <0.300)	37.09	1.66±0.08	4.48±0.21	11.85± 0.57
($\|\delta E\|$ <0.40&$\|\delta P\|$ <0.250)	36.77	1.56±0.07	4.24±0.18	11.22± 0.51
($\|\delta E\|$ <0.30&$\|\delta P\|$ <0.200)	36.14	1.24±0.06	3.43±0.16	9.08± 0.43
($\|\delta E\|$ <0.20&$\|\delta P\|$ <0.150)	34.35	1.08±0.04	3.14±0.12	8.31± 0.34
($\|\delta E\|$ <0.15&$\|\delta P\|$ <0.125)	31.50	1.00±0.04	3.18±0.11	8.40± 0.31
($\|\delta E\|$ <0.10&$\|\delta P\|$ <0.100)	24.73	0.77±0.03	3.12±0.11	8.24± 0.31
((1.45+1.5) GeV)				
($\|\delta E\|$ <0.50&$\|\delta P\|$ <0.300)		3.71±0.11	9.98±0.23	13.31± 0.42
($\|\delta E\|$ <0.40&$\|\delta P\|$ <0.250)		3.16±0.10	8.57±0.27	11.43± 0.38
($\|\delta E\|$ <0.30&$\|\delta P\|$ <0.200)		2.51±0.08	6.92±0.31	9.23± 0.32
($\|\delta E\|$ <0.20&$\|\delta P\|$ <0.150)		2.16± 0.06	6.25±0.18	8.33± 0.25
($\|\delta E\|$ <0.15&$\|\delta P\|$ <0.125)		1.99±0.05	6.27±0.16	8.36± 0.23
($\|\delta E\|$ <0.10&$\|\delta P\|$ <0.100)		1.55±0.04	6.21±0.16	8.28± 0.22

Table N.1.: A tabulation of the efficiency ε, $N^{rec}_{\omega\to\pi^0\gamma}$, $N^{\circ}_{\omega\to\pi^0\gamma}$ and $BR^{measured}_{\omega\to\pi^0\gamma}$ for different energy-momentum conservation constraints is presented for three data sets. The final values obtained by fitting the distributions in Fig. 4.16 are highlighted as blue.

O. Systematic Effect Due to the Monochromatic γ Selection Criterion

The specifications of the systematic studies of monochromatic γ selecting criterion discussed in Section 5.2.3.5 are elaborated in this chapter. The sample missing mass spectra, the numbers N^{rec}_{ω}, N°_{ω}, $N^{rec}_{\omega\to\pi^0\gamma}$ and $N^{\circ}_{\omega\to\pi^0\gamma}$, and the measured branching ratio $BR^{measured}_{\omega\to\pi^0\gamma}$ are summarized in the following.

O.1. Missing Mass Spectra for Different Criteria

The exclusive missing mass spectra for two extreme monochromatic γ selections are presented in Fig. O.1. The missing mass distributions and fits for the final cut are demonstrated in Fig. 4.16. Evidently, the monochromatic γ cuts are causing an immense effect on the kinematics, and thereby on the phase space of the backgrounds and signal. The line shape and the statistics are varied for two cuts. This is quantitatively seen in the reconstruction efficiencies ε_{exc} and the extracted numbers $N^{rec}_{\omega\to\pi^0\gamma}$ listed in Table O.1. The cuts in Table O.1 are

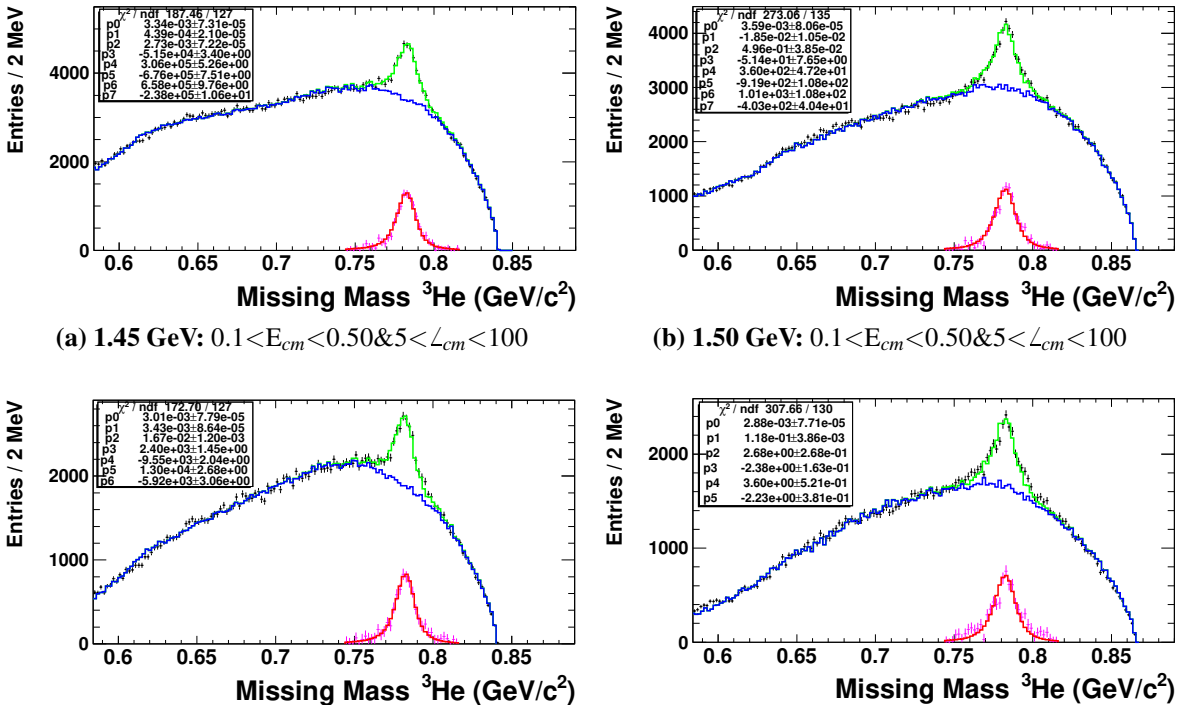

(a) 1.45 GeV: $0.1<E_{cm}<0.50\&5<\angle_{cm}<100$ **(b) 1.50 GeV:** $0.1<E_{cm}<0.50\&5<\angle_{cm}<100$

(c) 1.45 GeV: $0.22<E_{cm}<0.4\&35<\angle_{cm}<60$ **(d) 1.50 GeV:** $0.22<E_{cm}<0.4\&35<\angle_{cm}<60$

Figure O.1.: The exclusive missing mass spectra are shown for the two extreme cases of the monochromatic γ selection. The left and the right columns are the 1.45 GeV and 1.50 GeV data sets, respectively. The fit functions are shown. The numbers in the background-subtracted peaks $N^{rec}_{\omega\to\pi^0\gamma}$ are listed in Table O.1.

arranged from top to bottom in the decreasing order of efficiency. $N^{\circ}_{\omega\to\pi^0\gamma}$ is estimated from the corresponding ε_{exc} and $N^{rec}_{\omega\to\pi^0\gamma}$. The numbers for two energies are combined to estimate

the numbers in the entire data set. The branching ratio $BR^{measured}_{\omega\to\pi^0\gamma}$ for each cut is measured using the N°_{ω} from the final measurement, as listed in Table 4.1. The estimated $BR^{measured}_{\omega\to\pi^0\gamma}$ values have been arranged in Table O.1. The uncertainty that arises due to the systematic effect of the monochromatic γ selection is quantified Table 5.7.

Monochromatic cut	ε_{exc} (%)	$N^{rec}_{\omega\to\pi^0\gamma}(\times(10^4)$	$N^{\circ}_{\omega\to\pi^0\gamma}(10^4)$	$BR^{measured}_{\omega\to\pi^0\gamma}(\%)$
(1.45 GeV)				
(0.1< E_{cm} <0.50&5< $\angle_{cm}$ <100)	36.42	1.15±0.05	3.16±0.14	8.49± 0.39
(0.2< E_{cm} <0.50&5< $\angle_{cm}$ <100)	36.38	1.13±0.05	3.11±0.14	8.36± 0.38
(0.15< E_{cm} <0.48&20< $\angle_{cm}$ <90)	36.12	1.13±0.05	3.13±0.13	8.41± 0.38
(0.2< E_{cm} <0.50&30< $\angle_{cm}$ <80)	34.74	1.08±0.05	3.11±0.13	8.36± 0.37
(0.2< E_{cm} <0.45&35< $\angle_{cm}$ <75)	33.45	1.02±0.04	3.05±0.13	8.20± 0.37
(0.22< E_{cm} <0.4&30< $\angle_{cm}$ <80)	30.44	0.95±0.04	3.12±0.14	8.39± 0.39
(0.2< E_{cm} <0.50&35< $\angle_{cm}$ <60)	29.37	0.91±0.04	3.10±0.14	8.33± 0.39
(0.25< E_{cm} <0.42&37< $\angle_{cm}$ <61)	27.73	0.86±0.04	3.10±0.13	8.33± 0.38
(0.22< E_{cm} <0.4&35< $\angle_{cm}$ <60)	25.76	0.78±0.04	3.03±0.15	8.15± 0.41
(1.50 GeV)				
(0.1< E_{cm} <0.50&5< $\angle_{cm}$ <100)	36.02	1.10±0.05	3.05±0.13	8.07± 0.36
(0.2< E_{cm} <0.50&5< $\angle_{cm}$ <100)	35.98	1.12±0.05	3.11±0.13	8.22± 0.35
(0.15< E_{cm} <0.48&20< $\angle_{cm}$ <90)	35.71	1.11±0.05	3.11±0.13	8.22± 0.35
(0.2< E_{cm} <0.50&30< $\angle_{cm}$ <80)	34.35	1.08±0.04	3.14±0.12	8.31± 0.34
(0.2< E_{cm} <0.45&35< $\angle_{cm}$ <75)	33.04	1.04±0.05	3.15±0.12	8.33± 0.34
(0.22< E_{cm} <0.4&30< $\angle_{cm}$ <80)	29.98	0.92±0.04	3.07±0.13	8.12± 0.37
(0.2< E_{cm} <0.50&35< $\angle_{cm}$ <60)	28.94	0.91±0.04	3.15±0.13	8.31± 0.36
(0.25< E_{cm} <0.42&37< $\angle_{cm}$ <61)	27.31	0.81±0.04	2.97±0.13	7.86± 0.35
(0.22< E_{cm} <0.4&35< $\angle_{cm}$ <60)	25.30	0.78±0.04	3.08±0.14	8.15± 0.38
((1.45+1.5) GeV)				
(0.1< E_{cm} <0.50&5< $\angle_{cm}$ <100)		2.25±0.07	6.21±0.19	8.28± 0.26
(0.2< E_{cm} <0.50&5< $\angle_{cm}$ <100)		2.25±0.07	6.22±0.18	8.29± 0.26
(0.15< E_{cm} <0.48&20< $\angle_{cm}$ <90)		2.24±0.07	6.24±0.19	8.32± 0.26
(0.2< E_{cm} <0.50&30< $\angle_{cm}$ <80)		2.16±0.06	6.25±0.18	8.33± 0.25
(0.2< E_{cm} <0.45&35< $\angle_{cm}$ <75)		2.06±0.06	6.20±0.18	8.37± 0.25
(0.22< E_{cm} <0.4&30< $\angle_{cm}$ <80)		1.87±0.06	6.19±0.19	8.25± 0.27
(0.2< E_{cm} <0.50&35< $\angle_{cm}$ <60)		1.82±0.06	6.25±0.19	8.33± 0.26
(0.25< E_{cm} <0.42&37< $\angle_{cm}$ <61)		1.67±0.05	6.07±0.19	8.09± 0.26
(0.22< E_{cm} <0.4&35< $\angle_{cm}$ <60)		1.56±0.05	6.11±0.20	8.14± 0.28

Table O.1.: Various monochromatic γ selection criteria have been listed in the first column. The corresponding reconstruction efficiencies ε, $N^{rec}_{\omega\to\pi^0\gamma}$, $N^{\circ}_{\omega\to\pi^0\gamma}$ and $BR^{measured}_{\omega\to\pi^0\gamma}$ are arranged in the second, third, fourth and fifth column, respectively. The blue texts are the values for the cut employed in the final analysis.

Bibliography

[1] E. Czerwinski, S. Eidelman, C. Hanhart, B. Kubis, A. Kupsc, et al. MesonNet Workshop on Meson Transition Form Factors. 2012. v, 2, 5, 6, 7, 16

[2] M. Hayakawa and T. Kinoshita. Pseudoscalar pole terms in the hadronic light-by-light scattering contribution to muon $g-2$. Phys. Rev. D, 57:465–477, Jan 1998. v, 2

[3] Johan Bijnens and Joaquim Prades. The Hadronic Light-by-Light Contribution to the Muon Anomalous Magnetic Moment: Where do we stand? Mod.Phys.Lett., A22:767–782, 2007. v, 2

[4] Joaquim Prades, Eduardo de Rafael, and Arkady Vainshtein. The hadronic light-by-light scattering contribution to the muon and electron anomalous magnetic moments. In Lepton Dipole Moments, pages 303–317. WORLD SCIENTIFIC, dec 2009. v, 2

[5] Fred Jegerlehner and Andreas Nyffeler. The Muon g-2. Phys.Rept., 477:1–110, 2009. v, 2

[6] Igor Danilkin, Christoph Florian Redmer, and Marc Vanderhaeghen. The hadronic light-by-light contribution to the muon's anomalous magnetic moment. Prog. Part. Nucl. Phys., 107:20–68, 2019. v, 2

[7] T. Aoyama, N. Asmussen, M. Benayoun, J. Bijnens, T. Blum, M. Bruno, I. Caprini, C.M. Carloni Calame, M. C, G. Colangelo, and et al. The anomalous magnetic moment of the muon in the standard model. Physics Reports, 887:1166, Dec 2020. v, 2

[8] B. Abi, T. Albahri, S. Al-Kilani, D. Allspach, L.P. Alonzi, A. Anastasi, A. Anisenkov, F. Azfar, K. Badgley, S. Baeler, and et al. Measurement of the positive muon anomalous magnetic moment to 0.46 ppm. Physical Review Letters, 126(14), Apr 2021. v, 2

[9] T. Albahri et al. Magnetic Field Measurement and Analysis for the Muon g-2 Experiment at Fermilab. Phys. Rev. A, 103(4):042208, 2021. v, 2

[10] Sz. Borsanyi, Z. Fodor, J. N. Guenther, C. Hoelbling, S. D. Katz, L. Lellouch, T. Lippert, K. Miura, L. Parato, K. K. Szabo, F. Stokes, B. C. Toth, Cs. Torok, and L. Varnhorst. Leading hadronic contribution to the muon magnetic moment from lattice QCD. Nature, 593(7857):51–55, apr 2021. v, 2

[11] L.G. Landsberg. Electromagnetic decays of light mesons. Phys.Rept., 128:301–376, 1985. v, 4, 5, 7, 8, 9

[12] R.I. Dzhelyadin et al. Study of the electromagnetic transition form-factor in $\omega \to \pi^0\mu^+\mu$ decay. Physics Letters B, 102(4):296 – 298, 1981. v, 9, 11, 13, 15, 17, 19, 20

[13] R. Arnaldi et al. Study of the electromagnetic transition form-factors in $\eta \to \mu^+\mu^-\gamma$ and $\omega \to \mu^+\mu^-\pi^0$ decays with NA60. Phys.Lett., B677:260–266, 2009. v, 9, 11, 13, 15, 17, 18, 19, 20

[14] Antonio Uras. Measurement of the η and ω dalitz decays transition form factors in p-A collisions at 400 GeV/c with the NA60 apparatus. J.Phys.Conf.Ser., 270:012038, 2011. v, 9, 13, 15, 19, 20

[15] R. Arnaldi, K. Banicz, K. Borer, J. Castor, B. Chaurand, W. Chen, C. Cical, A. Colla, P. Cortese, S. Damjanovic, and et al. Precision study of the $\eta \to e^+e^-\gamma$ and $\omega \to \mu^+\mu^-\pi^0$ electromagnetic transition form-factors and of the $\rho \to \mu^+\mu^-$ line shape in na60. Physics Letters B, 757:437444, Jun 2016. v, 9, 11, 13, 15, 17, 18, 19

[16] Carla Terschlüsen. Electromagnetic Transition Form Factors of Pseudoscalar and Vector Mesons. Diploma thesis, Justus-Liebig-Universität Gießen, 2010. v, 10, 11, 12, 13, 15

[17] C. Terschlusen and S. Leupold. Electromagnetic Transition Form Factors of Mesons. Prog. Part. Nucl. Phys., 67:401–405, 2012. v, 10, 12, 13, 15

[18] Carla Terschlüsen and Stefan Leupold. Electromagnetic transition form factors of light vector mesons. Phys.Lett., B691:191–201, 2010. v, 11, 12, 13, 15, 16

[19] C. Terschlüsen, S. Leupold, and M.F.M. Lutz. Electromagnetic Transitions in an Effective Chiral Lagrangian with the η' and Light Vector Mesons. Eur.Phys.J., A48:190, 2012. v, 11, 12, 13, 15, 18

[20] Sebastian P. Schneider, Bastian Kubis, and Franz Niecknig. The $\omega \to \pi^0\gamma^*$ and $\phi \to \pi^0\gamma^*$ transition form factors in dispersion theory. Phys.Rev., D86:054013, 2012. v, 11, 13, 14, 15, 16, 18

[21] I.V. Danilkin, C. Fernández-Ramírez, P. Guo, V. Mathieu, D. Schott, M. Shi, and A.P. Szczepaniak. Dispersive analysis of $\omega/\phi \to 3\pi, \pi\gamma*$. Phys. Rev. D, 91(9):094029, May 2015. v, 11, 15, 16, 17, 18

[22] I. Caprini. Testing the consistency of the $\omega\pi$ transition form factor with unitarity and analyticity. Phys. Rev. D, 92(1):014014, 2015. v, 11, 16

[23] B. Ananthanarayan, I. Caprini, and B. Kubis. Constraints on the $\omega\pi$ form factor from analyticity and unitarity. Eur. Phys. J. C, 74(12):3209, 2014. v, 15, 16

[24] B. Ananthanarayan, Irinel Caprini, and Bastian Kubis. Constraints on the $\omega\pi$ form factor from analyticity and unitarity. Int. J. Mod. Phys., 31(14n15):1630020, 2016. v, 15

[25] Pere Masjuan and Pablo Sanchez-Puertas. Phenomenology of bivariate approximants: the $\pi^0 \to e^+e^-$ case and its impact on the electron and muon g-2. ARXIV.1504.07001, 4 2015. v, 16

[26] M. Albaladejo, I. Danilkin, S. Gonzalez-Solis, D. Winney, C. Fernandez-Ramirez, A.N. Hiller Blin, V. Mathieu, M. Mikhasenko, A. Pilloni, and A. Szczepaniak. $\omega \to 3\pi$ and $\omega\pi^0$ transition form factor revisited. ARXIV.2006.01058, 6 2020. v, 16, 17, 18

[27] Mohammad Ahmady, Satvir Kaur, Chandan Mondal, and Ruben Sandapen. Light-front holographic radiative transition form factors for light mesons. Physical Review D, 102(3), aug 2020. v, 17, 18, 19, 158

[28] P. Adlarson et al. Measurement of the $\omega \to \pi^0 e^+ e^-$ and $\eta \to e^+ e^- \gamma$ Dalitz decays with the A2 setup at MAMI. Phys. Rev. C, 95(3):035208, 2017. v, 10, 11, 13, 15, 16, 17, 18, 19, 158

[29] M. H. Johnson and E. Teller. Classical field theory of nuclear forces. Phys. Rev., 98:783–787, May 1955. 1

[30] Hans-Peter Duerr and Edward Teller. Interaction of antiprotons with nuclear fields. Phys. Rev., 101:494–495, Jan 1956. 1

[31] Hans-Peter Duerr. Relativistic effects in nuclear forces. Phys. Rev., 103:469–480, Jul 1956. 1

[32] Yoichiro Nambu. Possible existence of a heavy neutral meson. Phys. Rev., 106:1366–1367, Jun 1957. 1

[33] G. Breit. Nucleon-nucleon spin-orbit interaction and the repulsive core. Phys. Rev., 120:287–292, Oct 1960. 1

[34] Yasunori Fujii. On the analogy between strong interaction and electromagnetic interaction. Progress of Theoretical Physics, 21(2):232–240, 1959. 1

[35] J.J Sakurai. Theory of strong interactions. Annals of Physics, 11(1):1 – 48, 1960. 1

[36] Geoffrey F. Chew. Three-pion resonance or bound state. Phys. Rev. Lett., 4:142–143, Feb 1960. 1

[37] Maglić, B. C. and Alvarez, L. W. and Rosenfeld, A. H. and Stevenson, M. L. Evidence for a $t = 0$ three-pion resonance. Phys. Rev. Lett., 7:178–182, Sep 1961. 1

[38] B. Maglich. Discovery of omega meson-first neutral vector meson: one researcher's personal account - Discovery story. Adv. Exp. Phys., 5:79, 1976. 1

[39] Beringer et al. Review of particle physics. Phys. Rev. D, 98:030001, Aug 2018. 1, 5, 7, 18, 39, 45, 65, 92, 98, 101, 104, 117, 127

[40] V. A. Beylin, V. I. Kuksa, and G. M. Vereshkov. Radiative decay of vector mesons in the gauge model of quark-meson interaction. ARXIV:0803.0061, 2008. 1

[41] Norman M. Kroll, T. D. Lee, and Bruno Zumino. Neutral Vector Mesons and the Hadronic Electromagnetic Current. Phys. Rev., 157:1376–1399, May 1967. 4, 5, 7

[42] Heath Bland O'Connell, B. C. Pearce, Anthony William Thomas, and Anthony Gordon Williams. $\rho - \omega$ mixing, vector meson dominance and the pion form-factor. Prog. Part. Nucl. Phys., 39:201–252, 1997. 4

[43] John F. McGowan. An isobar model for $e^+e^- \to \pi^+\pi^-\pi^0\pi^0$. ARXIV.HEP-PH/9501399, 1995. 5, 7

[44] Norman M. Kroll and Walter Wada. Internal pair production associated with the emission of high-energy gamma rays. Phys.Rev., 98:1355–1359, 1955. 8

[45] Susan Schadmand. Electromagnetic Transition Form Factors of Light Mesons. JPS Conf. Proc., 26:022001, 2019. 10

[46] M.F.M. Lutz and S. Leupold. On the radiative decays of light vector and axial-vector mesons. Nucl.Phys., A813:96–170, 2008. 10, 11

[47] S. Leupold and M. F. M. Lutz. Hadronic three-body decays of light vector mesons. Eur. Phys. J., A39:205–212, 2009. 10

[48] M. F. M. Lutz and E. E. Kolomeitsev. On meson resonances and chiral symmetry. Nucl. Phys., A730:392–416, 2004. 10

[49] G. Köpp. Dispersion calculation of the transition form factor $f_{\pi\omega\gamma}(t)$ with cut contributions. Phys. Rev. D, 10:932–940, Aug 1974. 11, 13, 15, 16

[50] Franz Niecknig, Bastian Kubis, and Sebastian P. Schneider. Dispersive analysis of $\omega \to 3\pi$ and $\phi \to 3\pi$ decays. Eur.Phys.J., C72:2014, 2012. 14, 17

[51] N. N. Khuri and S. B. Treiman. Pion-pion scattering and $K^{\pm} \to 3\pi$ decay. Phys. Rev., 119:1115–1121, Aug 1960. 16

[52] Carla Terschlüsen, Bruno Strandberg, Stefan Leupold, and Fabian Eichstädt. Reactions with pions and vector mesons in the sector of odd intrinsic parity. Eur. Phys. J. A, 49:116, 2013. 17

[53] P. Adlarson et al. Measurement of the $\omega \to \pi^+\pi^-\pi^0$ Dalitz plot distribution. Phys. Lett. B, 770:418–425, 2017. 17

[54] M. Ablikim et al. Dalitz Plot Analysis of the Decay $\omega \to \pi^+\pi^-\pi^0$. Phys. Rev. D, 98(11):112007, 2018. 17

[55] H.M. Choi and Chueng-Ryong Ji. Light cone quark model predictions for radiative meson decays. Nucl. Phys. A, 618:291–316, 1997. 18

[56] Ho-Meoyng Choi. Space and time-like form factors for $\omega \to \pi\gamma^*$ and $K^* \to K\gamma^*$ in light-front quark model. Phys. Rev. D, 77:097301, 2008. 18

[57] Jiang-hao Yu, Bo-Wen Xiao, and Bo-Qiang Ma. Space-like and time-like pion-rho transition form factors in the light-cone formalism. J. Phys. G, 34:1845–1860, 2007. 18

[58] J.R. Forshaw and R. Sandapen. An AdS/QCD holographic wavefunction for the rho meson and diffractive rho meson electroproduction. Phys. Rev. Lett., 109:081601, 2012. 18

[59] M. Ahmady and R. Sandapen. Predicting the isospin asymmetry in $B- > K*\gamma$ using holographic AdS/QCD Distribution Amplitudes for the K*. Phys. Rev. D, 88:014042, 2013. 18

[60] Mohammad Ahmady, Ruben Sandapen, and Neetika Sharma. Diffractive ρ and ϕ production at HERA using a holographic AdS/QCD light-front meson wave function. Phys. Rev. D, 94(7):074018, 2016. 18

[61] Mohammad Ahmady, Chandan Mondal, and Ruben Sandapen. Dynamical spin effects in the holographic light-front wavefunctions of light pseudoscalar mesons. Phys. Rev. D, 98(3):034010, 2018. 19

[62] K. Shekhter, C. Fuchs, Amand Faessler, M. Krivoruchenko, and B. Martemyanov. Dilepton production in heavy ion collisions at intermediate energies. Phys. Rev. C, 68:014904, 2003. 19

[63] C. Fuchs, Amand Faessler, D. Cozma, B.V. Martemyanov, and M.I. Krivoruchenko. Dilepton and vector meson production in elementary and in heavy ion reactions. Nucl. Phys. A, 755:499–502, 2005. 19

[64] Wen Qian and Bo-Qiang Ma. Tri-meson-mixing of π-η-η′ and ρ-ω-ϕ in the light-cone quark model. Eur. Phys. J. C, 65:457–465, 2010. 19

[65] S. Schadmand. ω decays in the reaction $pd \rightarrow {}^{3}\mathrm{HeX}$ at t_p=1.45 GeV, proposal nr. 208. Proposal, IKP / WASA-at-COSY, http://wasasrv.ikp.kfa-juelich.de/WasaWiki/images/5/59/Su100406_omega_proposal.pdf, 2010. 20, 35

[66] S. Schadmand. Study of ω decays in proton-proton interactions, proposal nr. 209. Proposal, IKP / WASA-at-COSY, http://wasasrv.ikp.kfa-juelich.de/WasaWiki/images/0/05/MW100405_omega_pac38.pdf, 2010. 20, 35

[67] Chr. Bargholtz et al. The WASA detector facility at CELSIUS. Nucl.Instrum.Meth., A594:339–350, 2008. 21, 33

[68] COSY Collaboration, B. Hoistad, and J. Ritman. Proposal for the wide angle shower apparatus (WASA) at COSY-julich: WASA at COSY. ARXIV.NUCL-EX/0411038, 2004. 21, 22, 23, 25, 29, 33, 43, 82

[69] R. Maier, U. Bechstedt, J. Dietrich, S. Martin, D. Prasuhn, et al. Cooler synchrotron COSY. Nucl.Phys., A626:395C–403C, 1997. 21

[70] R. Maier. Cooler synchrotron COSY: Performance and perspective. Nucl.Instrum.Meth., A390:1–8, 1997. 21

[71] U. Bechstedt et al. Luminosity considerations for internal and external experiments at cosy. EPAC-2004-TUPLT046, 2004. 21

[72] C. F. Redmer. In Search of the Box-Anomaly with the WASA facility at COSY. Phd thesis, Bergischen Universitaet Wuppertal, 2010. 21, 27, 31, 32, 39, 42, 44, 46, 51, 66, 82

[73] D. Prasuhn, J. Dietrich, R. Maier, R. Stassen, H.J. Stein, et al. Electron and stochastic cooling at COSY. Nucl.Instrum.Meth., A441:167–174, 2000. 21

[74] H. Stockhorst. Compensation of mean energy loss due to an internal target by application of a barrier bucket and stochastic momentum cooling at COSY. In Cooling Conference, COOL 09, 2009. Record converted from VDB: 12.11.2012. 21

[75] Curt Ekstrom. The CELSIUS/WASA pellet target system. Phys.Scripta, T99:169–172, 2002. 23

[76] F. Lang. Development of a hydrogen pellet target for the panda experiment. diploma thesis, Uppsala Universitet / Innsbruck University, 2004. 23

[77] M. Zielinski. Feasibility study of the $\eta \to \pi^+\pi^-\pi^0$ decay using WASA-at-COSY apparatus. diploma thesis, Jagiellonian University, 2008. 29

[78] C. Pauly. Light Meson Production in pp Reactions at CELSIUS/WASA above the η Threshold. Phd thesis, Universitet Hamburg. 29, 39, 40

[79] R.J.M.Y Ruber et al. An ultra-thin-walled solenoid for the CELSIUS/WASA experiments. Nuclear Instruments and Methods in Physics Research Section A: Accelerators, Spectrometers, Detectors and Associated Equipment, 503(3):431 – 444, 2003. 29

[80] M. Jacewicz. Measurement of the Reaction $pp \to pp\pi^+\pi^-\pi^0$ with CELSIUS/WASA at 1.36 GeV. Phd dissertation, Uppsala University, 2004. 30, 31, 42, 43

[81] L. Yurev. Performance of the MDC−Central Part of WASA−Before Installation at COSY. Phd thesis, Voronezh State University, 2006. 30

[82] H. Bhatt. Study of a rare decay $\eta \to \pi^+\pi^-\gamma$ using WASA-at-COSY. Phd thesis, Indian Institute of Technology, Bombay, 2011. 31, 32

[83] I. Koch. Measurements of $2\pi^0$ and $3\pi^0$ Production in Proton-Proton Collisions at a Center of Mass Energy of 2.465 GeV. Doctoral thesis, Uppsala University, 2004. 31, 32, 46

[84] D. Coderre. The Branching Ratio and CP-Violating Asymmetry of $\eta \to \pi^+\pi^-e^+e^-$. Doctoral thesis, Ruhr-Universitaet Bochum, 2012. 33, 43, 46, 51, 52, 53, 54, 59, 66, 67, 103

[85] H. Kleines et al. The new DAQ system for WASA at COSY. In Real Time Conference, 2005. 14th IEEE-NPSS, https://ieeexplore.ieee.org/document/1547439, June 2005. 33

[86] H. Kleines et al. Performance issues of the new DAQ system for WASA at COSY. IEEE Transactions on Nuclear Science, 55(1):261–264, Feb 2008. 33

[87] H. Kleines, W. Erven, P. Wstner, A. Ackens, G. Kemmerling, M. Wolke, and K. Zwoll. Development of a High Resolution TDC Module for the WASA Detector System Based on the GPX ASIC. In IEEE NSS 2006 Conference Record, San Diego, CA, USA, 29.10.2006 - 04.11.2006, 2006. Record converted from VDB: 12.11.2012. 33

[88] K Fransson and CELSIUS/WASA Collaboration. The Trigger System of the CELSIUS/WASA Detector. Physica Scripta, 2002(T99):176, jan 2002. 33, 34

[89] C. Zheng. Matching trigger effciency of forward detector of WASA-at-COSY. Annual report, IKP / COSY, 2009. 34

[90] K. Schönning et al. Production of the ω meson in the $pd \rightarrow {}^3He\omega$ reaction at 1450-MeV and 1360-MeV. Phys. Rev., C79:044002, 2009. 35, 37, 38, 63, 66, 91, 103, 127

[91] S. Barsov et al. Study of omega-meson production in pp collisions at ANKE. Eur. Phys. J., A31:95–104, 2007. 35

[92] I. Fröhlich, Lorenzo Cazon, T. Galatyuk, V. Hejny, R. Holzmann, et al. PLUTO: A Monte Carlo simulation tool for hadronic physics. PoS, ACAT2007:076, 2007. 36, 37

[93] CERN Application Software Group Computing and Network Division. GEANT - Detector Description and Simulation Tool. Technical report, CERN Program Library Long Writeup W5013, 1993. 36, 38

[94] A. Mussgiller V. Hejny, M. Hartmann. RootSorter : A new analysis framework for ANKE. Annual report, IKP / COSY, 2002-2003. 37, 38

[95] Rene Brun and Fons Rademakers. ROOT an object oriented data analysis framework. Nuclear Instruments and Methods in Physics Research Section A: Accelerators, Spectrometers, Detectors and Associated Equipment, 389(1-2):81 – 86, 1997. New Computing Techniques in Physics Research V. 37

[96] CERN. http://www.cern.ch. 37

[97] G. Agakishiev et al. The High-Acceptance Dielectron Spectrometer HADES. Eur. Phys. J., A41:243–277, 2009. 37

[98] F. James. W515: N-Body Monte Carlo Event Generator. Technical report, CERNLIB Documentation: Short Writeups, 1975. https://cmd.inp.nsk.su/old/cmd2/manuals/cernlib/shortwrups/node266.html. 37

[99] Schönning et al. Production of η and 3π mesons in the pd→ 3HeX reaction at 1360 and 1450 MeV. The European Physical Journal A, 45(1):11–21, 2010. 37, 63, 66, 91, 127

[100] Karin Schönning. Meson production in pd collisions. Phd thesis, Uppsala University, 2009. 37, 127

[101] M. Bashkanov et al. Exclusive measurements of : The {ABC} effect revisited. Physics Letters B, 637(4-5):223 – 228, 2006. 37, 91, 127

[102] M. Andersson et al. Isospin resolved double pion production in the reaction p+d→ ^{3}He+2π. Phys. Lett., B485:327–333, 2000. 37, 127

[103] B. Mayer et al. The Reactions $pd \rightarrow {}^3He\eta$ and $pd \rightarrow {}^3He\pi^+\pi^-$ near the eta threshold. Phys. Rev., C53:2068–2074, 1996. 37, 127

[104] J. M. Cameron, P. Kitching, J. Pasos, J. Thekkumthala, R. Abegg, D. A. Hutcheon, C. A. Miller, S. A. Elbakr, and A. H. Hussein. Differential Cross-section and Analyzing Powers for the $PD \rightarrow {}^3$He π^0 Reaction in the Δ Resonance Region. Nucl. Phys., A472:718–732, 1987. 37, 127

[105] S. Leupold and M.F.M. Lutz. Hadronic three-body decays of light vector mesons. Eur.Phys.J., A39:205–212, 2009. 38

[106] C. Amsler et al. η-decays into three pions. Physics Letters B, 346(1):203 – 207, 1995. 38

[107] Thimo Petri. Anomalous decays of pseudoscalar mesons. PhD thesis, Juelich, Forschungszentrum, 2010. 38

[108] W. R. Leo. Techniques for Nuclear and Particle Physics Experiments. Springer-Verlag, 1994. 39, 45

[109] L. Heijkenskjöld. $\omega \to \pi^+\pi^-\pi^0$ / $\omega \to \pi^+\pi^-$ (*pd*). Analysis report, IKP / COSY, May 2014. 40, 54

[110] Lena Heijkenskjöld. Hadronic Decays of the ω Meson. Phd thesis, Uppsala Universitet, 2016. 40, 46, 53, 54, 60, 117

[111] P. N. Vlasov. Analysis of the $\eta \to 3\pi^0$ decay in the pp interaction. Phd thesis, Ruhr-Universitaet Bochum, 2008. 42

[112] V. Hejny. Photoproduktion von η -Mesonen an Helium 4. Doctoral thesis, Justus-Liebig-Universität Gieβen, 1998. 42

[113] T. C. Awes et al. A simple method of shower localization and identification in laterally segmented calorimeters. Nuclear Instruments and Methods in Physics Research Section A: Accelerators, Spectrometers, Detectors and Associated Equipment, 311(1-2):130 – 138, 1992. 42

[114] A. Povtorejko M. Komogorov, B. Morosov and V. Tikhomirov. Track recognition algorithm for wasa mini drift chamber (mdc). Technical report, IKP / COSY : WASA Collaboration Internal Report,. 43

[115] Rudolph Emil Kalman. A new approach to linear filtering and prediction problems. Transactions of the ASME–Journal of Basic Engineering, 82(Series D):35–45, 1960. 43

[116] R. Fruhwirth. Application of Kalman filtering to track and vertex fitting. Nucl. Instrum. Meth. A, 262:444–450, 1987. 43

[117] M. Zurek. Determination of the neutron detection efficiency in the WASA-at-COSY detector setup. Bachelor thesis, Jagiellonian University Cracow, Poland, 2011. 44

[118] M. Nanova et al. In-medium omega mass from the $\gamma + Nb \to \pi^0\gamma + X$ reaction. Phys. Rev., C82:035209, 2010. 47

[119] V. Hejny. Calorimeter calibration. Technical report, IKP / COSY, WASA-at-COSY Collaboration Internal Wiki - Software: Calorimeter Calibration, 2010. 49

[120] L. Landau. On the energy loss of fast particles by ionization. J.Phys.(USSR), 8:201–205, 1944. 51, 52

[121] Cesare Bini. Data analysis in Experimental Elementary Particle Physics. Technical note, Dipartimento di Fisica, Sapienza Universitá and INFN, Roma, 2013-2014. 61, 72, 96

[122] D. Lersch. Investigation of Dipion Final State Interactions in $pp \to pp\eta[\eta \to \pi^+\pi^-\gamma]$ with the WASA-at-COSY Facility. Phd thesis, Bergische Universitaet Wuppertal, 2014. 67, 69, 70

[123] Benno List. Why and when to optimize efficiency times purity. Technical note, ETH Zürich, Institute for Particle Physics, https://www.desy.de/ blist/notes/whyeffpur.ps.gz, 2002. 72

[124] Roberto Versaci et al. Study of the $\eta \to \pi^+\pi^- e^+ e^-$ decay at KLOE. J.Phys.Conf.Ser., 171:012050, 2009. 86

[125] Eugenia Maria Teresa Irene Puccio. First observation of the charmless decay $B^+ \to K^+\pi^0\pi^0$ and study of the Dalitz plot structure. Doctor of Philosophy, University of Warwick, 2011. 97

[126] E. Byckling and K. Kajantie. Particle Kinematics. A Wiley-Interscience Publication, 1973. 98, 129

[127] D. V. Bugg, D. C. Salter, G. H. Stafford, R. F. George, K. F. Riley, and R. J. Tapper. Nucleon-nucleon total cross sections from 1.1 to 8 GeV/c. Phys. Rev., 146:980–992, Jun 1966. 103

[128] Patrik Adlarson. Studies of the Decay $\eta \to \pi^+\pi^-\pi^0$ with WASA-at-COSY. Doctoral thesis, Uppsala Universitet, 2012. 104

[129] Roger Barlow. Systematic errors: Facts and fictions. In Advanced Statistical Techniques in Particle Physics., pages 134–144, http://www.ippp.dur.ac.uk/Workshops/02/statistics/proceedings//barlow.pdf, 2002. 104, 105

[130] John R. Taylor. An Introduction to Error Analysis - The Study of Uncertainties in Physical Measurements. Springer-Verlag, 1994. 106

[131] John Philpott Joseph Rothberg Roberta Bigelow, Michael J. Moloney. Nuclear and Particle Physics Simulations: The Consortium of Upper-Level Physics Software. Wiley, 1995. 129, 130

List of Figures

List of Tables

List of acronyms

CELSIUS Cooling with Electrons and Storing of Ions from the Uppsala Synchrotron

CLEO Particle detector used at the Cornell Electron Storage Ring (CESR)

KLOE K LOng Experiment

WASA Wide Angle Shower Apparatus

QCD Quantum Chromodynamics

QED Quantum Electrodynamics

QFT Quantum Field Theory

ChPT Chiral Perturbation Theory

LbL Light by Light

EFT Effective Field Theories

VMD Vector Meson Dominance

KT Khuri-Treiman

PDG Particle Data Group

CAD Computer-Aided Design

COSY COoler SYnchrotron accelerator

ANKE Apparatus for Studies of Nucleon and Kaon Ejectiles

PAX Polarized Antiproton eXperiments

FD Forward Detector

FRH Forward Range Hodoscope

FPC Forward Proportional Chamber

FTH Forward Trigger Hodoscope

CD Central Detector

MDC Mini Drift Chamber

PSB Plastic Scintillator Barrel

SEC Scintillator Electromagnetic Calorimeter

SQDC Slow Charge-to-Digital Converter

SCS Superconducting Solenoid

PMT Photomultiplier Tube

RAID Redundant Array of Independent Disks

DAQ Data Acquisition System

TF Track Fitting

PID Particle Identification

PR Pattern Recognition

TR Trigger

$\mathbf{L}_A$ Average Luminosity

BR Branching Ratio

cs Cross Section

PS Phase Space

Acknowledgements

Completion of this doctoral dissertation was possible with the support of several people. I would like to express my sincere gratitude to all of them. First of all, I am extremely grateful to my research supervisors, Prof. Frank Goldenbaum and PhD habil. Susan Schadmand, for their valuable guidance, scholarly inputs and consistent encouragement, I received throughout the research work. This feat was possible only because of the unconditional support provided by them.

I am very thankful to Prof. James Ritman for making it possible for me to write this thesis at the Forschungszentrum Jülich by giving me an opportunity to work there, providing me with the infrastructure to work and taking keen interest in the project, and for his helpful advice and critical reading of my thesis.

"Thanks"is a small word to say for all great support and kindness I have always received from Dr. Daniel Lersch. He is a person who was always upfront for any help I needed from him even before I ask him. I owe my deepest gratitude to Dr. Daniel Lersch, for always being there as a good friend, mentor, well wisher, office mate and peer. He was always there as a strong support pillar in all ups and downs throughout and in all possible ways, sometimes, beyond his comfort zone. His valuable guidance have helped me polishing my thesis throughout. The thesis would not have come to successful completion without his support and encouragement.

My sincere thanks to Dr. Volker Hejny for all worthwhile discussions, providing his support and encouragement, and for his valuable remarks to shape the scientific approach and this dissertation.

My thanks are due to Dr. Andrzej Kupsc, Prof. Dr hab. Pawe Moskal and Dr. Magnus Wolke for their valuable suggestions and comments on the WASA analysis to improve the techniques.

I would also like to express my deep sense of gratitude to Dr. Florian Hauenstein for his immense support as a friend and peer. His selfless support gave a me a positive push to face the hurdles came in my way during my PhD work with great courage.

I also take this opportunity to express tremendous thanks to Dr. Florian Bergmann for providing moral and technical support as a friend by accompanying me in various tough and cheerful occasions during my stay at Jülich.

My hearty thanks are due especially to Dr. Lena Heijkenskjöld, Dr. Elena Perez del Rio and Dr. Daniel Coderre to always be there as a good friend, for supporting me morally, emotionally and functionally and for taking pain to read the proof of my thesis.

I would like to Dr. Siddesh Sawant, Dr. Kacper Topolnick to for all friendly discussions and idea sharing, and going through my dissertation.

My special thanks to Dr. Amit Shukla to always motivate and support to accomplish my PhD. He has acted as a friend, peer and mentor based upon situations.

I would also like to thank all the members of WASA-at-COSY collaboration for vivid discussions on various topics during the FIKA and analysis meetings. I would especially like to thank for Kay Demmich for being a good friend, and discussions related to the data analysis. Many thanks to Dr. Christoph Florian Redmer and Dr. Patrick Wurm for the

various helpful discussions about WASA analysis. I am thankful to Ms. Ankita Goswami, Mr. Wiktor Bardan and Dr. Himani Bhatt for their friendly support.

I am obliged to staff members of the Computer Center, library, and administration of WASA. I am grateful for their support during the period of my thesis. This work might not have reached the end without their help.

I wish to take this occasion pay my sincere regards to all my teachers from whom I have borrowed the building blocks of my knowledge, especially to the lecturers of the physics department, Goa University; Prof. Kaustubh R.S. Priolkar, Prof. Ramesh V. Pai, Prof. Joseph Alfred Erwin Desa and Prof. Prabhakar Sarode, from whom I learned the basics of Physics and Maths.

I sincerely acknowledge the Beam Allocation Committee of WASA for their generous time allocation.

I thank Prof. Dr. K. H. Kampert, Head of the Department of Physics, Wuppertal University, for support and guidance on administrative procedures.

Not the least, I will always cherish the memories of long association with Dr. Iryna Schaätti-Ozerianska and Dr. Magdalena Skurzok; many-many heartily thanks for being there to listen, cheer, drink, and console. Thanks for always providing me moral-emotional support, strengthen my moral and motivated me to move forward to the success. Thank you for sharing with me all cheerful moments and strengthen me in my weaknesses.

I have been blessed with a friendly and cheerful group of fellow students at WASA and IKP1. I would like to thank to IKP1 members for making my stay memorable, especially to; Dr. Ludovico Bianchi, Dr. Maria Zurek, Dr. Lu, Cao, Dr. Dariusch Deermann, Dr. Rene Dosdall, Dr. Simone Esch, Dr. Albrecht Gillitzer, Dr. Andre Goerres, Dr. Sedigheh Jowzaee, Dr. Elisabetta Prencipe, Dr. Matthias Röder, Guenther Sterzenbach, Dr. Tobias Stockmanns and Dr. Huagen Xu for the nice time during lunch and other occasions and for the funny and interesting PhD-seminar talks. My especial thanks and regards to Dr. Maria Zurek, Dr. Ludovico Bianchi and Michael C. Kunkel for supporting me in the bad phase of my life as friends. Thanks for sharing such cheerful moments and loving memories.

I will never forget the love and support of my friends Ms. Queenie Fernandes, Mr. Shashank Vyas and Mr. Salman Rayan Shariff.

I wish to express my gratitude to my loving family for their love and encouragement throughout my life. My especial thanks to my father who have always strengthened me and motivated me to never give up in my life. My heartily gratitude to my late grandmother for her warmth, love and best regards. Thereby, I dedicate this dessertation to my late granddmother Mrs. Sabreen Begum.

One of the joys of completion is to look over the journey past and remember all the friends and family who have helped and supported me along this long but fulfilling road.

Erklärung

Ich versichere, die Arbeit selbständig verfasst zu haben, nur die in der Dissertation angegebenen Hilfsmittel benutzt und alle wörtlich oder inhaltlich übernommenen Stellen als solche gekennzeichnet zu haben, und dass die Dissertation in der gegenwärtigen oder einer anderen Fassung noch keinem anderen Fachbereich, keiner Gesamthoch-schule und keiner anderen wissenschaftlichen Hochschule vorgelegen hat.